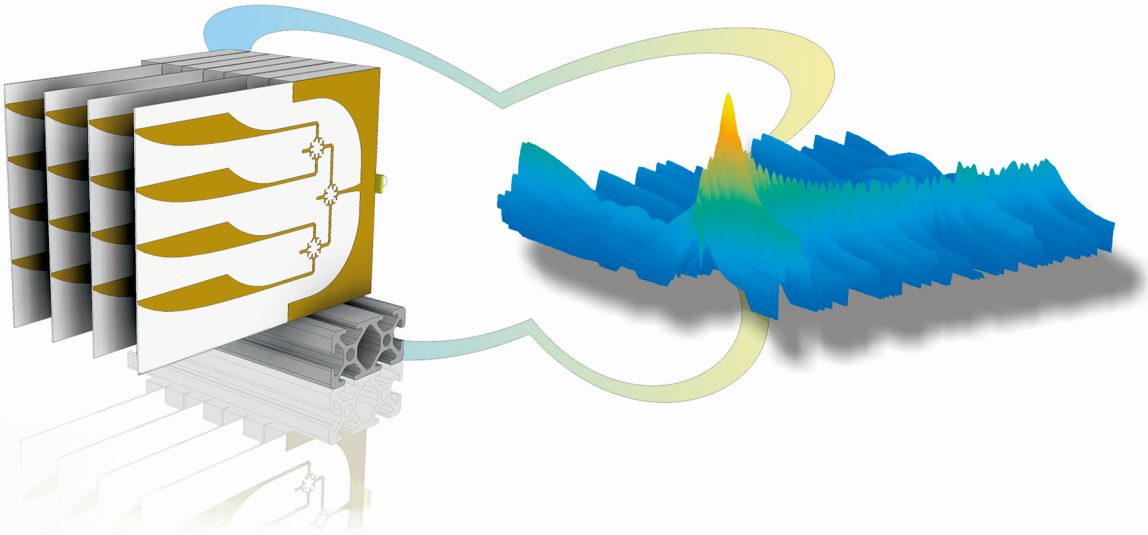

FAU Forschungen, Reihe B, Medizin, Naturwissenschaft, Technik 5

Markus Gardill

Characterization and Design of Small Array Antennas for Direction-Of-Arrival Estimation for Ultra-Wideband Industrial FMCW Radar Systems

FAU UNIVERSITY PRESS

Markus Gardill

Characterization and Design of Small Array Antennas for Direction-Of-Arrival Estimation for Ultra-Wideband Industrial FMCW Radar Systems

FAU Forschungen, Reihe B

Medizin, Naturwissenschaft, Technik

Band 5

Herausgeber der Reihe:
Wissenschaftlicher Beirat der FAU University Press

Markus Gardill

Characterization and Design of Small Array Antennas for Direction-Of-Arrival Estimation for Ultra-Wideband Industrial FMCW Radar Systems

Erlangen
FAU University Press
2015

Bibliografische Information der Deutschen Nationalbibliothek:
Die Deutsche Nationalbibliothek verzeichnet diese Publikation in der Deutschen Nationalbibliografie; detaillierte bibliografische Daten sind im Internet über http://dnb.d-nb.de abrufbar.

Der vollständige Inhalt des Buchs ist als PDF über den OPUS Server der Friedrich-Alexander-Universität Erlangen-Nürnberg abrufbar:
https://opus4.kobv.de/opus4-fau/home

Verlag und Auslieferung:

FAU University Press, Universitätsstraße 4, 91054 Erlangen

Druck: docupoint GmbH

ISBN: 978-3-944057-35-4
ISSN: 2198-8102

Characterization and Design of Small Array Antennas for Direction-Of-Arrival Estimation for Ultra-Wideband Industrial FMCW Radar Systems

Charakterisierung und Entwurf
von kleinen Gruppenantennen
zur Winkelschätzung
für ultrabreitbandige industrielle
FMCW-Radarsysteme

Der Technischen Fakultät
der Friedrich-Alexander-Universität
Erlangen-Nürnberg
zur
Erlangung des Doktorgrades Dr.-Ing.

vorgelegt von

Markus Gardill

aus Bamberg

Als Dissertation genehmigt
von der Technischen Fakultät
der Friedrich-Alexander-Universität Erlangen-Nürnberg
Tag der mündlichen Prüfung: 16.06.2015

Vorsitzende des Promotionsorgans: Prof. Dr.-Ing. habil. Marion Merklein

Gutachter: Prof. Dr.-Ing. Dr.-Ing. habil. Robert Weigel
Prof. Dr.-Ing. habil. Stefan Lindenmeier

Abstract

This thesis covers the characterization and design of small array antennas for ultra-wideband (UWB) industrial linear frequency-modulated continuous-wave (FMCW) radio detection and ranging (RADAR) systems. Although the techniques developed in this work are not limited to a certain application scenario, in particular the design of a four-element uniform linear and four-element uniform circular array antenna is considered. The antenna arrays are used for implementing direction-of-arrival (DOA) estimation in a novel UWB secondary RADAR system for industrial local positioning applications. The system's frequency range is from 6 GHz to 9 GHz and hence possesses a relative bandwidth of 40 %. State of the art industrial FMCW RADAR systems in contrast traditionally operate in the narrowband regime with relative bandwidths much smaller than 10 %. In consequence methods traditionally used for characterizing the antennas, for modeling the influence of the antennas on the RADAR system performance, for implementing direction-of-arrival estimation in FMCW RADAR systems, and for designing antenna arrays are not sufficient. Their application to UWB FMCW RADAR systems is carefully reviewed, and where necessary extended to take into account effects emerging due to the large relative bandwidth.

In particular an exact model for the received intermediate-frequency (IF) signal of a multi-channel UWB FMCW RADAR system employing an array of ideal point sensors is developed first. Approximations are then applied to the exact model until a suitable description for developing DOA estimation algorithms in the UWB FMCW RADAR system is achieved. It is further shown how this model is related to the narrowband models used for DOA estimation in traditional multi-channel FMCW RADAR systems. Subsequently refined beamforming algorithms based on the approaches of Bartlett and Capon, which take into account the received IF signal of the UWB FMCW sensor array, are proposed. Those algorithms are further extended to allow for simultaneous DOA and range estimation. A careful comparison of the refined algorithms with the traditional algorithms is used to demonstrate their superior performance in UWB FMCW RADAR systems. In addition it is shown that a sensor element spacing larger than the traditionally known limit may be used, which simplifies the design of UWB array antennas.

The proposed models based on ideal sensor elements are then extended to take into account the simulated or measured characteristics of realistic an-

tennas. Therefore, state-of-the-art methods for the characterization of isolated UWB antenna elements are used. Those methods are then refined to provide the necessary characterization of small array antennas, in particular including the effects of mutual coupling. Based on the antenna characterization, a simplified comprehensive model is developed which allows for taking into account the antenna array characteristics into the output of a multi-channel UWB FMCW RADAR system. This enables for directly assessing the influence of the antennas onto the performance of signal processing algorithms already during antenna development.

Finally a four-element uniform linear and a four-element uniform circular array antenna are designed for the local positioning application. The linear array antenna employs a novel method referred to as column-coupling for achieving the desired characteristics in the frequency range from 6 GHz to 9 GHz. The circular antenna array is optimized for vehicle rooftop integration and is based on mechanically robust Monocone antenna elements.

Zusammenfassung

Die vorliegende Arbeit befasst sich mit der Charakterisierung sowie der Entwicklung von kleinen Gruppenantennen für ultra-breitbandige (engl. ultra-wideband, UWB) linear frequenzmodulierte Dauerstrich-Radarsysteme (engl. frequency-modulated continuous-wave, FMCW). Obwohl die im Rahmen dieser Arbeit entwickelten Verfahren nicht auf eine bestimmte Anwendung beschränkt sind, wird im Speziellen die Entwicklung einer gleichförmigen linearen sowie einer gleichförmigen zirkularen Gruppenantenne mit je vier Elementen betrachtet. Diese sollen für die Einfallswinkel-Schätzung (engl. direction of arrival, DOA) in einem neuartigen UWB Sekundärradarsystem zur lokalen Positionierung in Industrieumgebungen verwendet werden. Der Frequenzbereich dieses Radarsystems reicht von 6 GHz bis 9 GHz, was einer relativen Bandbreite von 40 % entspricht. Industrielle FMCW-Radarsysteme nach dem Stand der Technik hingegen sind typischerweise schmalbandige Systeme mit relativen Bandbreiten weit unter 10 %. Aus diesem Grund sind traditionelle Methoden für die Charakterisierung von Antennen, für die Modellierung des Einflusses von Antennen auf das Radarsystem, zur Implementierung von DOA-Schätzalgorithmen sowie für die Entwicklung von Gruppenantennen nicht ausreichend. Die Anwendbarkeit dieser Methoden auf UWB-FMCW-Radarsysteme wird sorgfältig geprüft und wo nötig erweitert, um die durch die große relative Bandbreite auftretenden Effekte zu berücksichtigen.

Hierfür wird zuerst ein exaktes Modell für das Zwischenfrequenz-Empfangssignal (engl. intermediate frequency, IF) eines Mehrkanal-FMCW-Radarsystems unter der Annahme von idealen Punktsensoren aufgestellt. Näherungen werden dann auf dieses exakte Modell angewandt, um eine brauchbare Beschreibung für die Entwicklung von DOA-Schätzverfahren im betrachteten UWB-FMCW-Radarsystem zu erhalten. Es wird im Weiteren gezeigt, wie dieses Modell in Beziehung zu den für die Winkelschätzung in traditionellen FMCW-Radarsystemen verwendeten Schmalband-Modellen steht. Schließlich werden weiterentwickelte Verfahren zur Strahlformung basierend auf den Herangehensweisen von Bartlett und Capon vorgestellt, die die Eigenschaften des IF-Empfangssignals der UWB-FMCW-Sensorgruppe berücksichtigen. Diese Verfahren werden erweitert, um die gleichzeitige Schätzung von DOA und Zielentfernung zu ermöglichen. Ein sorgfältiger Vergleich zwischen den traditionellen und den weiterentwickelten Verfahren wird verwendet, um deren überlegene Leistungsfähigkeit in UWB-FMCW-

Radarsystemen aufzuzeigen. Des Weiteren wird gezeigt, dass der Abstand zwischen den Sensorelementen der Gruppe größer als traditionell bekannt gewählt werden kann, was die Entwicklung von kleinen UWB-Gruppenantennen signifikant erleichtert.

Die auf idealen Sensorelementen basierenden Modelle werden schließlich vervollständigt, um simulierte oder gemessenen Eigenschaften von realen Antennen einzubeziehen. Hierfür werden herkömmliche Methoden zur Charakterisierung von UWB Einzelantennen herangezogen. Die Methoden werden erweitert um die notwendige Charakterisierung von kleinen Gruppenantennen, insbesondere unter Berücksichtigung der gegenseitigen Verkopplung, zu ermöglichen. Basierend auf der experimentellen Charakterisierung der Antennen wird dann ein vereinfachtes umfassendes Modell entwickelt, welches es erlaubt den Einfluss der Eigenschaften der Gruppenantenne auf das Empfangssignal eines Mehrkanal-UWB-FMCW-Radarsystems direkt zu modellieren. Hiermit kann der Einfluss der Antennen auf die Leistungsfähigkeit der Signalverarbeitungs Algorithmen bereits während der Antennenentwicklung berücksichtigt werden.

Schließlich werden eine gleichförmige lineare und eine gleichförmige zirkulare Gruppenantenne mit je vier Antennenelementen für die betrachtete Anwendung entwickelt. Die lineare Gruppenantenne basiert auf einer neuen Methode, die als Spaltenverkopplungsmethode bezeichnet wird. Hierdurch können die benötigten Eigenschaften im Frequenzbereich von 6 GHz bis 9 GHz erreicht werden. Die zirkulare Gruppenantenne ist für die Integration auf einem Fahrzeugdach optimiert und basiert auf einer mechanisch robusten Realisierung von konischen Antennen-Elementen.

Contents

1 Introduction

1.1 Motivation

Wireless positioning - the determination of the presence, position, and velocity of one or several objects, or parts of objects, without the need to provide any mechanical connection to that object - is one key technology enabling state-of-the-art industrial, automotive, infotainment, as well as medical applications. The maturity of state-of-the art wireless positioning systems is such large, that they can be found in a variety of all-day life applications. They are deeply integrated into larger systems and their precise and reliable operation is often taken as granted, without any need for the user to understand the operation principle of that positioning system. For example in automotive and traffic applications adaptive cruise control relies on continuously measuring the distance and speed towards other vehicles. Parking assistants rely on measuring the distance towards possible obstacles, parking guidance systems dynamically acquire traffic and occupancy to generate guiding information, and intelligent traffic signal control systems measure the presence and number of vehicles. In law enforcement, wireless positioning systems enable the determination of road user's velocity. Infotainment applications utilize local positioning of the user's limbs to realize gesture control of e.g. TV systems, or user interaction with gaming consoles. Automated door openers use local positioning systems to detect the presence of users. Collision warning systems simplify the operation of industrial vehicles such as straddle carriers and fork lifters, and the control of automated production processes relies on a variety of positioning information obtained from wireless sensing systems. Those examples provide only a very small collection of nowadays typical applications of wireless positioning systems. But it clearly shows: wireless positioning systems can be found everywhere, and they are a key-enabling technology for modern life.

Wireless positioning systems can be classified using various criteria. A fundamental categorization is based on the underlying physical principle, also referred to as the *signaling scheme* of the positioning system [1]. For example the propagation of light is used in light detection and ranging (LIDAR)

and laser detection and ranging (LADAR) systems or in visual systems using e.g. time of flight (TOF) or light-field cameras for 3D object recognition and positioning. Another physical principle is the propagation of acoustic waves, which is used e.g. in ultrasound systems. Some recent approaches even use the measurement of the disturbances of the earth's magnetic field caused by structural steel elements in a building for indoor local positioning [2]. But probably the most common and well-known signaling scheme is the use of electromagnetic waves in the radio frequency (RF) and mm-wave frequency ranges: the so-called RADAR systems.

RADAR systems all rely on the same basic principle: radiate electromagnetic energy into space, detect the signal passively reflected or actively radiated from an object, and compare the received signal with a prototype signal known to the receiver [3]. By doing so, presence, position as well as velocity of an object, in RADAR terminology also referred to as *target*, can be determined. The great benefit of RADAR technology compared to other signaling schemes is that RADAR systems can be designed to perform their function at distances up to hundreds of kilometers, or also very short distances, about a few millimeters. They both function in indoor as well as outdoor scenarios, and they can operate under conditions often limiting the use of ultrasound or light-based systems such as darkness, haze, fog, rain and snow [3].

RADAR systems itself can be subdivided into categories according to the *signaling waveform*, i.e. the shape of the prototype waveform used [4]. Although not limited to, the two most famous types are pulsed RADAR systems and frequency-modulated continuous-wave (FMCW) RADAR systems [5]. Especially FMCW RADAR-based wireless positioning is of interest for industrial applications. The wide distribution of automatic control systems and sophisticated process technologies requires high-precision wireless sensing systems [6] and often RADAR is the signaling scheme of choice. It is the specific characteristics of FMCW RADAR systems which make it the preferred RADAR waveform for industrial applications [7]. Such they provide the ability to measure small and very small ranges, a high range resolution and the ability to simultaneously measure distance and relative speed of several targets. The fact that signal processing is performed using a relatively low sample rate, the absence of pulsed radiation which simplifies power amplifier (PA) design and relieves safety considerations, as well as the compactness, size, small weight and energy consumption are further beneficial characteristics of FMCW RADAR systems. The use of early FMCW RADAR technology in the industrial sector began already in the end of the 1960's [6]. It still can

be considered as one of the key enabling technologies for realizing the industry of the future, since reliable and precise positioning systems are the fundamental basis for the next revolutionary change in industry by the extensive integration of cyber physical systems (CPS) in the industrial production processes [8], [9]. Typical applications of industrial FMCW RADAR sensors range from 1D scenarios requiring only the measurement of distances such as the measurement of the filling level of different technological reservoirs or the traversing axis position of a production machine, over 2D scenarios requiring either the measurement of the position along two axes or the simultaneous measurement of distance and velocity in e.g. collision warning systems, to full 3D scenarios such as automated asset tracking, robot and tool positioning as well as close human-machine interaction.

	Extrinsic Param.			Intrinsic Param.		
Company/Product	f_c [GHz]	BW [GHz]	$BW^{rel.}$ [%]	Δd^{tgt}	ϵd^{tgt}	Ref.
ELVA 1 / FMCW 94/10	94	0.5	0.5 %	n/a	±5 cm	[10]
Bosch / LRR3	76.5	1	1.3%	n/a	±10 cm	[11]
Navtech / SafeGuard	76.5	1	1.3%	n/a	±25 cm	[12]
Continental / ARS 300	76.5	1	1.3%	2 m	±25 cm	[13]
Symeo / LPR-1DHP	61.25	0.5	0.8 %	n/a	±10 cm	[14]
Innosent / IVS Line	24.125	0.25	1%	FO	FO	[15]
SAGE Millimeter / SSD	24.125	0.3	1.2%	FO	FO	[16]
Sivers IMA / RS3400K	24.75	1.5	6%	FO	FO	[17]
Banner Eng. / R-GAGE	24.125	0.25	1%	n/a	n/a	[18]
Sivers IMA / RS3400X	10	1.5	15%	FO	FO	[19]
Symeo / LPR-2D	5.8	0.150	2.5 %	n/a	±5 cm	[20]

Tab. 1.1: Overview of industrial FMCW RADAR sensors with performance metrics obtained from the data sheets provided by the manufacturer. Operating frequencies range from 5.8 GHz to 94 GHz, with absolute bandwidths up to 1.5 GHz. Typically relative bandwidths below 10 % are used. For front-end-only (FO) sensors (i.e. sensors having analog base-band signal outputs, no signal processing included) resolution and accuracy cannot be determined.

A wide range of commercial FMCW RADAR sensors and systems for industrial applications exists, a selection is listed in table 1.1. In this work, FMCW RADAR sensors are characterized based on two classes of criteria: *extrinsic* and *intrinsic* properties. Extrinsic criteria are those which define properties of the radiated signal. In particular, the two most prominent extrinsic characteristics of FMCW RADAR systems are the center frequency f_c and the

sweep bandwidth BW, which is defined as

$$\mathrm{BW} = f_\mathrm{h} - f_\mathrm{l}, \tag{1.1}$$

i.e. the difference between f_h, the highest instantaneous frequency, and f_l, the lowest instantaneous frequency of the linear frequency modulation (LFM) waveform. The center frequency f_c is defined as the arithmetic mean of f_h and f_l. Thus it can be expressed by

$$f_\mathrm{c} = f_\mathrm{l} + \mathrm{BW}/2. \tag{1.2}$$

In the scope of RF circuit and antenna design, where the electrical size of structures in terms of wavelength plays a major role, it is not the absolute but the relative bandwidth expressed in percent of the center frequency [10]

$$\mathrm{BW}^\mathrm{rel.} = \frac{\mathrm{BW}}{f_\mathrm{c}} \cdot 100\,\% \tag{1.3}$$

which imposes operating limits on the circuit structures. Intrinsic characteristics typically include the most important performance metrics of the FMCW RADAR system, which are positioning resolution Δd^tgt and positioning accuracy ϵd^tgt. Whereas the latter describes how accurate the distance d^tgt of a target can be determined, the former describes how close two targets can be located such that they still can be resolved as two distinct targets. It is an inherent property of all radio based positioning systems, and of course of FMCW RADAR systems in particular, that the extrinsic properties define the maximum achievable intrinsic performance metrics. In particular, as will be shown in detail in section 3.2, it is the sweep bandwidth BW of the FMCW waveform that defines the minimum achievable resolution.

From table 1.1 it can be seen that industrial FMCW RADAR sensors operating at different frequency bands are available. Typically, high resolution systems using a large absolute sweep bandwidth operate at high frequency bands. This is mainly based on the fact that of course industrial FMCW RADAR systems are subject to frequency plans allocated by frequency regulation authorities. Typical operating bands for industrial RADAR systems are listed in table 1.2. Traditionally the industrial, scientific, and medical (ISM) bands, which allow for unlicensed use of RADAR systems, are the preferred operating frequencies for general purpose industrial RADAR sensors, since the automotive RADAR bands are limited to traffic applications. It can be seen that it is basically regulation aspects which limit the bandwidth of

FMCW RADAR systems operating at given center frequency. Only at very high center frequencies in the mm-wave regime bandwidths of more that 1 GHz, which allow for the implementation of high-resolution RADAR sensors, become available. In consequence, if a high-resolution RADAR system is desired, traditionally this meant that also a high-center frequency must be used and existing FMCW RADAR systems thus typically operate at very small relative bandwidths, typically below 3 %. Although they indeed might use large absolute bandwidths, from a circuit design perspective they consequently can be regarded as narrowband systems. This fact is favorable from the system and circuit design perspective, since a vast amount of design techniques, architectures as well as commercial off-the-shelf (COTS) components are available for narrowband systems operating in the microwave and mm-wave frequency bands. In addition, traditional and well-understood narrowband methods for designing the digital signal processing (DSP) algorithms for range as well as spatial processing such as direction of arrival (DOA) estimation can be used.

However, there are two challenges which cannot be addressed by implementing high-resolution RADAR systems in the ISM frequency bands: Firstly, even if extremely high center frequencies in the mm-wave range are selected, the available bandwidth still is limited to about 2 GHz, which might not be enough for achieving the desired range resolution. Secondly the use of mm-wave frequency bands strongly increases propagation path loss, which prevents their use in e.g. industrial positioning systems for indoor and outdoor use such as [11], [12]. To overcome those problems a frequency band ranging from 3.1-10.6 GHz, which was allocated for unlicensed use of ultra-wideband (UWB) systems by various international regulation authorities beginning with 2002 [1], is attractive. The term UWB refers to signals whose absolute bandwidth is at least 500 MHz, or the relative bandwidth exceeds 20 % [1]. It is not only the tremendous amount of bandwidth which is available at those bands making them attractive for the implementation of high-resolution UWB FMCW RADAR systems. Also the relatively low frequency around the 5.8 GHz ISM frequency band, where the majority of the available positioning systems operate, is favorable for extending local positioning applications such as [12], [13] to UWB operation. Firstly, compared to the mm-wave bands the relatively large wavelength found in the UWB frequency range is favorable due to the lower free-space path loss, and also allows for antennas with relatively low gain for, e.g., omni-directional radiation and reception. Secondly, both circuit and antenna design up to 10 GHz can easily be han-

dled with standard printed circuit board (PCB) technologies. No integrated solutions or high-precision circuit technologies, which e.g. are necessary for handling mm-wave frequencies, are necessary. Hence also systems for relatively low-volume and low-cost markets, which are typically addressed by companies providing industrial positioning applications, can be implemented. In addition the operation of UWB systems is subject to quite low stringent emission limits in terms of equivalent isotropically-radiated power (EIRP), depending on the country typically below –41.3 dB/MHz, and hence the maximum range of purely UWB wireless positioning systems is limited compared to traditional local positioning systems operating in the 5.8 GHz ISM bands [14], who have been reported to achieve maximum ranges of up to 400 m [15]. Since the 5.8 GHz ISM band is a subset of the UWB frequency bands, it is obvious that once the design of a FMCW local positioning RADAR system has been extended to UWB operation, a large gain in flexibility, performance and reliability can be achieved: if a large operating range is necessary, traditional ISM operation with large transmit (TX) power, but a bandwidth limited to 150 MHz is selected. If high resolution is necessary the system can switch to UWB operation with extremely large sweep bandwidth but limited operating range. Extending existing 5.8 GHz systems to UWB operation thus offers a great potential for increasing the robustness, accuracy, and overall performance of industrial FMCW RADAR systems.

However, the implementation of a FMCW RADAR system with a sweep bandwidth significantly more than 1 GHz in the UWB frequency bands brings up an entirely new challenge, which is not observed in traditional systems: the RADAR system now operates at a large relative bandwidth. This means that wideband circuits and systems have to be designed and the wideband characteristics of the FMCW waveform has to be taken into account in the DSP algorithms. It is those aspects of future UWB industrial FMCW RADAR systems, which is the fundamental motivation for this thesis.

Band	f_l	f_h	f_c	BW	$BW^{rel.}$
ISM	5.725 GHz	5.875 GHz	5.8 GHz	150 MHz	2.5%
ISM	24 GHz	24.25 GHz	24.125 GHz	250 MHz	1%
ISM	61 GHz	61.5 GHz	61.25 GHz	500 MHz	0.8%
AUTO	76 GHz	77 GHz	76.5 GHz	1 GHz	1.3 %
AUTO	77 GHz	81 GHz	79 GHz	4 GHz	5%
ISM	122 GHz	123 GHz	122.5 GHz	1 GHz	0.8%
ISM	244 GHz	246 GHz	245 GHz	2 GHz	0.8%
UWB	3.1 GHz	10.6 GHz	6.85 GHz	7.5 GHz	109.5%

Tab. 1.2: Typical frequencies of interest for industrial FMCW RADAR systems are located in the industrial, scientific, and medical (ISM), the automotive (AUTO) and the ultra-wideband (UWB) frequency bands.

1.2 Goals of this Work

This work is concerned with the particular challenge of extending an existing system for 2D local positioning based on a secondary FMCW RADAR principle operating in the 5.8 GHz frequency bands [11], [12] to UWB operation. Although the possible application scenario is not limited to a specific case, a typical example could be the problem of localizing a fork lift in an industrial scenario, such as a warehouse or production hall, as illustrated in figure 1.1. As proposed in [11], [12] this can be achieved by using a secondary FMCW RADAR system with reference units (RUs) at known positions, in the considered example mounted on the walls of the localization area, and a measurement unit (MU), whose position is to be determined, in the given example mounted on the roof of an industrial vehicle, e.g. a forklift. By measuring the distance between MU and at least three RUs, the position of the MU can be determined by trilateration and by continuously monitoring the position of the forklift a precise tracking of its position is possible. If this position information is fusioned with some more side information in a localization engine, it can easily be imagined that a variety of applications such as driver assistance systems or automated asset tracking are possible. Note that, in addition to the scenario illustrated in 1.1, the addressed positioning system should not be limited to indoor use. By providing a grid of RUs mounted e.g. on masts used for lighting of outdoor storage and production areas, the area for localization can easily be extended to outdoor use and a seamless indoor-outdoor localization is possible. The primary moti-

vation for increasing the bandwidth of existing solutions [11], [12] operating in the 5.8 GHz to a UWB RADAR system is, that the larger the bandwidth, the larger the range resolution, i.e. the minimum distance at which two RADAR targets can be detected as two separate objects, of an FMCW RADAR system is. This will also be shown in chapter 2 in more detail. Although on a first view a very fine range resolution may not be necessary for the application of fork-lift tracking, since the minimum distance between two forklifts is limited by the vehicle size and thus will be typically larger than 1 m, it is particularly useful for mitigating multi-path propagation phenomena occurring in the challenging industrial environments and hence for increasing the overall robustness, reliability and accuracy of the local positioning system. In addition to UWB FMCW operation, the system should be extended by DOA estimation capabilities and further spatial receive (RX) signal processing. This allows for, e.g., an instantaneous estimation of the heading of the forklift, it provides a further data-basis for position estimation not only by trilateration but also by triangulation, and the possibility to detect parasitic non-line-of-sight (NLOS) propagation paths, which would degrade a lateration-only based position estimation. The RX spatial processing capabilities are introduced by using a FMCW RADAR front-end with four coherent receive channels together with four-element antenna arrays. Besides the challenges of analog circuit design, such as highly-linear and UWB FMCW ramp synthesizers [16], low-noise receivers, and providing multiple coherent receive channels, the overall system performance is strongly dependent on a component at the foremost front of every RADAR system: the antennas.

The primary goal of this thesis is the design of the antenna arrays, which are the key components for enabling spatial processing such as DOA estimation in the UWB FMCW RADAR system, as well as a general treatment of antenna arrays for DOA estimation in UWB FMCW RADAR systems. An optimum design of antennas for systems implementing spatial processing can however never be achieved without considering all system aspects, since the characteristics of the antennas strongly influence the DSP algorithms, and vice versa the DSP algorithms used strongly define the major design constraints for the antenna arrays. Hence antenna design and DSP, which traditionally were considered as two exclusive worlds, have to be considered hand in hand. In particular the design of antenna arrays for DOA estimation in UWB FMCW RADAR systems requires methods for directly evaluating the influence of antenna array candidates on the performance of the DSP algorithms used for range and DOA estimation. Hence a second major goal of this thesis is to

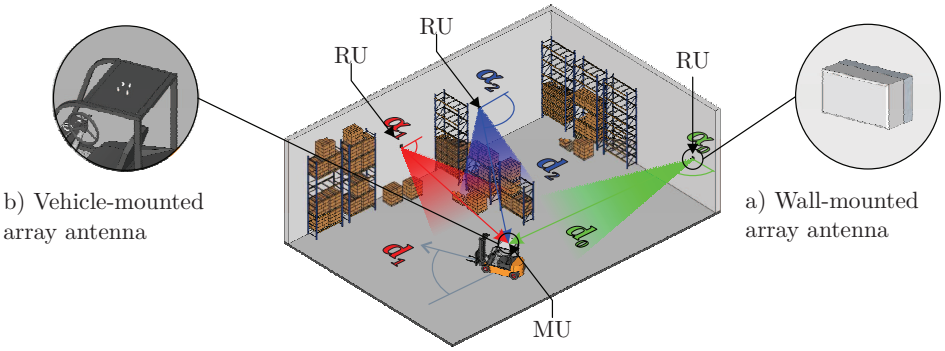

Fig. 1.1: Application scenario for UWB FMCW local positioning as described by the author in [MG1], [MG2]. The position of e.g. a forklift is determined by trilateration, measuring the distances between fixed RUs at known positions and the MU mounted on the vehicle at the unknown position. Those measurements can be implemented by means of a secondary FMCW RADAR system. By increasing the bandwidth of the RADAR system as well as using array processing techniques, the reliability, functionality, and accuracy of the system can be increased.

provide a methodology, mathematical treatment and simulation framework to directly asses the performance of an antenna or a small antenna array, whose characteristics are either obtained by electromagnetic simulations or by measurement, on the intrinsic properties of a UWB FMCW RADAR system.

Scenario	T	μ	BW	f_s	f_l	f_h	N
NB	1 ms	150 MHz/ms	150 MHz	50 kHz	6 GHz	6.15 GHz	100
WBS	20 ms	150 MHz/ms	3 GHz	50 kHz	6 GHz	9 GHz	2000
WBF	1 ms	3 GHz/ms	3 GHz	1 MHz	6 GHz	9 GHz	2000

Tab. 1.3: Parameters of narrowband (NB) and wideband (WB) RADAR system scenarios. Since UWB operation can either be achieved by keeping the sweep rate as well as sample rate constant and increasing the duration T of the sweep, or by increasing both the sweep rate as well as sample rate and reducing the sweep duration T, it is further distinguished between wideband slow-sweep (WBS) and wideband fast-sweep (WBF) systems.

To provide a suitable baseline for comparing the performance between narrowband (NB) and wideband (WB) FMCW RADAR systems, two basic classes of RADAR systems with distinct extrinsic properties, referred to as *RADAR system scenarios* are considered and compared in this thesis,

whose properties are given in table 1.3. The narrowband (NB) RADAR system closely resembles the parameters of traditional FMCW RADAR systems for industrial local positioning, such as e.g. proposed in [11], [12], having a sweep bandwidth of BW $= 150\,\mathrm{MHz}$ and a relative bandwidth of $BW_{\text{rel.}} = 2.2\,\%$. The NB RADAR system scenario is used throughout this thesis to compare and point out the differences between narrowband and UWB FMCW RADAR. As a design goal, two wideband RADAR system scenarios are considered, both having a sweep bandwidth of $BW = 3\,\mathrm{GHz}$, i.e. exactly a bandwidth 20 times larger than the NB system, and a relative bandwidth of $BW_{\text{rel.}} = 40\,\%$. In both cases the start frequency of the sweeps corresponds to the start frequency of the narrowband system, such that the WB systems can be seen as a direct extension of the NB scenario. Since the relationship between the different RADAR system extrinsic properties given in 1.3 are related by inherent properties of the FMCW RADAR principle, whose exact relation is explained in chapter 2, the particular definition of the NB and WB RADAR scenarios from table 1.3 enable a careful comparison by limiting the change of extrinsic properties when going from narrowband to wideband operation. Basically two system parameters can be used to increase the bandwidth of an FMCW RADAR system and consequently, the WB RADAR system scenario is itself subdivided into two systems. The wideband slow-sweep (WBS) system uses the same sweep rate as the narrowband system and the increase in bandwidth is achieved by increasing the sweep duration. The wideband fast-sweep (WBF) system in contrast uses the same sweep duration, but an increased sweep-rate.

1.3 Organization of this Work

In the first part of this thesis, covered by chapters 2 to 6, a holistic characterization and design approach is proposed, which allows for directly assessing the in-system performance of small array antennas when used for spatial processing in UWB FMCW RADAR systems. This design approach, illustrated in 1.2, is referred to as the *antenna in the loop* design cycle. In the second part of this thesis, covered by chapters 7 and 8, the observations as well as modeling framework establishing the direct link between antenna characteristics and intrinsic RADAR system metrics is then used to *design* two small array antenna designs optimized for the local positioning application from figure 1.1. In particular, one array design is optimized for implementing the wall-mounted RUs and the other for implementing the vehicle-mounted MU.

Clearly, the ultimate figure of merit characterizing the antenna array is the expected *intrinsic* performance of the RADAR system, i.e. the results of used DSP algorithms. It is the ultimate goal to answer already during antenna array design, if and how large the properties of the designed antenna array influence the signal processing algorithms, and might introduce errors in range and DOA estimation. However, from figure 1.2 the particular challenge in trying to achieve this goal is obvious: the array antenna is the component at the very front of the RADAR system. It is the interface between electromagnetic waves $\underline{e}$ propagating through space and the RF signals x^{rx} propagating on the transmission lines of the FMCW RADAR front end In contrast, the DSP is the last processing block of a RADAR system. Only after the received signals have been processed in the various components of the RADAR system (SYST) they are sampled, stored, processed by algorithms for DOA and range estimation and the intrinsic RADAR system performance metrics such as resolution and accuracy can be obtained. It is obvious that the desired evaluation of the performance of the antennas based on intrinsic RADAR system performance metric hence requires for a complete system model of the FMCW RADAR front end.

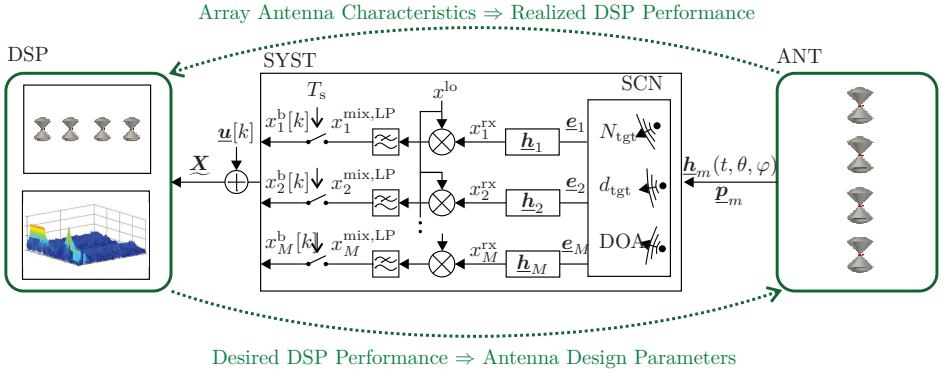

Fig. 1.2: Antenna in the loop development cycle for the design of small antenna arrays for DOA estimation in FMCW RADAR systems: The evaluation criteria for an array antenna design (ANT) is the performance of the selected DSP algorithms, e.g. range and DOA estimation algorithms. However, since DSP is the last step in the signal and data flow in a FMCW RADAR system, a complete system model (SYST) is necessary to be able to conduct the evaluation in the DSP domain.

This general structure dividing the thesis in between *characterization* and *design* of antenna arrays is further subdivided by considering that the *char-*

acterization, i.e the complete mathematical treatment of the RADAR system as illustrated in figure 1.2, can be broken down into several topics covering different research disciplines: the antenna (ANT) topic dealing with electromagnetic theory of radiation and their description and modeling, the system (SYST) topic covering FMCW RADAR system theory, as well as the digital-signal processing (DSP) topic, covering signal processing for range and DOA estimation. It is the step-by-step coverage of all those disciplines which will provide the golden threat throughout this thesis.

The System Model (SYST) is the representation of a typical multi-channel FMCW RADAR front end in receive mode using LFM which operates in a certain scenario defined by the Scenario Model (SCN). Both SYST and SCN will be described in chapter 2 of this thesis. The SCN defines the number N of RADAR targets, the distance d^{tgt} of all targets as well as the DOA of all targets with respect to a certain coordinate origin. Based on the scenario defined in the SCN, the received E-fields $\underline{\boldsymbol{e}}_m$ at each antenna m can be generated. The received E-fields can be considered as the inputs to linear time invariant (LTI) systems $\underline{\boldsymbol{h}}_m$, which completely capture the characteristics of the antennas used and transduce the received E-fields into a dimensionless RX signal x_m^{rx}. The received signals are then processed according to the FMCW principle, which includes a coherent down-conversion in each channel using a locally generated signal x^{lo} and a low-pass filtering operation. The analog-to-digital conversion of the signals is modeled by obtaining a number of K samples with a sampling period $T_{\mathrm{s}} = 1/f_{\mathrm{s}}$. Its details are presented at beginning of chapter 3. The output of the SYST is a matrix $\underset{\sim}{\boldsymbol{X}}$, which contains in every of its M rows a number of K recorded samples of the processed FMCW front end output signal. This matrix then serves as an input to the Digital Signal Processing (DSP) block, whose discussion constitutes the main part of chapter 3. Signal processing algorithms which operate on $\underset{\sim}{\boldsymbol{X}}$ are used to estimate the number of targets N, their distance d^{tgt} as well as their DOAs. In chapter 3 traditional algorithms for target distance and DOA estimation are reviewed first, and subsequently some improved algorithms for range and DOA estimation in UWB FMCW RADAR systems are proposed. Their performance is then evaluated and compared to the traditional algorithms.

The Antenna Model (ANT) is an exact description of the characteristics of the small array antenna. It includes the geometry of the antenna array, i.e. the number M of antenna elements used and the position $\underline{\boldsymbol{p}}_m$ of each antenna element, and a time-domain description $\underline{\boldsymbol{h}}_m$ of the radiation charac-

teristics of each antenna element in the array antenna, which can be obtained either from computational electro-magnetics (CEM) simulations, or from measurements of real antenna arrays. While the discussion on antenna array geometries is already conducted at the end of chapter 2, in chapter 4 the state-of-the-art in time- and frequency domain-modeling of UWB antenna elements is introduced and the used CEM simulation, measurement, as well as numerical post-processing techniques are presented. In chapter 5 the theory is then extended from the isolated element case to small array antennas. In chapter 6, the theory of the preceding chapters regarding FMCW RADAR system- as well as antenna-modeling is taken together to derive a comprehensive model which establishes the direct link between antenna element characteristics and the signal matrix $\underset{\sim}{\boldsymbol{X}}$, such that the influence of the antennas on the DSP performance can directly be evaluated.

1.4 State of the Art

An overview and comparison of current research and commercial high-accuracy local positioning systems is provided in [14], where state-of-the-art high-precision local positioning systems are categorized into carrier-based [14], [17]–[20], impulse-based [21]–[24] and FMCW [25]–[31] systems. Among the carrier based local positioning systems are e.g. the works by Meier, Lindenmeier et al. [18], [19], [32], where wideband pseudo-noise signals with a bandwidth up to $3.2\,\mathrm{GHz}$ at $24\,\mathrm{GHz}$ are used for precise distance estimation. Impulse based positioning systems such as proposed by Fujii, Kohno, et al. [22] and Ossberger, Weigel, et al. [21] utilize short wideband time-domain pulses to enable time of arrival (TOA) or time difference of arrival (TDOA) measurements. In the last category, the FMCW RADAR principle is used for distance measurement. All FMCW state-of-the-art (SoA) approaches can be considered as narrowband systems, since their relative bandwidth does not exceed 5 %. The approach by Waldmann [17], [33], although originally being categorized as carrier-based method in [14], can be regarded as one of the first UWB FMCW systems, since in the receiver the intermediate frequency (IF) signals as found in traditional FMCW RADAR systems are restored, and DSP relies on traditional FMCW RADAR signal processing. The system has a sweep bandwidth of $\mathrm{BW} = 1\,\mathrm{GHz}$ at a center frequency $f_\mathrm{c} = 7.5\,\mathrm{GHz}$, thus a relative bandwidth of $\mathrm{BW}^{\mathrm{rel.}} \approx 13\,\%$. Antenna aspects are reduced to good impedance matching and a proper antenna radiation pattern. In addition the proposed system is a single-channel system without spatial processing.

More recent approaches towards FMCW RADAR-based local positioning systems have been proposed by Scherz, Stelzer, et al. in [34], where an array processing system is integrated into a local position measurement system operating with a sweep bandwidth of $150\,\mathrm{MHz}$ in the 5.8 GHz ISM frequency bands. The system is narrowband and traditional narrowband beamforming is used for spatially processing the signals. Feger, Stelzer, et al. [35], propose a local positioning system with 1 GHz sweep bandwidth operating in the 77 GHz automotive RADAR bands, including spatial processing using antenna arrays. Due to the high center frequency of $f_c = 77.5\,\mathrm{GHz}$ the relative bandwidth of the RADAR system is $\mathrm{BW}^{\mathrm{rel.}} \approx 1.2\,\%$ The system can hence be regarded as narrowband, and also the narrowband model is applied in the design of DOA estimation algorithms in [35]. Ebelt, Vossiek, et al. propose a single-channel FMCW-based local positioning RADAR system operating at 24 GHz with a sweep bandwidth of $\mathrm{BW} = 250\,\mathrm{MHz}$ and hence a relative bandwidth of $\mathrm{BW}^{\mathrm{rel.}} \approx 1\,\%$ in [36]. Comparable approaches operating in the 5.8 GHz bands have been proposed earlier by Roehr, Vossiek, et. al [11] and Gierlich, Huemer, et al. [37]. Whereas the former is a single-channel system without spatial processing, the latter is referred to by the authors as a MIMO system, since four receive channels are employed in the RADAR stations. Since the system operates in the narrowband scenario, traditional narrowband spatial processing algorithms are employed.

FMCW RADAR systems taking into account wideband effects in the design of signal processing algorithms have been proposed by Feger, Stelzer et al. in [38], where the DOA estimation is implemented by means of a time-dependent spatial beamformer based on the minimum variance distortionless response (MVDR). The RADAR system uses a sweep bandwidth of $\mathrm{BW} = 900\,\mathrm{MHz}$ and a center frequency of $f_c = 24.450\,\mathrm{GHz}$ and thus operates at a relative bandwidth of $\mathrm{BW}^{\mathrm{rel.}} \approx 3.7\,\%$. Although the authors take into account the time dependence of the array model, no time-dependence on the signal covariance matrix is taken into account. It is shown in chapter 3 of this thesis, how a modified covariance matrix computation can further improve the results shown in [38] for relative sweep bandwidths as large as 40 %. A similar signal model taking into account the wideband effects is proposed by Feger, Stelzer, et al. in [30] and [39]. A wideband signal model for the output of an RX FMCW RADAR antenna array including the effects of antenna switching has also been proposed by Lee in [40].

UWB FMCW RADAR systems have been proposed recently by Jaeschke, Pohl, et al. in [41]. The authors propose a FMCW RADAR system for imaging ap-

plications with a sweep bandwidth of $\mathrm{BW} = 60\,\mathrm{GHz}$ at a center frequency of $f_\mathrm{c} = 234\,\mathrm{GHz}$ operating at a relative bandwidth of $\mathrm{BW}^{\mathrm{rel.}} = 25.6\,\%$. The proposed system is a single channel system without applying spatial RX processing, the angular resolution of the RADAR system is entirely achieved using a mechanical positioner together with an on-chip plus lens pencil-beam antenna. No frequency-dependent or transient effects, respectively, of the antenna are taken into account. In [42] Anghel, Ciochina, et al. propose a wideband FMCW RADAR system operating at a center frequency of $f_\mathrm{c} = 10\,\mathrm{GHz}$ with a sweep bandwidth of $\mathrm{BW} = 4\,\mathrm{GHz}$, i.e. a relative bandwidth of $\mathrm{BW}^{\mathrm{rel.}} = 40\,\%$. The proposed system is a single-channel RADAR system, angular resolution is implemented by means of mechanical antenna displacement together with a synthetic aperture radar (SAR) signal processing. No effects of the antennas on the RADAR system are reported. Galin, Jansen, et al. propose an UWB FMCW RADAR system for snow depth measurements operating at a relative bandwidth of $\mathrm{BW}^{\mathrm{rel.}} = 120\,\%$ with a center frequency of $f_\mathrm{c} = 5\,\mathrm{GHz}$ and a sweep bandwidth of $\mathrm{BW} = 6\,\mathrm{GHz}$. The proposed system is a single channel RADAR without spatial processing and hence to particular DSP algorithms taking into account the UWB properties are used. The antennas are only characterized by means of their narrowband radiation patterns.

Significant contributions to UWB antenna characterization have been proposed in the Ph.D. thesis by Licul [43] and Soergel [44], together with several publications of Soergel, Wiesbeck et al. [45], [46] as well as Licul and Davis [47]. Previous fundamental work on time-domain antenna characterization has been published by Allen [48], Shlivinksy [49], and Baum [50], [51]. The works on UWB antenna characterization have also been more recently extended to characterize small UWB arrays. In [52], [53], system models for the impulse response of antenna elements in an array environment are proposed. Ciattaglia and Marrocco propose in [54] a detailed investigation on antenna coupling in pulsed arrays, and extend the conventional array coupling models [55], [56] by the definition of a time-domain active array factor and active element factor. A cross-correlation formulation for the time-domain array factor is given in [57]. Further work on signal distortion in UWB arrays is shown in [58], a transfer function formulation for UWB arrays is derived in [59], and the effects of single and multiple scattering are investigated in [60]. The author contributed in [MG3] to the modeling of UWB arrays in RX mode, and in [MG4] an investigation of the response of antennas to FMCW excitation was conducted.

A recent review on the evolution of wideband array designs is given by Livingston and Lee in [61] and by Crosswell et. al in [62] and in Munk's book [63] the theory of designing wideband array antennas from small narrowband elements is presented. However, the design approaches shown there typically utilize the coupling of a very large number of active array elements to achieve good wideband characteristics. For low-cost industrial RADAR systems, where the number of channels is typically limited to four, those approaches are not attractive. It is shown in chapter 7 of this thesis, how mutual coupling between array elements can be used also in small array antennas. Those findings have also been published by the author in [MG5], [MG6]. In contrast to utilizing mutual coupling, several UWB small array antennas based on antenna elements being wideband in isolation have been proposed. Arrays using planar wideband Dipole- and monopole-like elements can be found in [64]–[70] and contributions of the author to that class of UWB small array antennas are given in [MG1], [MG2], [MG7]. Volumetric antennas such as Bicone antennas and mono-cone antennas are, due to their excellent wideband characteristics and their thorough analytical description as e.g. provided in [71]–[74], also preferred elements for small UWB array antennas and have been used in e.g. [58], [75], [76] for designing array antennas. Contributions of the author to that class with a particular focus on practically relevant, robust and low-cost designs can be found in [MG8], [MG9]. Variants of the tapered slot antenna are famous candidates for UWB antennas and arrays. Fundamental work on tapered slot antennas has been published in [74], [77]–[79]. Small arrays based on tapered slot can e.g. be found in [80]–[87], and the author's work from [MG5], [MG6] is based on size-reduced tapered slot antenna elements.

2 Multi-Channel Wideband Linear FMCW Radar System Model

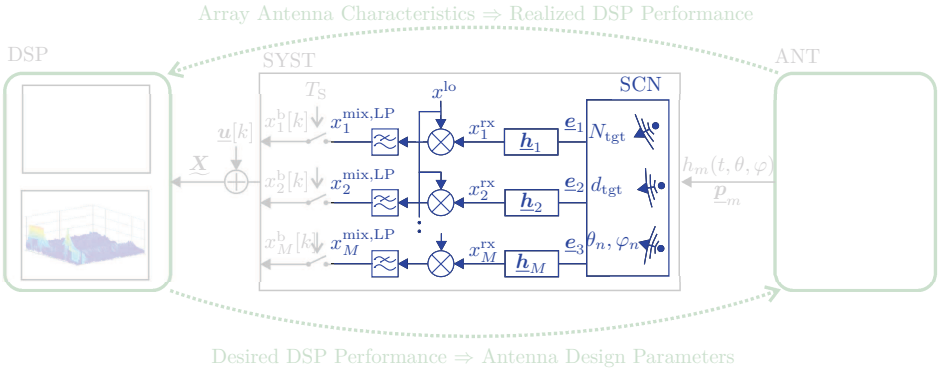

Fig. 2.1: Multi-channel FMCW RADAR system model.

Traditionally FMCW RADAR systems operate in the narrow-band regime, i.e. the center frequency f_c of the signal is much larger than the sweep bandwidth BW. Hence the treatment of FMCW RADAR systems if often based on simplifications, the so-called narrow-band models. In contrast, impulse-based UWB systems are generally purely treated in time-domain, since narrow-band assumptions for impulsive like signals cannot be applied. UWB FMCW RADAR systems clearly bring up several questions: neither do they use impulse-like waveforms, nor is their bandwidth small enough to apply narrow-band models. Hence in this chapter, the basic operation principles of FMCW RADAR systems will be derived from a time-domain perspective, to get an accurate description of the fundamental operating principles and a precise system description. In addition, abstract time-domain models will be used for describing radiation, scattering and reception of electromagnetic waves. This allows to replace those models with characteristics of realized antennas in a later step.

2.1 Operation Principles of Linear FMCW Radar Systems

Linear frequency-modulated continuous-wave (LFMCW) RADAR systems are based on radiating a signal into space whose amplitude is constant but whose instantaneous frequency changes linearly with time: a LFM signal. The signal's frequency can either increase or decrease with time. While the first case is referred to as an up-sweep signal, the second is referred to as a down-sweep signal. Using either up-sweep or down-sweep FMCW is conceptually identical, both allow for estimating presence and distance of targets. By using up-sweep and down-sweep together also the velocity of targets can be estimated. In case of a primary RADAR system it is then the presence and distance of passive scatterers which are measured by the RADAR unit. In a secondary RADAR system it is the distance between at least two separate RADAR units which has to be measured.

2.1.1 Single-Upsweep Primary Linear FMCW Radar System

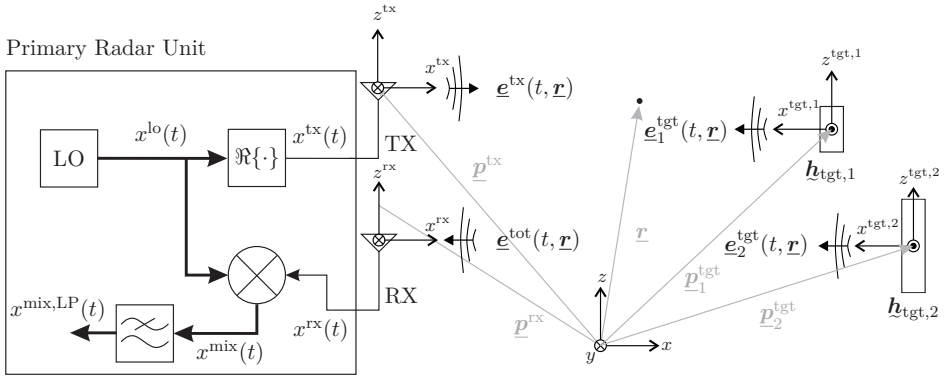

Fig. 2.2: Primary RADAR scenario.

A simplified model of a primary FMCW RADAR system is illustrated in figure 2.2. The real part of a locally generated FMCW signal $x^{\mathrm{lo}}(t)$ is radiated using the transmit antenna at position $\underline{\boldsymbol{p}}^{\mathrm{tx}}$, scattered by two targets at positions $\underline{\boldsymbol{p}}_1^{\mathrm{tgt}}$ and $\underline{\boldsymbol{p}}_2^{\mathrm{tgt}}$, respectively, and received by the receive antenna at position $\underline{\boldsymbol{p}}_m^{\mathrm{rx}}$. The mixing product $x_m^{\mathrm{mix}}(t)$ is obtained by multiplying the received signal $x_m^{\mathrm{rx}}(t)$ with $x^{\mathrm{lo}}(t)$. The output of the RADAR unit is the the low-pass

filtered mixing product $x_m^{\text{mix,LP}}(t)$, also referred to as the IF signal.

In this thesis, a global as well as local coordinate systems are used. The global coordinate system has its origin at an arbitrary point in space and is used to describe the positions of sensors, such as TX and RX antennas, and the position of targets. The local coordinate systems centered at the antennas and targets are used for describing direction and polarization of radiated, incident, and scattered electro-magnetic (EM) fields. Depending on the particular problem, any coordinate is then either defined using right-handed cartesian or spherical coordinates after ISO 80000-2 [88].

2.1.1.1 FMCW Signal Definition

Throughout this work, the RADAR unit is modeled to generate a local complex continuous-wave (CW) signal

$$x^{\text{lo}}(t) = \exp\left(\phi(t)\right) = \frac{1}{2}\left[\cos\left(\phi(t)\right) + \mathrm{j}\sin\left(\phi(t)\right)\right], \tag{2.1}$$

where $\phi(t)$ is the instantaneous phase of the signal. Since the instantaneous phase is the time integral of the instantaneous frequency, both are related by

$$\phi(t) = 2\pi \int_{-\infty}^{t} f(t)dt. \tag{2.2}$$

Although FMCW can refer to an arbitrary type of frequency modulation, i.e. an arbitrary modulating signal $f(t)$, the most common used modulation in practically relevant RADAR systems is a LFM, with an either linearly increasing (upsweep) or linearly decreasing (downsweep) instantaneous frequency versus time. For the particular case of a single-upsweep LFM signal of sweep duration T, the instantaneous frequency $f(t)$ is defined as

$$f(t) = \begin{cases} f_{\text{l}} & -\infty \leq t < 0 \\ f_{\text{l}} + \mu t & 0 \leq t < T \\ f_{\text{h}} & T \leq t < \infty \end{cases}, \tag{2.3}$$

where f_{l} is the lowest or the start frequency of the sweep and f_{h} the highest or stop frequency of the sweep. The variable μ is referred to as the sweep-rate, and describes how fast the frequency changes with time, i.e. it is a

measure for the slope of $f(t)$. It is given as the ratio of sweep bandwidth BW to sweep duration T

$$\mu = \frac{f_\mathrm{h} - f_\mathrm{l}}{T} = \frac{\mathrm{BW}}{T}. \tag{2.4}$$

To express the local signal $x^{\mathrm{lo}}(t)$ from (2.1) for the particular case of upsweep LFM, the instantaneous phase must be expressed explicitly by performing the integration (2.2), which results in

$$\phi(t) = \begin{cases} 2\pi f_\mathrm{l} t + \phi_0 & -\infty \leq t < 0 \\ 2\pi f_\mathrm{l} t + \pi\mu t^2 + \phi_0 & 0 \leq t < T \\ 2\pi f_\mathrm{h} t - 2\pi f_\mathrm{h} T + 2\pi f_\mathrm{l} T + \pi\mu T^2 + \phi_0 & T \leq t < \infty \end{cases}, \tag{2.5}$$

where ϕ_0 accounts for an arbitrary but constant phase at $t = 0$. The obtained instantaneous frequency and instantaneous phase functions are plotted in figure 2.3 a) and b) using normalized values for all parameters. It can be seen that for $t < 0$ the instantaneous frequency is constant at $f = f_\mathrm{l}$. Accordingly, since phase is the time integral of frequency, the instantaneous phase of the signal is a linear increasing function with slope f_l. Since the signal is modeled based on its instantaneous frequency the instantaneous phase cannot be determined uniquely. Hence the integration constant ϕ_0 is used to pinpoint the instantaneous phase at $t = 0$ to a fixed value, yielding a unique expression for $\phi(t)$.

In the interval $0 \leq t < T$ the signal's frequency increases linearly with a slope of μ. Accordingly the corresponding instantaneous phase is a quadratic function. A continuous phase at $t = 0$ is assured by the proper use of ϕ_0 for $t < 0$ and $0 \leq t < T$ in (2.5). After a sweep time of T the instantaneous frequency equals f_h, and $f(t)$ remains constant at $f(t) = f_\mathrm{h}$ for $t > T$. Consequently the instantaneous phase now has a linear slope of f_h. To ensure a continuous phase at $t = T$, an extended integration constant depending on the sweep duration T has to be used. This results in the lengthy formulation of the last row in (2.5).

The LFM single-upsweep signal is obtained by combining equations (2.1) and (2.5). It is plotted in figure 2.3 c). Expressed explicitly the FMCW signal model for $x^{\mathrm{lo}}(t)$ which will be used throughout this thesis is given by

$$x^{\mathrm{lo}}(t) = \begin{cases} \exp \mathrm{j}\left(2\pi f_\mathrm{l} t + \phi_0\right) & -\infty \leq t < 0 \\ \exp \mathrm{j}\left(2\pi f_\mathrm{l} t + \pi\mu t^2 + \phi_0\right) & 0 \leq t < T \\ \exp \mathrm{j}\left(2\pi f_\mathrm{h}(t - T) + 2\pi f_\mathrm{l} T + \pi\mu T^2 + \phi_0\right) & T \leq t < \infty \end{cases}. \tag{2.6}$$

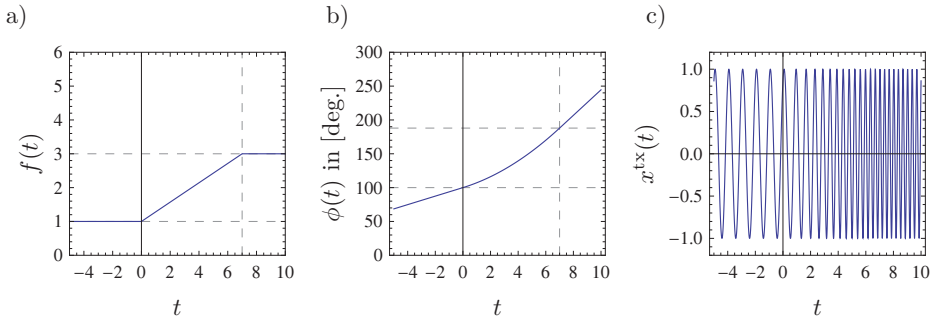

Fig. 2.3: Single-upsweep LFMCW signal. a) Instantaneous frequency $f(t)$, b) phase $\phi(t)$, and c) time-domain signal $x^{\mathrm{tx}}(t)$ for normalized parameters $f_{\mathrm{l}} = 1$, $f_{\mathrm{h}} = 3$, $T = 7$ and $\mu = 2/7$. The linear slope of the instantaneous frequency for $t \in [0, T]$ is clearly visible, resulting in a quadratic slope of the instantaneous phase.

2.1.1.2 Radiated, Scattered, and Total Fields

The real part $x^{\mathrm{tx}}(t) = \Re\left\{x^{\mathrm{lo}}(t)\right\}$ of the local signal is then radiated using the RADAR system's TX antenna. In this introductory section the TX antenna is modeled as an isotropic transducer, which maps the excitation signal $x^{\mathrm{lo}}(t)$ onto a homogeneous spherical wave $\underline{\boldsymbol{e}}^{\mathrm{tx}}$ propagating away from the TX antenna. This wave is expressed by

$$\underline{\boldsymbol{e}}^{\mathrm{tx}}(t, \underline{\boldsymbol{r}}) = \frac{1}{\left|\underline{\boldsymbol{r}} - \underline{\boldsymbol{p}}^{\mathrm{tx}}\right|} \delta\left(t - \frac{\left|\underline{\boldsymbol{r}} - \underline{\boldsymbol{p}}^{\mathrm{tx}}\right|}{c_0}\right) * \underline{\boldsymbol{h}}^{\mathrm{ant,tx}}(t) * x^{\mathrm{tx}}(t), \tag{2.7}$$

where the conversion from the scalar signal $x^{\mathrm{lo}}(t)$ to the vector field $\underline{\boldsymbol{e}}^{\mathrm{tx}}(t)$ is entirely captured by $\underline{\boldsymbol{h}}^{\mathrm{ant,tx}}$. The direction of $\underline{\boldsymbol{h}}^{\mathrm{ant,tx}}$ and consequently the polarization of $\underline{\boldsymbol{e}}^{\mathrm{tx}}$(t, $\underline{\boldsymbol{r}}$) is described in terms of the basis vectors $\underline{\boldsymbol{\theta}}^{\mathrm{tx}}, \underline{\boldsymbol{\varphi}}^{\mathrm{tx}}$ of the local coordinate system centered at the TX antenna, such that $\underline{\boldsymbol{h}}^{\mathrm{ant,tx}}$ can be expressed by its $\underline{\boldsymbol{\theta}}^{\mathrm{tx}}$- and $\underline{\boldsymbol{\varphi}}^{\mathrm{tx}}$-components

$$\underline{\boldsymbol{h}}^{\mathrm{ant,tx}}(t) = \underline{\boldsymbol{\theta}}^{\mathrm{tx}} h_{\theta}^{\mathrm{ant,tx}}(t) + \underline{\boldsymbol{\varphi}}^{\mathrm{tx}} h_{\phi}^{\mathrm{ant,tx}}(t) = \begin{bmatrix} h_{\theta}^{\mathrm{ant,tx}}(t) \\ h_{\phi}^{\mathrm{ant,tx}}(t) \end{bmatrix}. \tag{2.8}$$

As will be seen in chapter 4 $\underline{\boldsymbol{h}}^{\mathrm{ant,tx}}$ is typically used to model the far field radiation of an antenna, and hence (2.8) only contains transversal components. Propagation in free space is captured by the first convolution operand from (2.7), a weighted delta distribution. This formalism is closely related to the

principles of UWB antenna characterization [46]. The wavelength of the radiated signal is then related to the velocity of propagation by

$$\lambda = \frac{c_0}{f}, \quad \lambda_l = \frac{c_0}{f_\mathrm{l}}, \quad \lambda_\mathrm{h} = \frac{c_0}{f_\mathrm{h}}. \tag{2.9}$$

Implicitly, in (2.7) it is assumed that the transmission medium is isotropic and linear, i.e. the physical properties of the medium do not depend on the direction of wave propagation and the signals at any particular point can be superimposed linearly. This is a traditional assumption for propagation in e.g. air [89] and will be maintained throughout this thesis. The velocity of propagation is given by c_0. Note that the realization of a true isotropic antenna as used in 2.7 is impossible [90], [91]. It serves as a simplified model for the antenna in this chapter and will be substituted with models for realistic UWB antennas in chapter 4. Defining the distance $d^{\mathrm{tx,r}}$ between the TX antenna located at $\underline{\boldsymbol{p}}^{\mathrm{tx}}$ and an arbitrary coordinate $\underline{\boldsymbol{r}}$ by $d^{\mathrm{tx,r}} = \left|\underline{\boldsymbol{p}}^{\mathrm{tx}} - \underline{\boldsymbol{r}}\right|$, the propagation delay between both points is given by $T^{\mathrm{tx,r}} = d^{\mathrm{tx,r}}/c_0$. Then equation (2.7) can be expressed in a more compact form

$$\underline{\boldsymbol{e}}^{\mathrm{tx}}(t, \underline{\boldsymbol{r}}) = \underline{\boldsymbol{h}}^{\mathrm{ant,tx}}(t) * \frac{1}{d^{\mathrm{tx,r}}} x^{\mathrm{tx}}\left(t - T^{\mathrm{tx,r}}\right). \tag{2.10}$$

The electric field propagates through free space, until it hits one or several targets where it is scattered. For the scattering process, also a very simplified model is used: The targets simply map the locally incident field at the position $\underline{\boldsymbol{p}}_n^{\mathrm{tgt}}$ of target n to an E-field isotropically propagating away from the target position according to

$$\underline{\boldsymbol{e}}_n^{\mathrm{tgt}}(t, \underline{\boldsymbol{r}}) = \frac{1}{\left|\underline{\boldsymbol{r}} - \underline{\boldsymbol{p}}^{\mathrm{tx}}\right|} \delta\left(t - \frac{\left|\underline{\boldsymbol{p}}_n^{\mathrm{tgt}} - \underline{\boldsymbol{r}}\right|}{c_0}\right) * \underline{\underline{\boldsymbol{h}}}_n^{\mathrm{tgt}}(t) * \underline{\boldsymbol{e}}^{\mathrm{tx}}\left(t, \underline{\boldsymbol{p}}_n^{\mathrm{tgt}}\right). \tag{2.11}$$

The matrix $\underline{\underline{\boldsymbol{h}}}_n^{\mathrm{tgt}}$ can be interpreted as the time-domain radar cross section (RCS) of target n [92], since it captures how much of the incident field is scattered. It models how both transverse components of the incident field are mapped to the transverse components of the scattered field. To evaluate (2.11), all fields have to be expressed in terms of the target's local coordinate system with basis vectors $\underline{\boldsymbol{\theta}}_m^{\mathrm{tgt}}$ and $\underline{\boldsymbol{\varphi}}_m^{\mathrm{tgt}}$. In this thesis it is generally assumed that all coordinate systems have identically oriented z-axes. Then, as illustrated in figure 2.4, the scalar product of the transverse basis vectors of two local coordinate systems is given by $\underline{\boldsymbol{\theta}}_m^{\mathrm{tgt}}\underline{\boldsymbol{\theta}}^{\mathrm{tx}} = 1$ and $\underline{\boldsymbol{\varphi}}_m^{\mathrm{tgt}}\underline{\boldsymbol{\varphi}}^{\mathrm{tx}} = -1$ [44]. The

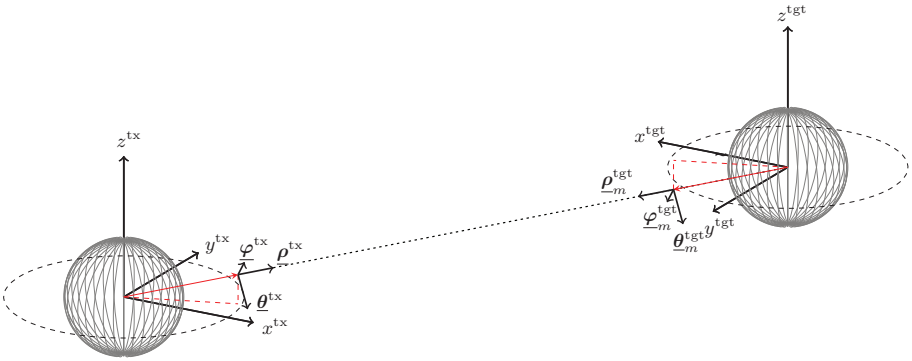

Fig. 2.4: Definition of local spherical coordinate system and relation of transverse basis vectors for line-of-sight (LOS) connection, e.g. for TX antenna and target. It is assumed that all local coordinate systems have identical z-axes. Then the scalar product of the transverse basis vectors is $\underline{\boldsymbol{\theta}}_m^{\mathrm{tgt}}\underline{\boldsymbol{\theta}}^{\mathrm{tx}} = 1$ and $\underline{\boldsymbol{\varphi}}_m^{\mathrm{tgt}}\underline{\boldsymbol{\varphi}}^{\mathrm{tx}} = -1$.

basis vector conversion thus reduces to taking into account the sign change in the $\underline{\boldsymbol{\varphi}}$ direction. For evaluation of (2.11) the RCS matrix $\underset{\sim}{\boldsymbol{h}}_n^{\mathrm{tgt}}$ can consequently be expressed by

$$\underset{\sim}{\boldsymbol{h}}_n^{\mathrm{tgt}}(t) = \begin{bmatrix} h_{\theta\theta}^{\mathrm{tgt}}(t) & -h_{\theta\phi}^{\mathrm{tgt}}(t) \\ h_{\varphi\theta}^{\mathrm{tgt}}(t) & -h_{\varphi\varphi}^{\mathrm{tgt}}(t) \end{bmatrix}, \tag{2.12}$$

where, e.g., the element $h_{\theta\varphi}^{\mathrm{tgt}}(t)$ quantifies the scattering process from the $\underline{\boldsymbol{\varphi}}_m^{\mathrm{tgt}}$ component of the incident field to the $\underline{\boldsymbol{\theta}}_m^{\mathrm{tgt}}$ component of the scattered field. It is assumed in this formulation that the target scatters the incident field $\underline{\boldsymbol{e}}^{\mathrm{tx}}$ isotropically, since $\underset{\sim}{\boldsymbol{h}}_n^{\mathrm{tgt}}(t)$ is independent of the direction.

The distances and propagation delays between TX antenna and target as well as target and $\underline{\boldsymbol{r}}$ are given by

$$\begin{aligned} d_n^{\mathrm{tx,tgt}} &= \left|\underline{\boldsymbol{p}}_n^{\mathrm{tgt}} - \underline{\boldsymbol{p}}^{\mathrm{tx}}\right|, \; T_n^{\mathrm{tx,tgt}} = \frac{d_n^{\mathrm{tx,tgt}}}{c_0} \\ d_n^{\mathrm{tgt,r}} &= \left|\underline{\boldsymbol{r}} - \underline{\boldsymbol{p}}_n^{\mathrm{tgt}}\right|, \; T_n^{\mathrm{tgt,r}} = \frac{d_n^{\mathrm{tgt,r}}}{c_0} \end{aligned} \tag{2.13}$$

The field observed at $\underline{\boldsymbol{r}}$ due to scattering by target n can be expressed by inserting (2.7) into (2.11) and simplifying using (2.13)

$$\underline{\boldsymbol{e}}_n^{\mathrm{tgt}}(t, \underline{\boldsymbol{r}}) = \frac{1}{d_n^{\mathrm{tgt,r}} d_n^{\mathrm{tx,tgt}}} \cdot \underset{\sim}{\boldsymbol{h}}_n^{\mathrm{tgt}}(t) * \underline{\boldsymbol{h}}^{\mathrm{ant,tx}}(t) * x^{\mathrm{tx}}\left(t - T_n^{\mathrm{tgt,r}} - T_n^{\mathrm{tx,tgt}}\right). \tag{2.14}$$

Since the medium is considered as linear, at the position $\underline{\boldsymbol{p}}^{\mathrm{rx}}$ of the receive antenna the total E-Field is a superposition of the transmitted E-field and the E-fields due to scattering at all N targets

$$\underline{\boldsymbol{e}}^{\mathrm{tot}}(t, \underline{\boldsymbol{p}}^{\mathrm{rx}}) = \underline{\boldsymbol{e}}^{\mathrm{tx}}(t, \underline{\boldsymbol{p}}^{\mathrm{rx}}) + \sum_{n=1}^{N} \underline{\boldsymbol{e}}_n^{\mathrm{tgt}}(t, \underline{\boldsymbol{p}}^{\mathrm{rx}}). \tag{2.15}$$

2.1.1.3 Received Signal

In accordance with the TX antenna the RX antenna is also modeled as isotropic. It transduces the E-field at position $\underline{\boldsymbol{p}}^{\mathrm{rx}}$ to the received signal $x^{\mathrm{rx}}(t)$ according to

$$x^{\mathrm{rx}}(t) = \left(\underline{\boldsymbol{h}}^{\mathrm{ant,rx}}(t)\right)^{\mathsf{T}} * \underline{\boldsymbol{e}}^{\mathrm{tot}}(t, \underline{\boldsymbol{p}}^{\mathrm{rx}}), \tag{2.16}$$

where the vector $\underline{\boldsymbol{h}}^{\mathrm{ant,rx}}(t)$ captures how both transverse components of the incident field defined in the local coordinate frame of the RX antenna are mapped to the scalar signal $x^{\mathrm{rx}}(t)$. Again the sign change of the $\underline{\boldsymbol{\varphi}}$ component occurring in the transition from TX or target local coordinate frame to RX antenna coordinate frame is directly taken into account and $\underline{\boldsymbol{h}}^{\mathrm{ant,rx}}$ for direct evaluation of (2.16) can be expressed by

$$\underline{\boldsymbol{h}}^{\mathrm{ant,rx}}(t) = \underline{\boldsymbol{\theta}}^{\mathrm{rx}} h_{\theta}^{\mathrm{ant,rx}}(t) + \underline{\boldsymbol{\varphi}}^{\mathrm{rx}} h_{\phi}^{\mathrm{ant,rx}}(t) = \begin{bmatrix} h_{\theta}^{\mathrm{ant,rx}}(t) \\ -h_{\phi}^{\mathrm{ant,rx}}(t) \end{bmatrix}. \tag{2.17}$$

Inserting (2.10) and (2.14) in (2.15) and finally into (2.16), the following expression for the received signal is obtained

$$\begin{aligned} x^{\mathrm{rx}}(t) = \left(\underline{\boldsymbol{h}}^{\mathrm{ant,rx}}(t)\right)^{\mathsf{T}} * \underline{\boldsymbol{h}}^{\mathrm{ant,tx}}(t) * \frac{1}{d^{\mathrm{tx,rx}}} x^{\mathrm{tx}}\left(t - T^{\mathrm{tx,rx}}\right) \\ + \Bigg[\left(\underline{\boldsymbol{h}}^{\mathrm{ant,rx}}(t)\right)^{\mathsf{T}} * \underset{\sim}{\boldsymbol{h}}_n^{\mathrm{tgt}}(t) * \underline{\boldsymbol{h}}^{\mathrm{ant,tx}}(t) \\ * \sum_{n=1}^{N} \frac{1}{d_n^{\mathrm{tgt,rx}}} \frac{1}{d_n^{\mathrm{tx,tgt}}} x^{\mathrm{tx}}\left(t - T_n^{\mathrm{tx,tgt}} - T_n^{\mathrm{tgt,rx}}\right) \Bigg], \end{aligned} \tag{2.18}$$

In (2.18) the definitions of distance and propagation time between TX and RX antenna as well as between target n and RX antenna according to

$$\begin{aligned} d^{\mathrm{tx,rx}} &= \left|\underline{\boldsymbol{p}}^{\mathrm{rx}} - \underline{\boldsymbol{p}}^{\mathrm{tx}}\right|, \; T^{\mathrm{tx,rx}} = \frac{d^{\mathrm{tx,rx}}}{c_0}, \\ d_n^{\mathrm{tgt,rx}} &= \left|\underline{\boldsymbol{p}}^{\mathrm{rx}} - \underline{\boldsymbol{p}}_n^{\mathrm{tgt}}\right|, \; T_n^{\mathrm{tgt,rx}} = \frac{d_n^{\mathrm{tgt,rx}}}{c_0} \end{aligned} \tag{2.19}$$

are used. Without loss of generality it is assumed that antenna TX and RX effective heights as well as the time-domain RCS introduces no distortion into transmitted and received signals

$$\left(\underline{\boldsymbol{h}}^{\text{ant,rx}}(t)\right)^{\mathsf{T}} * \underline{\boldsymbol{h}}^{\text{ant,tx}}(t) = const. \tag{2.20}$$

$$\left(\underline{\boldsymbol{h}}^{\text{ant,rx}}(t)\right)^{\mathsf{T}} * \underset{\sim}{\boldsymbol{h}}_n^{\text{tgt}}(t) * \underline{\boldsymbol{h}}^{\text{ant,tx}}(t) = const. \tag{2.21}$$

Then constant coefficients a_n^{tgt} capturing the attenuation of the signal due to free-space path loss, target RCS and antenna effective heights can be defined. They are indexed for the direct component with $n = 0$ and for all targets with $n = 1 \dots N$ and are expressed by

$$a_0^{\text{tgt}} = \frac{1}{d^{\text{tx,rx}}} \cdot \left(\underline{\boldsymbol{h}}^{\text{ant,rx}}(t)\right)^{\mathsf{T}} * \underline{\boldsymbol{h}}^{\text{ant,tx}}(t), \tag{2.22}$$

$$a_n^{\text{tgt}} = \frac{1}{d_n^{\text{tgt,rx}} d_n^{\text{tx,tgt}}} \cdot \left(\underline{\boldsymbol{h}}^{\text{ant,rx}}(t)\right)^{\mathsf{T}} * \underset{\sim}{\boldsymbol{h}}_n^{\text{tgt}}(t) * \underline{\boldsymbol{h}}^{\text{ant,tx}}(t). \tag{2.23}$$

Thus (2.18) simplifies to a convenient expression for the received signal

$$x^{\text{rx}}(t) = \sum_{n=0}^{N} a_n^{\text{tgt}} x^{\text{tx}}\left(t - T_n^{\text{rt}}\right). \tag{2.24}$$

It is obvious, that the received signal $x^{\text{rx}}(t)$ is a superposition of $N+1$ time-delayed and weighted copies of the transmitted signal $x^{\text{tx}}(t)$, where the 0^{th} component is used to model the direct path between transmit and receive antenna, and the remaining N components are due to scattering of the transmitted E-field at the targets. The propagation delay T_n^{rt} is also referred to as the round-trip time, since it is the time the signal needs to propagate from the TX antenna to the scatterer n and back to RX antenna. It is hence given by the sum of both one-way paths

$$T_n^{\text{rt}} = T_n^{\text{tgt,rx}} + T_n^{\text{tx,tgt}}. \tag{2.25}$$

Note the similarity of (2.23) to the simplified form of the classical RADAR equation as e.g. given in [3]: Since the received power from target n can be interpreted as a_n^{tgt} to the power of two, it is obvious that it decreases with the distance to the power of four (assuming a monostatic scenario with TX and RX antennas at the same position). The traditional gains of TX and RX antennas are taken into account by $\underline{\boldsymbol{h}}^{\text{ant,tx}}(t)$ and $\underline{\boldsymbol{h}}^{\text{ant,rx}}(t)$, and the RCS is modeled by $\underset{\sim}{\boldsymbol{h}}_n^{\text{tgt}}(t)$.

2.1.1.4 Downconversion

After reception, $x^{\text{rx}}(t)$ is multiplied with $x^{\text{lo}}(t)$ (compare figure 2.2) yielding the mixing product

$$x^{\text{mix}}(t) = x^{\text{lo}}(t)x^{\text{rx}}(t) = \sum_{n=0}^{N} a_n^{\text{tgt}} x^{\text{lo}}(t)x^{\text{tx}}\left(t - T_n^{\text{rt}}\right). \tag{2.26}$$

As shown in Appendix A (2.26) can equivalently be expressed by

$$x^{\text{mix}}(t) = \sum_{n=0}^{N} \frac{1}{2} a_n^{\text{tgt}} \left[\exp\left(\text{j}\phi_n^{\text{mix,diff}}(t)\right) + \exp\left(\text{j}\phi_n^{\text{mix,sum}}(t)\right)\right], \tag{2.27}$$

where the explicit solution for the phase functions $\phi_n^{\text{mix,diff}}(t)$ and $\phi_n^{\text{mix,sum}}(t)$ is also provided in Appendix A. In figure 2.5, both instantaneous phase functions $\phi_n^{\text{mix,diff}}(t)$ and $\phi_n^{\text{mix,sum}}(t)$ as well as the corresponding instantaneous frequency functions

$$f_n^{\text{mix,diff}}(t) = \frac{1}{2\pi}\frac{d}{dt}\phi_n^{\text{mix,diff}}(t) \tag{2.28}$$

$$f_n^{\text{mix,sum}}(t) = \frac{1}{2\pi}\frac{d}{dt}\phi_n^{\text{mix,sum}}(t) \tag{2.29}$$

are plotted versus time, for a received signal consisting of a single scattering component $n = 1$ and neglecting the direct component between TX and RX antenna. It can be seen that the instantaneous frequency of the sum component $f_1^{\text{mix,sum}}(t)$ oscillates at twice the lowest frequency f_{l} for $t < 0$. For $t > 0$ the instantaneous frequency of the sum component monotonically increases, with a slope depending on the actual instantaneous frequencies of the locally generated and the received single scattering component. After $t = T + T_n^{\text{rt}}$, i.e. when both the locally generated and the received components oscillate at $f(t) = f_{\text{h}}$, the sum component oscillates at twice the highest sweep frequency f_{h}. Correspondingly, the instantaneous phase of the sum component is a linear function of time for $t < 0$ and $t > T + T_n^{\text{rt}}$. In between, where the frequency increases linear, the instantaneous phase is a quadratic function of time, where the coefficient of the quadratic term is directly proportional to the slope of the instantaneous frequency.

The instantaneous frequency $f_n^{\text{mix,diff}}(t)$ of the difference component is zero for $t < 0$. Beginning with the frequency ramp of the locally generated signal

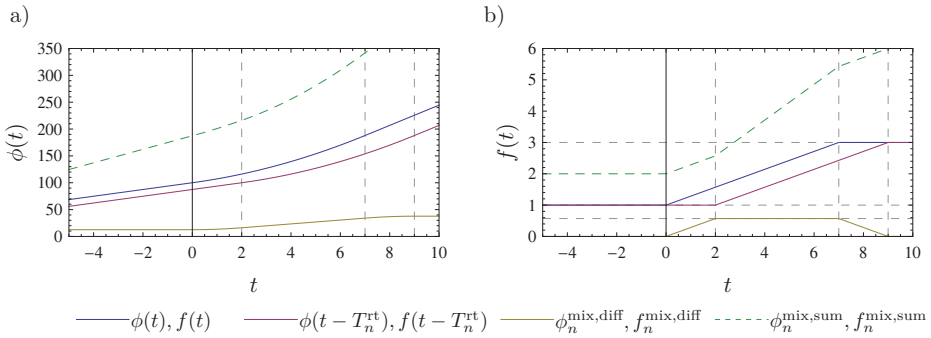

Fig. 2.5: Difference and sum a) phases $\phi_n^{\mathrm{mix,diff}}$, $\phi_n^{\mathrm{mix,sum}}$ and b) frequencies $f_n^{\mathrm{mix,diff}}$, $f_n^{\mathrm{mix,sum}}$, respectively, for a single-upsweep LFM signal and a single target return. Normalized parameters $f_{\mathrm{l}} = 1$, $f_{\mathrm{h}} = 3$, $T = 7$, $\mu = 2/7$, and $T_n^{\mathrm{rt}} = 2$ are used. Note that the instantaneous frequency of the difference component of the beat frequency signal is constant and directly proportional to the time delay T_n^{rt} for $t \in [T_n^{\mathrm{rt}}, T]$.

at $t = 0$, while the frequency of the received signal still is constant, $f_n^{\mathrm{mix,diff}}(t)$ starts to increase linearly with a slope corresponding to μ. After the time delay T_n^{rt} the instantaneous frequency of the received signal also starts to increase and now the slopes of both the locally generated and received signal coincide for a time of $T - T_n^{\mathrm{rt}}$. It is the *fundamental principle of FMCW RADAR* that in this interval $f_n^{\mathrm{mix,diff}} = const.$ and directly proportional to T_n^{rt}, with the proportionately constant being the sweep rate μ. By estimating this constant $f_n^{\mathrm{mix,diff}}(t)$ the round-trip time T_n^{rt} and correspondingly the distance between TX antenna, target and RX antenna can be measured. After $t = T$ the instantaneous frequency of the locally generated signal equals f_h and its frequency remains constant for $t \geq T$. Since the instantaneous frequency of the time-delayed received signal still increases for an additional time of T_n^{rt}, the frequency of the difference component linearly decreases with a slope of $-\mu$ for $T < t < T + T_n^{\mathrm{rt}}$. Beginning with $t = T_n^{\mathrm{rt}}$ both the locally generated as well as the received signals oscillate at the sweep upper frequency f_h resulting in $f_n^{\mathrm{mix,diff}} = 0$.

2.1.1.5 Low Pass Filtering

For each target n the mixing product $x^{\mathrm{mix}}(t)$ of received and locally generated signals contains two harmonic components: one oscillating at the sum frequency $f_n^{\mathrm{mix,sum}}(t)$ and one oscillating at the difference frequency $f_n^{\mathrm{mix,diff}}(t)$.

However, as shown above it is only the signal oscillating at $f_n^{\text{mix,diff}}(t)$ which is used for distance estimation. Hence all components oscillating at $f_n^{\text{mix,sum}}(t)$ must be eliminated from the mixing product.

It can easily be seen that the maximum possible difference frequency is limited by $f_n^{\text{mix,diff}}(t) < \mu T$, which occurs if $T_n^{\text{rt}} \geq T$, compare also the derivation in Appendix A. The minimum possible sum frequency in contrast is limited by $f_n^{\text{mix,sum}}(t) \geq 2f_l$ which occurs if $T_n^{\text{rt}} = 0$. Thus difference and sum components never overlap, i.e. $f_n^{\text{mix,diff}}(t) < f_n^{\text{mix,sum}}(t)$ if

$$\mu T < 2f_{\text{l}}, \tag{2.30}$$

i.e. the sweep bandwidth $\text{BW} = \mu T$ is lower than twice the sweep start frequency. The possible regions of the difference and sum phases and frequencies are illustrated in figure 2.6.

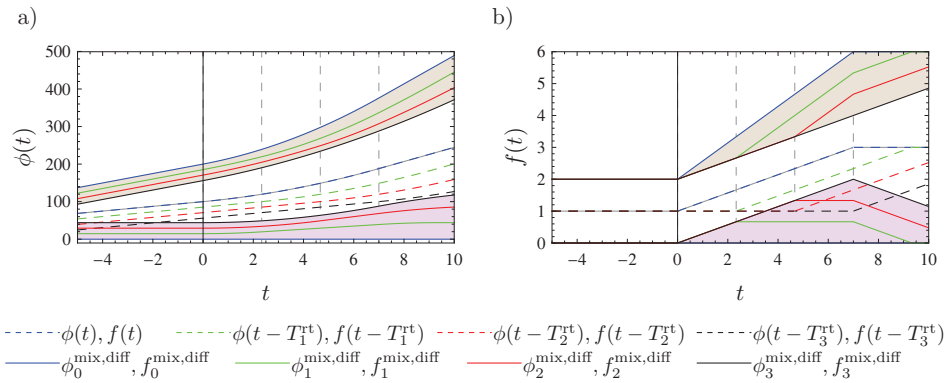

Fig. 2.6: Difference and sum a) beat phases $\phi_n^{\text{mix,diff}}$, $\phi_n^{\text{mix,sum}}$ and b) beat frequencies $f_n^{\text{mix,diff}}$, $f_n^{\text{mix,sum}}$, for a single-upsweep LFM signal with multiple target returns. Normalized parameters $f_{\text{l}} = 1$, $f_{\text{h}} = 3$, $T = 7$, $\mu = 2/7$, and $T_1^{\text{rt}} = 2$, $T_1^{\text{rt}} = 4$, $T_1^{\text{rt}} = T$ are used. $\phi_0^{\text{mix,diff}}$ and $f_0^{\text{mix,diff}}$ are obtained from zero-delay return signal with $T_1^{\text{rt}} = 0$.

However, considering as an example a FMCW RADAR system operating in the UWB band with $f_{\text{l}} = 5\,\text{GHz}$, $f_{\text{h}} = 10\,\text{GHz}$, and $\text{BW} = 5\,\text{GHz}$ it can easily be seen that RADAR system parameter can be selected such that (2.30) does not hold. Consequently a low-pass filtering operation may in a strict sense not be able to eliminate components oscillating at $f_n^{\text{mix,sum}}(t)$ from the mixing product $x^{\text{mix}}(t)$ for all time instants t.

Restricting the attention to the interval of interest for distance estimation, $\max\{T_n^{\text{rt}}\} \leq t \leq T$, it follows that $f_n^{\text{mix,diff}}(t) \leq \mu \max\{T_n^{\text{rt}}\}$ and $f_n^{\text{mix,sum}}(t) \geq 2f_l + \mu \max\{T_n^{\text{rt}}\}$. Hence all components oscillating at the sum frequency $f_n^{\text{mix,sum}}(t)$ can be removed in this interval using a low-pass filter. The necessary filter parameters are a pass band width of $\mu \max\{T_n^{\text{rt}}\}$, a transition region of $2f_l$ and a sufficient attenuation beginning at $f = 2f_l + \mu \max\{T_n^{\text{rt}}\}$. In the remainder of this thesis perfect canceling of the sum component is assumed and the low-pass filtered mixing product reduces to

$$x^{\text{mix,LP}}(t) = \sum_{n=0}^{N} \frac{a_n^{\text{tgt}}}{2} \exp(\mathrm{j}\phi_n^{\text{mix,diff}}(t)). \tag{2.31}$$

2.1.1.6 Range Information

The range information is entirely contained in $f_n^{\text{mix,diff}}(t)$ for $\max\{T_n^{\text{rt}}\} \leq t \leq T$, where the difference frequencies of all components in $x^{\text{mix,LP}}(t)$ are constant. Then (2.31) can be expressed as a sum of $N+1$ complex exponentials, each having a constant frequency f_n^{b} and a phase ϕ_n^{b}. Equation (2.31) can thus be expressed by

$$x^{\text{mix,LP}}(t) = \sum_{n=0}^{N} \frac{a_n^{\text{tgt}}}{2} \exp \mathrm{j}(2\pi f_n^{\text{b}} t + \phi_n^{\text{b}}), \max\{T_n^{\text{rt}}\} \leq t \leq T. \tag{2.32}$$

where f_n^{b} is referred to as beat frequency and ϕ_n^{b} as beat phase. As shown in appendix A, both are given by

$$f_n^{\text{b}} = \mu \cdot T_n^{\text{rt}}, \tag{2.33}$$

$$\phi_n^{\text{b}} = \phi_n^{\text{mix,diff}}(T_n^{\text{rt}}) = 2\pi f_{\text{l}} T_n^{\text{rt}} + \pi\mu (T_n^{\text{rt}})^2. \tag{2.34}$$

It is obvious that the problem of estimating the presence and distance of the targets reduces to the problem of estimating the number of components and the beat-frequency f_n^{b} of each component from $x^{\text{mix,LP}}(t)$ using the interval $\max\{T_n^{\text{rt}}\} \leq t \leq T$. Once N and $f_n^{\text{b}} = \mu T_n^{\text{rt}}$ are known, the setup of the RADAR unit, e.g. used sweep rate μ, TX and RX antenna positions, as well as the propagation conditions allow to interrelate T_n^{rt} to the target positions: RADAR is achieved.

Note that typically the duration of the LFMCW ramp is much longer than the maximum round-trip time, i.e. $T_n^{\text{rt}} << T$. Hence it is common practice to assume that the low-pass filtered mixing product can be observed in the interval $0 \leq t \leq T$. It is thus convenient to define an auxiliary function, which is the extrapolation of the low-pass filtered mixing product (2.32), i.e. valid $\forall t$. This auxiliary function is referred to as the beat signal in the following and is defined by

$$x^{\text{b}}(t) = \sum_{n=0}^{N} \frac{a_n^{\text{tgt}}}{2} \exp \text{j}(2\pi f_n^{\text{b}} t + \phi_n^{\text{b}}). \tag{2.35}$$

It is only the finite observation time which distinguishes the beat signal from the low-pass filtered mixing product. Hence (2.35) can be related to the signal (2.34) by multiplying it with a time window.

2.1.1.7 Summary of the FMCW Principle

In conclusion, equations (2.32) and (2.33) describe the operation principle of primary FMCW RADAR in a compact but exact way. A LFM frequency ramp of duration T is generated, radiated, and the echoes scattered from the targets are received. The return echoes are mixed with the locally generated frequency ramp and the beat signal consisting of a sum of constant-frequency complex sinusoids (cisoids), within a time interval ranging from the maximum round-trip-time $\max\{T_n^{\text{rt}}\}$ to the ramp duration T, is obtained. The frequency of each exponential is directly proportional to T_n^{rt}, where the sweep rate μ is the proportionality constant. Once the number and corresponding frequency of the beat-signal components has been estimated, the round trip time T_n^{rt} for scatterer n is given by (2.33). The path length between transmit, target, and receive antenna is given by (2.19) and (2.13), and depending on the RADAR station's geometrical setup the distance between RADAR station and each target can be estimated. As can be seen from (2.34), range information is also contained in the phase. Although approaches have been reported that this phase can be taken into account for increasing the precision of distance estimation, [93], [94] it is only the frequency information which is traditionally used for distance estimation, and will be used for distance estimation in this thesis.

2.1.2 Secondary Linear FMCW Radar Systems

Whereas it was shown that the primary RADAR system concept is suitable for estimating the distance between a RADAR station and several passive targets scattering the incident E-Field, a secondary RADAR system is used to estimate the distance between two active RADAR stations, as e.g. used by several state-of-the-art systems [11], [17], [25]–[31], [33]–[37]. Figure 2.7 shows the basic setup of a secondary FMCW RADAR system. In principle it

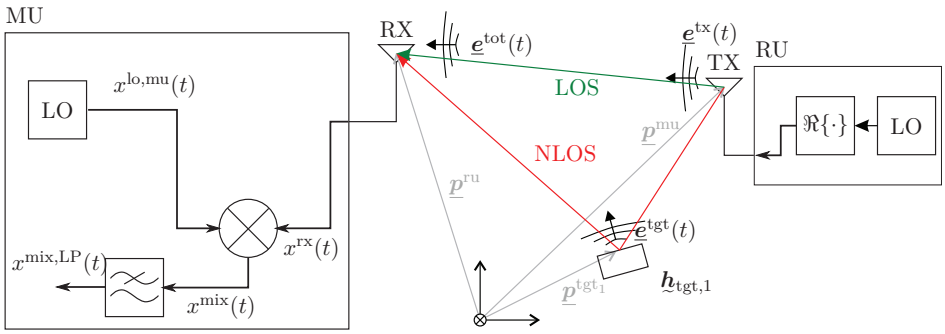

Fig. 2.7: Setup of a secondary RADAR system. A FMCW signal $x^{\mathrm{lo,ru}}(t)$ is generated in the reference unit (RU) and received by the measurement unit (MU) after a propagation delay proportional to the distance between both units. Here, the beat frequency signal $x^{\mathrm{mix}}(t)$ is obtained by mixing the received signal $x^{\mathrm{rx}}(t)$ with the locally generated oscillator signal $x^{\mathrm{lo,mu}}(t)$.

is treated identically to the primary FMCW RADAR system from figure 2.7, as the only difference is that TX and RX antennas are located at two or several physically separated RADAR units, and each RADAR unit generates its own local signal $x^{\mathrm{lo}}(t)$. In accordance with the application scenario from figure 1.1 the RADAR station radiating the FMCW RADAR signal is referred to as the RU, and the receiving RADAR station as the MU.

Both RADAR stations locally generate a FMCW signal as defined in (2.6), where perfectly synchronized coherent operation across reference and measurement units is assumed

$$x^{\mathrm{lo,mu}}(t) = x^{\mathrm{lo,ru}}(t). \tag{2.36}$$

Note that this simple assumption is one of the key points in implementing secondary FMCW RADAR systems [12] and technically challenging to

achieve. The RU radiates the real part of the locally generated signal, i.e. $x^{\mathrm{tx}}(t) = \Re\{x^{\mathrm{lo,ru}}(t)\}$ and the transmitted electromagnetic wave $\underline{\boldsymbol{e}}^{\mathrm{tx}}$ propagates towards the MU where it corresponds to the direct component of the received signal. The transmitted electric field $\underline{\boldsymbol{e}}^{\mathrm{tx}}$ might however also be scattered by one or several targets, e.g. walls or any structures present in the scenario, and those scattered fields $\underline{\boldsymbol{e}}^{\mathrm{tgt}}(t)$ superimpose with the direct LOS component. Consequently, the received signal $x^{\mathrm{rx}}(t)$ in the secondary RADAR scenario can be described identically to the received signal in the primary RADAR scenario (2.24), as a sum of direct component with index $n = 0$ and several components due to scattering at targets with indices $n = 1 \ldots N$. Whereas the direct component was considered as parasitic in the primary RADAR scenario since only components due to scattering at the targets were of interest, in the secondary RADAR scenario it is now the direct component which is of interest and all components scattered by the targets present in the scenario are considered as parasitic. It is the propagation delay T_0^{rt} of the LOS path which must be estimated for measuring the distance $d^{\mathrm{ru,mu}}$ between MU and RU. For the LOS path the round-trip time thus is

$$T_0^{\mathrm{rt}} = T^{\mathrm{tx,rx}} = \frac{\left|\underline{\boldsymbol{p}}^{\mathrm{mu}} - \underline{\boldsymbol{p}}^{\mathrm{ru}}\right|}{c_0} = \frac{d^{\mathrm{ru,mu}}}{c_0}. \tag{2.37}$$

For a NLOS path it is

$$T_n^{\mathrm{rt}} = \frac{\left|\underline{\boldsymbol{p}}_n^{\mathrm{tgt}} - \underline{\boldsymbol{p}}^{\mathrm{ru}}\right|}{c_0} + \frac{\left|\underline{\boldsymbol{p}}^{\mathrm{mu}} - \underline{\boldsymbol{p}}_n^{\mathrm{tgt}}\right|}{c_0}. \tag{2.38}$$

2.1.3 Model Abstraction for Receiving Antenna Arrays

Since the focus of this thesis lies on the design and characterization of RX antenna arrays for DOA estimation in UWB RADAR systems, a single abstract model capturing all important effects for both, primary and secondary RADAR systems is derived in this section. This abstract model is illustrated in figure 2.8. The fundamental idea of the abstract model is to draw the attention to the properties of the RX part of the RADAR system, while hiding the specific processes behind the generation of the target E-fields. The antenna symbols previously used in figures 2.2 and 2.7 have been replaced by dots, explicitly indicating that at this point the antennas are modeled as ideal sensor elements with an isotropic and distortion-less characteristic. Beginning with chapter 4, the sensor model at the RX side will then be replaced by a

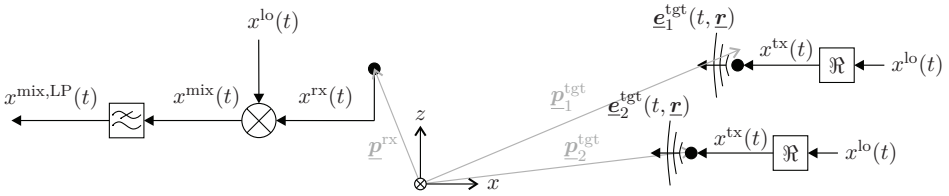

Fig. 2.8: Abstract model used to describe RX processing in FMCW RADAR systems. The antenna symbol is replaced by a dot symbol, indicating that a general ideal sensor model is used for the antennas.

realistic description of UWB antennas, such that antenna effects on FMCW processing can precisely be taken into account.

Hence every target in the RADAR system scenario, may it be a passive scatterer or an actively radiating RU, is modeled as an object radiating a homogeneous spherical wave

$$\underline{e}_n^{\mathrm{tgt}}(t,\underline{r}) = \left(\underline{\boldsymbol{\theta}}^{\mathrm{tx}} h_{n,\vartheta}^{\mathrm{tgt}} + \underline{\boldsymbol{\varphi}}^{\mathrm{tx}} h_{n,\varphi}^{\mathrm{tgt}}\right) \frac{1}{d^{\mathrm{tx,r}}} x^{\mathrm{tx}}\left(t - T^{\mathrm{tx,r}}\right). \tag{2.39}$$

The distance between target n and RX antenna is now referred to as $d_n^{\mathrm{tgt,rx}}$ and the propagation delay by T_n^{d}. Both are given by

$$d_n^{\mathrm{tgt}} = \left|\underline{\boldsymbol{p}}_n^{\mathrm{tgt}} - \underline{\boldsymbol{p}}^{\mathrm{rx}}\right|, \qquad T_n^{\mathrm{d}} = \frac{d_n^{\mathrm{tgt,rx}}}{c_0}. \tag{2.40}$$

Consequently, the received signal $x^{\mathrm{rx}}(t)$, the beat signal $x^{\mathrm{b}}(t)$ as well as beat frequency and beat phase are now given by

$$\boxed{x^{\mathrm{rx}}(t) = \sum_{n=1}^{N} a_n^{\mathrm{tgt}} x^{\mathrm{tx}}\left(t - T_n^{\mathrm{d}}\right)} \tag{2.41}$$

$$\boxed{x^{\mathrm{b}}(t) = \sum_{n=1}^{N} \frac{a_n^{\mathrm{tgt}}}{2} \exp \mathrm{j}(2\pi f_n^{\mathrm{b}} t + \phi_n^{\mathrm{b}})} \tag{2.42}$$

$$\boxed{f_n^{\mathrm{b}} = \mu \cdot T_n^{\mathrm{d}}} \tag{2.43}$$

$$\boxed{\phi_n^{\mathrm{b}} = \phi_n^{\mathrm{mix,diff}}(T_n^{\mathrm{d}}) = 2\pi f_1 T_n^{\mathrm{d}} + \pi\mu (T_n^{\mathrm{d}})^2} \tag{2.44}$$

$$\boxed{a_n^{\text{tgt}} \propto \frac{1}{d_n^{\text{tgt,rx}}}.} \tag{2.45}$$

Since in the abstract model there is no difference between the signal received on the LOS path (direct component) and signals due to scattering, the summation starts with $n = 1$.

2.2 Receiving Sensor Arrays for Linear FMCW Radar Systems

The preceding sections outlined the underlying principles of distance estimation in primary and secondary FMCW RADAR systems, respectively. To simplify the formulations the mathematical treatment in the preceding sections was limited to RADAR systems with a single receive antenna. By introducing several receive antennas, advanced functionality such as DOA estimation or other kinds of spatial processing can be implemented into the RADAR system. This section treats modeling of receiving sensor arrays for wideband FMCW RADAR systems in detail.

As illustrated in figure 2.9, modeling the output of the RX sensor array starts by formulating the exact response of the array. In the exact response the output of the array, in particular the signal properties across the sensor elements, is not only dependent on the direction of arrival, but also on absolute target distance. Since typically the target distance is much larger than the

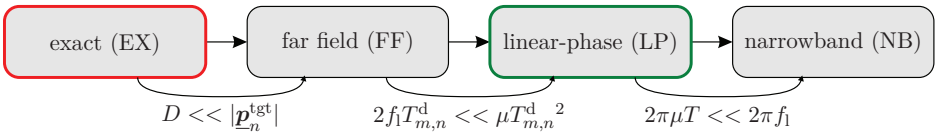

Fig. 2.9: Approximation steps in modeling the output of sensor array. The formulation begins with the exact model (EX). If it is assumed that the array aperture D is much smaller that the target distance, the EX can be simplified to the far field (FF) model. Further assuming a sufficiently small sweep rate and round-trip time yields the linear-phase model, and assuming a small bandwidth of the LFM chirp the narrowband (NB) model is obtained.

maximum dimension D of the sensor array, the array output can be simplified based on the far field assumption. Then the cross-sensor signal characteristics become independent of the target distance and dependent on the

DOA only. This is the preferred model for general spatial array processing. In the particular case of LFM signals, the beat-phase of the signals observed at the individual sensors obeys a nonlinear dependency of the round trip time. However, this nonlinear dependency can be neglected for realistic operation conditions and a linear-phase (LP) model can be derived. This is the model which serves as a basis for the DOA estimation used throughout this work.

In sensor array processing, often a further simplification is used for modeling the array output: the narrowband (NB) model. It is based on the assumption that the bandwidth of the signal impinging on the sensor array is so small compared to the array dimension, that it can be assumed that the only effect of the incident signal's DOA is a phase shift across the signals observed at the individual sensors. This narrowband model also is the basis for the state-of-the-art industrial RADAR systems. With an focus on wideband LFM signals in this thesis, it will be shown that the NB model however cannot be used for accurate DOA estimation in UWB FMCW RADAR systems.

2.2.1 Exact Model

Consider the RX sensor array FMCW RADAR scenario shown in figure 2.10, which is derived from the abstract LFMCW RADAR model introduced in section 2.1.3 by adding several coherent receive channels. The system has

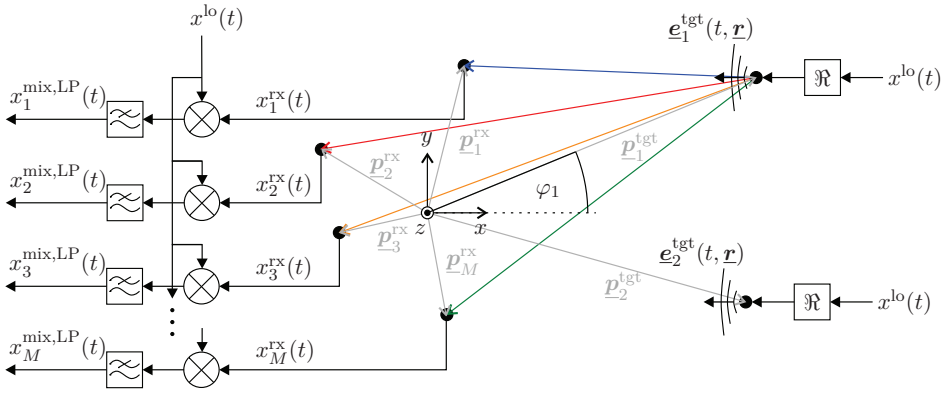

Fig. 2.10: Array of receiving sensors in FMCW RADAR systems. To simplify the treatment, the radiated field as well as the locally generated signals for downmixing the received signals are assumed to be perfectly coherent.

M sensors and N targets are present. The origin of the global coordinate system is set to the center of mass of the RX sensor array, as illustrated in figure 2.10. The position of sensor m is given by $\underline{\boldsymbol{p}}_m^{\text{rx}}$ and the position of target n by $\underline{\boldsymbol{p}}_n^{\text{tgt}}$. The distance between target n and sensor m is then given by $d_{m,n}^{\text{tgt,rx}} = \left|\underline{\boldsymbol{p}}_n^{\text{tgt}} - \underline{\boldsymbol{p}}_m^{\text{rx}}\right|$. As a special case the coordinate system origin is referred to with the index $m = 0$, i.e. a virtual sensor at the array origin. The distance between target n and coordinate system origin is then given by $d_{0,n}^{\text{tgt,rx}} = \left|\underline{\boldsymbol{p}}_n^{\text{tgt}}\right|$. The distance of target n to the coordinate origin, i.e. the array center, is now also simply referred to as the target's range

$$r_n = d_{0,n}^{\text{tgt,rx}}. \tag{2.46}$$

Following the formulations from section 2.1 and modeling the RX antennas as ideal, uncoupled isotropic sensors, the beat signal at sensor m due to n targets is given by

$$\boxed{x_m^{\text{b}}(t) = \sum_{n=1}^{N} \frac{a_{m,n}^{\text{tgt}}}{2} \exp \text{j}(2\pi f_{m,n}^{\text{b}} t + \phi_{m,n}^{\text{b}})} \tag{2.47}$$

where the beat frequency and beat phase are given by

$$\boxed{f_{m,n}^{\text{b}} = \mu \cdot T_{m,n}^{\text{d}}} \tag{2.48}$$

$$\boxed{\phi_{m,n}^{\text{b}} = 2\pi f_{\text{l}} T_{m,n}^{\text{d}} + \pi\mu (T_{m,n}^{\text{d}})^2} \tag{2.49}$$

and the coefficients $a_{m,n}^{\text{tgt}}$ are proportional to the inverse of the distance between target and RX antenna m, i.e. $a_{m,n}^{\text{tgt}} \propto 1/d_{m,n}^{\text{tgt,rx}}$. Introducing vectorial notation, the received signal from all m antennas can be expressed compactly by

$$\underline{\boldsymbol{x}}^{\text{b}}(t) = \begin{bmatrix} x_1^{\text{b}}(t) \\ x_2^{\text{b}}(t) \\ \vdots \\ x_M^{\text{b}}(t) \end{bmatrix} = \frac{1}{2} \sum_{n=1}^{N} \begin{bmatrix} a_{1,n}^{\text{tgt}} \exp \text{j}(2\pi f_{1,n}^{\text{b}} t + \phi_{1,n}^{\text{b}}) \\ a_{2,n}^{\text{tgt}} \exp \text{j}(2\pi f_{2,n}^{\text{b}} t + \phi_{2,n}^{\text{b}}) \\ \vdots \\ a_{M,n}^{\text{tgt}} \exp \text{j}(2\pi f_{M,n}^{\text{b}} t + \phi_{M,n}^{\text{b}}) \end{bmatrix}. \tag{2.50}$$

Equation (2.50) is referred to as the exact model for the IF output of a FMCW sensor array. Note that the beat signal for a certain target n obtained at the

different sensors varies in amplitude, beat frequency, and beat-phase across the sensors.

The time delay $T^{\mathrm{d}}_{m,n}$ to each sensor of the array is a function of target position $\underline{\boldsymbol{p}}^{\mathrm{tgt}}_n$ and the position $\underline{\boldsymbol{p}}^{\mathrm{rx}}_m$ of the m-th sensor. It can be decomposed into two terms according to

$$T^{\mathrm{d}}_{m,n}(\underline{\boldsymbol{p}}^{\mathrm{tgt}}_n, \underline{\boldsymbol{p}}^{\mathrm{rx}}_m) = T^{\mathrm{d}}_{0,n}(r_n) + \Delta T^{\mathrm{d}}_{m,n}(\underline{\boldsymbol{p}}^{\mathrm{rx}}_m, \underline{\boldsymbol{p}}^{\mathrm{tgt}}_n), \tag{2.51}$$

where $T^{\mathrm{d}}_{0,n}$ is the time-delay between target and array center and $\Delta T^{\mathrm{d}}_{m,n}$ is the Delta time-delay, which captures the difference between coordinate origin and sensor element m. Note that $T^{\mathrm{d}}_{0,n}$ is only dependent on the target's range, in contrast to $\Delta T^{\mathrm{d}}_{m,n}$ which depends on the full position of sensor element m and target n.

Consequently, by inserting (2.51) into (2.48) the beat frequency can also be decomposed into two terms

$$f^{\mathrm{b}}_{m,n} = \mu T^{\mathrm{d}}_{0,n} + \mu \Delta T^{\mathrm{d}}_{m,n} = f^{\mathrm{b}}_{0,n} + \Delta f^{\mathrm{b}}_{m,n}, \tag{2.52}$$

where the first term is only dependent on the distance of the target to the coordinate system origin and the latter is dependent on the absolute position of target and sensor. The explicit dependence of both frequency functions from target position $\underline{\boldsymbol{p}}^{\mathrm{tgt}}_n$ and sensor position $\underline{\boldsymbol{p}}^{\mathrm{rx}}_m$ was dropped for convenience. The beat phase can also be decomposed in such manner by inserting (2.51) into (2.49)

$$\phi^{\mathrm{b}}_{m,n} = 2\pi f_1 (T^{\mathrm{d}}_{0,n} + \Delta T^{\mathrm{d}}_{m,n}) + \pi \mu (T^{\mathrm{d}}_{0,n} + \Delta T^{\mathrm{d}}_{m,n})^2 = \phi^{\mathrm{b}}_{0,n} + \Delta \phi^{\mathrm{b}}_{m,n}. \tag{2.53}$$

Expressing both components individually yields

$$\phi^{\mathrm{b}}_{0,n} = 2\pi f_1 T^{\mathrm{d}}_{0,n} + \pi \mu (T^{\mathrm{d}}_{0,n})^2, \tag{2.54}$$

$$\Delta \phi^{\mathrm{b}}_{m,n} = 2\pi f_1 \Delta T^{\mathrm{d}}_{m,n} + \pi \mu \left((2 T^{\mathrm{d}}_{0,n} \Delta T^{\mathrm{d}}_{m,n} + (\Delta T^{\mathrm{d}}_{m,n})^2 \right), \tag{2.55}$$

which reveals an interesting phenomenon: Due to the quadratic term in (2.49), $\Delta \phi^{\mathrm{b}}_{m,n}$ is not only dependent on the time-delay difference $\Delta T^{\mathrm{d}}_{m,n}$, but also on the absolute time delay $T^{\mathrm{d}}_{0,n}$ to the array center.

2.2.2 Far Field Approximation

If the target is at a sufficiently far distance from the RX array, i.e. the minimum diameter D of a sphere completely enclosing the sensor array is much

smaller than r_n, the spherical wave generated by the source can be approximated by a local plane wave across the antenna array. As illustrated in figure 2.11, this means that the vectors from target n to all sensor elements m can be considered as parallel. Then, the Delta time delay to each sensor is *independent* of the target's range, but only is a function of its spherical coordinates θ_n, φ_n also referred to as the DOA of the target. The time delay to sensor m can then be expressed by

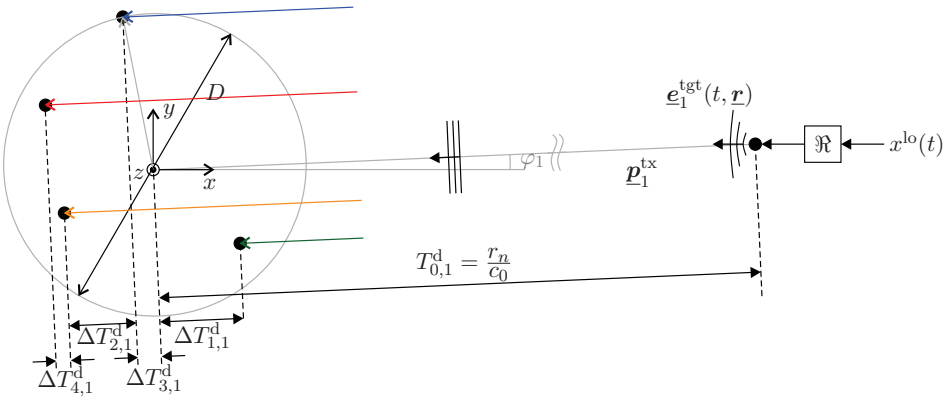

Fig. 2.11: Array far field approximation. In the far field assumption, the incident signal is approximated by a plane wave, i.e. all vectors between target and and sensor element are parallel.

$$T_{m,n}^{\mathrm{d}}(\underline{\boldsymbol{p}}_n^{\mathrm{tgt}}, \underline{\boldsymbol{p}}_m^{\mathrm{rx}}) \approx T_{0,n}^{\mathrm{d}}(r_n) + \Delta T_m^{\mathrm{d}}(\underline{\boldsymbol{p}}_m^{\mathrm{rx}}, \theta_n, \varphi_n). \tag{2.56}$$

In addition it can be assumed that the coefficients $a_{m,n}^{\mathrm{tgt}}$ are equal across all sensor elements and they can be replaced by $a_{0,n}^{\mathrm{tgt}}$. By inserting (2.56) into (2.48) and into (2.49) the beat frequency $f_{m,n}^{\mathrm{b}}$ and beat phase $\phi_{m,n}^{\mathrm{b}}$ observed at each array element can again be separated into the two terms given in (2.52) and (2.53). Inserting those decompositions into (2.50) the far field approximation for the IF output of a FMCW sensor array is obtained.

$$\underline{\boldsymbol{x}}^{\mathrm{b,FF}}(t) = \frac{1}{2}\sum_{n=0}^{N} \underbrace{a_{0,n}^{\mathrm{tgt}} \exp \mathrm{j}(2\pi f_{0,n}^{\mathrm{b}} t + \phi_{0,n}^{\mathrm{b}})}_{s_n(t)} \underbrace{\begin{bmatrix} \exp \mathrm{j}(2\pi \Delta f_{1,n}^{\mathrm{b}} t + \Delta\phi_{1,n}^{\mathrm{b}}) \\ \exp \mathrm{j}(2\pi \Delta f_{2,n}^{\mathrm{b}} t + \Delta\phi_{2,n}^{\mathrm{b}}) \\ \vdots \\ \exp \mathrm{j}(2\pi \Delta f_{M,n}^{\mathrm{b}} t + \Delta\phi_{M,n}^{\mathrm{b}}) \end{bmatrix}}_{\underline{\boldsymbol{a}}^{\mathrm{FF}}(\underline{\boldsymbol{p}}_n^{\mathrm{tgt}}, t)}. \tag{2.57}$$

Interestingly, the beat signal for each target n can now be separated into two parts: The first is referred to as the signal $s_n(t)$, which contains the beat signal as it would be observed at the coordinate origin, i.e. the array center. This component is *identical* to all sensors. The second component is referred to as the far field steering vector $\underline{\boldsymbol{a}}^{\mathrm{FF}}$, which captures the deviation of the signal across the sensors of the array. Although the delta time delays using the far field approximation are only dependent on the DOA of the target, due to the quadratic beat phase (2.34) the far field steering vector is still dependent on the absolute position of the targets, i.e. on both distance as well as DOA.

2.2.3 Linear Phase Approximation

Since the time-delay $T^{\mathrm{d}}_{m,n}$ is very small the linear component from (2.44) is assumed to be the dominant term and the quadratic term is frequently neglected [38], [95], [96]. This is referred to as the linear phase approximation. The beat phase observed at each sensor m for target n can then be expressed by

$$\phi^{\mathrm{b}}_{m,n} \approx 2\pi f_1 T^{\mathrm{d}}_{0,n} + 2\pi f_1 \Delta T^{\mathrm{d}}_{m,n} = \phi^{\mathrm{b}}_{0,n} + \Delta\phi^{\mathrm{b}}_{m,n}, \tag{2.58}$$

and the Delta phase $\Delta\phi^{\mathrm{b}}_{m,n}$ is now *only* dependent on the Delta time-delay $\Delta T^{\mathrm{d}}_{m,n}$ and consequently only dependent on the DOA of the target. Based on the linear phase approximation, the IF output of the FMCW sensor array can then be expressed by

$$\underline{\boldsymbol{x}}^{\mathrm{b,LP}}(t) = \sum_{n=0}^{N} \underbrace{\frac{1}{2} a_n^{\mathrm{tgt}} \exp \mathrm{j}(2\pi f^{\mathrm{b}}_{0,n} t + \phi^{\mathrm{b}}_{0,n})}_{s_n(t)} \underbrace{\begin{bmatrix} \exp \mathrm{j}\left((2\pi\mu t + 2\pi f_1)\Delta T^{\mathrm{d}}_{1,n}\right) \\ \exp \mathrm{j}\left((2\pi\mu t + 2\pi f_1)\Delta T^{\mathrm{d}}_{2,n}\right) \\ \vdots \\ \exp \mathrm{j}\left((2\pi\mu t + 2\pi f_1)\Delta T^{\mathrm{d}}_{M,n}\right) \end{bmatrix}}_{\underline{\boldsymbol{a}}^{\mathrm{LP}}(\theta,\varphi,t)} \tag{2.59}$$

Whereas the signal component $s_n(t)$ is conceptually not changed much (although in $\phi^{\mathrm{b}}_{0,n}$ also the dependence is linearized) the great simplification of the linear phase approximation becomes apparent in the array steering vector $\underline{\boldsymbol{a}}^{\mathrm{LP}}(\theta, \varphi, t)$. Now, the steering vector is *independent* of target range and only dependent on the DOA of the target's incident wave front. Hence

two independent terms constitute the linear-phase array output: The signal term $s_n(t)$ which captures the effects of target range on the beat signal as well as the steering vector $\underline{\boldsymbol{a}}^{\mathrm{LP}}(\theta_n, \varphi_n, t)$, which captures the effects of target DOA.

2.2.4 Narrowband Approximation

In (2.59) the beat signals obtained at the array sensors differ in both, frequency and phase. Consequently, the phase difference across the elements is not only dependent on the DOA but also on time. The time-dependent phase difference is due to the term $2\pi\mu t$ in the steering vector. It reaches its maximum at the end of the sweep for $t = T$. For an array with maximum diameter D it is easy to see that an upper limit for the phase difference between two sensors due to the time dependent term is given by $2\pi \mathrm{BW} D/c_0$. Consequently, if the phase difference due to the time-dependent term is much smaller than the phase difference do to the constant term, i.e.

$$2\pi \mathrm{BW} D/c_0 << 2\pi f_{\mathrm{l}} D/c_0, \tag{2.60}$$

the time-dependent term may be neglected and the steering vector becomes independent of time and simplifies to its narrowband approximation

$$\underline{\boldsymbol{a}}^{\mathrm{NB}}(\theta, \varphi) = \begin{bmatrix} \exp \mathrm{j}\left(2\pi f_{\mathrm{l}} \Delta T_1^{\mathrm{d}}(\theta, \varphi)\right) \\ \exp \mathrm{j}\left(2\pi f_{\mathrm{l}} \Delta T_2^{\mathrm{d}}(\theta, \varphi)\right) \\ \vdots \\ \exp \mathrm{j}\left(2\pi f_{\mathrm{l}} \Delta T_M^{\mathrm{d}}(\theta, \varphi)\right) \end{bmatrix} \in \mathbb{C}^{M \times 1}. \tag{2.61}$$

2.2.5 Linear and Circular Arrays

2.2.5.1 Uniform Linear Array

An M-element uniform linear array (ULA) is constructed by placing all sensor array elements uniformly on a straight line. Without loss of generality, in this thesis the antenna elements of a ULA are placed along the y-coordinate of a rectangular coordinate system, as shown in figure 2.12. The distance between two neighboring elements is d_{el}. In particular, the ULAs in this thesis are always defined to be symmetric around the origin, i.e. the sensor elements are placed symmetrically to the x-axis. Then, the position $y[m]$ of

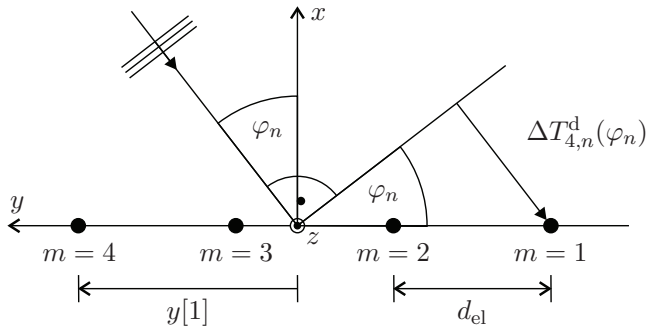

Fig. 2.12: Uniform linear sensor array.

element m is given by

$$y[m] = (m-1)d_{\mathrm{el}} - (M-1)\frac{d_{\mathrm{el}}}{2}, \quad m = 1 \ldots M. \tag{2.62}$$

The difference time $\Delta T^{\mathrm{d}}_{m,n}$ between array center and ULA element m can be expressed by

$$\begin{aligned} \Delta T^{\mathrm{d}}_{m,n}(\varphi_n) &= -y[m]\frac{\sin\varphi_n}{c_0} \\ &= -\left((m-1)d_{\mathrm{el}} - (M-1)\frac{d_{\mathrm{el}}}{2}\right)\frac{\sin\varphi_n}{c_0}, \end{aligned} \tag{2.63}$$

where a positive $\Delta T^{\mathrm{d}}_{m,n}$ indicates that the wave front arrives at element m after it arrives at the array center, and a negative $\Delta T^{\mathrm{d}}_{m,n}$ indicates that the wave front arrives at element m before it arrives at the array center. It is obvious that the delta-times are only dependent on φ_n. Hence, linear arrays cannot differentiate between plane waves that lie on the cone whose axis contains the linear array [97].

The traditional narrowband definition of spatial frequency [89] is now extended taking into account the linear time-dependence of the steering vector in LFM RADAR systems. This linear time-dependent spatial frequency is given by

$$u(\varphi_n, t) = \frac{2\pi f_{\mathrm{l}} \sin\varphi_n}{c_0} + \frac{2\pi\mu t \sin\varphi_n}{c_0}. \tag{2.64}$$

The array steering vector based on the linear-phase approximation thus can

be expressed by

$$\underline{\boldsymbol{a}}^{\mathrm{LP}}(\varphi_n, t) = \begin{bmatrix} 1 \\ \exp\left(\mathrm{j} d_{\mathrm{el}} u(\varphi_n, t)\right) \\ \exp\left(\mathrm{j} 2 d_{\mathrm{el}} u(\varphi_n, t)\right) \\ \vdots \\ \exp\left(\mathrm{j} M d_{\mathrm{el}} u(\varphi_n, t)\right) \end{bmatrix} \exp\left(-\mathrm{j} u(\varphi_n, t)(M-1)\frac{d_{\mathrm{el}}}{2}\right) \quad (2.65)$$

and it can be seen, that the ULA performs sampling of a complex sinusoid with frequency $u(t, \varphi_n)$ at equi-distant points with spacing, i.e. sampling period d_{el}. The additional exponential term is present since the origin of the coordinate system does not coincide with the position of sensor $m = 1$, but is in the center of the array. As known from the Nyquist theorem on traditional time-sampling, the maximum sampling period must be smaller than one-half of the minimum period of the sampled signal to avoid aliasing. It can be concluded that this corresponds to $d_{\mathrm{el}} < \pi / \max_{t,\varphi_n}\{u(t, \varphi_n)\}$. Since the maximum spatial frequency occurs for $\varphi_n = \pi/2$ and at the end of the LFM sweep for $t = T$, it can be followed that the necessary condition for alias-free spatial sampling is $d_{\mathrm{el}} < \lambda_{\mathrm{h}}/2$, where λ_{h} is the wavelength at the highest frequency of the LFM sweep.

Using the narrowband approximation the spatial frequency becomes independent of time and corresponds to its traditional definition [89]

$$u^{\mathrm{NB}}(\varphi_n) = \frac{2\pi f_{\mathrm{l}} \sin \varphi_n}{c_0}. \quad (2.66)$$

The narrowband steering vector $\underline{\boldsymbol{a}}^{\mathrm{NB}}(\varphi_n)$ can then be related to the linear-phase approximation steering vector $\underline{\boldsymbol{a}}^{\mathrm{LP}}(\varphi_n, t)$ by

$$\underline{\boldsymbol{a}}^{\mathrm{LP}}(\varphi_n, t) = \underline{\boldsymbol{a}}^{\mathrm{NB}}(\varphi_n + \Delta\varphi_n(t)), \quad (2.67)$$

and $\Delta\varphi_n(t)$ is implicitly defined by equating (2.64) and (2.66)

$$\sin\left(\varphi_n + \Delta\varphi_n(t)\right) = \sin \varphi_n + \frac{\mu t}{f_{\mathrm{l}}} \sin \varphi_n. \quad (2.68)$$

Without explicit solution of (2.68) it is easy to see that the narrowband steering vector observed for a ULA seems to come from an angle differing by $\Delta\varphi_n(t)$ from the true DOA φ_n. This difference increases with time, FMCW bandwidth, and the true DOA φ_n. Clearly, if $\varphi_n = 0$ no deviation will be

observed since $\Delta\varphi_n(t) = 0$ and for a narrowband system with BW $<<$ f_l the deviation will be negligible small.

Of great interest in array processing are the ambiguity properties of sensor array geometries. It is clear that if any two $[\theta_1, \varphi_1] \neq [\theta_2, \varphi_2]$ exist such that $\underline{\boldsymbol{a}}^{\mathrm{LP}}(\theta_1, \varphi_1, t) = \underline{\boldsymbol{a}}^{\mathrm{LP}}(\theta_2, \varphi_2, t)$, the DOA cannot uniquely be determined. This type of ambiguity is referred to as type-1 or rank-1 ambiguity. To characterize the ambiguity of arrays, an ambiguity I function χ is defined in [97]. This function can be straightforward extended to the linear time-dependent steering vectors found in FMCW RADAR systems, such that χ is expressed by

$$\chi(\theta_1, \varphi_1, \theta_2, \varphi_2, t) = \frac{\left(\underline{\boldsymbol{a}}^{\mathrm{LP}}(\theta_1, \varphi_1, t)\right)^{\mathbf{H}} \cdot \underline{\boldsymbol{a}}^{\mathrm{LP}}(\theta_2, \varphi_2, t)}{|\underline{\boldsymbol{a}}^{\mathrm{LP}}(\theta_1, \varphi_1, t)|\,|\underline{\boldsymbol{a}}^{\mathrm{LP}}(\theta_2, \varphi_2, t)|}. \tag{2.69}$$

The ambiguity function characterizes how similar the array steering vector is for various angles $[\theta, \varphi]$ at a certain time t during the FMCW sweep. In the ideal case it would return $\chi = M$ only for $[\theta_1, \varphi_1] = [\theta_2, \varphi_2]$, and be zero elsewhere. For practically relevant arrays it can be used to measure two properties: Firstly, the ambiguity function indicates if there exist any steering directions $[\theta_1, \varphi_1] \neq [\theta_2, \varphi_2]$ for which the array steering vectors are identical, i.e. $\chi(\theta_1, \varphi_1, \theta_2, \varphi_2, t) = M$ or similar, i.e $\chi(\theta_1, \varphi_1, \theta_2, \varphi_2, t) \approx M$. If this is the case then the array is considered to be ambiguous, since assuming the value of the steering vector is known, the angles $[\theta, \varphi]$ cannot uniquely be determined. Secondly, the ambiguity function can be used to measure how sharp the spatial response of a certain array geometry is, by determining the width around the maxima of χ. If there is a large region $[\Delta\theta_1, \Delta\varphi_1]$ such that $\chi(\theta_1, \varphi_1, \varphi_1 \pm \Delta\varphi_1, \theta_1 \pm \Delta\theta_1, t) \approx M$, clearly the response of the array is not very sharp. The ambiguity function can also be interpreted as the beam-pattern of the sensor array using traditional beamforming.

Utilizing the linear dependence between time and frequency found in LFM RADAR systems, the ambiguity-I function can also be expressed in dependence of the instantaneous frequency using the substitution $t = (f - f_\mathrm{l})/\mu$, which then corresponds to its traditional definition as e.g. found in [97]. The type-I ambiguity functions for a four-element ULA are shown in figure 2.13. Two cases are considered: element spacing of $d_\mathrm{el} = \lambda_\mathrm{h}/2$ and element spacing of $d_\mathrm{el} = \lambda_l/2$. In both cases, the ambiguity function is evaluated for the lowest frequency f_l, the center frequency f_c and the upper frequency f_h of the WB signal scenario from table 1.3. If $\varphi_1 = \varphi_2$ the ambiguity function of the $M = 4$ element ULA is $\chi = 4$, which is the line along the main diag-

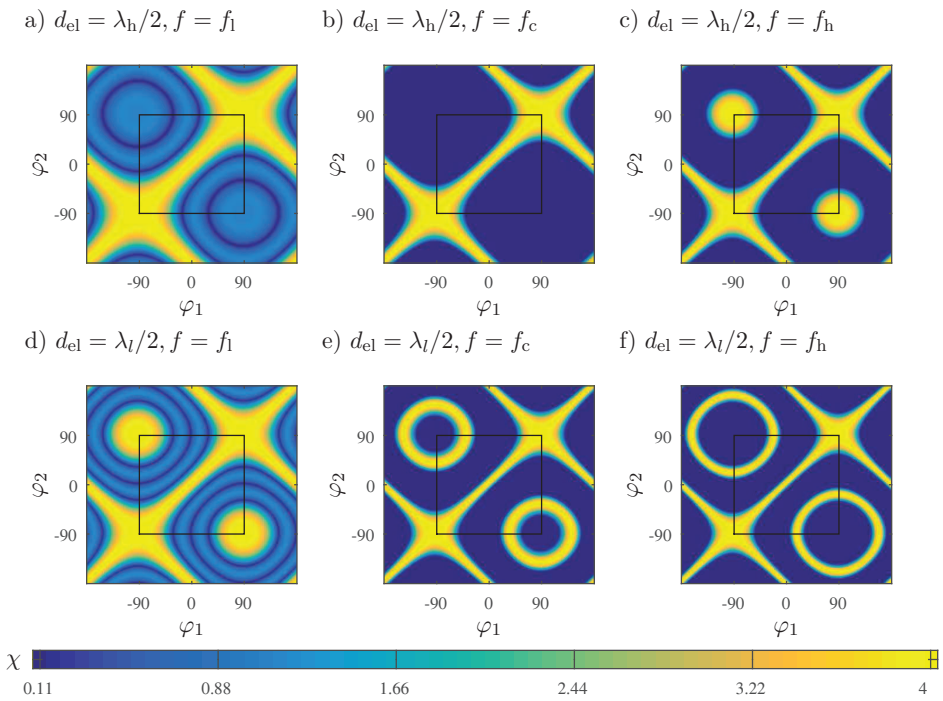

Fig. 2.13: Ambiguity patterns of ULA. Element distance in a)-c) is $d_{el} = \lambda_h/2$, in d)-f) $d = \lambda_l/2$. Excitation frequencies are $f_l = 6\,\text{GHz}$, $f_c = 7.5\,\text{GHz}$, and $f_h = 9\,\text{GHz}$ corresponding to the WB RADAR system scenario from table 1.3.

onal of the plots a)-f). This is the desired array behavior. By comparing the width of the main diagonal in a) and f) it further can be seen that the spatial response of the array is very sharp if the array diameter $D = Md_{el}$ is large compared to the wavelength. Furthermore the width increases for large φ, i.e. the resolution is reduced towards large DOAs. Both are the properties traditionally associated with ULAs. Since the ULA cannot differentiate between plane waves that lie on the cone whose axis contains the linear array, the two cross diagonal maxima exist outside the region $-90° \leq \varphi_1 \leq 90°$, independent of frequency. Inside this region of $\varphi_1 \in -90°, \ldots, 90°$ the ULA with $d_{el} = \lambda_h/2$ is ambiguity free for the whole frequency range. First ambiguities occur at $\varphi_1 = \pm 90°$ for $f = f_h$. Consequently, the ULA with $d_{el} = \lambda_l/2$ is ambiguous over the entire frequency range. At $f = f_l$ the first ambiguities occur at $\varphi_1 = \pm 90°$. For higher frequencies the ambiguity occurs as a circle centered at $\varphi_1 = \pm 90°$ with a frequency-dependent radius.

The deviation of the narrowband approximation steering vector from the linear-phase approximation steering vector can be illustrated using a modified definition of the type-I ambiguity function. It is defined as

$$\chi^{\mathrm{NB}}(\theta_1, \varphi_1, \theta_2, \varphi_2, t) = \frac{\left(\underline{\boldsymbol{a}}^{\mathrm{NB}}(\theta_1, \varphi_1)\right)^{\mathbf{H}} \cdot \underline{\boldsymbol{a}}^{\mathrm{LP}}(\theta_2, \varphi_2, t)}{|\underline{\boldsymbol{a}}^{\mathrm{NB}}(\theta_1, \varphi_1)|\,|\underline{\boldsymbol{a}}^{\mathrm{LP}}(\theta_2, \varphi_2, t)|}. \tag{2.70}$$

The evaluation of (2.70) is then conducted for $\varphi_2 = const.$ and $\varphi_1 \in \{-90° \ldots 90°\}$. Since the ULA steering vectors are independent on θ the dependence is dropped in the following discussion. If the narrowband approximation holds, then it is expected that $\arg\max_{\varphi_1}\{\chi^{\mathrm{NB}}(\varphi_1, \varphi_2, t)\}$ corresponds to φ_2. If not then $\Delta\varphi_1(t) = \arg\max_{\varphi_1}\{\chi^{\mathrm{NB}}(\varphi_1, \varphi_2, t)\} - \varphi_2$.

The modified type-I ambiguity function for a 4-element ULA is plotted in figure 2.14, for a) $\varphi_2 = 0°$ and b) $\varphi_2 = 40°$. The steering vectors obtained for

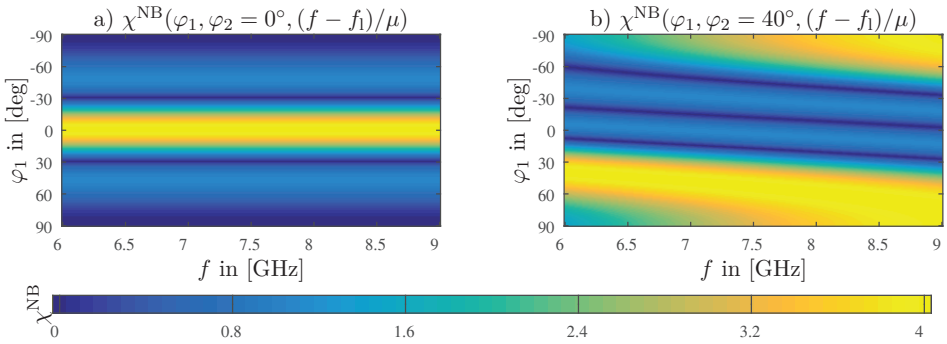

Fig. 2.14: Modified ambiguity patterns of ULA versus frequency for $\varphi_2 = 0°$ and $\varphi_2 = 40°$. Element distance is $d = \lambda_l/2$. Evaluation frequency range corresponds to parameters of WB RADAR system scenarios from table 1.3.

the WB RADAR scenario from table 1.3 are used. Equation (2.70) is evaluated in a frequency range from $f = f_{\mathrm{l}}$ to $f = f_{\mathrm{h}}$. It can be seen that for $\varphi_2 = 0°$, no change of the steering vector occurs with frequency. This can be reasoned since the time-dependent factor from (2.64) becomes zero in this case. For $\varphi_2 = 40°$, a significant dependence of the steering vector on frequency can be observed. With increasing frequency the φ_1 which maximizes the modified ambiguity function also increases. In addition at about $f = 7\,\mathrm{GHz}$ the ULA becomes ambiguous, since a second maximum enters the range. Note that the position of the ambiguity also moves with frequency, which is one property that will be further described during the performance analysis of DOA estimation algorithms in section 3.5.

2.2.5.2 Uniform Circular Array

A uniform circular array (UCA) is constructed by placing all sensors uniformly along a circle with radius R_{UCA} centered around the origin. Without loss of generality, in this thesis the UCA is placed in the xy-plane of the coordinate system. Then, as indicated in figure 2.15, the position of sensor m is determined by the radius R_{UCA} and an angle

$$\phi_{\text{ant}}[m] = \frac{2\pi}{M}(m-1) + \phi_{\text{ant},0}, \tag{2.71}$$

where $\phi_{\text{ant},0}$ is the angle of the element $m = 1$. Without loss of generality in

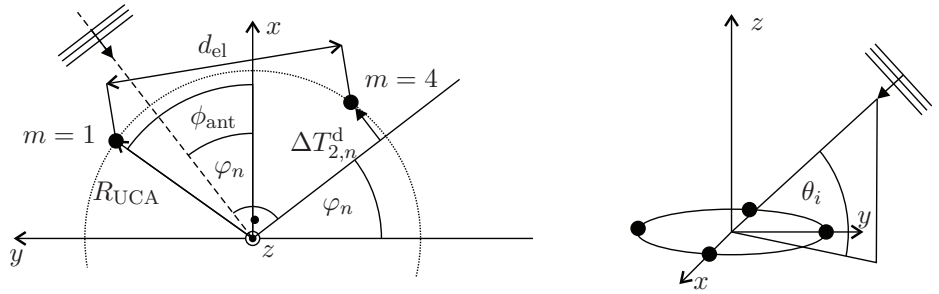

Fig. 2.15: Uniform circular sensor array. View from top (left) and isometric view (right).

this thesis the first element $m = 1$ is located on the x-axis of the coordinate system, such that $\phi_{\text{ant},0} = 0$. As e.g. shown in [10], the time-delay difference between array center and sensor element m is then given by

$$\Delta T^{\text{d}}_{m,n}(\theta_n, \varphi_n) = -\left(\cos\left(\varphi_n - \frac{2\pi}{M}(m-1)\right)\sin\theta_n r\right)/c_0, \tag{2.72}$$

The steering vectors for the UCA can then be derived inserting (2.72) into (2.59) and (2.61), respectively. Note that, in contrast to the ULA, now the delta-times and consequently the steering vectors both depend on φ_n and θ_n. Hence the UCA can be used for estimation of the DOA in both dimensions.

The ambiguity patterns of the UCA are shown in figure 2.16. It can be seen from a) and b) that the UCA is ambiguity free in the total region $-180° \leq \varphi_1 \leq 180°$ if the element spacing is smaller than half the wavelength of the incident wave front, as also mentioned in e.g. [98]. From c) and d) it

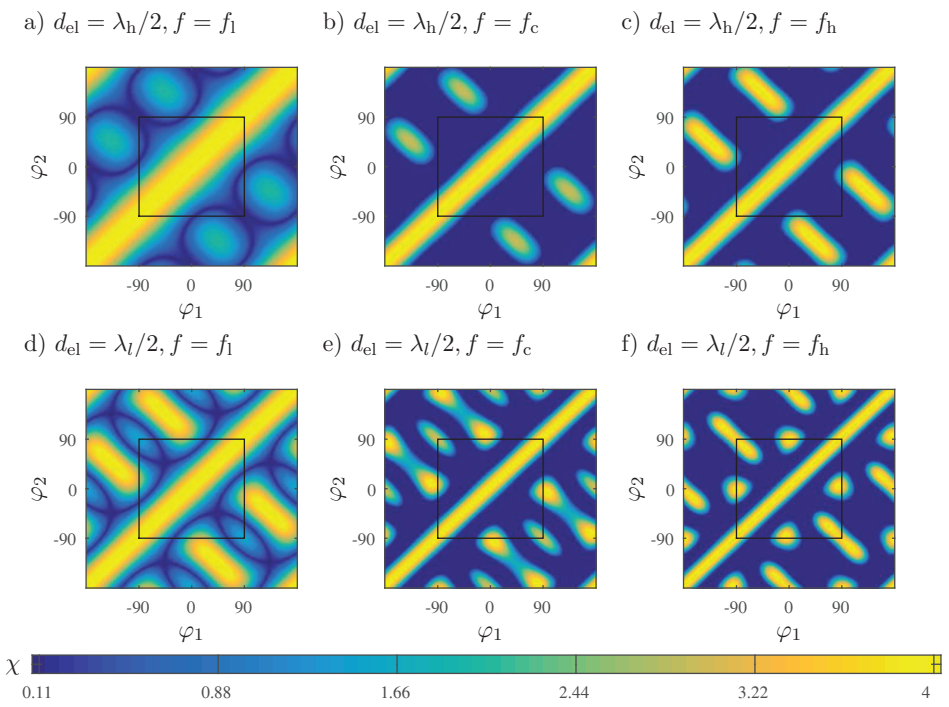

Fig. 2.16: Ambiguity patterns of UCA. Element distance in a)-c) is $d_{el} = \lambda_h/2$, in d)-f) $d = \lambda_l/2$. Excitation frequencies are $f_l = 6\,\text{GHz}$, $f_c = 7.5\,\text{GHz}$, and $f_h = 9\,\text{GHz}$ corresponding to the WB RADAR system scenario from table 1.3.

is obvious that already an ambiguity occurs if d_{el} corresponds to half the wavelength of the incident wave front, and consequently the $M = 4$ element ULA is not ambiguity free for $d_{el} > \lambda/2$. The ambiguous angles in both cases are approximately $\varphi_1 \in \pm\{32° \ldots 62°\} \cup \pm\{123° \ldots 153°\}$. Generally, the UCA has interesting ambiguity properties depending on the number of elements. Further details can be found in [99].

It can generally be seen, that the degradation of the spatial response towards larger angles, as was observed for the ULA, is not present in the UCA. The resolution remains constant irrespectively of φ_1. The UCA differs from the ULA in the following properties: the azimuthal coverage of a UCA is $360°$ in contrast to the ULA, which covers only $180°$. This can be seen from figure 2.16 where in contrast to 2.13 only one diagonal maximum is present. Furthermore the resolution of UCA is relatively uniform around the azimuth angle while that of ULA broadens as its beam is steered away from the bore sight.

This is obvious since the width of the diagonal maximum from 2.16 is constant with φ. In addition, compared to the ULA whose narrowband steering vector was shown to move to larger angles with frequency, UCAs are known to be able to form beam patterns that are relatively invariant with frequency [100]. Although the last observation can be shown on a mathematical basis and be used for frequency-independent DOA estimation [98], [101], [102], in the scope of this thesis it is sufficient to simplify the treatment an show the effects on a qualitative basis using the modified type-I ambiguity function from (2.70). The modified ambiguity functions for a four-element UCA with element distance $d_{\mathrm{el}} = \lambda_l/2$ are plotted for a) $\varphi_2 = 0°$ and b) $\varphi_2 = 40°$ in figure 2.17. 5 It can be seen, that in both cases the maximum of the modi-

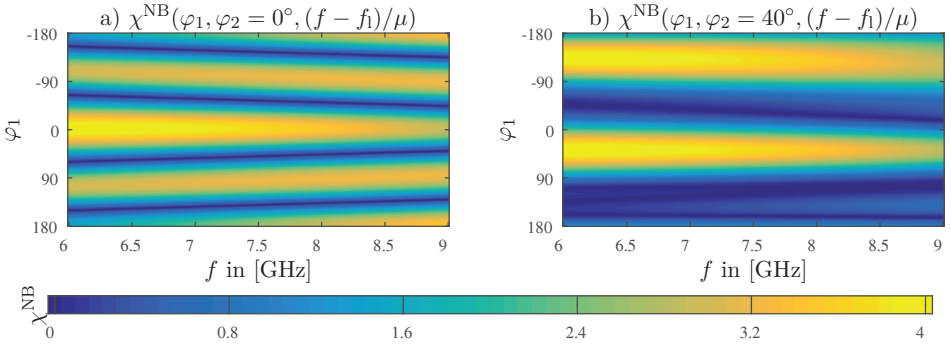

Fig. 2.17: Modified ambiguity patterns of UCA versus frequency for $\varphi_2 = 0°$ and $\varphi_2 = 40°$. Element distance is $d = \lambda_l/2$. Evaluation frequency range corresponds to parameters of WB RADAR system scenarios from table 1.3.

fied ambiguity function is constant across the whole frequency range. That means the displacement of the steering vector to larger angles is not present for the UCA. Indeed with increasing frequency there is a certain deviation between $\underline{\boldsymbol{a}}^{\mathrm{NB}}$ and $\underline{\boldsymbol{a}}^{\mathrm{LP}}$, but it appears as a different effect: the desired self ambiguity, i.e. the value of the maximum of $\chi^{\mathrm{NB}}(\varphi_1, \varphi_2, t)$ for $\varphi_1 = \varphi_2$ decreases with frequency. This effect is especially apparent from figure 2.17 b). Whereas the value of χ^{NB} for $f = f_{\mathrm{l}} = 6\,\mathrm{GHz}$ at $\varphi_1 = 40°$ corresponds to its theoretical maximum value of $\chi^{\mathrm{NB}} = 4$ for the 4-element UCA, at $f = f_{\mathrm{h}} = 9\,\mathrm{GHz}$ the value of the modified ambiguity function is reduced to $\chi^{\mathrm{NB}} = 2.83$. The same effect can be observed from a), where the maximum for $\varphi_1 = 0°$ is reduced to $\chi^{\mathrm{NB}} = 2.88$ at $f = f_{\mathrm{h}}$. In addition, the large values of $\chi^{\mathrm{NB}} = 2.98$ at $\varphi_1 = \pm 106°$ for $\varphi_2 = \pm 0°$ at $f = f_{\mathrm{l}}$ indicate that there exists some approximate ambiguity for the UCA with element spacing $d_{\mathrm{el}} = \lambda_l/2$.

3 Signal Processing for Wideband Linear FMCW Radar Systems

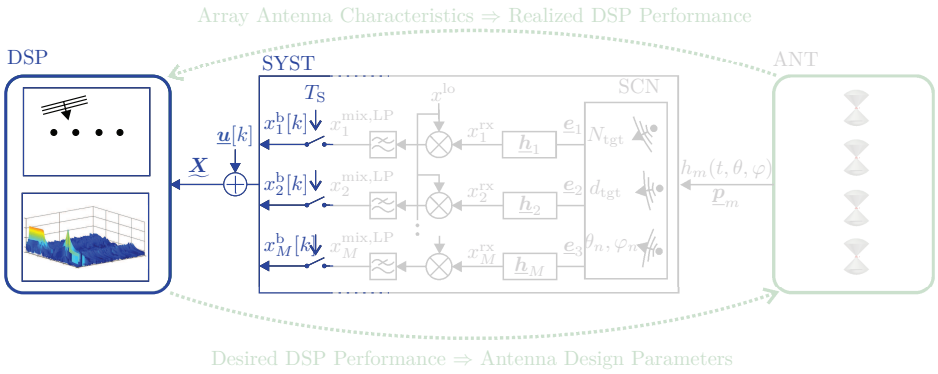

Fig. 3.1: Signal processing in FMCW RADAR systems.

In the preceding section, the operation principles of LFMCW RADAR systems were introduced. It was shown that using the FMCW RADAR principle, the received signals from all targets are transformed into the beat signal, in which each target is represented by a complex sinusoid with a frequency proportional to target distance and amplitude proportional to target RCS and distance. In addition, it was shown that using an array of multiple sensors not only information about target distance, but also information about the DOA of the target wavefront is contained in the multi-channel beat signal.

In this chapter, the fundamental principles of signal processing in FMCW RADAR systems for estimating the range as well as DOA of one or several targets from the information contained in the beat signal is shown. As illustrated in figure 3.1, DSP processing in the scope of this thesis begins with obtaining a discrete-time representation of the beat signals by sampling, then models any noise generated in the FMCW RADAR system by adding the discrete-time noise component $\underline{\boldsymbol{u}}[k]$, collects a certain number of samples in the signal matrix $\underline{\underline{\boldsymbol{X}}}$ and finally processes the collected data using algorithms for range and angle estimation.

3.1 General Concepts and Methods

3.1.1 Discrete-Time Signal Representation

The discrete-time representation $\underline{\boldsymbol{x}}^{\mathrm{b}}[k]$ of the beat signal is obtained by sampling the continuos-time signal $\underline{\boldsymbol{x}}^{\mathrm{b}}(t)$ at time instants $t = kT_{\mathrm{s}} + T_{\mathrm{s,delay}}, k \in 0 \ldots K-1$, where T_s is the sampling period, $f_s = 1/T_s$ the sampling frequency, K is the total number of samples and $T_{\mathrm{s,delay}}$ is an arbitrary time delay before sampling begins. The discrete-time beat signal is thus related to the continuous-time beat signal by

$$\underline{\boldsymbol{x}}^{\mathrm{b}}[k] = \underline{\boldsymbol{x}}^{\mathrm{b}}(kT_{\mathrm{s}} + T_{\mathrm{s,delay}}). \tag{3.1}$$

Since the beat signal is a sum of complex sinusoids, alias free sampling of the beat signal can be ensured if f_s is greater or equal to the maximum frequency occurring in the beat signal. The time-delay $T_{\mathrm{S,delay}}$ is used to delay sampling until the beat signal is valid, i.e. until the received signals of all targets are in the linear ramp phase and thus the beat signal only contains complex sinusoids of constant frequency, compare figure 2.5. Note, however, that for practically relevant secondary FMCW RADAR systems with assumed target distances up to 200 m, the maximum propagation delay T_n^{d} is $\max\{T_n^{\mathrm{d}}\} \approx 666\,\mathrm{ns}$. As mentioned in chapter 1 the sample rates considered in this work are limited to about $f_s = 1\,\mathrm{MHz}$, and thus the sample period is $T_s = 1\,\mathrm{s}$. Hence, by practically setting $T_{\mathrm{S,delay}} = 0$, i.e. starting sampling of the received signal synchronously with the start of the locally generated ramp, in the worst case only the first sample of $\underline{\boldsymbol{x}}^{\mathrm{b}}[k]$ will be corrupted. Within the simulation framework developed in this thesis, the maximum propagation delay is exactly known, since the maximum target distance is exactly known. Hence, the system model developed generates a discrete-time beat signal starting exactly at the first valid time instant, i.e. using $T_{\mathrm{S,delay}} = \max\{T_{m,n}^{\mathrm{rt}}\}$. The total number K of samples obtained is then given by the total available remaining observation time of the valid beat signal. It is limited by the time instant when the locally generated ramp transitions from the sweep region to the region where it remains at $f = f_{\mathrm{h}}$. To stop sampling at the last valid beat signal time instant, the number of samples must hence be selected such that $K = \lfloor (T - T_{\mathrm{S,delay}})/T_{\mathrm{s}} \rfloor$. As discussed above for practically relevant RADAR systems again $T_{\mathrm{S,delay}} = 0$ can be assumed. Furthermore assuming that the duration of the FMCW sweep is an integer multiple of the sampling-clock it follows that, the number of samples

can simply be obtained by

$$K = T/T_\mathrm{s}. \tag{3.2}$$

3.1.2 Beat Signal Representation

Based on the discrete-time representation of the beat signal, the discrete-time representation of the M-sensor FMCW array output from (2.50) is given by

$$\underline{\boldsymbol{x}}^\mathrm{b}[k] = \frac{1}{2}\sum_{n=1}^{N} \begin{bmatrix} a_{1,n}^\mathrm{tgt} \exp \mathrm{j}\left(2\pi f_{1,n}^\mathrm{b}(kT_\mathrm{s} + T_\mathrm{s,delay}) + \phi_{1,n}^\mathrm{b}\right) \\ a_{2,n}^\mathrm{tgt} \exp \mathrm{j}\left(2\pi f_{2,n}^\mathrm{b}(kT_\mathrm{s} + T_\mathrm{s,delay}) + \phi_{2,n}^\mathrm{b}\right) \\ \vdots \\ a_{M,n}^\mathrm{tgt} \exp \mathrm{j}\left(2\pi f_{M,n}^\mathrm{b}(kT_\mathrm{s} + T_\mathrm{s,delay}) + \phi_{M,n}^\mathrm{b}\right) \end{bmatrix} \in \mathbb{C}^{M\times 1} \tag{3.3}$$

Assuming the far field model (2.57), the beat signal at each sensor can be expressed using the term $s_n^\mathrm{FF}[k]$ modeling the signal as it would be observed at the array center and a the steering vector $\underline{\boldsymbol{a}}^\mathrm{FF}(\underline{\boldsymbol{p}}_n^\mathrm{tgt}, kT_\mathrm{s})$ taking into account the inter-element deviation

$$\underline{\boldsymbol{x}}^\mathrm{b,FF}[k] = \sum_{n=1}^{N} s_n^\mathrm{FF}[k]\underline{\boldsymbol{a}}^\mathrm{FF}(\underline{\boldsymbol{p}}_n^\mathrm{tgt}, kT_\mathrm{s} + T_\mathrm{s,delay}). \tag{3.4}$$

Of particular interest for range and DOA estimation algorithms is the linear-phase model (2.59), where the steering vector becomes only dependent on target DOA. The effects of target distance and target DOA are then completely separated in the two components $s_n^\mathrm{LP}[k]$ and $\underline{\boldsymbol{a}}^\mathrm{LP}(\theta_n, \varphi_n, kT_\mathrm{s}+T_\mathrm{s,delay})$, respectively. The discrete-time representation of the linear-phase model is given by

$$\underline{\boldsymbol{x}}^\mathrm{b,LP}[k] = \sum_{n=1}^{N} s_n^\mathrm{LP}[k]\underline{\boldsymbol{a}}^\mathrm{LP}(\theta_n, \varphi_n, kT_\mathrm{s} + T_\mathrm{s,delay}) = \underset{\sim}{\boldsymbol{A}}^\mathrm{LP}[k]\underline{\boldsymbol{s}}^\mathrm{LP}[k], \tag{3.5}$$

where the sum can be replaced by a matrix product, if the steering vectors for each target are collected in the matrix $\underset{\sim}{\boldsymbol{A}}^\mathrm{LP}[k] \in \mathbb{C}^{M\times N}$ according to

$$\underset{\sim}{\boldsymbol{A}}^\mathrm{LP}[k] = \left[\underline{\boldsymbol{a}}^\mathrm{LP}(\theta_1, \varphi_1, kT_\mathrm{s} + T_\mathrm{s,delay}), \ldots, \underline{\boldsymbol{a}}^\mathrm{LP}(\theta_N, \varphi_N, kT_\mathrm{s} + T_\mathrm{s,delay})\right]. \tag{3.6}$$

The linear-phase model is the basis of the DSP algorithms used in this thesis. The steering vectors $\underline{\boldsymbol{a}}^{\mathrm{LP}}(\theta_n, \varphi_n, kT_\mathrm{s} + T_{\mathrm{s,delay}})$ can be expressed by

$$\underline{\boldsymbol{a}}^{\mathrm{LP}}(\theta_n, \varphi_n, kT_\mathrm{s}+T_{\mathrm{s,delay}}) = \begin{bmatrix} \exp \mathrm{j}(2\pi\mu(kT_\mathrm{s} + T_{\mathrm{s,delay}}) + 2\pi f_\mathrm{l})\Delta T_1^{\mathrm{rt}} \\ \exp \mathrm{j}(2\pi\mu(kT_\mathrm{s} + T_{\mathrm{s,delay}}) + 2\pi f_\mathrm{l})\Delta T_2^{\mathrm{rt}} \\ \vdots \\ \exp \mathrm{j}(2\pi\mu(kT_\mathrm{s} + T_{\mathrm{s,delay}}) + 2\pi f_\mathrm{l})\Delta T_M^{\mathrm{rt}} \end{bmatrix} \in \mathbb{C}^{M\times 1} \tag{3.7}$$

and accordingly can the signal vector be expressed by

$$\underline{\boldsymbol{s}}^{\mathrm{LP}}[k] = \begin{bmatrix} a_1^{\mathrm{tgt}} \exp \mathrm{j}(2\pi f_{0,1}^{\mathrm{b}}(kT_\mathrm{s} + T_{\mathrm{s,delay}}) + \phi_{0,1}^{\mathrm{b}}) \\ a_2^{\mathrm{tgt}} \exp \mathrm{j}(2\pi f_{0,2}^{\mathrm{b}}(kT_\mathrm{s} + T_{\mathrm{s,delay}}) + \phi_{0,2}^{\mathrm{b}}) \\ \vdots \\ a_N^{\mathrm{tgt}} \exp \mathrm{j}(2\pi f_{0,N}^{\mathrm{b}}(kT_\mathrm{s} + T_{\mathrm{s,delay}}) + \phi_{0,N}^{\mathrm{b}}) \end{bmatrix} \in \mathbb{C}^{N\times 1}. \tag{3.8}$$

It is interesting, that the array steering vector based on the linear-phase approximation (3.7) is time dependent. Not only is the phase of each sensor's output dependent on the DOA of the incident LFMCW wave fronts, but inter-element time-delay also results in a small frequency difference. Hence, the array signal model for FMCW RADAR systems does not correspond to the narrowband array model typically found in literature covering DOA estimation [89], [103].

3.1.3 Noise

In the preceding sections, the SYST block was modeled as a noise-free system. Although in this thesis the noise mechanisms in FMCW RADAR front end is not of concern, since the focus is strictly limited to the influence of the antennas on the RADAR system aspects, noise has to be taken into account since it is a major factor influencing the performance of estimation algorithms for both frequency and DOA. The existence of noise is taken into account by adding complex additive white Gaussian noise (AWGN) noise represented by $\underline{\boldsymbol{u}}[k]$ to the discrete-time beat signal

$$\underline{\boldsymbol{x}}^{\mathrm{b}}[k] = \underline{\boldsymbol{x}}^{\mathrm{b}}[k] + \underline{\boldsymbol{u}}[k]. \tag{3.9}$$

To keep the formulations simple in the course of the further discussion, the introduction of a new symbol for the noise-corrupted beat signal is refrained

from. Instead, $\underline{\boldsymbol{x}}^{\mathrm{b}}[k]$ is always referred to in conjunction with the signal-to-noise ratio (SNR) present in the signal. The noise vector $\underline{\boldsymbol{u}}[k]$ is defined as

$$\underline{\boldsymbol{u}}[k] = \begin{bmatrix} u_1[k] \\ \vdots \\ u_M[k] \end{bmatrix} \in \mathbb{C}^{M\times 1}, \quad u_m[k] \sim \mathcal{CN}(0, \sigma_u) \tag{3.10}$$

and all noise samples are i.i.d. and drawn from a complex zero-mean normal distribution with variance σ_u. The variance of the noise is selected such, that a desired SNR is achieved. The signal power is computed as the total average power contained in $\underline{\boldsymbol{x}}^{\mathrm{b}}$ by

$$P_{\text{sig.}} = \frac{1}{MK} \sum_{k=0}^{K-1} (\underline{\boldsymbol{x}}^{\mathrm{b}}[k])^H \underline{\boldsymbol{x}}^{\mathrm{b}}[k] \tag{3.11}$$

Then, for a given SNR (in dB), the necessary noise variance is given by

$$\sigma_u^2 = P_{\text{sig.}} - 10^{SNR/10}. \tag{3.12}$$

3.1.4 Block Processing and Block Fragmentation

The DSP algorithms proposed in this thesis operate on a block-by block basis. That means, always K samples corresponding to a complete up-sweep are collected in a matrix $\underset{\sim}{\boldsymbol{X}}$ such that

$$\underset{\sim}{\boldsymbol{X}} = \begin{bmatrix} x_1^{\mathrm{b}}[0] & x_1^{\mathrm{b}}[1] & \cdots & x_1^{\mathrm{b}}[K-1] \\ x_2^{\mathrm{b}}[0] & x_2^{\mathrm{b}}[1] & \cdots & x_2^{\mathrm{b}}[K-1] \\ & & \ddots & \\ x_M^{\mathrm{b}}[0] & x_M^{\mathrm{b}}[1] & \cdots & x_M^{\mathrm{b}}[K-1] \end{bmatrix}, \tag{3.13}$$

which is also referred to as a *sample matrix*. The matrix $\underset{\sim}{\boldsymbol{X}}$ containing the total data can further be fragmented into a number of P frames, each frame holding a certain amount of time-samples. Then each column of $\underset{\sim}{\boldsymbol{X}}$ can be indexed by its frame number p, and the sample number q in the frame by

$$\underset{\sim}{\boldsymbol{X}} = \begin{bmatrix} \overbrace{x_1^{\mathrm{b}}[0] \quad \cdots \quad x_1^{\mathrm{b}}[Q-1]}^{p=0} & \cdots & \overbrace{x_1^{\mathrm{b}}[q+pQ]}^{p} & \cdots & \overbrace{\cdots \quad x_1^{\mathrm{b}}[PQ-1]}^{p=P-1} \\ x_2^{\mathrm{b}}[0] \quad \cdots \quad x_2^{\mathrm{b}}[Q-1] & \cdots & x_M^{\mathrm{b}}[q+pQ] & \cdots & \cdots \quad x_2^{\mathrm{b}}[PQ-1] \\ \\ x_M^{\mathrm{b}}[0] \quad \cdots \quad x_M^{\mathrm{b}}[Q-1] & \cdots & x_M^{\mathrm{b}}[q+pQ] & \cdots & \cdots \quad x_M^{\mathrm{b}}[PQ-1] \end{bmatrix}. \tag{3.14}$$

If the number of frames is an integer multiple of the number of available samples, clearly each frame exactly contains $Q = K/P$ samples. If the number of frames is not an integer multiple of K, then per definition each but the last frame contain $Q[p] = \lceil K/P \rceil, p \in [0, P-2]$ samples, and the very last frame with index $p = P-1$ contains $Q[P-1] = K - (P-1)\lceil K/P \rceil$ samples. If this is the case, note that for simplicity the number of all but the very last frame will be simply denoted by $Q[p] = Q, \forall p \in [0, P-2]$. If any sample k from $\underset{\sim}{\boldsymbol{X}}$ is required, the frame index $p[k]$ can be computed by $p[k] = \lfloor k/Q \rfloor$. The sub-matrix containing only samples of frame p is referred to as $\underset{\sim}{\boldsymbol{X}}[p]$.

3.1.5 Total Covariance Matrix and Frame Covariance Matrix

The total array output covariance matrix is estimated by taking the normalized sum over the dot products of all sampled array output vectors. It is expressed by

$$\hat{\underset{\sim}{\boldsymbol{R}}}_{xx} = \frac{1}{N}\sum_{n=0}^{N-1} \underline{\boldsymbol{x}}[n](\underline{\boldsymbol{x}}[n])^{\mathbf{H}} = \frac{1}{N}\sum_{n=0}^{N-1} \underset{\sim}{\boldsymbol{A}}[n]\underline{\boldsymbol{s}}[n](\underline{\boldsymbol{s}}[n])^{\mathbf{H}}\big(\underset{\sim}{\boldsymbol{A}}[n]\big)^{\mathbf{H}} + \hat{\underset{\sim}{\boldsymbol{R}}}_{uu} \quad (3.15)$$

Equation (3.15) is also referred to as the sample spectral matrix [104]. In the narrowband case the array manifold matrix is not a function of time $\underset{\sim}{\boldsymbol{A}}[n] = \underset{\sim}{\boldsymbol{A}}$ and thus (3.15) reduces to $\hat{\underset{\sim}{\boldsymbol{R}}}_{xx} = \underset{\sim}{\boldsymbol{A}}\underset{\sim}{\boldsymbol{R}}_{ss}\underset{\sim}{\boldsymbol{A}}^{\mathbf{H}} + \underset{\sim}{\boldsymbol{R}}_{nn}$, where $\underset{\sim}{\boldsymbol{R}}_{ss}$ is the signal covariance matrix and $\underset{\sim}{\boldsymbol{R}}_{uu}$ the noise covariance matrix. This is the traditional model for the covariance matrix of the array output used in narrowband DOA estimation [89].

Instead of estimating the covariance matrix using a sum over all available samples, based on the fragmentation of $\underset{\sim}{\boldsymbol{X}}$ into P frames in this thesis also an individual estimate of the covariance matrix of each frame is proposed. This is done by taking the sum over the dot product of all array output vectors belonging to frame p, and normalizing to the number $Q[p]$ of samples per frame

$$\hat{\underset{\sim}{\boldsymbol{R}}}_{xx}[p] = \frac{1}{Q[p]}\sum_{q=0}^{Q[p]-1} \underline{\boldsymbol{x}}[q+pQ](\underline{\boldsymbol{x}}[q+p\cdot Q])^{\mathbf{H}} = \frac{1}{Q[p]}\big(\underset{\sim}{\boldsymbol{X}}[p]\big)^{\mathbf{H}}\underset{\sim}{\boldsymbol{X}}[p]. \quad (3.16)$$

Since the total matrix spans a time duration corresponding to the sweep duration T, clearly the larger the number of frames, the smaller is the time

spanned by each frame. However, note that the smaller the time duration spanned by each frame is, the better can the frame covariance matrix be modeled by a narrowband model, since the time-dependence of the manifold matrix in the frame apparently becomes less and less pronounced. Hence, although not true narrowband, the approximation $\hat{\underset{\sim}{\boldsymbol{R}}}_{xx}[p] \approx \underset{\sim}{\boldsymbol{A}}[pQ]\hat{\underset{\sim}{\boldsymbol{R}}}_{ss}[p]\left(\underset{\sim}{\boldsymbol{A}}[pQ]\right)^{\mathbf{H}} + \hat{\underset{\sim}{\boldsymbol{R}}}_{nn}[p]$ is expected to become better with an increasing frame number.

In contrast in can be argued that the larger the number of frames becomes, less and less samples are available for estimating the framed covariance matrix $\hat{\underset{\sim}{\boldsymbol{R}}}_{xx}[p]$ and clearly, the estimate will get worse. However, comparing the WB RADAR systems proposed in this thesis with the baseline NB system (see table 1.3), it is obvious that the larger the bandwidth becomes, the larger the amount of collected samples per FMCW sweep is. In particular the number of collected samples will always scale up linearly with the bandwidth increase factor. Hence it can be concluded that when going from a NB to WB RADAR system, no loss in covariance matrix estimation will be introduced, if the number of frames equals the bandwidth increase factor.

In this thesis for the NB RADAR system always the total covariance matrix is computed using the 100 available samples. In both WB RADAR scenarios, if framing is used, then the matrix $\underset{\sim}{\boldsymbol{X}}$ of all received samples is fragmented into $P = 20$ frames, each holding 100 samples.

To increase the robustness of algorithms which rely on an inversion of $\hat{\underset{\sim}{\boldsymbol{R}}}_{xx}$ or $\hat{\underset{\sim}{\boldsymbol{R}}}_{xx}[p]$ (the so called sample matrix inversion (SMI)), a technique referred to as diagonal loading [104]–[106] is applied to the estimated covariance matrix. The diagonally loaded covariance matrix $\hat{\underset{\sim}{\boldsymbol{R}}}_{xx,\mathrm{DL}}$ is then given by

$$\hat{\underset{\sim}{\boldsymbol{R}}}_{xx,\mathrm{DL}} = \hat{\underset{\sim}{\boldsymbol{R}}}_{xx} + \epsilon_{\mathrm{DL}}\underset{\sim}{\boldsymbol{I}}, \tag{3.17}$$

where the constant ϵ_{DL} determines the amount of loading. Diagonal loading can be interpreted as indicating in the covariance matrix, that the level of spatially white noise is larger than the actual amount of noise in $\underset{\sim}{\boldsymbol{X}}$ [107]. This can be used to improve the robustness of adaptive beamformers. In this thesis, similar to the method proposed in [107], the amount of diagonal loading is based on the power in the received signals and the loading factor is computed by

$$\epsilon_{\mathrm{DL}} = \Delta_{\mathrm{DL}}\,\mathrm{Tr}\{\hat{\underset{\sim}{\boldsymbol{R}}}_{xx}\}. \tag{3.18}$$

where $\mathrm{Tr}\{\cdot\}$ is the trace of a matrix. Based on the results from [107] and on empirical observations, $\Delta_{\mathrm{DL}} = 0.08/M$ is used in this thesis.

3.2 Range Estimation

The fundamental signal processing task for determining the number and range of targets is to estimate the number and corresponding frequencies of the cisoids contained in $x^{\mathrm{b}}[n]$. Note that for range-only estimation a single antenna element is sufficient. Hence in this section the fundamentals of range estimation will be reviewed using a single-channel RADAR setup.

Classically, if one wants to find the frequencies of a sum of cisoids, one traditional approach is to apply a spectral analysis and detect the peaks of the signal's spectrum. It has been shown in e.g. [108] that this principle can be applied to FMCW RADAR systems, and that the location of the maxima of the discrete-time Fourier transform (DTFT) of $x^{\mathrm{b}}[n]$ indeed provide the maximum likelihood (ML) estimator for well-separated RADAR targets. Since the DTFT can be approximately computed using a discrete Fourier transform (DFT) with sufficiently large number of frequency bins, or by its fast and efficient implementation the Fast Fourier Transform (FFT), the DTFT-based range estimation provides an interesting choice for the computationally efficient implementation of a range estimation algorithms.

As will be discussed in the remainder of this section in more detail, DTFT-based frequency estimation is subject to some classical resolution limitations. Hence, model-based or parametric frequency estimation algorithms have been proposed [108], [109] and applied to FMCW RADAR systems [110], [111] to overcome the classical limitations. However, as mentioned in [13], [108], although superior from a theoretical view, in practical applications parametric methods suffer from several drawbacks: parametric methods require an estimation of the model order, i.e. before being able to estimate the beat frequencies of the targets, the number of targets has to be estimated which is a difficult problem by itself. Furthermore, whereas the AWGN condition assumed for the noise is not a critical one when using the DFT as a range estimator, it was shown that it can yield consistent range estimates also for colored noise, the performance of parametric methods often strongly degrades in colored-noise conditions. Also the threshold level, i.e. the SNR where the performance of the estimator degrades rapidly and leaves the Cramer-Rao lower bound (CRLB) was shown to be very low for DFT based range estimation, compared to other estimators. In addition, model mismatch may e.g. be introduced by diffuse multipath components, and hence parametric methods often do not provide the expected results when used in typi-

cal application scenarios [13]. Hence the DFT is traditionally used in FMCW RADAR systems [12], [13] for the range estimation, and will also serve as the range estimation algorithm in this thesis.

To quantify the performance of range estimation, two figure of merits are used in this thesis: *range resolution* and *range accuracy*. Range resolution describes how close two targets can be separated such that they can be distinguished as two separate peaks in the spectral domain and hence detected as two targets. When using the FFT as range estimator, the range resolution is inherently linked with signal bandwidth. It is only the finite width of the main lobe of the window function that limits resolution [109]. Two targets can theoretically be discriminated, i.e. appear as separate peaks in the frequency domain, if they are separated at least by the 6 dB width of the window's main lobe [112]. The rectangular window is the one having the minimum 6 dB bandwidth of $1.21/T$ among all window functions [112], although in trade-off it has higher side-lobes compared to other window functions. Just truncating the data without applying a particular window function corresponds to using the rectangular window. In this thesis the data contained in $\underset{\sim}{\boldsymbol{X}}$ thus is subject to a rectangular window. As mentioned before for practically relevant FMCW RADAR systems it holds that $T_n^{\mathrm{d}} << T$ and it can be assumed that the beat signal is observed for a time duration of T. Then by inserting (2.43) into (2.40) and finally into the theoretical resolution limit of $\Delta f_{\mathrm{min}} = 1.21/T$ it can be solved for the range resolution d_{min} of the abstract model (i.e. a secondary RADAR system)

$$\Delta d_{\mathrm{min}} = 1.21 \frac{c_0}{T\mu} = 1.21 \frac{c_0}{\mathrm{BW}}. \tag{3.19}$$

In a primary RADAR system, Δd_{min} is half the value from (3.19). Interestingly, the minimum range resolution is only dependent on the bandwidth BW utilized by the FMCW sweep and it is a fundamental property of DTFT-based range estimation, that the bandwidth limits range resolution. For achieving a high resolution in range the BW of the system has to be increased. This is the fundamental motivation for using UWB FMCW RADAR systems.

Starting from a NB system, two methods can be identified to increase the bandwidth: either, if the sweep rate μ is held constant, the main lobe of the window function can be narrowed by increasing the observation time T. Since increasing the observation time means increasing the sweep duration, it is obvious that the sweep bandwidth will also increase. This is the fundamental principle applied in the WBS RADAR system. Alternatively the

observation time can be held constant, which in conclusion means that the frequency resolution of the DTFT also remains unchanged. Then by increasing the sweep-rate of the RADAR system, the beat frequency obtained for a certain range can be increased and although frequency resolution of the DTFT does not increase, range resolution does. This is the fundamental principle applied in the WBF RADAR system.

Figure 3.2 shows the results of a numerical simulation for determining the resolution limit of DTFT-based range estimation. Therefore, a discrete-time beat signal consisting of two cisoids is generated according to

$$x^{\mathrm{b}}[k] = \exp \mathrm{j}(2\pi f_1^{\mathrm{b}} k T_{\mathrm{s}}) + \exp \mathrm{j}(2\pi f_2^{\mathrm{b}} k T_{\mathrm{s}} + \phi_2^{\mathrm{b}}) + u[k], \tag{3.20}$$

where $f_2^{\mathrm{b}} = \Delta f + f_1^{\mathrm{b}}$ and $u[k]$ is AWGN. A phase term ϕ_2^{b} taken into account in the second cisoid is used to model arbitrary phase differences between both signal components. The FFT of (3.20) is computed for $\phi_2^{\mathrm{b}} \in \{0, \pi/32, \ldots, \pi\}$ and its magnitude is plotted for $\Delta f = 1.4T$ in figure 3.2 a). The positions of the true frequencies are indicated by two vertical black lines and the FFTs of each single component is shown as a thick green and blue plot, respectively. It can be seen, that depending on the relative phase of both cisoids

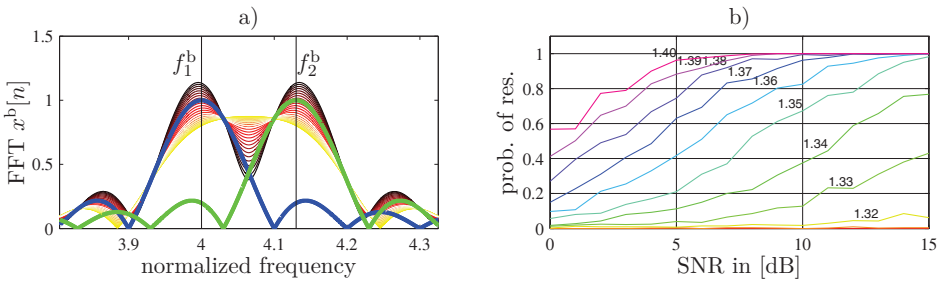

Fig. 3.2: Beat signal spectrum and probability of resolution. a) Fourier spectrum $\mathcal{F}\{x^{\mathrm{b}}(t)\}$ for beat signal obtained from two closely separated targets and b) probability of resolution vs. SNR for different target separations.

the existence of two distinct peaks is more or less pronounced. Both peaks can clearly be resolved for $\phi_2^{\mathrm{b}} = 0$, but merge for $\phi_2^{\mathrm{b}} = 0.75\pi$. To get a more quantitative description of the expected range resolution, a numerically computed estimate for the probability of resolution is plotted in figure 3.2 b). Therefore, at different SNRs the FFT of (3.20) is computed for all $\phi_2^{\mathrm{b}} \in \{0, \pi/32, \ldots, \pi\}$. Then a peak detection is performed, where a peak is defined as a FFT sample which is larger than the two neighboring samples.

If two peaks are detected for all $\phi_2^{\mathrm{b}} \in \{0, \pi/32, \ldots, \pi\}$, then this trail is taken into account as a success. A Monte Carlo simulation with 200 trails per SNR value is performed, and the number of successes to the total number of trails is used as an estimate for the probability of resolution. It can be seen that with an estimated probability of $90\,\%$, two targets can be separated for a SNR down to 4 dB if their frequency spacing is at least $1.4/T$. Correspondingly this implies that a practically relevant range resolution of

$$\Delta d_{\mathrm{min}} \approx 1.4 \frac{c_0}{\mathrm{BW}} \tag{3.21}$$

can be assumed. Reviewing section 1.2, this means that using a NB secondary FMCW RADAR system with $\mathrm{BW} = 150\,\mathrm{MHz}$, a range resolution of about $\Delta d_{\mathrm{min.}} \approx 2.8\,\mathrm{m}$ can be achieved. Note that this value is close to the range resolution of the secondary RADAR system proposed in [12]. By increasing the bandwidth to $\mathrm{BW} = 3\,\mathrm{GHz}$, theoretically a range resolution of $\Delta d_{\mathrm{min.}} \approx 14\,\mathrm{cm}$ can be achieved.

Range resolution only characterizes if two targets can be resolved as two distinct peaks in the spectral domain. It does not contain any information about the accuracy, i.e. the location, of both peaks. As can be seen from 3.2 a), both cisoids contained in the beat signal influence the position of the spectral peak of the other cisoid. Consequently, the position of each spectral peak does not coincide with the true position, and a range estimation error will be introduced.

Range accuracy describes the error between estimated target range and true target range. In a RADAR system with ideal linear components and AWGN being the only perturbation to the beat signal, such as the system model assumed in this thesis, accuracy is mainly influenced by three factors: limited resolution of FFT, presence of other targets and noise.

The DTFT, which is a purely analytic mathematical tool yields a continuous spectrum. Numerically it is implemented by means of a FFT, which in contrast results in a series of frequency bins, obtained by sampling the DTFT at equally spaced frequency points. If the position of the FFT maximum is used for estimating beat frequency and target range, respectively, it is obvious that the maximum estimation error equals half the width of a FFT bin [113], occurring if the true beat frequency is exactly in between two FFT bins. The range accuracy is the limited by

$$\epsilon d = f_s / N_{\mathrm{FFT}}. \tag{3.22}$$

To resolve this problem, the traditional method is to compute the FFT in a finer grid by zero-padding the beat signal data $x^{\mathrm{b}}[n]$ before FFT computation. However, this results in globally interpolating the DFT spectrum over the entire frequency range and to get a sufficiently fine FFT grid resolution around the frequency of interest a very large FFT size may result. Hence, alternative methods such as a zoom-FFT [12] or local FFT interpolation [113] have been proposed. In this thesis, only the pure FFT output will be used for frequency estimation, no interpolation or zoom-FFT is applied. Since computational cost plays a minor role in the scope of this thesis, if required the necessary FFT interpolation will be achieved by zero-padding.

In addition to the systematic accuracy error due to limited FFT resolution, stochastic accuracy errors are introduced by the presence of noise and other targets. Hence, the accuracy of the range estimate is defined in terms of the variance of the estimate. The CRLB forms a lower-bound for the minimum variance, any unbiased estimator can achieve. For the estimation of a single cisoid in noise, it is given by [108]

$$\mathrm{var}\{\hat{\omega}\} \geq \frac{6}{SNR \cdot N^3}. \tag{3.23}$$

3.3 Direction-Of-Arrival Estimation

Similar to the frequency estimation algorithms used for target range estimation, also algorithms for DOA estimation can be separated into two categories: spectral based methods and parametric methods [114]. Whereas in the former a spectrum-like function of the parameters of interest are formed, and the location of the highest peaks of the spectrum are recorded as parameter estimates, parametric methods require a simultaneous search for all parameters of interest. Indeed parametric methods often result in more accurate estimates and their statistical performance is superior to spectral based methods, but their computational complexity is strongly increased compared to spectral methods.

Spectral DOA estimation methods can further be subdivided into beamforming techniques and model-based subspace techniques. The most prominent beamforming techniques are the Bartlett beamformer and Capon's, or the MVDR, beamformer, and the most prominent subspace-based algorithm is multiple signal classification (MUSIC). Although beamforming techniques neither are statistically efficient, nor consistent (except the Bartlett beam-

former in the case of a single impinging signal) they found widespread use in applications requiring DOA estimation. In addition to their relatively low computational complexity, beamforming techniques are not model-based, compared to spectral subspace-based methods such as MUSIC. Hence model-order estimation, which is a separate problem in model-based techniques, is not necessary for beamforming techniques.

Finally beamforming DOA estimation techniques do not only give estimates on the DOA of the impinging wave fronts, but can also serve by means of a spatial filter, i.e. spatially separate several signals according to their DOA. This property will be exploited in this chapter to allow for combined range and angle estimation. Indeed combined range and angle-estimation methods based on model-based subspace spectral techniques have been proposed lately [115], but the computational-complexity as well as their requirements on model precision and model-order estimation.

As a consequence of the above discussion, the focus in this thesis lies on the implementation and performance of beamforming techniques for DOA estimation in wideband LFMCW RADAR systems. The property that beamforming cannot only be used for pure DOA estimation but also for spatially filtering a signal will then be used to derive combined range and DOA estimation algorithms in the following section.

3.3.1 Narrowband Beamforming Algorithms

Narrowband beamforming algorithms are based on the narrowband approximation of the sensor array response, see section 2.2.4. Although it will be shown that narrowband techniques yield wrong estimates for wideband FMCW RADAR systems, their principles are the foundation for the wideband algorithms developed in this chapter. Hence, the two most prominent traditional narrowband beamforming techniques will be reviewed first: Bartlett Beamforming and Capon's, or the MVDR beamformer.

3.3.1.1 Bartlett Beamforming

The spatially filtered output signal $\hat{s}_{\text{NB,BT}}[\alpha, n]$ of a narrowband Bartlett beamformer is given by [89]

$$\hat{s}_{\text{NB,BT}}[\alpha, k] = \frac{1}{\sqrt{(\underline{\boldsymbol{a}}^{\text{NB}}[\alpha])^{\mathbf{H}} \underline{\boldsymbol{a}}^{\text{NB}}[\alpha]}} (\underline{\boldsymbol{a}}^{\text{NB}}[\alpha])^{\mathbf{H}} \underline{\boldsymbol{x_b}}[k]. \tag{3.24}$$

To numerically evaluate (3.24) over a certain search range, spatially discrete steering vectors $\underline{\boldsymbol{a}}^{\text{NB}}[\alpha]$ are used. Since only DOA estimation in φ direction is of interest in this thesis, the spatially discrete steering vector $\underline{\boldsymbol{a}}^{\text{NB}}[\alpha]$ is related to $\underline{\boldsymbol{a}}^{\text{NB}}(\theta, \varphi)$ by

$$\underline{\boldsymbol{a}}^{\text{NB}}[\alpha] = \underline{\boldsymbol{a}}^{\text{NB}}(\theta_{\text{const}}, \alpha_{\varphi}). \tag{3.25}$$

The steering- or look direction α_{φ} of the beamformer is given by

$$\alpha_{\varphi}[\alpha] = \alpha\varphi_{\text{step}} + \varphi_{\text{start}} \tag{3.26}$$

and α is referred to as the look direction index. The step size of the angular search grid is defined by φ_{step} and the start angle by φ_{start}. By using $\alpha = 0 \ldots A-1$, a search range of $\alpha_{\varphi} = \varphi_{\text{start}} \ldots (A-1)\varphi_{\text{step}} + \varphi_{\text{start}}$ is realized. A known angle $\theta = \theta_{\text{const}}$ is assumed if a UCA is used. Since the ULA is independent on θ, the value of θ_{const} does not have any influence on the ULA steering vector. In contrast to traditional beamforming the linear-phase narrowband approximation of the steering vector $\underline{\boldsymbol{a}}^{\text{NB}}$, as introduced in section 2.2.4, is used in (3.24). By evaluating (3.24) over a desired range of look directions and for the complete length K data set the beat signal sample matrix $\underset{\sim}{\boldsymbol{X}}$ can be transformed into a spatially-filtered signal matrix $\underset{\sim}{\boldsymbol{S}}_{\text{NB,BT}} \in \mathbb{C}^{A \times K}$

$$\underset{\sim}{\boldsymbol{S}}_{\text{NB,BT}} = \begin{bmatrix} \hat{s}_{\text{NB,BT}}[0,0] & \hat{s}_{\text{NB,BT}}[0,1] & \cdots & \hat{s}_{\text{NB,BT}}[0,K-1] \\ \hat{s}_{\text{NB,BT}}[1,0] & \hat{s}_{\text{NB,BT}}[1,1] & \cdots & \hat{s}_{\text{NB,BT}}[1,K-1] \\ & & & \\ \hat{s}_{\text{NB,BT}}[A-1,0] & \hat{s}_{\text{NB,BT}}[A-1,1] & \cdots & \hat{s}_{\text{NB,BT}}[A-1,K-1] \end{bmatrix}, \tag{3.27}$$

where the rows of the matrix $\underset{\sim}{\boldsymbol{X}}$, which originally contained the output signals of a certain array element, are now transformed into the DOA space, i.e. each row corresponds to a certain steering direction. The number of rows in $\underset{\sim}{\boldsymbol{S}}$ corresponds to the number A of search angles. Figure 3.3 a) illustrates the

spatial filtering by plotting the real part of the spatially filtered signal matrix, which is obtained by filtering the beat signal matrix $\underset{\sim}{\boldsymbol{X}}$ obtained from a single target at distance $d = 5\,\mathrm{m}$ and DOA $(\theta_1, \varphi_1) = (0, 45°)$ incident on a four-element ULA using element distance of $\lambda_{\mathrm{low}}/2$ in the NB RADAR scenario. The SNR is 30 dB. Clearly it can be seen that the maximum signal

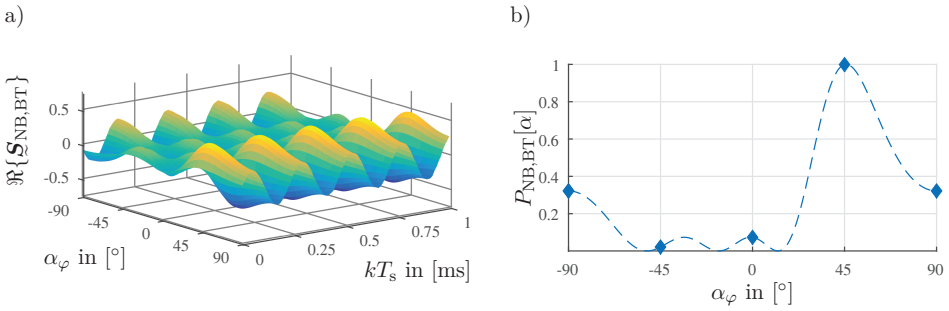

Fig. 3.3: a) Spatially filtered signal and b) normalized spatial spectrum obtained from Bartlett Beamforming. Results obtained from a single target at distance $d = 5\,\mathrm{m}$ and DOA $(\theta, \varphi) = (0, 45°)$ using on a four-element ULA with element distance of $\lambda_{\mathrm{low}}/2$ in the NB RADAR scenario, $SNR = 30\,\mathrm{dB}$. Search grid step size $\varphi_{\mathrm{step}} = 1\,°$.

amplitude is obtained around $\alpha_\varphi = 45\,°$ and that the temporal structure of $\underset{\sim}{\boldsymbol{S}}$ reveals the presence of the mono-frequent cisoid. In addition, it can be seen that a significant signal amplitude is obtained for neighboring steering angles. This effect corresponds to limited resolution due to windowing. In spatial filtering, it is the aperture size of the ULA which corresponds to the window function and hence determines the width of the main-lobe in $\underset{\sim}{\boldsymbol{S}}$.

By taking the sum of the element-wise squared magnitude of $\underset{\sim}{\boldsymbol{S}}$ along each row, the output power as a function of look direction index α is obtained

$$P_{\mathrm{NB,BT}}[\alpha] = \sum_{k=0}^{K-1} \left|\hat{s}_{\mathrm{NB,BT}}[\alpha, k]\right|^2 . \tag{3.28}$$

Equation (3.28) is referred to as the spatial spectrum. The estimate $\hat{\varphi}$ for the DOA of the target can then be found by applying a peak search on $P_{\mathrm{NB,BT}}[\alpha]$ to determine the index $\hat{\alpha}$ of the peak position. The index $\hat{\alpha}$ of the peak position is then related to the DOA estimate via the look direction

$$\hat{\varphi} = \alpha_\varphi[\hat{\alpha}]. \tag{3.29}$$

3.3.1.2 Minimum Variance Distortionless Response Beamforming

In contrast to Bartlett beamforming, where all degrees of freedom of the array are used to form a beam into the look direction α, the MVDR approach relies on using all but one degrees of freedom of the array to minimize the output power of the array, and the last degree of freedom to constrain the gain in the look direction to unity [89]. The spatially filtered signal output of the MVDR beamformer is then given by [89]

$$\hat{s}_{\text{NB,MV}}[\alpha, n] = \underline{\boldsymbol{h}}^{\mathbf{H}}[\alpha]\underline{\boldsymbol{x}}[n], \tag{3.30}$$

where the filter vector $\underline{\boldsymbol{h}}^{\mathbf{H}}[\alpha]$ is obtained using

$$\underline{\boldsymbol{h}}[\alpha] = \frac{\hat{\underset{\sim}{\boldsymbol{R}}}_{xx,\text{DL}}^{-1}\underline{\boldsymbol{a}}^{\text{NB}}[\alpha]}{(\underline{\boldsymbol{a}}^{\text{NB}}[\alpha])^{\mathbf{H}}\hat{\underset{\sim}{\boldsymbol{R}}}_{xx,\text{DL}}^{-1}\underline{\boldsymbol{a}}^{\text{NB}}[\alpha]}, \tag{3.31}$$

i.e. the MVDR uses the inverse of the diagonally loaded correlation matrix $\hat{\underset{\sim}{\boldsymbol{R}}}_{xx,\text{DL}}^{-1}$ to compute the filter vector. The spatial spectrum is obtained by

$$P_{\text{NB,MV}}[\alpha] = \sum_{n=0}^{N-1} \left|\hat{s}_{\text{NB,MV}}[\alpha, n]\right|^2. \tag{3.32}$$

Figure 3.4 a) illustrates the spatially filtered signal matrix $\underset{\sim}{\boldsymbol{S}}$ obtained by filtering the beat signal matrix $\underset{\sim}{\boldsymbol{X}}$ obtained from a single target at distance $d = 5\,\text{m}$ and DOA $(\theta, \varphi) = (0, 45°)$ using a four-element ULA with element distance of $\lambda_{\text{low}}/2$ in the NB RADAR scenario. The SNR is 30 dB. Compared to the Bartlett beamformer, it is eminent how the width of the main lobe is reduced.

3.3.2 Wideband Beamforming Algorithms

The traditional narrowband DOA estimation algorithms are, as their naming implies, based on the narrowband assumption, which is however not true for the signals obtained at the output of a FMCW RADAR sensor array (compare section 2.2). Indeed in FMCW RADAR systems with a small relative bandwidth the narrowband assumption may hold to a satisfactory degree and the use of narrowband DOA estimation algorithms may only contain relatively

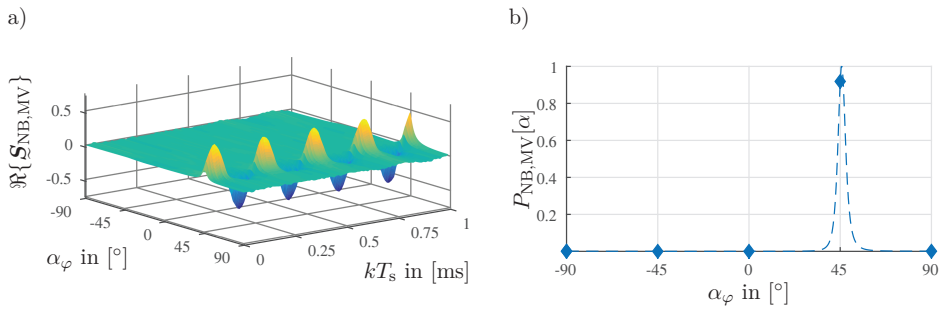

Fig. 3.4: a) Spatially filtered signal and b) normalized spatial spectrum obtained from Capon Beamforming. Results obtained from a single target at distance $d = 5\,\mathrm{m}$ and DOA $(\theta, \varphi) = (0, 45°)$ using a four-element ULA with element distance of $\lambda_{\mathrm{low}}/2$ in the NB RADAR scenario, $SNR = 30\,\mathrm{dB}$. Search grid step size $\varphi_{\mathrm{step}} = 1\,°$.

small estimation errors, but as will be shown in section 3.5, this ill-posed model assumption leads to intolerably large DOA estimation errors in WB RADAR scenarios. To overcome those problems, the traditional methods are extended to DOA estimation for UWB RADAR system in this section.

Wideband DOA estimation approaches can traditionally be classified into coherent and non-coherent methods [116]. Coherent methods rely on a linear preprocessor which combines the covariance matrices obtained at each frequency coherently into a single covariance matrix, and this focussed single covariance matrix is then used by a narrowband beamformer [116], [117]. Using incoherent methods the received signal matrix is decomposed into a set of narrowband signal bands, then DOA estimation is applied to this bands individually, and the total DOA estimate is obtained by combining the DOA estimation results of the individual narrow frequency bands incoherently.

In this section, two variants of non-coherent DOA estimation are proposed for wideband FMCW RADAR systems. In contrast to traditional non-coherent methods which rely on using a filterbank to decompose the received wideband signal into a set of several narrow-band signals, the linear time-frequency relation of LFM signals is exploited. It can easily be seen, that a segmentation of the received LFM sweep into multiple time windows corresponds to a filterbank, since the bandwidth present in each window is reduced. Consequently applying DOA estimation to each individual time window and then averaging the individual DOA estimates correspond to the non-coherent DOA estimate for the LFM sweep.

3.3.2.1 Wideband Bartlett Beamforming

Wideband Bartlett Beamforming is the result of a straight-forward extension of the classical narrowband Bartlett beamformer, taking into account the time-dependence of the steering vector. Equation (3.24) is extended by using the linear-phase model of the received signal and consequently, a different steering vector is used for each time sample k to filter the received signal matrix $\underset{\sim}{\boldsymbol{X}}$

$$\hat{s}_{\text{WB,BT}}[\alpha, k] = \frac{1}{\sqrt{(\underline{\boldsymbol{a}}^{\text{LP}}[\alpha, k])^{\mathbf{H}}(\underline{\boldsymbol{a}}^{\text{LP}}[\alpha, k])}}(\underline{\boldsymbol{a}}^{\text{LP}}[\alpha, k])^{\mathbf{H}}\underline{\boldsymbol{x}}[k]. \tag{3.33}$$

Again the spatial search range is discretized using $\underline{\boldsymbol{a}}^{\text{LP}}[\alpha, k]$, which is related to $\underline{\boldsymbol{a}}^{\text{LP}}(\theta_n, \varphi_n, kT_{\text{s}} + T_{\text{s,delay}})$ from (3.7) by

$$\underline{\boldsymbol{a}}^{\text{LP}}[\alpha, k] = \underline{\boldsymbol{a}}^{\text{LP}}(\theta_{\text{const}}, \alpha_\varphi, kT_{\text{s}} + T_{\text{s,delay}}), \tag{3.34}$$

where the definition of look direction α_φ from (3.26) is used.

Figure 3.5 a) illustrates the effects when using the narrowband Bartlett beamformer on a signal matrix $\underset{\sim}{\boldsymbol{X}}$ obtained in the WB RADAR scenario. Clearly, the spatially filtered signal is not fixed at look direction $\alpha_\varphi = 45\,^\circ$ corresponding to the true DOA of $\varphi = 45\,^\circ$. With increasing time, a second steering direction α_φ with significant output power arises. This second steering direction is referred to as a grating lobe and occurs due to the rank-1 ambiguity of the ULA with element spacing $d_{\text{el}} = \lambda_{\text{low}}/2$. In Figure 3.5 b), the effects of the wideband Bartlett beamformer are illustrated: the filtered signal for $\alpha_\varphi = 45^\circ$ becomes more stable. However, still the grating lobe exists.

3.3.2.2 Non-Coherent MVDR

The non-coherent wideband MVDR is normally implemented by decomposing the correlation matrix using a filter-bank [104], [116] in a set of narrowband matrices. This is typically done by e.g. applying a DFT to the received signal matrix, then obtaining several narrowband covariance matrices, using a modified version of (3.31) to obtain the optimum weight vectors for each frequency, and finally performing the actual beamforming (3.30) in each frequency bin yielding the non-coherent beamformer output [116]. From the inherent property of FMCW RADAR systems, that the instantaneous fre-

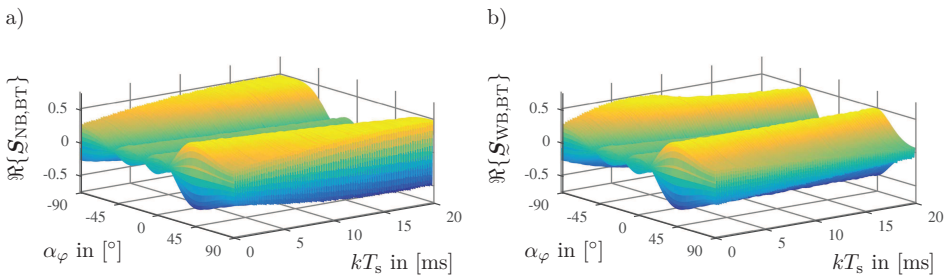

Fig. 3.5: Spatially filtered signals obtained from a) narrowband and b) wideband Bartlett Beamforming. Results obtained from a single target incident on a four-element ULA using element distance of $\lambda_{\mathrm{low}}/2$ at distance $d = 5\,\mathrm{m}$ and DOA $(\theta, \varphi) = (0, 45°)$ in the WBS RADAR scenario, $SNR = 30\,\mathrm{dB}$.

quency of the received signal is proportional to time, it gets obvious that a decomposition into several narrow frequency bands for incoherent wideband DOA estimation becomes equivalent to a decomposition of the received signal into smaller time-frames, where each time frame corresponds to a narrowband FMCW signal. This idea is the reason for proposing the fragmented covariance matrix concept in section 3.1.4. The wideband MVDR spatial filter coefficients are obtained by

$$\underline{\boldsymbol{h}}[\alpha, k] = \frac{\hat{\underline{\boldsymbol{R}}}^{-1}_{xx,\mathrm{DL}}[p[k]]\underline{\boldsymbol{a}}[\alpha, k]}{\underline{\boldsymbol{a}}^{\mathbf{H}}[\alpha, k]\hat{\underline{\boldsymbol{R}}}^{-1}_{xx,\mathrm{DL}}[p[k]]\underline{\boldsymbol{a}}[\alpha, k]}, \tag{3.35}$$

where depending on the sample index k, the corresponding frame correlation matrix $\underline{\boldsymbol{R}}_{xx}[p[k]]$ is used. The spatially filtered signal is obtained using the time-dependent filter coefficients

$$\hat{s}_{\mathrm{WB,MV}}[\alpha, k] = (\underline{\boldsymbol{h}}[\alpha, k])^{\mathbf{H}}\underline{\boldsymbol{x}}[k], \tag{3.36}$$

and the spatial spectrum is the obtained by inserting (3.36) into (3.32).

In figure 3.6 a), the performance of using narrowband MVDR beamforming on the WB signal scenario is illustrated. Clearly, effects similar to those observed for the Bartlett beamformer are obvious: the spatially filtered signal is no more fixed to a certain look direction. Instead it is spatially distorted across $\alpha_\varphi = 45°$ and the α_φ maximizing signal amplitude moves with increasing time. In addition, the existence of a grating lobe is significant and the narrow beamwidth of the MVDR beamformer is widened by a large degree. The benefits of using the wideband algorithm are illustrated in 3.6 b).

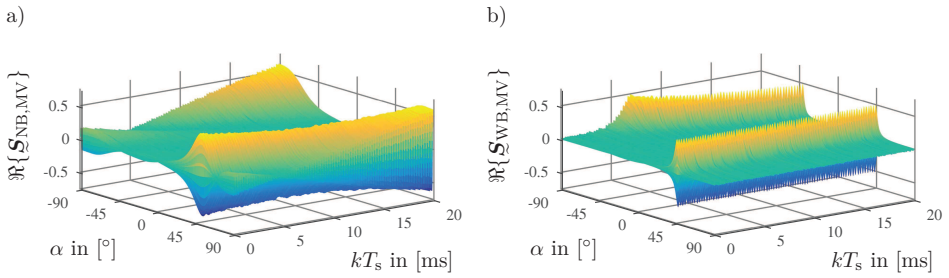

Fig. 3.6: Spatially filtered signals obtained from a) narrowband and b) wideband MVDR Beamforming. Results obtained from a single target incident on a four-element ULA using element distance of $\lambda_{\mathrm{low}}/2$ at distance $d = 5\,\mathrm{m}$ and DOA $(\theta, \varphi) = (0, 45°)$ in the WBS RADAR scenario, $SNR = 30\,\mathrm{dB}$.

The spatial distortion of the signal around its true DOA is mitigated: the signal remains stable at $\alpha_\varphi = 45°$. In addition, the desired narrow beam width of the MVDR beamformer is restored. The grating lobe is still present.

3.4 Combined Range and Direction-Of-Arrival Estimation

The fundamental principle of the combined algorithms proposed in this thesis is a straight-forward extension of the proposed spatial filtering methods: instead of obtaining a purely spatial spectrum by (3.28) or (3.32), a DFT is applied along each row of $\underset{\sim}{\boldsymbol{S}}$. This results in the angle-range spectral matrix $\underset{\sim}{\boldsymbol{J}}$ which can be expressed by

$$\underset{\sim}{\boldsymbol{J}} = \begin{bmatrix} \hat{j}[0,0] & \hat{j}[0,1] & \cdots & \hat{j}[0,\Psi-1] \\ \hat{j}[1,0] & \hat{j}[1,1] & \cdots & \hat{j}[1,\Psi-1] \\ & & & \\ \hat{j}[A-1,0] & \hat{j}[A-1,1] & \cdots & \hat{j}[A-1,\Psi-1] \end{bmatrix} \in \mathbb{C}^{A\times\Psi}, \tag{3.37}$$

where Ψ is the length of the DFT. Note that Ψ is greater or equal to the number of available time-samples K, since the DFT length may be increased by zero-padding $\underset{\sim}{\boldsymbol{S}}$. By doing so, the time-domain of $\underset{\sim}{\boldsymbol{S}}$ is transformed into frequency domain. Since $\underset{\sim}{\boldsymbol{S}}$ contains a spatially filtered version of the beat signal, it is obvious that applying the DFT along the columns of $\underset{\sim}{\boldsymbol{S}}$ corresponds to applying a DFT-based range estimation in each look direction α_φ. To distinguish angle-range spectral matrices from different beamforming algo-

rithms, as above corresponding indices are appended to $\underset{\sim}{\boldsymbol{J}}$ and its elements.

The individual entries of the angle-range matrix $\underset{\sim}{\boldsymbol{J}}$ are obtained from the spatially filtered signal by

$$\hat{j}[\alpha, \psi] = \left| \sum_{k=0}^{\Psi-1} \hat{s}[\alpha, k] e^{-\mathrm{j}\frac{2\pi}{\Psi}\psi k} \right|^2 . \tag{3.38}$$

The FFT index ψ is related to the frequency by $f = \psi \cdot f_\mathrm{s}/\Psi$. Consequently the range r is given using (2.43) and (2.40) by

$$r = c_0 \psi f_\mathrm{s}/(\Psi \mu). \tag{3.39}$$

A formulation similar to the Bartlett-based estimator has been obtained in [39] using a least-squares optimization. Here, the received signal matrix $\underset{\sim}{\boldsymbol{X}}$ in contrast is first transformed to frequency (range) domain, and then followed by a beamforming operation. Combined range and angle estimation based on the MVDR beamformer has been shown in [38]. However, although the approach shown there does take into account the time-dependence of the steering vector for MVDR weight-vector computation, the effect of the wideband FMCW model on the covariance matrix is not taken into account.

The angle-range matrices $\underset{\sim}{\boldsymbol{J}}$ obtained from Bartlett and MVDR beamforming for a single target at distance $d = 5\,\mathrm{m}$ and DOA $(\theta, \varphi) = (0, 45°)$ using a four-element ULA with element distance of $\lambda_\mathrm{low}/2$ in the WBS RADAR scenario are illustrated in figure 3.7. Note the very sharp peak obtained using the MVDR estimator.

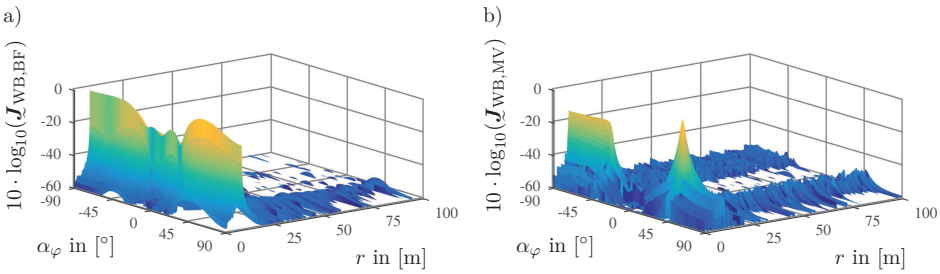

Fig. 3.7: Angle-range spectra using wideband a) Bartlett and b) MVDR beamformers. Results obtained from a single target at distance $d = 5\,\mathrm{m}$ and DOA $(\theta, \varphi) = (0, 45°)$ using a four-element ULA with element distance of $\lambda_\mathrm{low}/2$ in the WBS RADAR scenario, $SNR = 30\,\mathrm{dB}$.

To obtain estimates for the range as well as the DOA of the targets given the range-angle spectrum, a peak search is applied to $\underset{\sim}{\boldsymbol{J}}$. This peak search is based on finding regional maxima in $\underset{\sim}{\boldsymbol{J}}$, where a regional maximum is defined as the index $[\hat{\alpha}, \hat{\psi}]$ for which $\hat{j}[\hat{\alpha}, \hat{\psi}] > \hat{j}[\alpha, \psi] \, \forall \alpha \in \{\hat{\alpha} - 1, \hat{\alpha} + 1\}, \psi \in \{\hat{\psi} - 1, \hat{\psi} + 1\}$. That means for each $[\alpha, \psi]$, eight connected neighborhoods are used to check if it is a regional maximum. The identified peaks are then sorted in descending order according to their spectral value $\hat{j}[\hat{\alpha}, \hat{\psi}]$, and the largest N peaks are returned as estimated target distance and DOA. The estimate $\hat{\varphi}$ for the DOA and $\hat{r}$ for the distance of the target are similar to (3.29) then given by

$$\hat{\varphi} = \alpha_{\varphi}[\hat{\alpha}], \tag{3.40}$$

$$\hat{r} = c_0 \hat{\psi} f_s / (\Psi \mu). \tag{3.41}$$

3.5 Performance Evaluation

In this section, the performance of the proposed range and DOA estimation algorithms is evaluated. The evaluation begins with an qualitative assessment, illustrating the influence of NB and WB RADAR scenarios on the spatial spectra. In addition, the occurrence of grating lobes and the relation to element distance is examined. After the qualitative assessment, a statistical examination of the algorithms is presented.

3.5.1 Qualitative Assessment

3.5.1.1 Uniform Linear Array

To ensure an ambiguity free operation, traditionally the element spacing in a ULA must be smaller or equal to $\lambda_h/2$ [89]. Hence, an array with element spacing is $\lambda_h/2$ is considered first. Figure 3.8 a) - d) shows the spatial spectra obtained from WB and NB Bartlett and MVDR algorithms for a single wave front impinging from a DOA of 0°and 60°. The plots shown in a) and b) were obtained using the NB RADAR signal scenario and the plots from c) and d) using the WB signal scenario. For all signal scenarios the SNR was set to 30 dB. It is clearly visible that the MVDR algorithm results in a spatial spectrum with a narrower main lobe and smaller side lobes compared to the Bartlett beamformer. In addition, it is obvious that there is nearly no difference between the spatial spectra obtained from the NB and WB algorithms

in the NB signal scenario. However, in the WB scenario, a discrepancy between WB and NB algorithms is obvious. This is due to the fact, that the time-dependency of the steering vector is not taken into account by the NB methods. Whereas for an impinging angle of 0 ° only the width of the main lobe but not its peak position is influenced, it is clearly obvious that for larger DOA the spatial spectrum peak position deviates from the true DOA and the NB estimation algorithms get biased. In contrast, both WB DOA estimation algorithms taking into account the variation of the steering vector over time result in a spatial spectrum peak position at the true DOA.

In Figure 3.8 e) - h) the element spacing was set to $\lambda_l/2$. As a first observation, it can be seen by comparing plots a) and c) with e) and f), respectively, that the change of element spacing leads to a reduction in main-lobe width. This is due to the fact that main-lobe width is directly related to array aperture size, and increasing element spacing of course increases aperture size. However, from basic array processing theory it is known that the spacing of the array elements may not exceed $\lambda_h/2$ since otherwise ambiguities which result in grating lobes in the spatial spectrum would occur. As expected, the spatial spectra obtained from the NB algorithms for an incident wave front with DOA of 60 ° shown in figure 3.8 h) illustrates the existence of grating lobes. Interestingly, the grating-lobe problem is less distinct for the WB Bartlett estimator, and for the WB Capon algorithm almost no grating lobes seem to exist in the spatial spectrum.

This favorable behavior of both WB DOA estimation algorithms can be explained by looking at the magnitude $|\hat{s}[\alpha, k]|^2$ of the spatially filtered signals shown in figure 3.9. In the spatially filtered output signal of the NB estimators, both the desired signal component at 60°and the grating lobe due to spatial undersampling using an element distance of $\lambda_l/2$ appear as curves in the $[\alpha_\varphi, k]$-plane. Recalling that the spatial spectrum results from summing up all contributions along the n-axis, it is obvious that for both cases there will exist several angular bins with significant magnitude. In contrast, in the WB estimators the desired signal component at 60 ° occurs as a straight line, but the grating lobe occurs as a curve. In consequence, by summing along the k-coordinate the power of the desired signal component will be collected into the $\alpha_\varphi = 60\,^\circ$ look direction bin. Due to the curved appearance of the grating lobe however, the power of the grating lobe is distributed across several spatial bins. Since the width of the main-lobe of the MVDR spectrum is much smaller that the width of the Bartlett spectrum, this effect is more pronounced for the MVDR beamformer. Based on this fundamental result

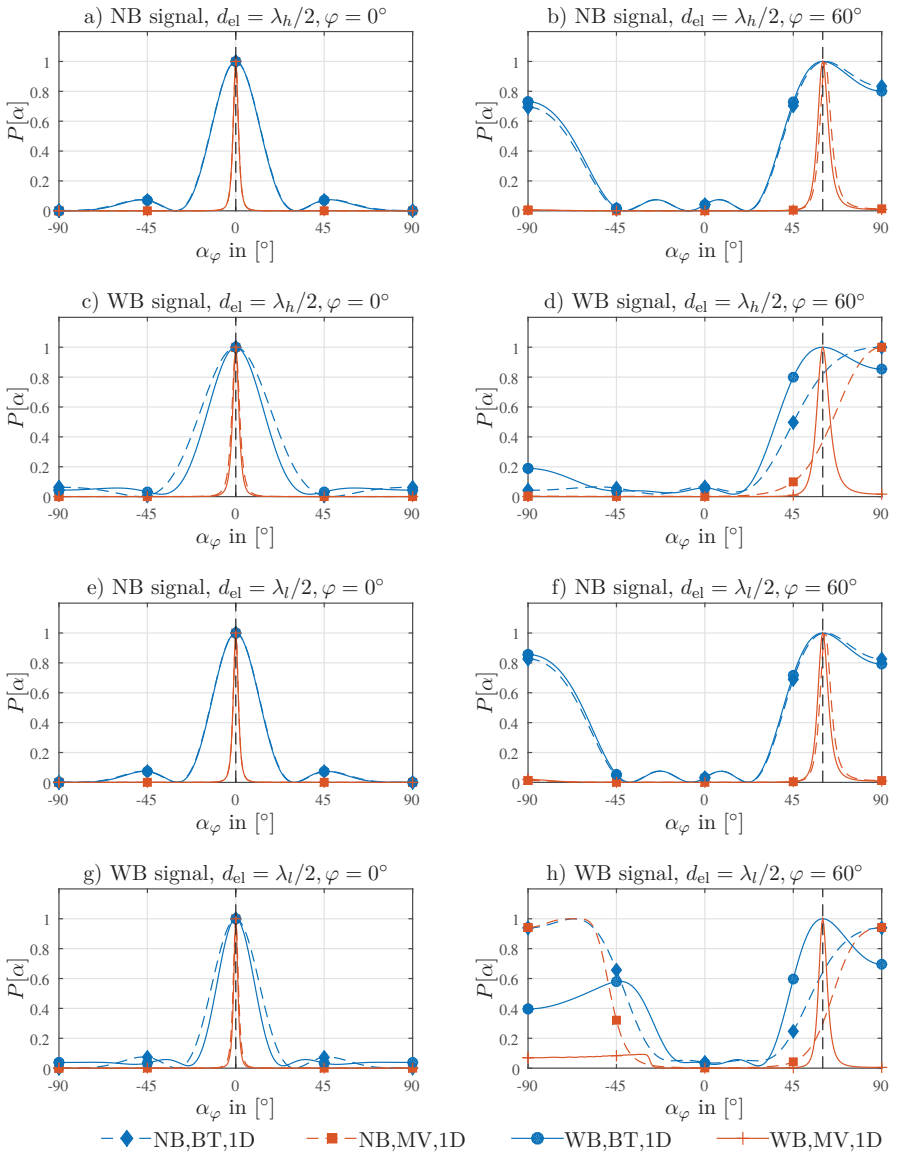

Fig. 3.8: Spatial spectra for ULA in NB and WB signal scenarios. Single signal impinging on uniform, 4-element linear array with element spacing a)-d) $\lambda_h/2$ and e)-h) $\lambda_l/2$. Spatial spectra obtained in a),b),e),f) NB and c),d),g),h) WB signal scenario from NB and WB Bartlett and MVDR DOA estimation algorithms. The true DOA is indicated by a dashed line. SNR is 30 dB and for the WB MVDR algorithms, the received data was subdivided into $P = 20$ frames.

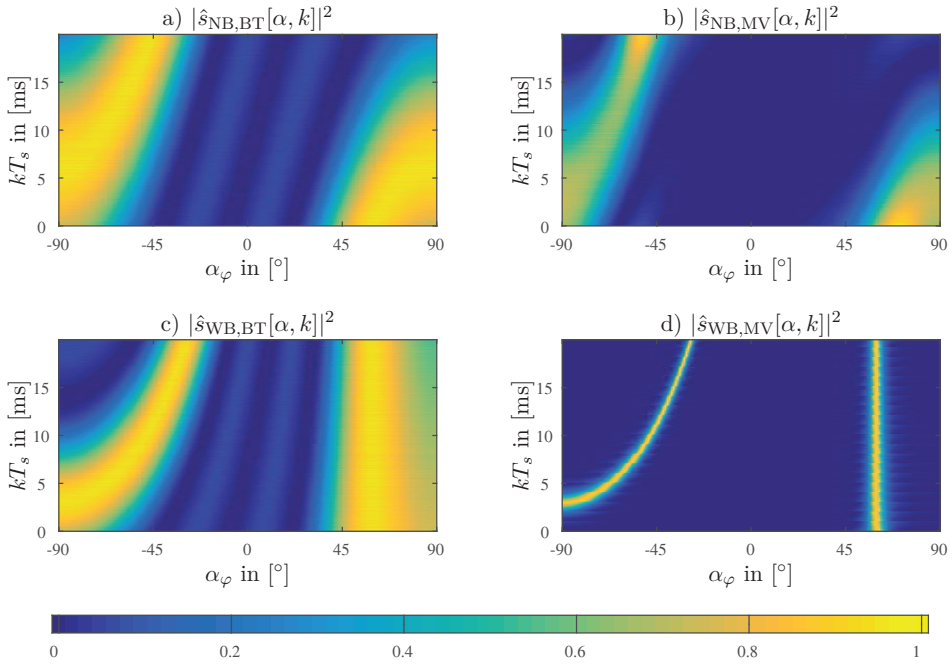

Fig. 3.9: Magnitude of spatially filtered signals obtained from NB (top) and WB (bottom) beamformers in WB signal scenario, normalized to maximum value. Single signal impinging on uniform, 4-element linear array with element spacing $\lambda_l/2$. Bartlett shown on the left and MVDR on the right.

that an element distance of $d_{\mathrm{el}} = \lambda_l/2$ is sufficient for ambiguity-free DOA estimation in UWB FMCW RADAR systems, in the remainder of this thesis this element distance will be used for the design of ULAs. The larger allowed element distance will be especially useful during the design of small UWB antenna arrays, where the size of the antenna elements becomes a major challenge.

The influence of the number of frames P used for estimation of the covariance matrix is shown in figure 3.10 where the number of frames is varied in the range $P = 1 \ldots 20$. Whereas in the low-SNR regime both side lobe level and main lobe width are dominated by the large SNR and hardly any dependence on P can be identified, it is clearly obvious that in the high-SNR regime the width of the main lobe gets narrower for increasing P and the performance of the WB MVDR algorithm improves. This can be reasoned since for a large P the individual frame covariance matrices better resem-

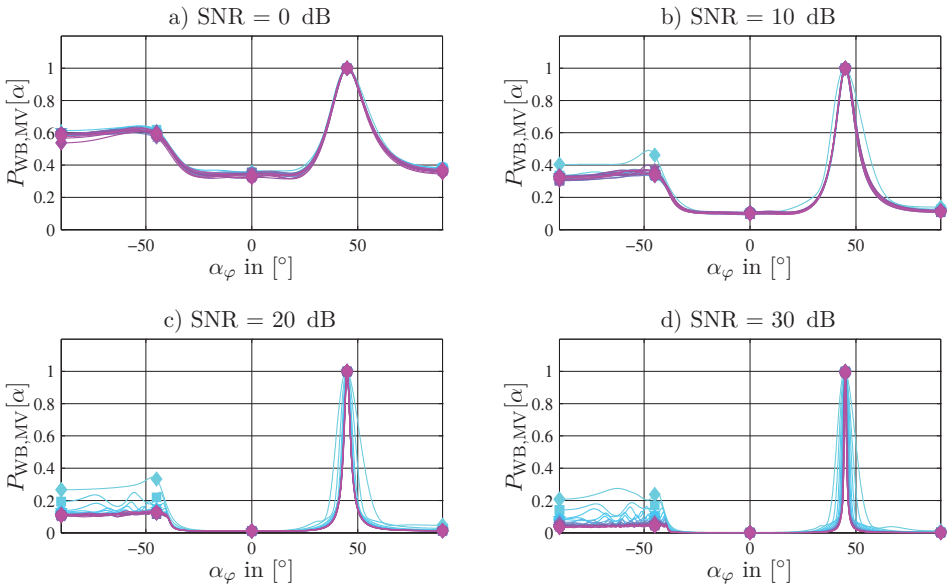

Fig. 3.10: Dependence of WB MVDR spatial spectra on number of frames. Single signal impinging on uniform, 4-element linear array with element spacing $\lambda_l/2$. Number of frames is $P = 1 \ldots 20$.

ble the NB approximation, i.e. the steering vector can be approximated as roughly constant during the frame. This behavior is even better illustrated by the spatially filtered signals shown in figure 3.11. It can clearly be seen from a) that without applying framing to $\underset{\sim}{\boldsymbol{X}}$ and estimating a single covariance matrix, relatively wide main-lobes result. This is due to the fact that the variation of the steering vector over the entire range spanned by $\underset{\sim}{\boldsymbol{X}}$ is large. In addition, the beam pattern drifts with respect to time. Subdividing $\underset{\sim}{\boldsymbol{X}}$ into $P = 20$ frames and estimating 20 individual covariance matrices for each frame the variation with time of the steering vector in each frame is low. Consequently the beam width remains favorably narrow and the maximum of the spatially filtered signal fixed at a certain look direction. The framing effect can clearly be seen from the periodic behavior in b): Indeed a pattern drift similar to the one observed in a) is present, but since $P = 20$ covariance matrices are used, the drift effect is reset beginning with each new frame and consequently the beam pattern remains stable.

The effect of the diagonal loading factor Δ_{DL} is illustrated in figure 3.12. If no loading is used, i.e. $\Delta_{\mathrm{DL}} = 0$, indeed the MVDR main peak in the spa-

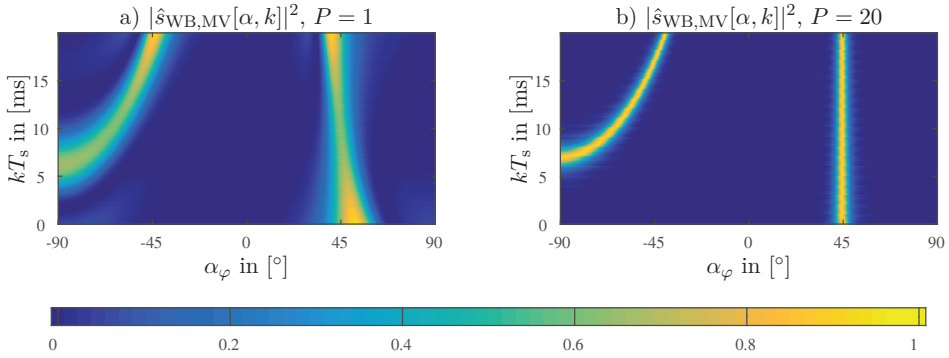

Fig. 3.11: Dependence of MVDR spatially filtered signals on number of frames, a) $P = 1$ and b) $P = 20$. Single signal impinging from $\varphi = 45°$ on 4-element ULA with element spacing $\lambda_l/2$, $SNR = 30\,\mathrm{dB}$.

tial spectrum is the narrowest obtained because the MVDR algorithms puts most effort in canceling the signal impinging from $\varphi = 45°$ when looking into directions $\alpha_\varphi \neq 45°$. Consequently also the grating lobe is maximal narrow and the ambiguity canceling effect is best. With increasing diagonal loading the main peak in the spatial spectrum gets wider and consequently also the ambiguity suppression effect is reduced. Hence diagonal loading reduces spatial resolution. In contrast, as can be seen from b), the larger the diagonal loading, the better the SNR in the range spectrum is. This is due to the fact that the weight vectors selected by the MVDR algorithm without diagonal loading may be selected such, that the spatially white noise present in $\underset{\sim}{\boldsymbol{X}}$ is increased in $\underset{\sim}{\boldsymbol{S}}$. This increase in noise then leads to a relatively large noise floor in the range spectrum. It can be seen that increasing the diagonal loading, the MVDR algorithm puts more effort into suppressing the spatially white noise, and the noise floor in the range spectrum decreases. Hence, a trade-off between spatial resolution and range-spectrum noise floor has to be made during selection of the diagonal loading factor. In the remainder of this thesis, $\Delta_{\mathrm{DL}} = 0.08/M$ is used, since it provides a good compromise.

3.5.1.2 Uniform Circular Array

The spatial spectra obtained from WB and NB Bartlett and MVDR algorithms for a single target at DOA $\varphi = 0°$ and $\varphi = 60°$ are shown in figure 3.13. Again the effect of element distance is examined first. Consequently, in a)-d) an

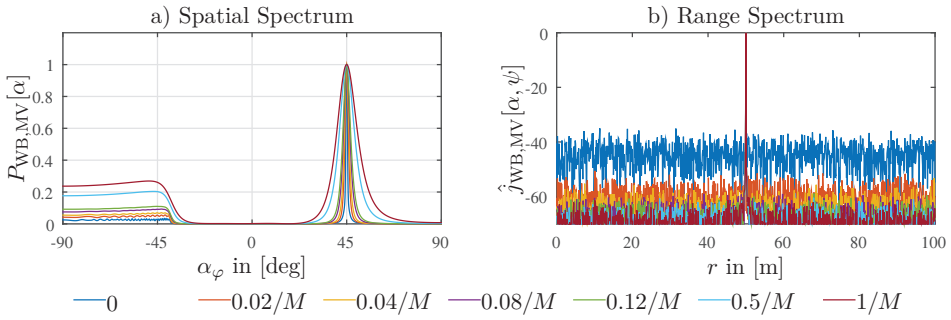

Fig. 3.12: Dependence of MVDR performance on diagonal loading factor Δ_{DL}, a) spatial spectrum and b) range spectrum. Single target at range $r = 50\,\mathrm{m}$ and DOA $\varphi = 45°$ on 4-element ULA with $d_{\mathrm{el}} = \lambda_l/2$. $SNR = 30\,\mathrm{dB}$

element spacing of $\lambda_h/2$ and for comparison in e)-h) an element spacing of $\lambda_l/2$ is used. For the UCA with element distance $d_{\mathrm{el}} = \lambda_h/2$ it can be seen that in the NB signal scenario both the WB and the NB DOA estimation algorithms show almost identical performance, where again the spatial resolution of the MVDR beamformer is superior to the Bartlett beamformer. Interestingly, for $\varphi = 0°$ the Bartlett beamformer shows two significant side-lobes at the look directions $\alpha_\varphi \approx \pm 122°$. This is an inherent property of the UCA, whose ambiguity function exhibits significant maxima for certain $\varphi_2 \neq \varphi_1$, if $\varphi_1 = 0°$. The closer the frequency f of the impinging signal to f_h, the larger the values of the ambiguity function are, compare figure 2.16 a) - c). Since in the NB signal scenario it can be assumed that $f \approx f_h$, it is clear that those large values of the ambiguity function can directly be observed in the spatial spectrum of the Bartlett beamformer shown in a). Since however this is not a true ambiguity, but only a certain look direction in which the steering vector is similar to the steering vector from another look direction, the MVDR algorithm is not influenced and no side-lobes are present in the MVDR spatial spectra. If the signal is impinging from $\varphi = 60°$ this effect is even more distinct, since the ambiguity function for the UCA has a very large value at $\varphi_2 \approx 150°$ for $\varphi_1 = 60°$. Hence, a large second peak exists in the Bartlett spatial spectrum shown in b) at look direction $\alpha_\varphi = 150°$. Again, it is not a true ambiguity but only a similarity and hence the MVDR algorithm is less influenced, but due to the large similarity also exhibits a peak at $\alpha_\varphi = 150°$.

In the WB signal scenario shown in c) and d) a difference of NB and WB

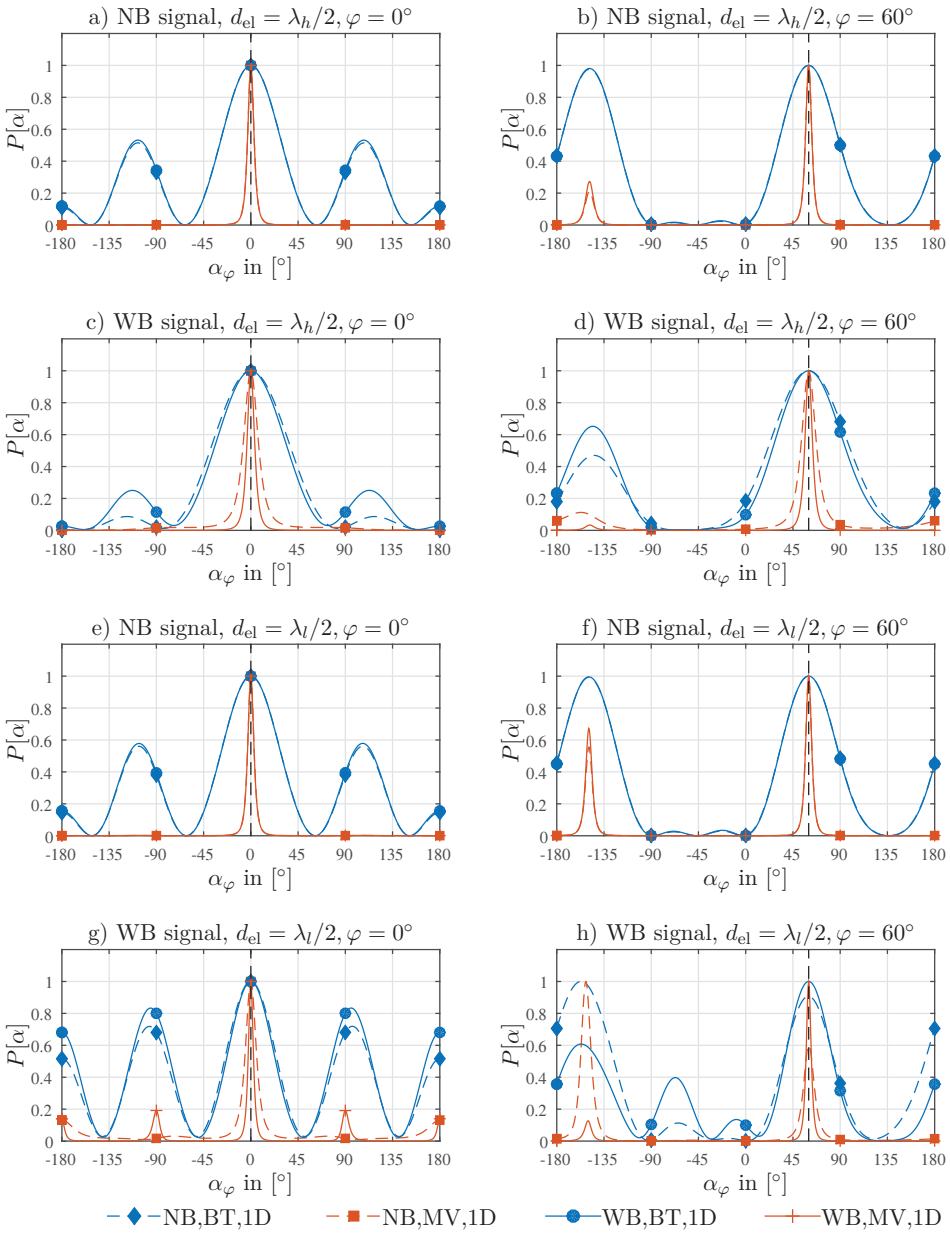

Fig. 3.13: Spatial spectra for UCA in NB and WB signal scenarios. Single signal impinging on uniform, 4-element circular array. Spatial spectra obtained in a),b),e),f) NB and c),d),g),h) WB signal scenario from NB and WB Bartlett and MVDR algorithms. The true DOA is indicated by a dashed line.

DOA estimation algorithms exists. Compared to the ULA the peak of the spatial spectrum remains stable also for the NB estimation algorithms. This effect is based on the WB properties of the UCA steering vectors, which already has been discussed in section 2.2.5. The performance of both, NB and WB algorithms is superior compared to the NB signal scenario. Especially the grating lobes are reduced, since their position as well as height in the spatially filtered signal $\underset{\sim}{\boldsymbol{S}}$ is frequency dependent, and hence reduced by the averaging operations (3.28) and (3.32) used to obtain the spatial spectrum.

The spatial spectra obtained from a UCA with element distance $d_{\text{el}} = \lambda_l/2$ are shown in 3.13 e) - f), for both the NB as well as WB signal scenarios. While the effects for the NB signal scenario are comparable to the results obtained from a UCA with $d_{\text{el}} = \lambda_h/2$, especially for $\varphi = 60°$ it can be seen that the increase in element distance leads to an increase in the grating lobe. Now, also the spatial spectrum obtained from the MVDR algorithm shows a significant second peak. A significant difference can be observed in the WB signal scenario. As previously explained for the UCA the position of the main peak in the spatial spectrum is indeed not influenced by the large bandwidth of the incident signal, but the number as well as height of the ambiguous peaks is. Interestingly, while all other algorithms show a relatively poor performance, for both incident angles the WB MVDR algorithm generates a single peak at a look direction α_φ corresponding to the true DOA. This behavior is again due to the narrow spectral response of the WB MVDR algorithm and the frequency-dependent position of ambiguities in $\underset{\sim}{\boldsymbol{S}}$, which leads to a suppression when calculating the spatial spectrum from the spatially filtered signal.

This averaging effect is again best illustrated considering the spatially filtered signals shown in figure 3.14. Although the ambiguities do not move change their position with time, as it was the case for the ULA, it can be seen from that their amplitude varies with frequency, i.e. with the time of the LFM sweep. Due to the high spatial resolution of the WB MVDR algorithm, the ambiguity approximately only has a non-negligible amplitude for $kT_s \leq 5\,\text{ms}$. Consequently, when computing the spatial spectrum its amplitude is reduced by a large amount due to the averaging effect of (3.32).

Based on the observations in this section, also for the ULA the further attention is limited to element distances of $d_{\text{el}} = \lambda_l/2$. In accordance with the observations made for the ULA, this is a fundamental result which greatly influences the design of UCAs for DOA estimation in FMCW RADAR systems.

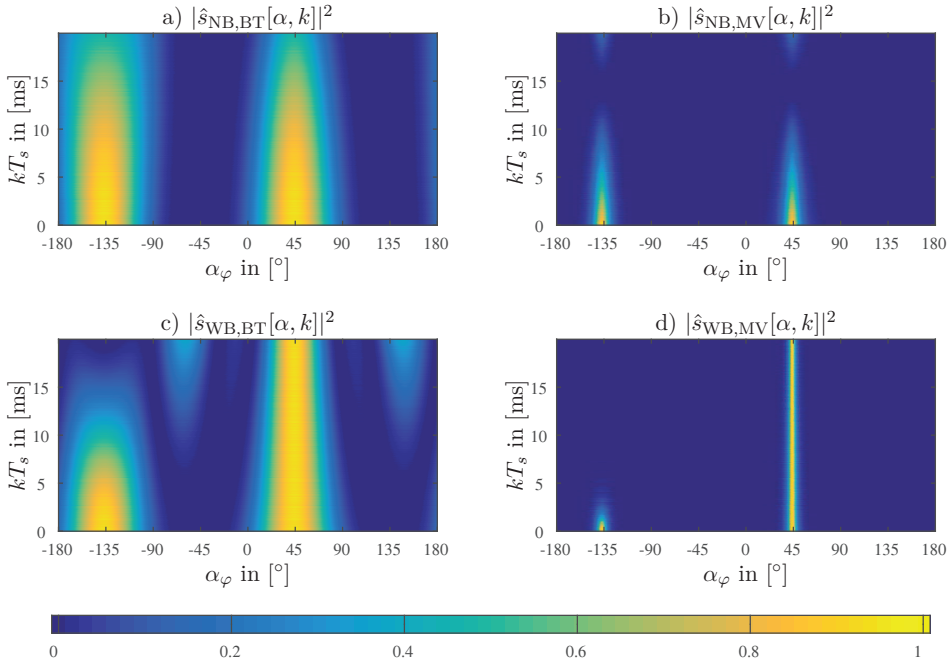

Fig. 3.14: Magnitude of spatially filtered signals obtained from NB (top) and WB (bottom) beamformers in WB signal scenario, normalized to maximum value. Single signal impinging 4-element UCA with element spacing $\lambda_l/2$. Bartlett shown on the left and MVDR on the right.

3.5.2 Statistical Analysis

3.5.2.1 Error Definition

The mean square error (MSE) of the estimator is used to measure the DOA and range finding accuracy. It is defined for the range and DOA estimates by

$$MSE\{\hat{\varphi}\} = \mathrm{E}\{|\hat{\varphi} - \varphi|^2\} \tag{3.42}$$

$$MSE\{\hat{r}\} = \mathrm{E}\{|\hat{r} - r|^2\}, \tag{3.43}$$

where r and φ are the true range and DOA, respectively. The MSE takes into account both, errors due to the bias of the estimator and the variance of the estimator. To estimate the performance of the combined range and angle estimation algorithms on a numerical basis, a Monte Carlo simulation with

L experiments is conducted and the MSE is estimated by

$$MSE\{\hat{\varphi}\} = \frac{1}{L}\sum_{l=1}^{L}|\hat{\varphi}[l]-\varphi|^2 + \left(\frac{\varphi_{\text{step}}}{2}\right)^2, \tag{3.44}$$

$$MSE\{\hat{r}\} = \frac{1}{L}\sum_{l=1}^{L}|\hat{r}[l]-r|^2 + \left(\frac{\Delta r}{2}\right)^2. \tag{3.45}$$

For the experiments, a very fine-resolution search grid is used and the true DOA as well as true range always exactly correspond to a certain search grid point. Consequently, the terms $\varphi_{\text{step}}/2$ and $\Delta r/2$ are used to estimate the worst-case MSE for the grid-search based estimation algorithms, when the true DOA or the true range lie in between two search grid points.

An algorithm independent benchmark against which estimation algorithms can be compared is provided by the CRLB, which provides a lower bound on the accuracy of any unbiased estimator [117]. The CRLB for estimating the frequency of a single cisoid is given in [118], [119]. Since $r = f^{\text{b}}c_0/\mu$ the variance of the range estimate $\hat{r}$ is given by

$$\text{var}(\hat{r}) \geq \frac{12}{SNR(2\pi)^2K(K^2-1)}\left(\frac{c_0 f_s}{\mu}\right)^2 \tag{3.46}$$

The CRLB in radians for an M-element linear array is given by [117]

$$\text{var}(\hat{\varphi}_{\text{ULA}}) \geq \frac{\lambda^2}{SNR\,8\pi^2K\cos^2(\varphi)\bar{y}[m]^2}. \tag{3.47}$$

Using the definition of the ULA element position from (2.62) $\bar{y}[m]^2$ can expressed in closed form as function of element distance d_{el} and number M of array elements

$$\bar{y}[m]^2 = \sum_{m=1}^{M} y[m]^2 = \frac{1}{12}\left({d_{\text{el}}}^2M^3 - d^2M\right). \tag{3.48}$$

The CRLB for an M-element circular array is given by [117]

$$\text{var}(\hat{\varphi}_{\text{UCA}}) \geq \frac{\lambda^2}{SNR\,8\pi^2KR^2\bar{c}^2} \tag{3.49}$$

where for a UCA it can be shown that $\bar{c}^2 = M/2$.

3.5.2.2 Uniform Linear Array

Figure 3.15 shows the MSE estimated using a Monte Carlo simulation with $L = 200$ trials obtained from a 4-element ULA with element spacing $d_{\text{el}} = \lambda_l/2$ in the WB RADAR signal scenario, for a target range of $r = 50\,\text{m}$. Plots a) and b) show the dependency of $MSE\{\hat{\varphi}\}$ on the SNR, for two different true DOAs of $\varphi = 0°$ and $\varphi = 80°$, respectively. For comparison also the CRLBs for a NB signal with $f = f_\text{l}$ and $f = f_\text{h}$ are plotted. It can be seen that the accuracy of the ULA is strongly dependent on the SNR and, especially in the low SNR regime, also strongly dependent on the true DOA. Both DOA estimation algorithms yield comparable performance and are close to the values predicted by the CRLB. The estimated MSE indicates, that the DOA accuracy can be slightly superior to the CRLB obtained from a NB signal with $f = f_\text{l}$, but as expected is always larger than the CRLB obtained for a NB signal with $f = f_\text{h}$. This may be dedicated to the fact, that the proposed DOA estimation algorithms take into account the whole bandwidth of the signal, but may also be an artifact due to the limited number of trails.

3.5.2.3 Uniform Circular Array

Figure 3.15 shows the MSE estimated using a Monte Carlo simulation with 200 trails obtained from a 4-element UCA with element distance $d_{\text{el}} = \lambda_l/2$, i.e. $R_{\text{UCA}} = \lambda_l/\sqrt{2}$ in the WB RADAR signal scenario, for a target a distance $r = 50\,\text{m}$. Due to the symmetry of the 4-element UCA its behavior is periodic with φ with a period of $90°$ and only a single period $\varphi = 0° \ldots 90°$ is shown in figure 3.15. The unique feature of the UCA, that the MSE of the DOA estimate is independent of the true DOA, is clearly obvious. Again the performance of both DOA estimators is close the the values predicted by the CRLB, where in the low SNR regime the performance is slightly better than the NB CRLB assuming a frequency of $f = f_\text{l}$ for the impinging signal. Of course, in all cases the performance is worse that the NB CRLB assuming a frequency of $f = f_\text{h}$ for the impinging signal.

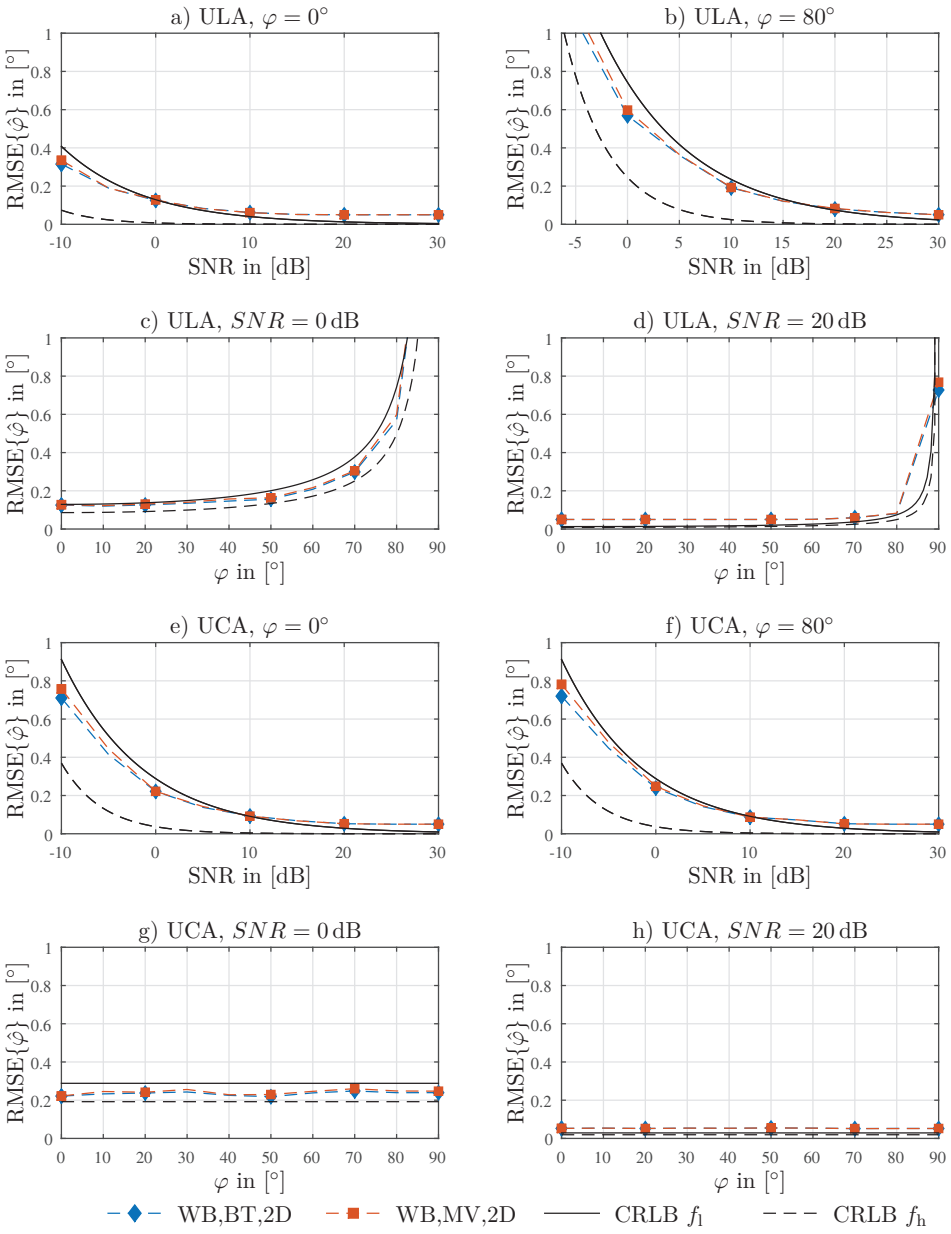

Fig. 3.15: Estimated root mean square error (RMSE) of DOA estimate $\hat{\varphi}$ using a) - d) ULA and e) - h) UCA for element spacing $d_\mathrm{el} = \lambda_l/2$ in WB signal scenario using the WB combined range and angle estimation algorithms. Target distance $d = 50\,\mathrm{m}$.

4 Characterization of Ultra-Wideband Antennas

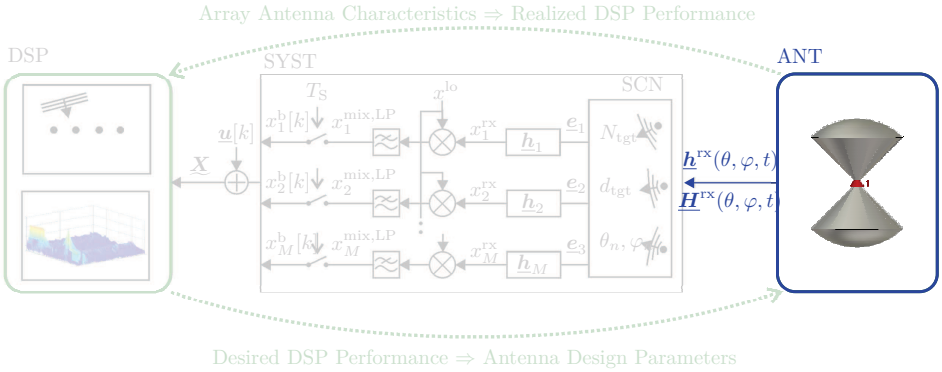

Fig. 4.1: Antenna model for FMCW RADAR systems.

In chapter 2 of this thesis models and signal definitions for the IF signal received in multi-channel wideband FMCW RADAR systems have been introduced. Subsequently in chapter 3 those models were used to define novel combined range and DOA estimation algorithms for wideband FMCW RADAR systems, to simulate the performance of those algorithms, and to show the improvements of using DOA estimation algorithms adopted to the wideband properties. It was assumed that the receiving sensors are of ideal and isotropic nature, and that they do not influence the received signals in any case. Beginning with this chapter, the ideal sensors are now replaced by models for the realistic UWB antennas.

In the field of antenna engineering an end-to-end transmission between two antennas is traditionally modeled using Friis transmission formula [10], which relates the transmitted power to the received power, depending on TX and RX antenna gains and the distance between both antennas. A slight modification, suitable for modeling the power received in primary RADAR systems is the well-known RADAR equation in it various forms [4], which models the received power in terms of transmit power, TX antenna gain, target RADAR cross section and target distance. However, both Friis trans-

mission formula as well as the RADAR equation are NB descriptions. Their application for modeling the influence of antennas onto WB LFMCW signals is limited.

With the emerging field of UWB systems, more attention was given to the matter of time-domain behavior of antennas and novel ways of characterizing antennas and modeling their transmitted and received signals became an active research topic. According to the state of the art, the far field characteristics of UWB antennas are modeled as LTI Systems, and antennas are treated as filters with spatially dependent impulse response, or transfer function, respectively. As illustrated in figure 4.2 this allows to model an UWB antenna link using a LTI system block model, while hiding the details of electromagnetic radiation. The key concepts for this modeling approach can be

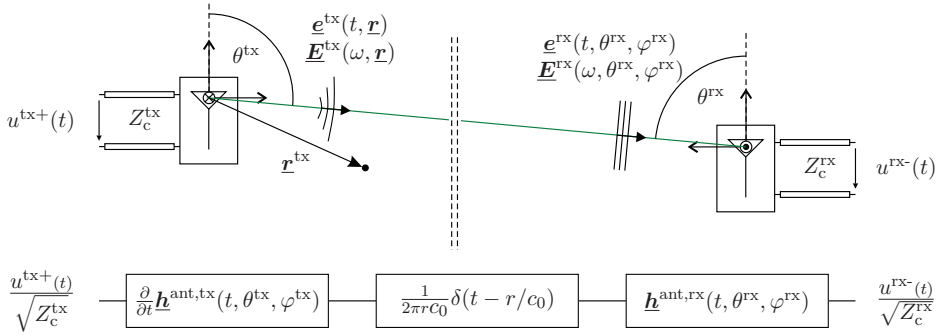

Fig. 4.2: UWB Antenna link and LTI system model. The TX antenna (left) radiates an electric field $\underline{\boldsymbol{e}}^{\mathrm{tx}}(t,\underline{\boldsymbol{r}})$, with its frequency domain representation $\underline{\boldsymbol{E}}^{\mathrm{tx}}(f,\underline{\boldsymbol{r}})$. Since TX and RX antenna are in the far field distance, the RX electric field $\underline{\boldsymbol{e}}^{\mathrm{rx}}(t,\theta^{\mathrm{rx}},\varphi^{\mathrm{rx}})$ with its frequency domain representation $\underline{\boldsymbol{E}}^{\mathrm{rx}}(f,\theta^{\mathrm{rx}},\varphi^{\mathrm{rx}})$ is a locally plane wave. This antenna link can be represented using a LTI system block model shown at the bottom.

found in the Ph.D. theses of Werner Soergel [44] and Stanislav Licul [43], several journal papers from the research group of Werner Wiesbeck [45], [46] as well as the key-paper of Shlivinsky [49].

It is easy to see that such an LTI model for antenna radiation and reception can be seamlessly integrated into the system model for UWB FMCW RADAR systems introduced in chapter 2. Since it is a fundamental prerequisite to understand the basic concepts of UWB antenna characterization and modeling, in this chapter the state-of-the-art concepts of UWB antenna characterization and modelling from [43]–[46], [49] are reviewed and where necessary

extended to fit in the modeling framework of this thesis.

4.1 Electromagnetic Theory of Time-Domain Radiation

Given a time-domain current density $\underline{\boldsymbol{j}}(t, \underline{\boldsymbol{r}'})$ defined over a source-volume V_s, such that $\underline{\boldsymbol{r}'} \in V_s$, e.g. the current density present on the surface of a metallic antenna, the retarded vector potential $\underline{\boldsymbol{a}}(t, \underline{\boldsymbol{r}})$ at any point $\underline{\boldsymbol{r}}$ in space $\mathbb{R}^3$ is given by [49]

$$\underline{\boldsymbol{a}}(t, \underline{\boldsymbol{r}}) = \mu_0 \iiint\limits_{V_s} \frac{\underline{\boldsymbol{j}}(\underline{\boldsymbol{r}'}, t - |\underline{\boldsymbol{r}} - \underline{\boldsymbol{r}'}|/c_0)}{4\pi|\underline{\boldsymbol{r}} - \underline{\boldsymbol{r}'}|} \, \mathrm{d}V_s. \tag{4.1}$$

This is illustrated in figure 4.3 The integration in (4.1) is conducted over the volume V_s with $\underline{\boldsymbol{r}'}$ being the integration variable. It is shown in [44] that far field conditions in the time-domain refer to distances $|\underline{\boldsymbol{r}}| >> 4r_A^2/c_0T'$, where r_A is the radius of a sphere enclosing the antenna and T' is the duration of the excitation impulse. In the far field equation (4.1) can be simplified to

$$\underline{\boldsymbol{a}}(t, \underline{\boldsymbol{r}}) = \frac{\mu_0}{4\pi r} \iiint\limits_{V_s} \underline{\boldsymbol{j}}(\underline{\boldsymbol{r}'}, t - r/c_0 + \hat{\underline{\boldsymbol{r}}} \cdot \underline{\boldsymbol{r}'}/c_0) \, \mathrm{d}V_s, \tag{4.2}$$

where $r = |\underline{\boldsymbol{r}}|$ and $\hat{\underline{\boldsymbol{r}}} = |\underline{\boldsymbol{r}}| / r$. Only delays with respect to the coordinate origin have to be taken into account. Once the vector potential has been computed from the current density using (4.1) or (4.2), the time-domain electric field $\underline{\boldsymbol{e}}(t, \underline{\boldsymbol{r}})$ can be expressed using only the vector potential $\underline{\boldsymbol{a}}(t)$ by [44]

$$\underline{\boldsymbol{e}}(t, \underline{\boldsymbol{r}}) = -\frac{\partial \underline{\boldsymbol{a}}(t, \underline{\boldsymbol{r}})}{\partial t} + \frac{1}{\epsilon_0 \mu_0} \int\limits_{t'=-\infty}^{t'=t} \text{grad div } \underline{\boldsymbol{a}}(t', \underline{\boldsymbol{r}}) \, \mathrm{d}t'. \tag{4.3}$$

For sufficiently large distances the relationship between vector potential $\underline{\boldsymbol{a}}$ and electric field $\underline{\boldsymbol{e}}$ then simplifies to [44]

$$\underline{\boldsymbol{e}}(t, \underline{\boldsymbol{r}}) = \hat{\underline{\boldsymbol{r}}} \times \left(\hat{\underline{\boldsymbol{r}}} \times \frac{\partial}{\partial t} \underline{\boldsymbol{a}}(t, \underline{\boldsymbol{r}}) \right), \tag{4.4}$$

i.e. $\underline{\boldsymbol{e}}(t, \underline{\boldsymbol{r}})$ can be calculated by the time-derivation of only the traversal components of $\underline{\boldsymbol{a}}$. Once $\underline{\boldsymbol{e}}(t, \underline{\boldsymbol{r}})$ is known, the radiated field is completely characterized, since radiated electric and magnetic fields are related by the free-space wave impedance Z_{F0}, which approximately is $Z_{\mathrm{F0}} \approx 377\Omega$ in vacuum.

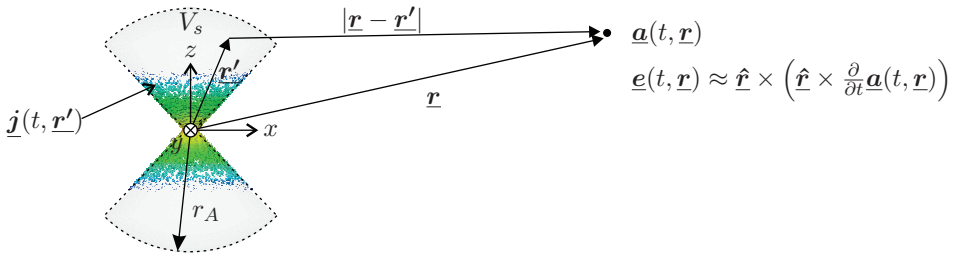

Fig. 4.3: Integration over the time-domain current density $\underline{j}(t,\underline{r}')$ yields the time-domain vector potential $\underline{a}(t,\underline{r})$ at any point $\underline{r}$ in space. For sufficiently large distances $|\underline{r}| >> r_A$ from the radiating current density, the electric field $\underline{e}(t,\underline{r})$ can be found by a time-derivative of the vector potential, only using the transverse components.

4.2 Transmit Antenna

The current density $\underline{j}(t,\underline{r}')$ on the antenna can be modeled as directly proportional to the excitation of the antenna on the antenna feed line. On the TX side, the electric field component of the radiated far field is modeled as inhomogeneous spherical wave $\underline{e}^{\text{tx}}(t,\underline{r}^{\text{tx}})$ emerging from the origin of the TX antenna reference coordinate system and propagating in a non-dispersive medium, as shown in figure 4.2. Its spatial dependency is given by the position vector in the TX antennas coordinate system $\underline{r}^{\text{tx}} = [\rho^{\text{tx}}, \theta^{\text{tx}}, \varphi^{\text{tx}}]^{\intercal}$, where $\rho^{\text{tx}} = r$ may be used alternatively. According to [44], [45] this transient electric far field $\underline{e}^{\text{tx}}$(t) radiated by an antenna is related to the voltage amplitude wave $u^{\text{tx+}}(t)$ incident on its terminal by

$$\frac{\underline{e}^{\text{tx}}(t,\underline{r}^{\text{tx}})}{\sqrt{Z_{\text{F0}}}} = \frac{1}{r}\delta(t - r/c_0) * \underline{o}^{\text{tx}}(t,\theta^{\text{tx}},\varphi^{\text{tx}}) * \frac{u^{\text{tx+}}(t)}{\sqrt{Z_{\text{c}}^{\text{tx}}}}. \tag{4.5}$$

The antenna TX mode is hence completely characterized by the transient function $\underline{o}^{\text{tx}}(t,\theta^{\text{tx}},\varphi^{\text{tx}})$, which is referred to as the tiem-domain antenna transmit factor. Since the electric field is measured in $[\underline{e}^{\text{tx}}] = [\text{V/m}]$ and the voltage in $[u^{\text{tx+}}] = [\text{V}]$, it follows that $[\underline{o}^{\text{tx}}] = [1/\text{s}]$ and in this context $[\delta(t - r/c_0)] = [1/\text{s}]$. The path loss of the radiated field is captured by the factor $1/r$ and the non-dispersive propagation with velocity c_0 is captured by the time retardation factor $\delta(t - r/c_0)$. The antenna transmit factor takes into account the directional dependency of the radiated field by its arguments θ^{tx} and φ^{tx} and determines polarization, as well as shape of

the radiated transient waveform. Since the far field of the antenna is purely transversal electro-magnetic (TEM) [44], the antenna transmit factor can be represented as a 2D vector with a basis orthogonal to $\underline{\boldsymbol{r}}$. Most conveniently, this can be done by using the basis vectors $\underline{\boldsymbol{\theta}}^{\mathrm{tx}}$ and $\underline{\boldsymbol{\varphi}}^{\mathrm{tx}}$ of the TX antenna's local reference coordinate system

$$\underline{\boldsymbol{o}}^{\mathrm{tx}}(t,\theta^{\mathrm{tx}},\varphi^{\mathrm{tx}}) = \underline{\boldsymbol{\theta}}^{\mathrm{tx}} \cdot o_{\theta}^{\mathrm{tx}}(t,\theta^{\mathrm{tx}},\varphi^{\mathrm{tx}}) + \underline{\boldsymbol{\varphi}}^{\mathrm{tx}} \cdot o_{\varphi}^{\mathrm{tx}}(t,\theta^{\mathrm{tx}},\varphi^{\mathrm{tx}}). \tag{4.6}$$

By inserting (4.2) into (4.4) and (4.5) and then solving for $\underline{\boldsymbol{o}}^{\mathrm{tx}}(t,\theta^{\mathrm{tx}},\varphi^{\mathrm{tx}})$, it is shown in [44] that the antenna transmit factor is defined in terms of

$$\underline{\boldsymbol{o}}^{\mathrm{tx}}(t,\underline{\boldsymbol{r}}) = -\frac{\mu_0}{4\pi}\sqrt{\frac{Z_{\mathrm{c}}^{\mathrm{tx}}}{Z_{\mathrm{F0}}}}\frac{\partial}{\partial t}\iiint\limits_{V} \underline{\boldsymbol{j}}_{||}^{\delta}(\underline{\boldsymbol{r}}', t - r/c_0 + \hat{\underline{\boldsymbol{r}}} \cdot \underline{\boldsymbol{r}}'/c_0)\,\mathrm{d}V_S, \tag{4.7}$$

where $\underline{\boldsymbol{j}}_{||}^{\delta}$ refers to the transverse component of the current density relative to the observation direction $\hat{\underline{\boldsymbol{r}}}$ if the antenna is excited with a ideal Dirac excitation pulse [49]. Using the properties and correspondences of the Fourier transform, equation (4.5) can equivalently be expressed in frequency domain

$$\frac{\underline{\boldsymbol{E}}^{\mathrm{tx}}(\omega,\underline{\boldsymbol{r}}^{\mathrm{tx}})}{\sqrt{Z_{\mathrm{F0}}}} = \frac{1}{r}\underline{\boldsymbol{O}}^{\mathrm{tx}}(\omega,\theta^{\mathrm{tx}},\varphi^{\mathrm{tx}})\frac{U^{\mathrm{tx+}}(\omega)}{\sqrt{Z_{\mathrm{c}}^{\mathrm{tx}}}}e^{-\mathrm{j}\omega\frac{r}{c_0}}, \tag{4.8}$$

where the time-retardation is now represented by the linear phase decay $e^{-\mathrm{j}\omega\frac{r}{c_0}}$. The units are now given by $[\underline{\boldsymbol{E}}^{\mathrm{tx}}] = [\mathrm{V}/(\mathrm{m\,Hz})]$ and $[U^{\mathrm{tx+}}] = [\mathrm{V}/\mathrm{Hz}]$. Consequently the frequency-domain antenna transmit factor becomes dimensionless $[\underline{\boldsymbol{O}}^{\mathrm{tx}}] = [1]$.

The voltage wave $U^{\mathrm{tx+}}$ incident on the TX antenna will, however, not only be the cause of a radiated field, but a certain part of it will be reflected since the antenna impedance may not perfectly match the reference impedance $Z_{\mathrm{c}}^{\mathrm{tx}}$. The relationship between incident and reflected voltage waves is typically quantized in frequency domain by the scattering parameter theory [120]. Therefore the voltage waves are represented by power waves a^{tx} incident and b^{tx} reflected from the antenna terminals using

$$a^{\mathrm{tx}} = U^{\mathrm{tx+}}/\sqrt{Z_{\mathrm{c}}^{\mathrm{tx}}}, \tag{4.9}$$

$$b^{\mathrm{tx}} = U^{\mathrm{tx-}}/\sqrt{Z_{\mathrm{c}}^{\mathrm{tx}}}. \tag{4.10}$$

The power waves are then related by

$$b^{\mathrm{tx}}(\omega) = S_{11}(\omega)a^{\mathrm{tx}}(\omega). \tag{4.11}$$

In the particular case of the TX antenna, where both power waves are referred to the same characteristic impedance, it is easy to see that (4.11) corresponds to $U^{\text{tx-}} = S_{11}U^{\text{tx+}}$. The squared magnitude of S_{11} is also referred to as the return loss, since it characterizes how much power of the wave incident on the antenna terminal is reflected and hence cannot be radiated. Neglecting the ohmic losses of the antenna in a first approximation, it is the return loss which defines how efficiently the antenna radiates. Since the antenna transmit factor is referenced to the incident voltage wave, it is obvious that the larger the the return loss, the lower the magnitude of the antenna transmit factor will be. The antenna will become a less efficient radiator. Typically an antenna is considered to be well-matched if the return loss is below –10 dB.

4.3 Receive Antenna

For far field conditions, it can be assumed that a plane wave $\underline{\boldsymbol{e}}^{\text{rx}}$ is incident onto the receive antenna [51], compare figure 4.2. The voltage wave leaving the antenna terminal is then given by [44], [45]

$$\frac{u^{\text{rx-}}(t)}{\sqrt{Z_{\text{c}}^{\text{rx}}}} = \underline{\boldsymbol{h}}^{\text{rx}}(t, \theta^{\text{rx}}, \varphi^{\text{rx}}) * \frac{\underline{\boldsymbol{e}}^{\text{rx}}(t, \theta^{\text{rx}}, \varphi^{\text{rx}})}{\sqrt{Z_{\text{F0}}}}, \tag{4.12}$$

where Z_{c}^{rx} is the characteristic impedance on RX side, Z_{F0} is the wave impedance of free space, and $[\underline{\boldsymbol{h}}^{\text{rx}}] = [\text{m/s}]$. The antenna receiving mode is completely characterized by the transient response $\underline{\boldsymbol{h}}^{\text{rx}}(t, \theta^{\text{rx}}, \varphi^{\text{rx}})$, also referred to as antenna impulse response. Similar to the antenna time-domain transmit factor, the antenna impulse response is a 2D vector with components orthogonal to direction of wave propagation and can conveniently be expressed in terms of the basis vectors $\underline{\boldsymbol{\theta}}^{\text{rx}}$ and $\underline{\boldsymbol{\varphi}}^{\text{rx}}$ of the RX antenna local reference coordinate system

$$\underline{\boldsymbol{h}}^{\text{rx}}(t, \theta^{\text{rx}}, \varphi^{\text{rx}}) = \underline{\boldsymbol{\theta}}^{\text{rx}} \cdot h_{\theta}^{\text{rx}}(t, \theta^{\text{rx}}, \varphi^{\text{rx}}) + \underline{\boldsymbol{\varphi}}^{\text{rx}} \cdot h_{\varphi}^{\text{rx}}(t, \theta^{\text{rx}}, \varphi^{\text{rx}}). \tag{4.13}$$

To evaluate (4.12), both the incident field $\underline{\boldsymbol{e}}^{\text{rx}}$ and the normalized antenna effective height $\underline{\boldsymbol{h}}^{\text{rx}}$ have to be defined in the RX antennas reference coordinate system. Then the convolution operator in (4.12) reduces to

$$\underline{\boldsymbol{h}}^{\text{rx}} * \underline{\boldsymbol{e}}^{\text{rx}} = h_{\theta}^{\text{rx}} * e_{\theta}^{\text{rx}} + h_{\varphi}^{\text{rx}} * e_{\varphi}^{\text{rx}}. \tag{4.14}$$

Equation (4.12) can also be expressed in frequency domain

$$\frac{U^{\text{rx-}}(\omega)}{\sqrt{Z_{\text{c}}^{\text{rx}}}} = \underline{\boldsymbol{H}}^{\text{ant}}(\omega, \theta^{\text{rx}}, \varphi^{\text{rx}}) \frac{\underline{\boldsymbol{E}}^{\text{rx}}(\omega, \theta^{\text{rx}}, \varphi^{\text{rx}})}{\sqrt{Z_{\text{F0}}}}, \tag{4.15}$$

where $\underline{\boldsymbol{H}}^{\text{ant}}$ is referred to as the antenna normalized effective height with $[\underline{\boldsymbol{H}}^{\text{ant}}] = [\text{m}]$. The product of both vectorial-valued functions in 4.15 is defined in terms of a scalar product and reduced to

$$\underline{\boldsymbol{H}}^{\text{ant}} \underline{\boldsymbol{E}}^{\text{rx}} = H_{\theta}^{\text{rx}} E_{\theta}^{\text{rx}} + H_{\varphi}^{\text{rx}} E_{\varphi}^{\text{rx}}. \tag{4.16}$$

4.4 Lorentz Reciprocity

Applying the time-domain Lorentz reciprocity theorem [49], the time-domain antenna transmit factor $\underline{\boldsymbol{o}}^{\text{tx}}$ of the TX antenna can be related to the antenna impulse response $\underline{\boldsymbol{h}}^{\text{tx}}$ of the TX antenna by [44], [45]

$$\underline{\boldsymbol{o}}^{\text{tx}} = \frac{1}{2\pi c_0} \frac{\partial}{\partial t} \underline{\boldsymbol{h}}^{\text{tx}}. \tag{4.17}$$

The need for the time derivative in (4.17) can also explained from an intuitive perspective: Applying a static electric field to an antenna will result in a non-zero voltage observed across its terminals. But applying a static voltage at the terminals of an antenna will indeed lead to a certain non-zero static electric near field close to the antenna, but the antenna will not radiate and no field will be observed in the far-zone. The time-derivative included in the antenna transmit factor ensures that for any static excitation $u^{\text{tx+}}$ the far fields given by equations (4.5) and (4.8) will be zero. Equation (4.17) can also be expressed in frequency domain

$$\underline{\boldsymbol{O}}^{\text{tx}} = \frac{\text{j}\omega}{2\pi c_0} \underline{\boldsymbol{H}}^{\text{tx}}. \tag{4.18}$$

Using (4.17) and (4.18), the electric field radiated from an antenna in time (4.5) or frequency domain (4.8) can also be expressed in terms of voltage wave $u^{\text{tx+}}$ incident on antenna terminal and antenna impulse response or normalized effective height, respectively

$$\frac{\underline{\boldsymbol{e}}^{\text{tx}}(t, r, \theta^{\text{tx}}, \varphi^{\text{tx}})}{\sqrt{Z_{\text{F0}}}} = \frac{1}{r} \frac{1}{2\pi c_0} \delta(t - r/c_0) * \frac{\partial}{\partial t} \underline{\boldsymbol{h}}^{\text{tx}}(t, \theta^{\text{tx}}, \varphi^{\text{tx}}) * \frac{u^{\text{tx+}}(t)}{\sqrt{Z_{\text{c}}^{\text{tx}}}}, \tag{4.19}$$

$$\frac{\underline{\boldsymbol{E}}^{\text{tx}}(\omega, r, \theta^{\text{tx}}, \varphi^{\text{tx}})}{\sqrt{Z_{\text{F0}}}} = \frac{1}{r} \frac{\text{j}\omega}{2\pi c_0} \underline{\boldsymbol{H}}^{\text{tx}}(\omega, \theta^{\text{tx}}, \varphi^{\text{tx}}) \frac{U^{\text{tx+}}(\omega)}{\sqrt{Z_{\text{c}}^{\text{tx}}}} e^{-\text{j}\omega \frac{r}{c_0}}. \tag{4.20}$$

Since antenna transmit factor and antenna normalized effective height are related by (4.18), it is obvious that the return loss also can be used to determine how efficiently an antenna will receive.

4.5 Free Space UWB Antenna Link

Assuming the origins of both antenna reference coordinate systems to be separated by a distance of r and an ideal channel, i.e. $\underline{\boldsymbol{E}}^{\mathrm{rx}}(t,\theta^{\mathrm{rx}},\varphi^{\mathrm{rx}}) = \underline{\boldsymbol{E}}^{\mathrm{tx}}(t,r,\theta^{\mathrm{tx}},\varphi^{\mathrm{tx}})$, and combining (4.8) and (4.15) or (4.5) and (4.12), respectively, the voltage wave leaving the RX antenna can directly be related to the voltage wave incident on the TX antenna terminal. Expressed in frequency domain this yields

$$U^{\mathrm{rx-}}(\omega) = \frac{\sqrt{Z_{\mathrm{c}}^{\mathrm{rx}}}}{\sqrt{Z_{\mathrm{c}}^{\mathrm{tx}}}} \frac{\mathrm{j}\omega}{2\pi r c_0} \underline{\boldsymbol{H}}^{\mathrm{rx}}(\omega,\theta^{\mathrm{rx}},\varphi^{\mathrm{rx}}) \underline{\boldsymbol{H}}^{\mathrm{tx}}(\omega,\theta^{\mathrm{tx}},\varphi^{\mathrm{tx}}) e^{-\mathrm{j}\omega\frac{r}{c_0}} U^{\mathrm{tx+}}(\omega). \quad (4.21)$$

Both antenna normalized effective heights functions are defined in the corresponding local reference coordinate systems of TX and RX antenna, respectively. They can be expressed by

$$\underline{\boldsymbol{H}}^{\mathrm{tx}} = \underline{\boldsymbol{\theta}}^{\mathrm{tx}} H_\theta^{\mathrm{tx}} + \underline{\boldsymbol{\varphi}}^{\mathrm{rx}} H_\varphi^{\mathrm{tx}}, \quad (4.22)$$

$$\underline{\boldsymbol{H}}^{\mathrm{rx}} = \underline{\boldsymbol{\theta}}^{\mathrm{rx}} H_\theta^{\mathrm{rx}} + \underline{\boldsymbol{\varphi}}^{\mathrm{rx}} H_\varphi^{\mathrm{rx}}. \quad (4.23)$$

The scalar product of the antenna normalized effective heights is then given by

$$\begin{aligned} \underline{\boldsymbol{H}}^{\mathrm{tx}} \underline{\boldsymbol{H}}^{\mathrm{rx}} =& (\underline{\boldsymbol{\theta}}^{\mathrm{tx}} \underline{\boldsymbol{\theta}}^{\mathrm{rx}})(H_\theta^{\mathrm{tx}} H_\theta^{\mathrm{rx}}) \\ &+ (\underline{\boldsymbol{\varphi}}^{\mathrm{tx}} \underline{\boldsymbol{\theta}}^{\mathrm{rx}})(H_\varphi^{\mathrm{tx}} H_\theta^{\mathrm{rx}}) \\ &+ (\underline{\boldsymbol{\theta}}^{\mathrm{tx}} \underline{\boldsymbol{\varphi}}^{\mathrm{rx}})(H_\theta^{\mathrm{tx}} H_\varphi^{\mathrm{rx}}) \\ &+ (\underline{\boldsymbol{\theta}}^{\mathrm{tx}} \underline{\boldsymbol{\varphi}}^{\mathrm{rx}})(H_\varphi^{\mathrm{tx}} H_\varphi^{\mathrm{rx}}). \end{aligned} \quad (4.24)$$

Reviewing 2.4, where it was shown that if the z-axes of both coordinate systems are indentical it follows that $\underline{\boldsymbol{\theta}}^{\mathrm{tx}} \underline{\boldsymbol{\theta}}^{\mathrm{rx}} = 1$, $\underline{\boldsymbol{\varphi}}^{\mathrm{tx}} \underline{\boldsymbol{\theta}}^{\mathrm{rx}} = 0$, $\underline{\boldsymbol{\theta}}^{\mathrm{tx}} \underline{\boldsymbol{\varphi}}^{\mathrm{rx}} = 0$,$\underline{\boldsymbol{\varphi}}^{\mathrm{tx}} \underline{\boldsymbol{\varphi}}^{\mathrm{rx}} = -1$ and consequently

$$\underline{\boldsymbol{H}}^{\mathrm{tx}} \underline{\boldsymbol{H}}^{\mathrm{rx}} = H_\theta^{\mathrm{tx}} H_\theta^{\mathrm{rx}} - H_\varphi^{\mathrm{tx}} H_\varphi^{\mathrm{rx}}. \quad (4.25)$$

In time-domain the free-space UWB antenna link can be expressed by

$$u^{\text{rx-}}(t) = \frac{\sqrt{Z_{\text{c}}^{\text{rx}}}}{\sqrt{Z_{\text{c}}^{\text{tx}}}} \frac{1}{2\pi r c_0} \Big[\frac{\partial}{\partial t} \underline{\boldsymbol{h}}^{\text{tx}}(t, \theta^{\text{tx}}, \varphi^{\text{tx}}) \\ * \delta(t - r/c_0) * \underline{\boldsymbol{h}}^{\text{rx}}(t, \theta^{\text{rx}}, \varphi^{\text{rx}}) \Big] * u^{\text{tx+}}(t), \quad (4.26)$$

where the convolution of both antenna impulse responses is interpreted in terms of a scalar product similar to (4.24)

$$\begin{aligned} \underline{\boldsymbol{h}}^{\text{tx}} * \underline{\boldsymbol{h}}^{\text{rx}} =& (\underline{\boldsymbol{\theta}}^{\text{tx}} \underline{\boldsymbol{\theta}}^{\text{rx}})(h_\theta^{\text{tx}} * h_\theta^{\text{rx}}) \\ &+ (\underline{\boldsymbol{\varphi}}^{\text{tx}} \underline{\boldsymbol{\theta}}^{\text{rx}})(h_\varphi^{\text{tx}} * h_\theta^{\text{rx}}) \\ &+ (\underline{\boldsymbol{\theta}}^{\text{tx}} \underline{\boldsymbol{\varphi}}^{\text{rx}})(h_\theta^{\text{tx}} * h_\varphi^{\text{rx}}) \\ &+ (\underline{\boldsymbol{\theta}}^{\text{tx}} \underline{\boldsymbol{\varphi}}^{\text{rx}})(h_\varphi^{\text{tx}} * h_\varphi^{\text{rx}}). \end{aligned} \quad (4.27)$$

A simplification similar to (4.25) can be used if the z-axes of the local antenna coordinate systems are assumed to be identical.

Although given for free-space propagation, this end-to-end model for the transmission between two antennas can easily be extended to take into account the effects of the propagation channel. This is typically done by using a polarimetric channel matrix for relating transmitted and received signals. For details, the reader is referred to [44].

4.6 Relationship to Classical Antenna Parameters

As shown in [44], traditionally known antenna parameters can be derived from the antenna normalized effective height $\underline{\boldsymbol{H}}^{\text{ant}}$. The realized gain of the antenna is thus given by

$$G = \frac{\omega^2}{\pi c_0^2} |\underline{\boldsymbol{H}}^{\text{ant}}|^2, \quad (4.28)$$

and the IEEE gain, which does not take into account the return loss due to antenna impedance mismatch, is related to (4.28) by

$$G_{\text{IEEE}} = \frac{G}{(1 - |S_{11}|^2)}. \quad (4.29)$$

From (4.28), the effective height of an ideal isotropic antenna with a gain of 0 dBi can easily be derived

$$H^{\text{id.}} = \sqrt{\frac{\pi c_0^2}{\omega^2}}. \tag{4.30}$$

Consequently, the transmit factor of the ideal isotropic antenna is

$$O^{\text{tx,id.}} = \frac{1}{2\sqrt{\pi}}. \tag{4.31}$$

4.7 Obtaining the Normalized Effective Antenna Height

4.7.1 By Electromagnetic Simulations

Several techniques exist for numerically simulating the electromagnetic behavior of structures. Those methods are referred to as CEM in this thesis. Since a detailed discussion of CEM would be beyond the scope of this work, the reader is referred to [121] for an introduction to computational methods for RF and microwave engineering. For UWB systems, it has been shown that one preferred method is the finite integration technique (FIT) [122], [123], which is a time-domain technique. Generally, the FIT is based on reducing the simulation domain to a bounded volume, often referred to as the *bounding box*, then spatially discretizing the integral form of Maxwell's equations by subdividing the simulation domain contained in the bounding box into mesh cells. The simulation structure is then excited with a time-domain impulse like waveform at certain predefined mesh cells (the so called excitation ports), and finally it is solved for the electric voltages at the edges of each mesh cell as well as for the magnetic fluxes on the faces of each mesh cell for succeeding discrete time instances. The simulation typically continues until the energy contained in the simulation volume has decreased below a certain threshold value. This decrease occurs since energy might be radiated by the structure, dissipated by loss materials, or absorbed by another excitation port contained in the simulation domain. Then the FIT algorithms terminates, and all time-domain fields within the bounding box as well as excitation port signals are supplied as simulation results to the user. By post-processing those direct time-domain FIT results, more intuitive characteristics can be derived. Typically, e.g. the time-domain simulation results observed at the excitation ports are transformed to frequency

domain using a FFT, and by then relating incident and leaving voltages classical measures such as the scattering parameters can be derived. The far field radiation characteristics of the structure can e.g. be computed by evaluating the simulated fields on the closed bounding box of the simulation domain and applying a near-field (FF) to far-field (FF) transform of the data.

A commercial CEM package implementing the FIT is the time-domain solver of computer simulation technology (CST) microwave studio (MWS), which is used for all CEM simulations in this thesis. CST MWS further includes a user interface for graphical modeling and computer aided design, a large collection of simulation data post-processing capabilities, as well as a graphical interface for displaying the simulation results. In addition, an application programming interface (API) is provided which allows to access the functionality of CST MWS by external programs. A simulation run of the time-domain solver from CST MWS starts by exciting the excitation port with an incident voltage wave $u^+(t)$. Typically, this port is defied at the mesh cell of the antenna feed point, such as in the illustration of simulating a Dipole provided in figure 4.4, or the simulation of a bicone antenna as illustrated in figure 4.5. The shape of the excitation waveform can be arbitrary, but typically a Gaussian impulse is selected, such that the spectral density of the excitation signal covers the desired simulation frequency range. An example excitation pulse is shown in figure 4.4 a). Then, as mentioned above, the time-domain solver calculates the propagation of the excitation signal through the simulation volume by evaluating the electric fields and magnetic fluxes at each mesh cell at discrete time-steps. Simultaneously, the voltage wave u^-(t), which is reflected from the excitation port is calculated, as illustrated in figure 4.4 b). In CST MWS per definition the signal of excitation ports (for discrete and waveguide ports) is normalized such that the port realizes an input power of 1 W peak power. Thus, precisely speaking the excitation signal at the port is the incident voltage u^+(t) divided by the square root of the characteristic impedance Z^c. Correspondingly, the signal leaving the excitation port is the voltage u^-(t) divided by the square root of the characteristic impedance Z^c. Note that this means, when accessing port signals from CST MWS simulations, always the quotient $u^+(t)/Z^c$ or $u^-(t)/Z^c$, respectively, is returned. This definition corresponds to the definition of power waves from (4.10) or as found in classical scattering matrix network theory [120]. If several ports are defined in the simulation domain then typically one simulation is performed for a single port being excited, while all other ports only record the voltage waves leaving it terminals.

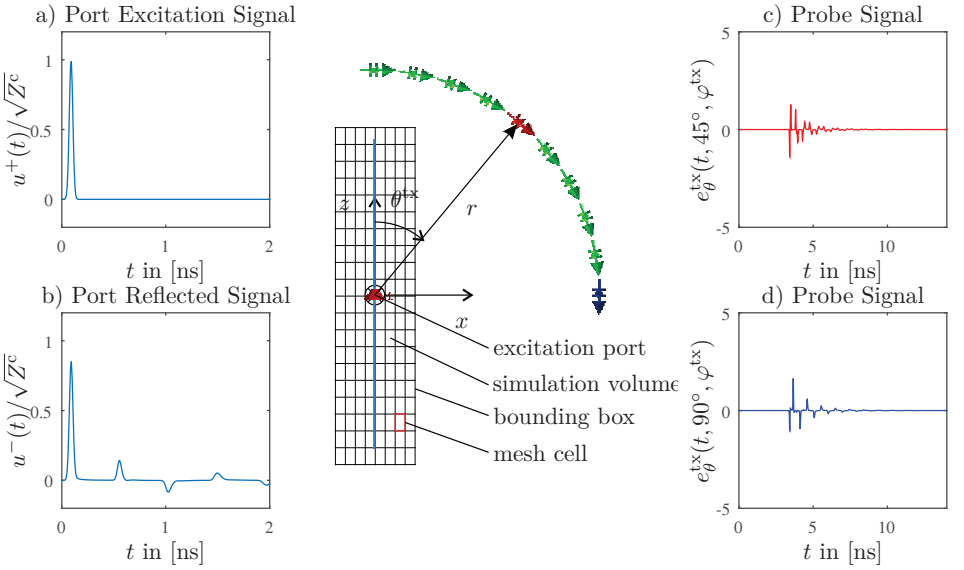

Fig. 4.4: Simulation setup for obtaining antenna effective height of Dipole antenna. A $\lambda/2$ Dipole at $f = 1\,\mathrm{GHz}$ is simulated using the time-domain solver of CST MWS. Plot a) and b) show the simulated port signals, and plots c) and d) the observed probe signals for $\theta = 45\,°$ and $\theta = 90\,°$, respectively. The mesh grid as well as bounding box serve as illustration and are not to scale, neither is the number of mesh cells. Shown are only $\underline{\boldsymbol{\theta}}$-oriented probes. Voltage waves are given in $[\sqrt{\mathrm{W}}]$, E-fields in $[\mathrm{V/m}]$.

After the total energy in the simulation has decreased below a certain threshold value the solver terminates. The time-domain electric as well as magnetic fields inside the simulation volume and on the bounding-box, as well as all port signals are then available for all discrete simulation time steps. The electric far field $\underline{\boldsymbol{e}}^{\mathrm{tx}}(t, \underline{\boldsymbol{r}}^{\mathrm{tx}})$ at an arbitrary point in space can be obtained by transforming the NF available on the bounding box using a NF to FF transform post-processing algorithm. Although several methods exist in CST MWS to obtain the electric far fields, in this thesis E-field probes are used, as illustrated in 4.4. This means that the E-field component co-polar to the probe $e_{\mathrm{Co}}^{\mathrm{tx}}(t)$ is recorded at a predefined set of points $\underline{\boldsymbol{r}}^{\mathrm{tx}}$ in the far field of the simulation volume. In doing so, the origin of the coordinate system is placed anywhere inside the simulation volume and the position of each probe is defined using spherical coordinates $\underline{\boldsymbol{r}}^{\mathrm{tx}} = [\rho^{\mathrm{tx}}, \theta^{\mathrm{tx}}, \varphi^{\mathrm{tx}}]$. Since each probe can only record one component of the E-field vector, for the complete

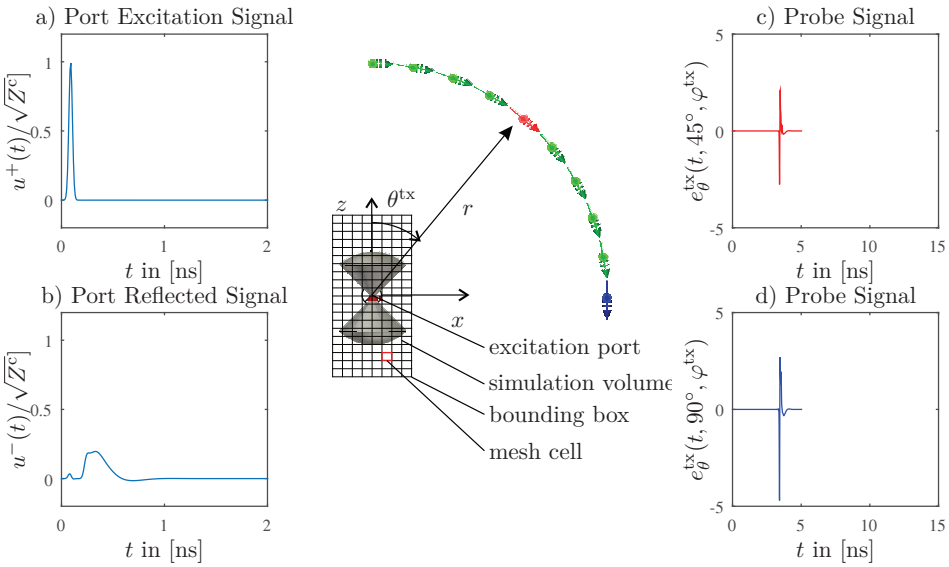

Fig. 4.5: Simulation setup for obtaining antenna effective height of Bicone antenna. A Bicone antenna with radius 20 mm and cone angle $\alpha = 90°$ is simulated using the time-domain solver of CST MWS. Plot a) and b) show the simulated port signals, and plots c) and d) the observed probe signals for $\theta = 45\,°$ and $\theta = 90\,°$, respectively. Compared to the Dipole the Bicone antenna is a wideband structure rapidly radiating the applied energy. Thus the simulation terminates after about 5 ns. Voltage waves are given in $[\sqrt{\mathrm{W}}]$, E-fields in $[\mathrm{V/m}]$.

representation of $\underline{\boldsymbol{e}}^{\mathrm{tx}}(t)$ in the far field two probes with linearly independent orientation, both orthogonal to $\underline{\boldsymbol{\rho}}^{\mathrm{tx}}$ are necessary at each coordinate. By convention, in this thesis the E-field vector is always decomposed into the basis vectors of the spherical coordinate system, and at each point a $\underline{\boldsymbol{\theta}}^{\mathrm{tx}}$- as well as a $\underline{\boldsymbol{\varphi}}^{\mathrm{tx}}$-oriented probe is used. Hence $\underline{\boldsymbol{e}}^{\mathrm{tx}}(t)$ is expressed in terms of the components $e_\theta^{\mathrm{tx}}(t)$ and $e_\varphi^{\mathrm{tx}}(t)$. Note that both the Dipole as well as the Bicone antenna exhibit a perfect rotational symmetry around their vertical axis. Hence it is known in advance, that the radiation characteristics of course also will exhibit the rotational symmetry and no variation will be observed with φ^{tx}. In consequence, those antenna elements do only have to be characterized in the θ^{tx}-dimension. In the case of non-symmetric antenna elements, of course also probes have to be placed along the φ^{tx} coordinate.

All antenna parameters of interest are then obtained by accessing the simulation results using the CST MWS API from matrix laboratory software pack-

age (MATLAB®), and by applying post-processing algorithms to the simulation results. The return loss is obtained by

$$S_{11}(\omega) = \frac{\mathrm{FFT}\left\{u^{-}(t)/Z^{\mathrm{c}}\right\}}{\mathrm{FFT}\left\{u^{+}(t)/Z^{\mathrm{c}}\right\}} = \frac{U^{-}(\omega)}{U^{+}(\omega)}, \tag{4.32}$$

i.e. by transforming the port signals to the frequency domain and relating the voltage wave spectral density leaving the port to the voltage wave spectral density incident on the port. From (4.32) it is obvious, that valid results for S_{11} can only be obtained at frequencies where the spectral density $U^{+}(\omega)$ of the incident wave is sufficiently large. Hence the time-domain excitation signal $u^{+}(t)$ must be selected appropriately. The component of the antenna transmit factor co-polar with probe orientation is obtained by re-arranging (4.8) to

$$O^{\mathrm{tx}}_{\mathrm{Co}}(\omega, \theta^{\mathrm{tx}}, \varphi^{\mathrm{tx}}) = r e^{\mathrm{j}\omega \frac{r}{c_0}} \frac{\sqrt{Z^{\mathrm{tx}}_{\mathrm{c}}}}{U^{\mathrm{tx}+}(\omega)} \frac{E^{\mathrm{tx}}_{\mathrm{Co}}(\omega, \underline{\boldsymbol{r}}^{\mathrm{tx}})}{\sqrt{Z_{\mathrm{F0}}}}, \tag{4.33}$$

and evaluating all factors of the right hand side numerically. The first factor compensates for the probe distance to the coordinate origin. The second factor is simply the inverse of the excitation signal transformed to frequency domain. The third factor is the signal recorded at the probe position $\underline{\boldsymbol{r}}^{\mathrm{tx}} = [\rho^{\mathrm{tx}}, \theta^{\mathrm{tx}}, \varphi^{\mathrm{tx}}]$ normalized to the free space wave impedance Z_{F0}. Hence, the probe and port signals obtained from a time-domain solver run together with the knowledge of the simulation setup are sufficient to compute the antenna transmit factor $\underline{\boldsymbol{O}}^{\mathrm{tx}}$ in the post-processing step. By evaluating (4.33) using the co-polar component of two probes with orthogonal orientation the vector-valued antenna transmit factor $\underline{\boldsymbol{O}}^{\mathrm{tx}}$ can be computed. Once $O^{\mathrm{tx}}_{\mathrm{Co}}$ has been computed, the antenna normalized effective height $H_{\mathrm{Co}}(\omega)$ can be derived using the Lorentz reciprocity theorem (4.18), and the antenna impulse response $h_{\mathrm{Co}}(t)$ can be obtained by an inverse Fourier transformation of $H_{\mathrm{Co}}(\omega)$.

For example, the plots from figure 4.6 show the computed return loss (a), the realized gain (b) as well as the phase of the antenna effective height obtained by post-processing the Dipole example simulation results from 4.4. The simulated return loss clearly indicates the resonances of the $\lambda/2$ Dipole occurring at frequencies $f = c_0/\lambda, 3 \cdot c_0/\lambda, 5 \cdot c_0/\lambda, \ldots$. Since only significant power is accepted by the Dipole antenna at the resonance frequencies, while most of the incident power is reflected otherwise, the realized gain also only

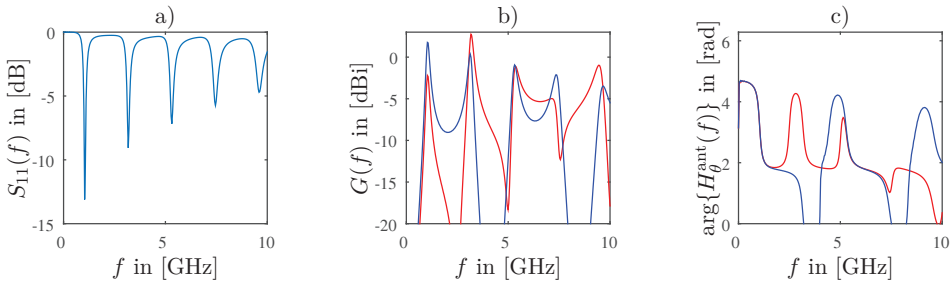

Fig. 4.6: Antenna parameters of Dipole antenna obtained by post-processing CST MWS time-domain simulation results. Antenna return loss (a), antenna realized gain (b), and antenna transfer function phase (c) of $\lambda/2$ Dipole antenna example from figure 4.4 for (blue) $\theta = 90°$ and (red) $\theta = 45°$

is comparably large for odd multiples of the fundamental frequency. In figure 4.7, the corresponding results for the Bicone antenna are shown. The WB characteristics of the Bicone antenna are eminent.

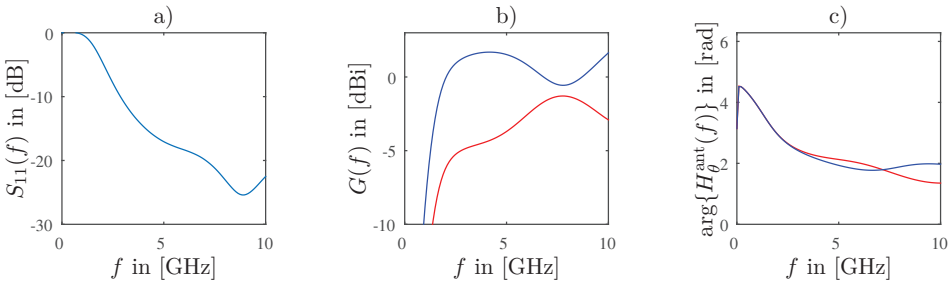

Fig. 4.7: Antenna parameters of Bicone antenna obtained by post-processing CST MWS time-domain simulation results. Antenna return loss (a), antenna realized gain (b), and antenna transfer function phase (c) of Bicone antenna example from figure 4.5 for (blue) $\theta = 90°$ and (red) $\theta = 45°$

In figure 4.8, the simulated current density of the Bicone antenna for $t = 0.05\,\text{ns}$ to $t = 0.28\,\text{ns}$ is shown. It is clearly obvious how the excitation begins at the center and then propagates outwards towards the cone ends. In addition it is obvious from the current density plot at $t = 0.28\,\text{ns}$ that a certain amount of the outward propagating current wave is reflected back at the cone ends, and propagates back to the center of the cone.

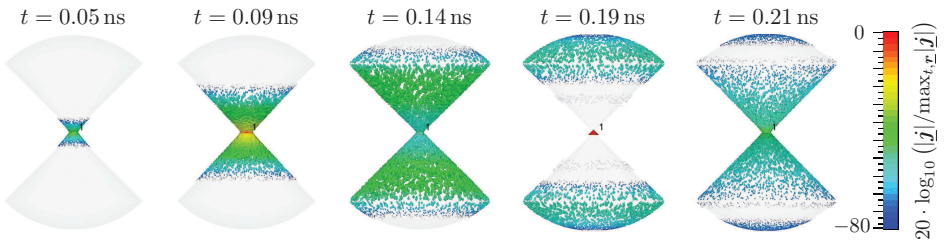

Fig. 4.8: Simulated current density on single Bicone antenna.

4.7.2 By Measurements

The measurement of the characteristics of wideband antennas is based on an extension of the absolute gain method [124] and the gain-transfer-method, also often referred to as the substitution method [124] according to the theory proposed in [44]. Based on [44] a short review of UWB antenna measurements in provided in this section.

In both cases the measurement of antenna radiation characteristics is performed in an anechoic shielded far field measurement chamber, as illustrated in figure 4.9 and figure 4.10. The purpose of the shielded measurement chamber is to mimic free-space far field propagation conditions between antenna under test (AUT) and excitation antenna (EXA) as good as possible, which means that the AUT should be illuminated by exactly a single planar wave front. In particular, only a single propagation path should exist between AUT and EXA, as indicated by the green line in figures 4.9 and 4.10. All multipath components, illustrated using red dashed lines, should be suppressed by the pyramidal horn absorbers, mounted on all surrounding walls of the measurement chamber. Note that, however, this multipath component suppression can practically not be achieved for the complete measurement chamber, but only for a limited volume referred to as the quiet zone. Since the AUT has to be placed in the quiet zone for achieving precise measurements, the possible geometrical measurement setup is limited. In addition to providing only a single propagation path, it has to be ensured that the distance between AUT and EXA is large enough such that the inhomogeneous spherical wave radiated by the EXA can be approximated by a local plane wave at the AUT. This is achieved if a sufficient distance, referred to as the far field distance, is provided between AUT and EXA. It is typically given by $d \geq 2D^2/\lambda$, where D refers to the maximum dimension of the AUT.

4.7.2.1 Absolute Method

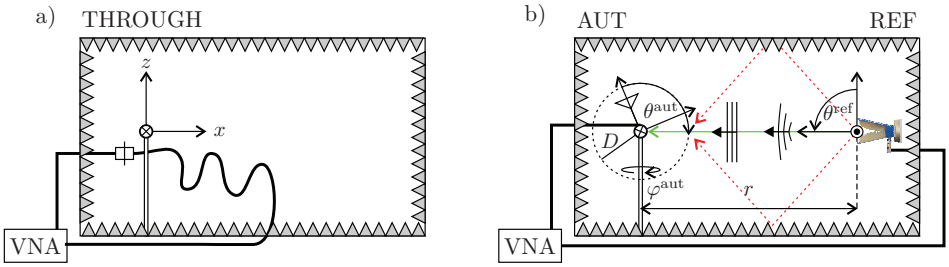

Fig. 4.9: Measurement setup for the absolute method. In a) the calibration setup is shown, where both antenna ports are directly connected using a through calibration standard. The measurement shown in b), is then performed by placing the AUT on the antenna positioner and using a reference antenna (REF) with known characteristics.

The absolute method begins with a characterization of the measurement system frequency response $S_{21,\text{sys}}$. This is done by directly connecting the AUT port with the reference antenna (REF) port using a through connection and performing a transmission measurement (compare figure 4.9 a), which is also known as the transmission-normalization vector network analyzer (VNA) calibration method [125]. Then, the raw data $S_{21,\text{raw}}$ of any subsequent transmission measurements can be referred to the measured system frequency response, and the compensated transmission measurement is given by

$$S_{21} = \frac{S_{21,\text{raw}}}{S_{21,\text{sys}}}. \tag{4.34}$$

Note that in (4.34) a perfect through connection is assumed. If the used through has a non-negligible insertion loss or insertion length, then the used through standard should be characterized separately and the measured system response $S_{21,\text{sys}}$ should be compensated by the characteristics of the used through standard. Using the compensated transmission measurement and a REF with a known antenna normalized effective height, the co-polar component $H_{\text{Co}}^{\text{AUT}}(\theta^{\text{aut}}, \varphi^{\text{aut}}, \omega)$ of the AUT can be obtained by performing a

deconvolution of the measured transmission with $H_{\mathrm{Co}}^{\mathrm{REF}}(\theta^{\mathrm{ref}}, \varphi^{\mathrm{ref}}, \omega)$

$$H_{\mathrm{Co}}^{\mathrm{AUT}}(\theta^{\mathrm{aut}}, \varphi^{\mathrm{aut}}, \omega) = 2\pi r c_0 \exp\left(+\mathrm{j}\omega r/c_0\right) \cdot \frac{\left(\mathrm{j}\omega H_{\mathrm{Co}}^{\mathrm{REF}}(\theta^{\mathrm{ref}}, \varphi^{\mathrm{ref}}, \omega)\right)^* S_{21}(\theta^{\mathrm{aut}}, \varphi^{\mathrm{aut}})}{|\mathrm{j}\omega H_{\mathrm{Co}}^{\mathrm{REF}}(\theta^{\mathrm{ref}}, \varphi^{\mathrm{ref}}, \omega)|^2 + K}. \quad (4.35)$$

Measure uncertainties can typically arise from errors in r,θ^{ref}, and φ^{ref}. To fully characterize the AUT in both polarization directions, two measurements have to be conducted, where the polarization of the EXA has to be changed by $90°$ between both measurements. Note that this technique requires an EXA with sufficiently low cross-polarization properties. If the EXA does not have the desired cross-polarization properties but both co-polar and x-polar components of the EXA are known, a cross-polarization compensation can be applied to 4.35, as further described in [44].

4.7.2.2 Substitution Method

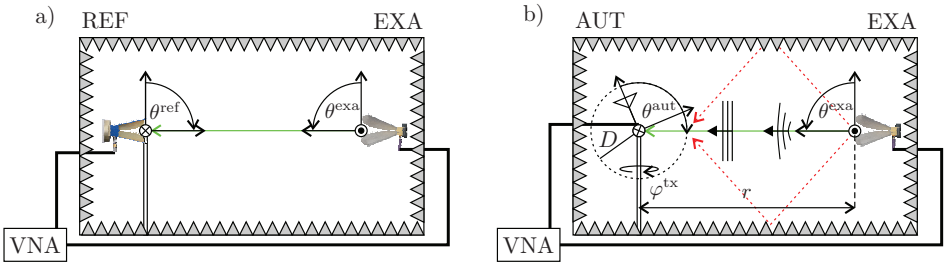

Fig. 4.10: Measurement setup for the substitution method. In a) the calibration setup is shown, where a transmission measurement between the excitation antenna (EXA) with unknown characteristics and the reference antenna (REF) is conducted. For the measurement, the REF is replaced by the AUT as shown in b).

Compared to the absolute method, no initial system frequency response calibration is necessary using the substitution method. Instead, as shown in figure 4.10, two radiation measurements are performed. In the first measurement, the calibration measurement, the AUT is replaced by the REF and the raw data of a transmission measurement $S_{21,REF,raw}$ are stored. It is important, that the direction of arrival $[\theta^{\mathrm{ref}}, \varphi^{\mathrm{ref}}]$ from the EXA to the REF is precisely known. Typically this is achieved by exactly aligning the REF such that the EXA directly is in the main-lobe of radiation, using leveling units

and laser-based alignment systems. In the second measurement the REF is replaced with the AUT. Now, for each angles $[\theta^{\text{aut}}, \varphi^{\text{aut}}]$ of interest, a transmission measurement $S_{21,AUT,raw}(\theta^{\text{aut}}, \varphi^{\text{aut}}, \omega)$ is conducted. The co-polar component $H_{\text{Co}}^{\text{AUT}}(\theta^{\text{aut}}, \varphi^{\text{aut}}, \omega)$ of the AUT normalized effective height can be computed by multiplying the ratio of AUT and REF transmission measurement with the known REF normalized effective height

$$H_{\text{Co}}^{\text{AUT}}(\theta^{\text{aut}}, \varphi^{\text{aut}}, \omega) = \frac{S_{21,AUT,raw}(\theta^{\text{aut}}, \varphi^{\text{aut}}, \omega)}{S_{21,REF,raw}(\theta^{\text{ref}}, \varphi^{\text{ref}}, \omega)} H_{\text{Co}}^{\text{REF}}(\theta^{\text{ref}}, \varphi^{\text{ref}}, \omega). \quad (4.36)$$

Note that cross-polarization properties of both the REF as well as the EXA are not taken into account by (4.36). This requires to use antennas with good cross-polarization properties for both the REF and the EXA for this method [44].

5 Characterization of Small Ultra-Wideband Antenna Arrays

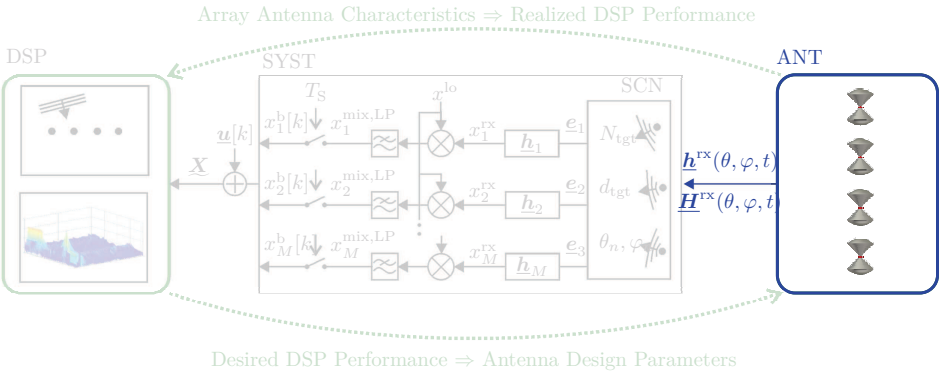

Fig. 5.1: Antenna array model for FMCW RADAR systems.

If several antenna elements are placed next to each other to form an array antenna they will electromagnetically interact, which is referred to as mutual coupling [126]. Hence an array antenna can not simply be described by using the normalized antenna effective height of a single isolated antenna element from chapter 4 and taking into account the antenna displacement in the array as was done when modeling the response of ideal sensor arrays in chapter 2, since depending on the antenna element type as well as on its position in the array antenna its electromagnetic properties will change compared to those when the antenna element is used in isolation. In this chapter the theory of modeling single isolated UWB antenna elements is thus consequently extended to model small arrays of UWB antenna elements.

In this context, *small* does not refer to the array geometrical dimensions, but to the array size in terms of number of antenna elements, which is considered to be around four to sixteen elements throughout this work. The distinction between small and large array antennas is made, since two fundamentally different concepts are used for modeling the responses of both array types in the design process, respectively. The design of large arrays typically starts by designing an array having an infinite number of elements,

where relatively simple calculation techniques for infinite array analysis can be used [127]. The finite array effects are then taken into account at the end of the design process. Real life antenna arrays for signal processing are typically small and the pattern differences across the elements are thus relatively large [128]. In consequence, the radiation characteristics of each element have to be modeled individually already at the beginning of the design process.

5.1 General Array Geometry

The general geometry assumed for the array antennas is shown in figure 5.2. A number of M identical RX antennas is located within a sphere of diameter D. Since each antenna does not operate in isolation but as elements in an array environment, the antennas are also referred to as antenna elements. A

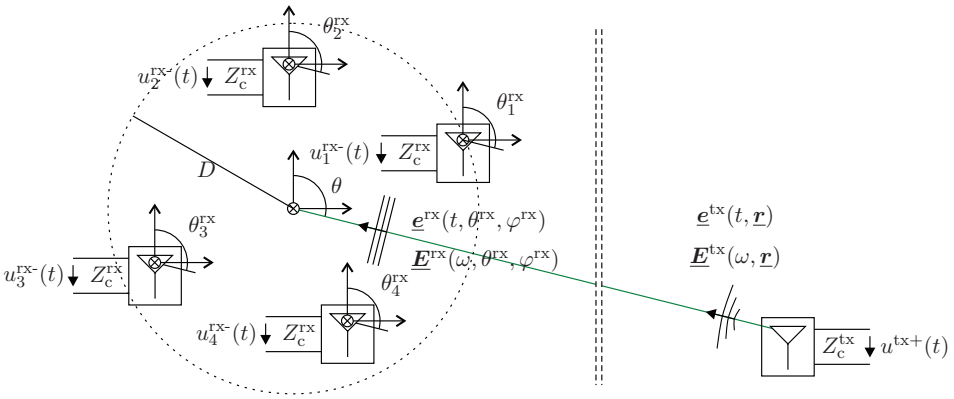

Fig. 5.2: Geometry for characterization of small UWB antenna arrays in receiving mode. All antenna elements of the array are located within a sphere of diameter D, also referred to as the aperture size of the array. A source in the far field radiates an electromagnetic field, and since source and AUT are assumed to be in the far field, the wave $\underline{e}^{\mathrm{rx}}$ impinging on the array can be considered as planar.

local coordinate system is assigned to each antenna element, and the origin of the global coordinate system is in the center of the array. The z-axes of all coordinate systems are parallel. A TX antenna located in the far field of the RX array radiates a spherical wave $\underline{e}^{\mathrm{tx}}(t, \underline{r})$. The received electric field is approximated as a locally plane wave $\underline{e}^{\mathrm{rx}}(t, \theta^{\mathrm{rx}}, \varphi^{\mathrm{rx}})$. Then, the θ^{rx} as seen from the array center and the θ_m^{rx} seen at each antenna element's local coordinate system are identical. A rotation around the z-axis of each coordinate system

is allowed. Hence the φ_m^{rx} need generally not to coincide.

The reference impedance on RX antenna side is identical across all antenna elements and denoted by $Z_{\mathrm{c}}^{\mathrm{rx}}$. The reference impedance on the TX antenna side may be different to $Z_{\mathrm{c}}^{\mathrm{rx}}$. It is referred to by $Z_{\mathrm{c}}^{\mathrm{tx}}$.

Of main interest is the characterization of the RX antenna array in terms of individual antenna element impulse response $\underline{\boldsymbol{h}}_m^{\mathrm{el}}(t, \theta_m^{\mathrm{rx}}, \varphi_m^{\mathrm{rx}})$ and antenna element effective height $\underline{\boldsymbol{H}}_m^{\mathrm{el}}(\omega, \theta_m^{\mathrm{rx}}, \varphi_m^{\mathrm{rx}})$, including the effect of mutual coupling. The effects of mutual coupling on the performance of array antennas can be roughly categorized into two effects: variation of element impedance and variation of element radiation pattern [126]. It will be those two effects which are used to characterize small UWB array antennas in this work. It has been shown by Pozar [56] how both effects can be related. Since it is conceptually simpler, the RX properties of the array elements will be derived by starting from their TX properties. The TX properties are then related to the RX properties by the Lorentz reciprocity theorems in time (4.17) and frequency domain (4.18).

5.2 Scan Reflection Coefficient and Scan Impedance

In this work antenna arrays are analyzed using the free-excitation model [127], where each element is assumed to be driven by a voltage source in series with an internal source resistance. This free-excitation model is illustrated in figure 5.3. Since the sources in the free-excitation model are of constant available power type, they are suitable for a scattering parameter analysis.

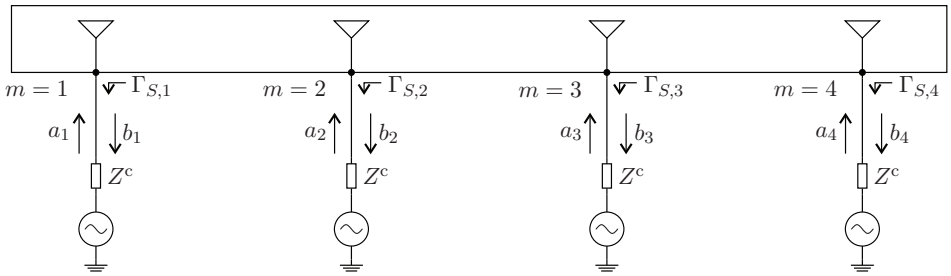

Fig. 5.3: The free-excitation model for analyzing mutual coupling in antenna arrays. For scan-reflection coefficient and scan-impedance characterization, the M-element array antenna is treated as M-port network.

The free-excitation model best resembles the case of practically relevant feed networks as well as transmitter architectures, since those typically are designed having a constant internal impedance and thus are of constant power type sources. Assuming that only antenna element $m = 1$ of the array transmits, the general free-excitation model from figure 5.3 can be adapted to capture this specific case, as illustrated in figure 5.4. Since all elements except

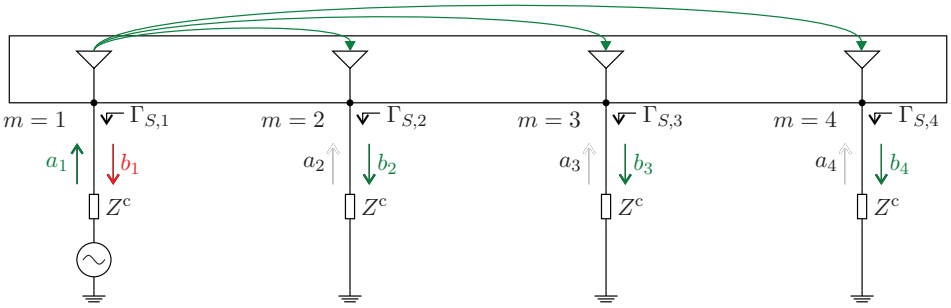

Fig. 5.4: Illustration of coupling in antenna array with element $m = 1$ excited. All other elements are terminated in the characteristic impedance Z^{c}. Since the passive elements act as receivers, power waves b_m leaving their terminals will be observed.

the active element 1 operate in RX mode, only the voltage source at antenna element 1 has a non-zero voltage and thus all remaining voltage sources are replaced by a short. As the first effect of mutual coupling, it is obvious that if element 1 transmits, all other elements in the array act as receivers. Hence a power wave b_m, leaving the terminal of each antenna element m will be observed. Using scattering parameter analysis those power waves b_m are related to the power wave a_1 incident on the terminal of antenna $m = 1$ by

$$\begin{bmatrix} b_1 \\ b_2 \\ b_3 \\ b_4 \end{bmatrix} = \begin{bmatrix} S_{11} \\ S_{21} \\ S_{31} \\ S_{41} \end{bmatrix} a_1. \tag{5.1}$$

Note that the received voltage waves here can generally not be derived using the free-space antenna link model from section 4.5, since the distance of the antenna elements in the array is so close that far field conditions cannot be assumed. The time-domain port voltages as well as the derived S-parameters obtained from a FIT simulation of a four-element Bicone antenna array are shown in figure 5.5. It can be seen that a significant amount of the incident wave is directly reflected by the antenna beginning at $t = 0.21\,\mathrm{ns}$. This is due

to the reflection of the current density wave on the cone ends from element $m = 1$, compare figure 4.8. In addition it can be seen that voltage waves

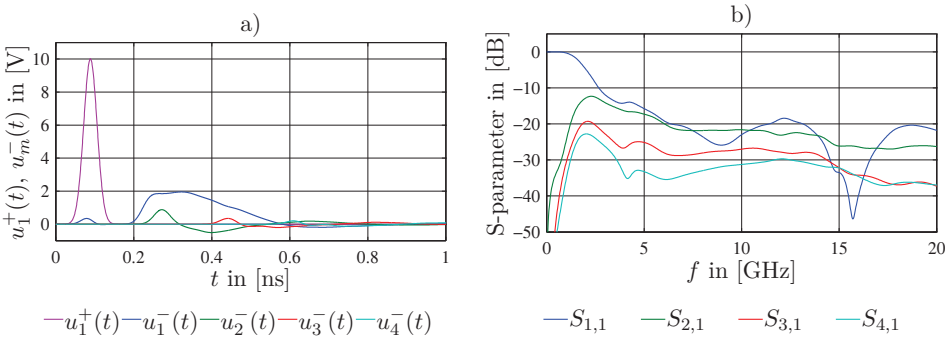

Fig. 5.5: Simulated a) time-domain port voltage waves and b) S-parameters for excitation of element $m = 1$ in four-element Bicone antenna array.

leaving the terminals of all other antenna elements are present. The farther the corresponding element is spaced from the excited antenna, the later this voltage wave is observed and the smaller the amplitude of the voltage wave is. Consequently the coupling in terms of S-Parameter magnitude shown in figure 5.5 b) is largest for closely spaced elements.

Extending the case of antenna element $m = 1$ being active only to a more general scenario where all elements of the array are excited by an arbitrary incident power wave a_m, the voltage waves b_m leaving the terminals of antenna element m can be related to the voltage waves a_m incident on the terminals of antenna element m by the scattering matrix

$$\begin{bmatrix} b_1 \\ b_2 \\ b_3 \\ b_4 \end{bmatrix} = \begin{bmatrix} S_{11} & S_{12} & S_{13} & S_{14} \\ S_{21} & S_{22} & S_{23} & S_{24} \\ S_{31} & S_{32} & S_{33} & S_{34} \\ S_{41} & S_{42} & S_{43} & S_{44} \end{bmatrix} \begin{bmatrix} a_1 \\ a_2 \\ a_3 \\ a_4 \end{bmatrix}. \tag{5.2}$$

It is obvious that the voltage wave b_m leaving the terminal of antenna element m depends on the excitation of all other elements of the array. The scan reflection coefficient [127] observed at antenna element m is now defined as the ratio of the power wave incident to port m and power wave leaving port m, while all other ports are excited simultaneously. It is given by

$$\Gamma_{S,m} = \sum_n S_{m,n} \frac{a_n}{a_m}. \tag{5.3}$$

Since all scattering and reflection coefficients are referred to the impedance Z^{c}, the mutual coupling effects captured by the scan reflection coefficient can equivalently be expressed as a scan-impedance [56]

$$Z_{S,m} = Z^{\mathrm{c}} \frac{1 + \Gamma_{S,m}}{1 - \Gamma_{S,m}}, \tag{5.4}$$

i.e. the effective impedance observed when looking into element's m feed for a certain array excitation. It is obvious that, depending on the actual array excitation and the scattering-parameter mutual coupling properties of the array, the scan reflection coefficient may either be lower or higher compared to using a single element in an isolated environment. If through antenna array design a proper scattering-matrix is achieved for a certain array excitation, the impedance match of the array may be improved. This observation is exploited for the design of a column-coupled array in chapter 7.

5.3 The Active Element Effective Height

In the preceding section, it was shown that if a single radiator is active in an array antenna, while all the others are terminated in passive loads, the passively terminated antennas act as receivers for the field transmitted by the active element. It is a well-known fact that if an antenna receives energy, it also almost always simultaneously radiates an electromagnetic field [129]. This phenomenon is illustrated by the FIT simulation example from figure 5.6. Element $m = 1$ of a four-element Bicone antenna array is excited with a Gaussian impulse, while all other elements are terminated in their reference impedance Z^{c}. The time-domain current density $\underline{\boldsymbol{j}}(t, \underline{\boldsymbol{r}})$ on the surface of all element is recorded and its normalized magnitude is plotted for various time instants. Up to $t = 0.14\,\mathrm{ns}$, the current density equals the current density of an isolated antenna element, compare figure 4.8. However, with increasing time the electromagnetic wave propagates across the other elements of the array, and a significant current density is induced on the surfaces on all other array elements.

It was shown in figure 4.3 of chapter 4 however, that the antenna transmit factor is obtained by integrating over the current density, which develops due to the voltage wave $u^{\mathrm{tx+}}$ incident on the antenna terminal. Consequently, the source volume for integration, which only included the surface of the single antenna in figure 4.3, has to be extended to now include the surface of all antenna elements of the array since the currents induced on the passively

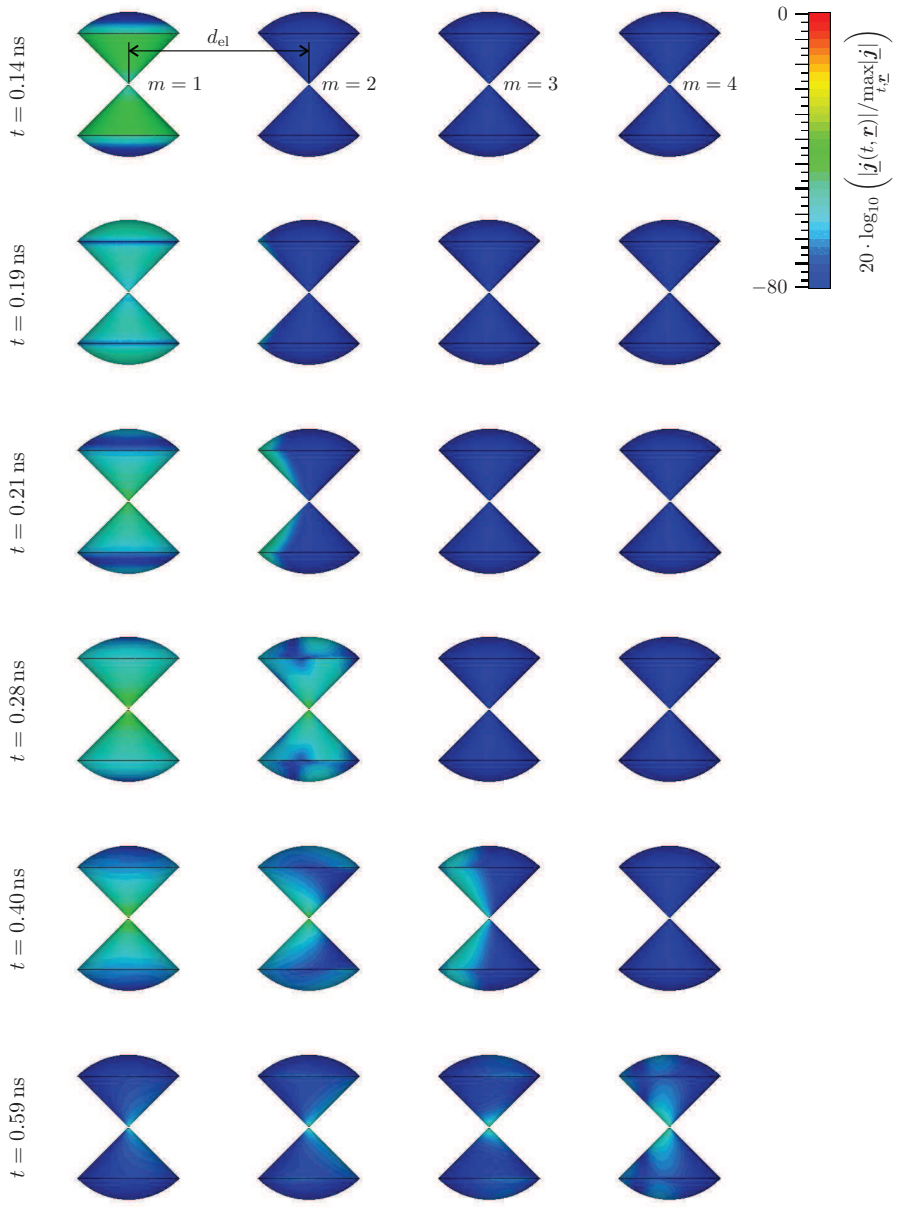

Fig. 5.6: Simulated current density on four-element Bicone antenna array. Although only element 1 is excited with a voltage wave while all the other elements are terminated in a load of 100Ω, a current density is induced an elements 2-4 due to $u^{\mathrm{tx}+}$.

terminated elements contribute to the radiated field of the excited antenna element. This is illustrated in figure 5.7.

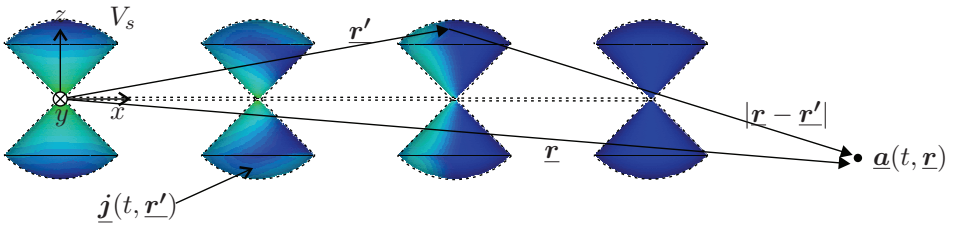

Fig. 5.7: Integration over current density in small array antenna. In contrast to the isolated-element case, the integration volume V_s now extends over all antenna elements in the array, since also the currents induced on the passively terminated elements contribute to the radiated field of the excited antenna element.

It is obvious that the radiation of the single active element embedded in the array environment with all other elements passively terminated will be different to the radiation of the element when used in isolation, since the current density associated with the antenna excitation changes. Hence the antenna element embedded in the array environment will have a transmit factor different to the one when operating in isolation. The transmit factor of the array element is referred to as the active element transmit factor, since it is closely related to the traditional definition of an active element pattern [55]. It is denoted by $\underline{o}_m^{\mathrm{el}}(t, \theta, \varphi)$. Although all elements of the array antenna are assumed to be identical, the active element transmit factor generally is different for each antenna element m of the array because every antenna element is embedded in a different environment and has a different number of neighbors. For example the element $m = 1$ at the edge of a four-element ULA has three neighbors, all placed on one side of element $m = 1$. In contrast, the next element $m = 2$ would have one neighbor on the one side and two neighboring elements on the other side. Clearly, the current density associated with the excitation of element m is different depending on its position in the antenna array, and since the element transmit factor is directly related to the current density the antenna transmit factor will be different for each antenna element.

The far field $\underline{e}^{\mathrm{tx}}(t, \underline{r}^{\mathrm{tx}})$ radiated by exciting antenna element m while all other antenna elements are terminated must be expressed by taking into account

this new transmit factor

$$\frac{\underline{\boldsymbol{e}}^{\mathrm{tx}}(t,\underline{\boldsymbol{r}}^{\mathrm{tx}})}{\sqrt{Z_{\mathrm{F0}}}} = \frac{1}{r}\delta(t-r/c_0) * \underline{\boldsymbol{o}}^{\mathrm{el}}_m(t,\theta,\varphi) * \frac{u^{\mathrm{tx+}}_m(t)}{\sqrt{Z^{\mathrm{tx}}_{\mathrm{c}}}}. \tag{5.5}$$

If a symmetry is present in an array of identical antenna elements, it is possible to obtain the transmit factor for symmetrical antenna pairs by coordinate transformation. Symmetry in this scope does not only mean symmetry in antenna position, but also symmetry in antenna orientation. For example the particular geometries of ULAs and UCAs shown in figure 5.8, which are of interest in the scope of this thesis, exhibit certain element symmetries. In a

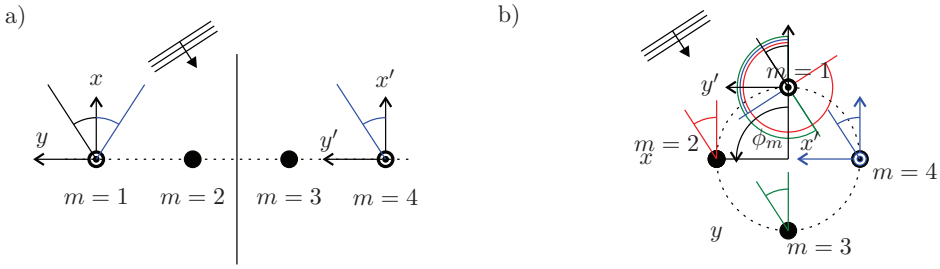

Fig. 5.8: Symmetry in array geometry maps to symmetry of active element effective height. In the case of a) a ULA, once the active element heights of all elements to the left of the symmetry plane are known, the active element heights of all elements right to the symmetry plane can be derived. For b) a UCA, the characterization of a single element is sufficient.

ULA with an even number M of elements, it is obvious that

$$\text{ULA:} \qquad \underline{\boldsymbol{o}}^{\mathrm{el}}_{M-m+1}(t,\theta,-\varphi) = \underline{\boldsymbol{o}}^{\mathrm{el}}_m(t,\theta,\varphi), \forall m \in \{1,\ldots,M/2\} \tag{5.6}$$

i.e. there exist pairs of antenna elements whose active element transmit factors are related by symmetry. In the case of a UCA once the active element transmit factor of a single antenna element is known, the active element transmit factors of all other antenna elements in the array can be obtained from this single element by

$$\text{UCA:} \qquad \underline{\boldsymbol{o}}^{\mathrm{el}}_m(t,\theta,\varphi) = \underline{\boldsymbol{o}}^{\mathrm{el}}_1(t,\theta,\varphi-\phi_m), \forall m \in \{1,\ldots,M\}. \tag{5.7}$$

Furthermore it seems natural to assume the radiation properties of the antenna element when used in isolation also being be preserved by a large extent also in the array environment. As shown by the author in [MG3] the

effect of mutual coupling can then conveniently be captured by taking into account a distortion term which is added to the element's isolated transmit factor. In doing so $\underline{\boldsymbol{o}}_m^{\mathrm{el}}$ is replaced by a sum of the isolated element transmit factor with a element distortion transmit factor $\underline{\boldsymbol{d}}_m^{\mathrm{tx,el}}(t,\theta,\varphi)$, which completely captures the influence of the passive array environment on the radiation characteristics of antenna element m

$$\frac{\underline{\boldsymbol{e}}^{\mathrm{tx}}(t,\underline{\boldsymbol{r}}^{\mathrm{tx}})}{\sqrt{Z_{\mathrm{F0}}}} = \frac{1}{r}\delta(t-r/c_0) * \left(\underline{\boldsymbol{o}}^{\mathrm{tx}}(t,\theta,\varphi) + \underline{\boldsymbol{d}}_m^{\mathrm{tx,el}}(t,\theta,\varphi)\right) * \frac{u_m^{\mathrm{tx+}}(t)}{\sqrt{Z_{\mathrm{c}}^{\mathrm{tx}}}}. \quad (5.8)$$

Clearly, if $\underline{\boldsymbol{d}}_m(t,\theta^{\mathrm{tx}},\varphi^{\mathrm{tx}}) = \underline{\mathbf{0}} \quad \forall m$ no coupling is present in the antenna array.

So far the influence of mutual coupling was discussed using TX antenna elements. Since Lorentz reciprocity as introduced in (4.17) and (4.18) can be applied, it can be deduced that the antenna impulse response $\underline{\boldsymbol{h}}_m^{\mathrm{el}}$, which is now referred to as the active element impulse response, is related to the active element transmit factor by

$$\underline{\boldsymbol{o}}_m^{\mathrm{el}} = \frac{1}{2\pi c_0}\frac{\partial}{\partial t}\underline{\boldsymbol{h}}_m^{\mathrm{el}}. \quad (5.9)$$

Similarly, the normalized antenna effective height $\underline{\boldsymbol{H}}_m^{\mathrm{el}}$, which is now referred to as the active element effective height, is given by

$$\underline{\boldsymbol{O}}_m^{\mathrm{el}} = \frac{\mathrm{j}\omega}{2\pi c_0}\underline{\boldsymbol{H}}_m^{\mathrm{el}}. \quad (5.10)$$

Due to the linearity of the time-derivation in (5.9), it can be concluded that the formalism from (5.8), i.e. the representation of active antenna time-domain transmit factor as sum of isolated transmit factor and distortion term also applies to the active element impulse response and active element antenna height, respectively.

5.4 Obtaining Active Element Normalized Antenna Height

5.4.1 By Electromagnetic Simulations

The active element effective height can be obtained from an EM simulation setup similar to the one used for the characterization of UWB antennas dis-

cussed in section 4.7.1. A typical simulation setup, where the characterization of a small ULA consisting of four Bicone antenna elements is considered as an example is shown in figure 5.9. Since no periodicity can be assumed

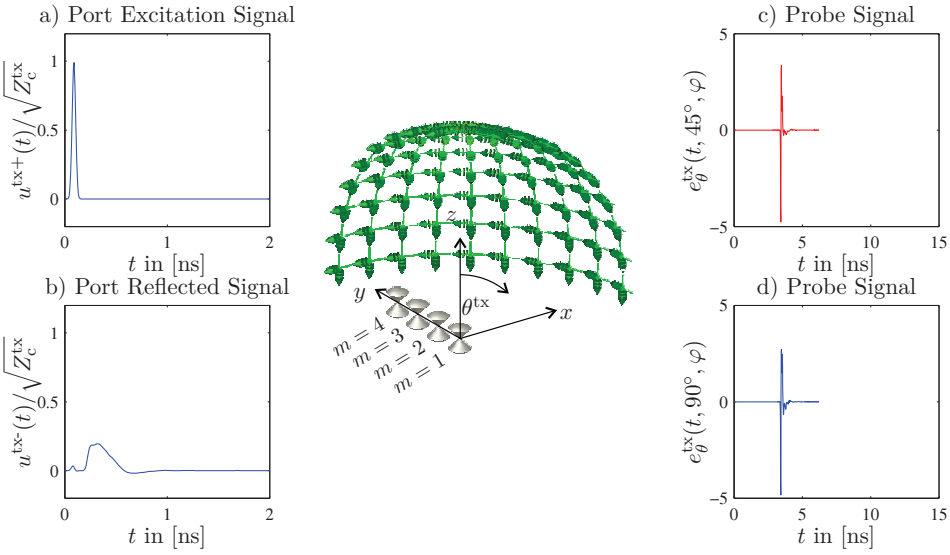

Fig. 5.9: Simulation setup for obtaining antenna effective height in Bicone antenna array. Element 1 is driven by a voltage source with internal impedance $Z^{\mathrm{c}} = 100\Omega$. All other elements are passive and terminated with an impedance of $Z^{\mathrm{c}} = 100\Omega$. The hemispherical region $\theta = 10° \ldots 90°$ and $\varphi = 0° \ldots 90°$ is covered with $\underline{\boldsymbol{\theta}}$- and $\underline{\varphi}$-polarized E-field probes. Units of the port signals are $[\sqrt{\mathrm{W}}]$ and of the prope signals [V/m].

across the array elements as done in the characterization of large antenna arrays [127], the simulation volume has to include the whole array. This greatly increases the simulation volume, in consequence the number of mesh-cells, and thus the number of unknowns which have to be computationally solved for. Excitation ports with a characteristic impedance of Z^{c} (in CST MWS referred to as S-parameter ports, in contrast to voltage or current ports representing a forced excitation [127]) are assigned to the feed region of all array elements, such that the computational model represents the free excitation model from figure 5.3.

For obtaining the active element antenna height of antenna element m, the coordinate system origin is set to the desired reference point on element m, typically at the feed region. Then two E-field probes with orthogonal polar-

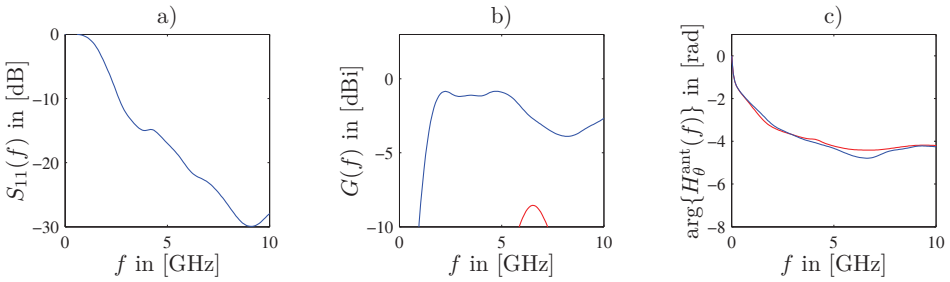

Fig. 5.10: Antenna parameters obtained by post-processing CST MWS time-domain simulation results of four-element Bicone ULA. Element $m = 1$ return loss (a), realized gain (b), and transfer function phase (c) of Bicone antenna example from figure 4.5 for (blue) $\theta = 90\,^\circ$ and (red) $\theta = 45\,^\circ$

ization are placed at each $[\theta, \varphi]$ of interest. Although the Bicone antenna element exhibits a perfect rotational symmetry around its vertical axis (the z-axis by definition), the complete antenna array structure does not exhibit this symmetry and the radiation characteristics will be dependent on φ. The array simulation model is then excited with a single voltage wave launched at the S-parameter port of antenna element m. The voltage sources in the ports of all other elements are shorted, thus that the simulation represents the scenario from figure 5.4. The simulation terminates if the energy in the simulation domain has exceeded a certain threshold value, and the electric as well as magnetic fields inside the calculation domain, as well as the far fields recorded on the E-field probe positions are returned. The active element transmit factor $\underline{o}_m^{\text{el}}$ as well as the active element effective height $\underline{\boldsymbol{h}}_m^{\text{el}}$ are then obtained by post-processing the results in MATLAB®. Consequently the simulation has to be repeated for each antenna element m with the coordinate system origin shifted to the reference position of the particular antenna element m for a characterization of the complete antenna array. However, if a symmetry can be identified in the array geometry such as for ULAs or UCAs, equations (5.6) and (5.6) can be used to reduce the necessary number of simulations.

Figure 5.10 shows the return loss, the realized gain as well as the phase of the active element effective height obtained for antenna element $m = 1$ in the Bicone array antenna. While the return loss as well as the transfer function phase are not influenced to a large extend, the realized gain for $\theta = 45\,^\circ$ is altered significantly compared to the isolated element realized gain shown in figure 4.7.

5.4.2 By Measurements

The measurement of active element effective height can be conducted similar to the procedures for measuring the antenna effective height of an isolated antenna elements, as described in section 4.7.2. Both the absolute as well as the substitution methods can be used, where the calibration steps are identical to the methods which have been discussed before. The measurement setup for obtaining active element effective height is shown in figure 5.11. Conceptually, to measure the active element effective height of element

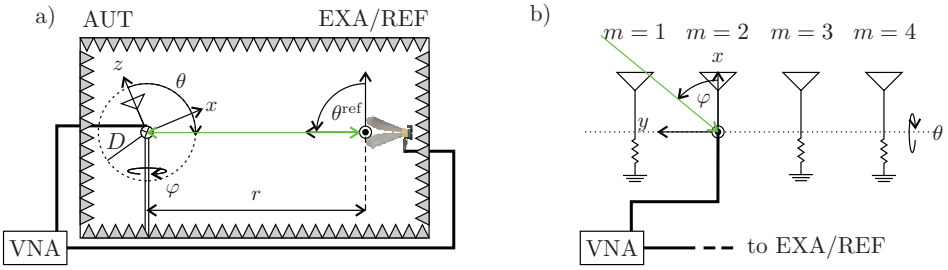

Fig. 5.11: Measurement setup for obtaining antenna effective height using the absolute or the substitution method. In a) the overall measurement setup is shown, where the calibration and measurement procedure is identical to the measurement of an isolated antenna element as shown in figure 4.9 and 4.10, respectively. In b) a detailed view (from top) of the array geometry at the positioner is illustrated.

m, it has to be connected to one port of a VNA and the EXA in case of the substitution method or the REF in case of the absolute method to the other port. All other elements have to be terminated with the impedance Z^{c}. As shown in 5.11 b), the mechanical setup of the positioner must then ensure, that the center of rotation coincides with the desired origin of the antenna element's local coordinate system. The active element pattern of each element of the array can then be obtained by subsequently repeating the measurement for all M antenna elements. To avoid the tedious re-connection and re-positioning of the array elements, a simultaneous measurement can be performed if a multi-port VNA or an appropriate switch matrix is available. The corresponding measurement setup is illustrated in figure 5.12.

For the center of rotation now typically the origin of the global coordinate system, i.e. the array center, is used. That means the center of rotation does not coincide with the origin of each antenna element's local coordinate system. The measured results thus can not directly be interpreted as element

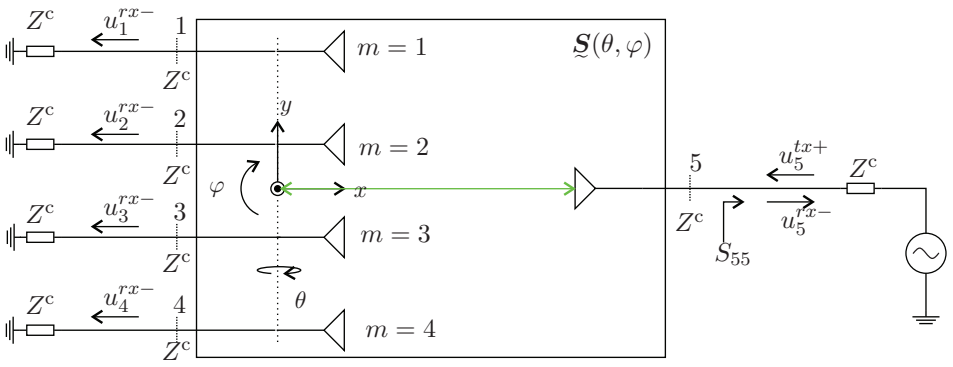

Fig. 5.12: Obtaining active element effective height using simultaneous measurement setup.

effective height. Instead, the displacement between center of rotation and antenna element local origin has to be accounted for in a post-processing step. All ports are referred to the characteristic impedance Z^c, which corresponds to the impedance of the VNA ports. The measurement procedure then reduces to measuring the transmission parameters from port $M+1$ to ports $m = 1 \ldots M$ of the scattering parameter matrix of the $M+1$ port network. In the example of a $M = 4$ element antenna array from figure 5.12 this is e.g. achieved by exciting only port $m = 5$ with an incident voltage wave u_5^{tx+} while all other ports are terminated in Z^c.

To calibrate the measurement, in case of the absolute method the system frequency response between the EXA port $M+1$ and *all* antenna ports $m = 1 \ldots M$ has to be measured and stored individually for each port, such that for each array port a reference $S_{m,M+1,sys}$ is available. Then, the transmission measurement $S_{m,M+1,REF,raw}$ is obtained for each antenna element m. The component of the active element height co-polar to the polarization of the REF is then given by

$$H_{m,\mathrm{Co}}^{\mathrm{el,AUT}}(\theta,\varphi,\omega) = 2\pi r c_0 \exp\left(+\mathrm{j}\omega r/c_0\right) \cdot \frac{\left(\mathrm{j}\omega H_{\mathrm{Co}}^{\mathrm{REF}}(\theta^{\mathrm{ref}},\varphi^{\mathrm{ref}},\omega)\right)^* \cdot S_{m,M+1}(\theta,\varphi)}{|\mathrm{j}\omega H_{\mathrm{Co}}^{\mathrm{REF}}(\theta^{\mathrm{ref}},\varphi^{\mathrm{ref}},\omega)|^2 + K}, \quad (5.11)$$

where the compensated transmission has to be computed for each array port m. It is given by

$$S_{m,M+1} = \frac{S_{m,M+1,\mathrm{raw}}}{S_{m,M+1,\mathrm{sys}}}. \quad (5.12)$$

For the substitution method a separate reference measurement has to be conducted for each array antenna port. The REF should be mounted such that its reference point coincides with the origin of the global coordinate system, i.e. the array center. Then, subsequently all antenna array ports are connected to the REF and a reference transmission measurement $S_{m,M+1,\text{REF,raw}}$ is stored for each array port m. After the reference measurements have been conducted, the AUT is mounted on the positioner and the raw transmission measurements $S_{m,M+1,\text{AUT,raw}}(\theta, \varphi, \omega)$ can be measured using the procedures as described above. The component of the active element height co-polar to the polarization of the REF is then given by

$$H_{m,\text{Co}}^{\text{el,AUT}}(\theta, \varphi, \omega) = \frac{S_{m,M+1,\text{AUT,raw}}(\theta, \varphi, \omega)}{S_{m,M+1,\text{REF,raw}}(\theta^{\text{ref}}, \varphi^{\text{ref}}, \omega)} H_{\text{Co}}^{\text{REF}}(\theta^{\text{ref}}, \varphi^{\text{ref}}, \omega). \quad (5.13)$$

Again note that there is only one fixed center of rotation which does not coincide with the antenna element reference points, i.e. the antenna element local coordinate system. This systematic error has to be accounted for by applying a post processing step to (5.13).

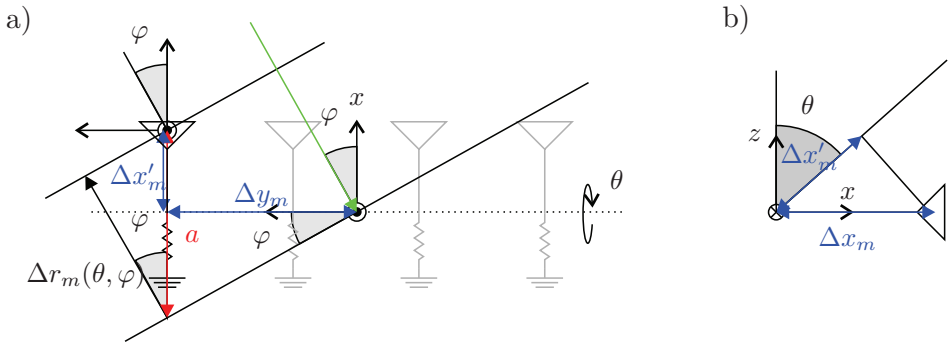

Fig. 5.13: Effects of antenna reference point displacement in array measurement. The leftmost antenna element is displaced by Δx_m and Δy_m from the global coordinate system. View from top a) and view from right b).

Figure 5.13 illustrates an antenna element, whose local coordinate system is displaced by Δx_m and Δy_m from the global coordinate system. Consequently for a wave impinging from direction $[\theta, \varphi]$ the antenna elements distance to the source of the wave differs by $\Delta r_m(\theta, \varphi)$ from the distance of the global coordinate system origin to the wave source. This distance can be expressed by

$$\Delta r_m(\theta, \varphi) = \sin\varphi \Delta y_m - \cos\varphi \sin\theta \Delta x_m. \quad (5.14)$$

While the influence of this translation on the magnitude of the transmission measurement can typically be neglected since the measurement is conducted in far field conditions and hence $D << d$, the influence of Δr on the phase of the transmission measurements has to be accounted for. The compensated co-polar component of element m can then be obtained by

$$H_{m,\mathrm{Co}}^{\mathrm{el,AUT}}(\theta, \varphi, \omega) = e^{\mathrm{j}\omega \frac{\Delta r_m(\theta,\varphi)}{c_0}} H_{m,\mathrm{Co}}^{\mathrm{el,AUT}}(\theta, \varphi, \omega). \tag{5.15}$$

6 A Comprehensive Model for the Beat Signal

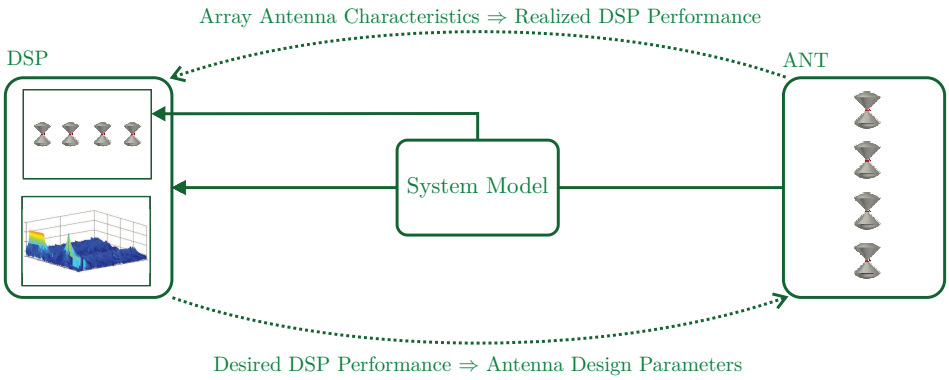

Fig. 6.1: The comprehensive model for the beat signal obtained from a FMCW UWB RADAR system using a small RX array antenna. All details of the RADAR system are hidden and the characteristics of the array antenna are directly mapped onto the beat signal. Knowledge on the array antenna characteristics is incorporated into the DSP algorithms.

In the preceding chapters various fundamental aspects necessary for the characterization of small antenna arrays for DOA estimation in UWB FMCW RADAR systems have been introduced. As illustrated in figure 6.1 in this chapter those aspects will be integrated into a single model to derive a simplified comprehensive formulation for the beat signal obtained from a FMCW UWB RADAR system using a small RX array antenna. Once this formulation is available the goal of assessing various types of UWB antennas and antenna arrays on the performance of range and angle estimation can be reached. In addition this model can be used to incorporate improved knowledge of the array antennas into the DSP algorithms and significantly improve the accuracy of the estimation algorithms used. As shown in figure 6.1 the details of the RADAR system are hidden. Such particular attention can be devoted to antenna and DSP algorithm development, without the need for an extensive system simulation of the FMCW RADAR system. The model proposed in this section will serve as a fundamental tool in the design pro-

cess of small array antennas for UWB industrial FMCW RADAR systems.

6.1 End-to-End Model for Linear FMCW Radar Systems

So far the characterization of UWB antennas and antenna array has been performed in terms of voltage or power waves traveling towards or leaving the antenna terminals. To establish the link between the dimensionless signals used for a system-theoretic analysis of UWB FMCW RADAR systems in chapter 2, the models used for signal processing in chapter 3, and the physical quantities occurring in realized FMCW RADAR systems, the model for the antenna end-to-end transmission from figure 4.2 is embedded in a generator load environment as shown in figure 6.2. Considering the realization

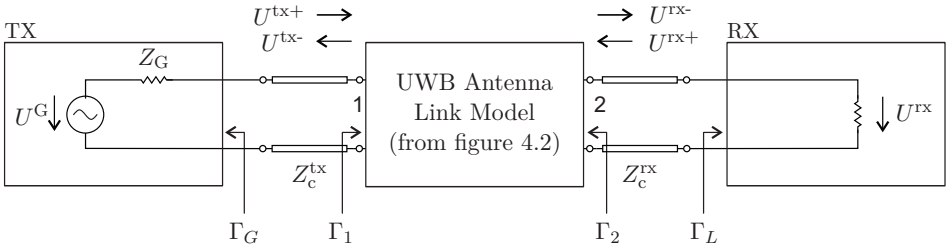

Fig. 6.2: Two-port model for antenna far field end-to-end transmission. The model can directly model the end-to-end transmission in secondary RADAR systems, and with slight modifications (treatment of antenna coupling) also be used for primary RADAR systems.

of a RADAR system, it is typically the generator voltage U^{G} which is interpreted as the TX signal an the voltage U^{rx} measured across the load which is interpreted as the RX signal. Hence, by normalizing both voltages to arbitrary normalization voltages $U^{\mathrm{tx}}_{\mathrm{norm}}$ and $U^{\mathrm{rx}}_{\mathrm{norm}}$ the dimensionless quantities introduced in chapter 2 can easily be related to the physical quantities by

$$x^{\mathrm{tx}}(t) = \frac{u^{\mathrm{G}}(t)}{U^{\mathrm{tx}}_{\mathrm{norm}}},\ X^{\mathrm{tx}}(\omega) = \frac{U^{\mathrm{G}}(\omega)}{U^{\mathrm{tx}}_{\mathrm{norm}}}, \tag{6.1}$$

$$x^{\mathrm{rx}}(t) = \frac{u^{\mathrm{rx}}(t)}{U^{\mathrm{rx}}_{\mathrm{norm}}},\ X^{\mathrm{rx}}(\omega) = \frac{U^{\mathrm{rx}}(\omega)}{U^{\mathrm{rx}}_{\mathrm{norm}}}. \tag{6.2}$$

As shown in [130], the voltage transfer function $U^{\mathrm{rx}}/U^{\mathrm{G}}$ in figure 6.2 is then given by

$$\frac{U^{\mathrm{rx}}}{U^{\mathrm{G}}} = \frac{S_{21}}{1 - S_{22}\Gamma_L} \cdot \frac{(1-\Gamma_{\mathrm{G}})(1+\Gamma_L)}{2(1-\Gamma_1\Gamma_{\mathrm{G}})}. \tag{6.3}$$

If the generator and load impedance is matched to the corresponding characteristic impedance $Z_{\mathrm{c}}^{\mathrm{tx}}$ and $Z_{\mathrm{c}}^{\mathrm{rx}}$, the reflection coefficients become $\Gamma_G = 0$ and $\Gamma_L = 0$ and (6.3) simplifies to

$$\frac{U^{\mathrm{rx}}}{U^{\mathrm{G}}} = \frac{S_{21}}{2} = \frac{1}{2}\frac{U^{\mathrm{rx\text{-}}}}{\sqrt{Z_{\mathrm{c}}^{\mathrm{rx}}}}\frac{\sqrt{Z_{\mathrm{c}}^{\mathrm{tx}}}}{U^{\mathrm{tx+}}}. \tag{6.4}$$

By using the relationship between transmitted and received voltage from (4.21), the received signal spectral density can be expressed by

$$X^{\mathrm{rx}}(\omega) = \frac{1}{2}\frac{U_{\mathrm{norm}}^{\mathrm{tx}}}{U_{\mathrm{norm}}^{\mathrm{rx}}}\frac{\mathrm{j}\omega}{2\pi r c_0}\underline{\boldsymbol{H}}^{\mathrm{rx}}(\omega, \theta^{\mathrm{rx}}, \varphi^{\mathrm{rx}}) \cdot \underline{\boldsymbol{H}}^{\mathrm{tx}}(\omega, \theta^{\mathrm{tx}}, \varphi^{\mathrm{tx}})e^{-\mathrm{j}\omega r/c_0}X^{\mathrm{tx}}(\omega). \tag{6.5}$$

A transformation from frequency- into time-domain then yields the corresponding relation between transmitted signal $x^{\mathrm{tx}}(t)$ and received signal $x^{\mathrm{tx}}(t)$

$$x^{\mathrm{rx}}(t) = \frac{1}{2}\frac{U_{\mathrm{norm}}^{\mathrm{tx}}}{U_{\mathrm{norm}}^{\mathrm{rx}}}\frac{1}{2\pi r c_0}\Big[\underline{\boldsymbol{h}}^{\mathrm{rx}}(t, \theta^{\mathrm{rx}}, \varphi^{\mathrm{rx}}) * \delta(t - r/c_0) * \frac{\partial}{\partial t}\underline{\boldsymbol{h}}^{\mathrm{tx}}(t, \theta^{\mathrm{tx}}, \varphi^{\mathrm{tx}})\Big] * x^{\mathrm{tx}}(t). \tag{6.6}$$

If the focus is limited to describing the effects of the RX antennas only, as proposed by using the abstract FMCW model from figure 2.8, the TX antenna can be assumed to be an ideal element with $\underline{\boldsymbol{o}}^{\mathrm{tx}}(t, \theta^{\mathrm{tx}}, \varphi^{\mathrm{tx}}) = \delta(t)/(2\sqrt{\pi})$. Then, the RX signal is only influenced by the RX antenna impulse response and (6.6) simplifies to

$$x^{\mathrm{rx}}(t) = \frac{1}{2}\frac{U_{\mathrm{norm}}^{\mathrm{tx}}}{U_{\mathrm{norm}}^{\mathrm{rx}}}\frac{1}{r}h_{\mathrm{Co}}^{\mathrm{rx}}(t, \theta^{\mathrm{rx}}, \varphi^{\mathrm{rx}}) * x^{\mathrm{tx}}(t - r/c_0). \tag{6.7}$$

Consequently, the abstract model from (2.41) can be extended to take into account antenna effects by

$$\boxed{x^{\mathrm{rx}}(t) = \sum_{n=1}^{N} a_n^{\mathrm{tgt}} h_{\mathrm{Co}}^{\mathrm{rx}}(t, \theta^{\mathrm{rx}}, \varphi^{\mathrm{rx}}) * x^{\mathrm{tx}}\left(t - T_n^{\mathrm{d}}\right).} \tag{6.8}$$

The amplitude coefficient for each target now is given by

$$\boxed{a_n^{\text{tgt}} = \frac{1}{2}\frac{U_{\text{norm}}^{\text{tx}}}{U_{\text{norm}}^{\text{rx}}}\frac{1}{2\sqrt{\pi}d_n^{\text{tgt,rx}}}.} \tag{6.9}$$

This model is referred to as the RX-only end-to-end model and is the basis for treating the influence of antennas on the FMCW RADAR system performance.

6.2 Quasi-Stationary Approximation of the Beat Signal

It was shown by the author in [MG4], that the convolution from (6.8) can be replaced by the quasi-stationary (QS) response of the antenna for practically relevant antennas and sweep rates. The error of the approximation is directly proportional to the sweeprate of the LFMCW signal and depends on the resonant characteristics of the used antennas: the more resonant an antenna, the larger the error introduced. It was shown, that e.g. for a resonant Dipole antenna of length $5\lambda_l$ the error due to the QS approximation stays below 2 % for sweep rates up to $\mu = 1 \cdot 10^{16}\,\text{Hz/s}$. For wideband antennas such as e.g. a Bicone antenna, the error stays below 0.01 % for an excitation within the same parameters.

As a result, the convolution of the transmitted signal $x^{\text{tx}}(t)$ with the co-polar component of the RX antenna effective height $h_{m,\text{Co}}^{\text{el}}(t)$ is approximated by an amplitude modulation (AM) and phase modulation (PM) of the RX signal

$$\begin{aligned} x^{\text{rx,QS}}(t) = \sum_{n=1}^{N} a_n^{\text{tgt}} AM^{\text{QS}}(t - T_n^{\text{d}}, \theta_n, \varphi_n) \\ \cdot \cos\left(\phi(t - T_n^{\text{d}}) + PM^{\text{QS}}(t - T_n^{\text{d}}, \theta_n, \varphi_n)\right). \end{aligned} \tag{6.10}$$

The amplitude and phase modulation signals are given by the normalized effective height of the RX antenna, evaluated at the instantaneous frequency $f(t)$ of the FMCW signal

$$\begin{aligned} AM^{\text{QS}}(t, \theta^{\text{rx}}, \varphi^{\text{rx}}) &= \left|H_{\text{Co}}^{\text{rx}}\left(2\pi f(t), \theta^{\text{rx}}, \varphi^{\text{rx}}\right)\right|, \\ PM^{\text{QS}}(t, \theta^{\text{rx}}, \varphi^{\text{rx}}) &= \arg\{H_{\text{Co}}^{\text{rx}}\left(2\pi f(t), \theta^{\text{rx}}, \varphi^{\text{rx}}\right)\}. \end{aligned} \tag{6.11}$$

As shown in Appendix A, the beat signal can then directly by expressed by

$$x^{\mathrm{b,QS}}(t) = \sum_{n=1}^{N} \frac{a_n^{\mathrm{tgt}}}{2} AM^{\mathrm{QS}}\left(t - T_n^{\mathrm{d}}, \theta_n, \varphi_n\right) \cdot \exp \mathrm{j}\left(2\pi f_n^{\mathrm{b}} t + \phi_n^{\mathrm{b}} - PM^{\mathrm{QS}}\left(t - T_n^{\mathrm{d}}, \theta_n, \varphi_n\right)\right) \tag{6.12}$$

6.2.1 Validation of Beat Signal Model

To prove the validity of the QS approximation of the beat signal, numerical experiments have been conducted in MATLAB®. In the first experiment, a reference beat signal $x^{\mathrm{b}}_{\mathrm{ref.}}[k]$ obtained using a complete ideal RF FMCW RADAR system simulation, i.e. using ideal point sensors as antennas, is compared to the QS approximation from (6.12), which for an ideal system reduces to the beat signal model from (2.42). To obtain the beat signal from the ideal RF model, the simulation setup illustrated in figure 6.3 is used. A discrete-time LFM single up-sweep signal $x^{\mathrm{lo}}[\kappa], \kappa = 0 \ldots K'$ is generated by a numerical implementation of (2.6). Note that the index variable κ is used for the RF signal, to distinguish from the index variable k introduced in chapter 3 used for the IF beat signals. The parameters of the WBF RADAR system scenario

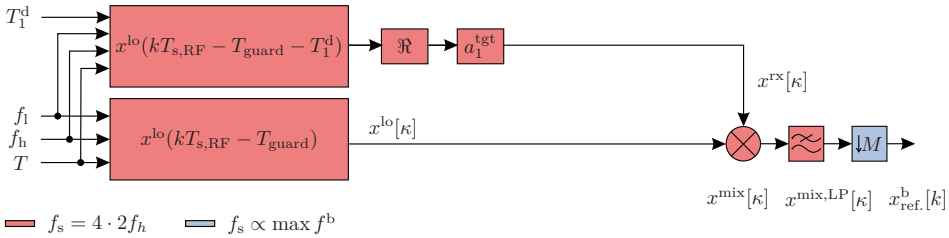

Fig. 6.3: RF simulation model for generating reference signal. A local FMCW signal $x^{\mathrm{lo}}[\kappa]$ and a delayed version $x^{\mathrm{rx}}[\kappa]$ representing a single target are generated, multiplied, filtered and down sampled. DSP blocks filled with red are evaluated at the RF sample rate, blocks filled with blue at the IF sample rate.

from table 1.3 are used. Since the LFM up-sweep signal is defined over an infinite interval, the time for evaluating (2.6) is set to $-T_{\mathrm{guard}} \leq t \leq T + T_{\mathrm{guard}}$. The time interval T_{guard} is selected such that all transient effects which may occur during the simulation are settled at $t = 0$, i.e. no transient effects overlap into the sweep region [MG4]. In particular T_{guard} has to be selected

larger than the sum of the length of the impulse response of the used low-pass filter and the length of the impulse response of the antennas. In this example, a guard interval of $T_{\text{guard}} \approx 336.359\,\text{ns}$ is used. A large sampling frequency of $f_{\text{s,RF}} = 4 \cdot 2f_{\text{h}} = 72\,\text{GHz}$ is used. Since a LFM signal strictly speaking has an infinite bandwidth [131] the large sampling frequency helps to reduce aliasing effects. From the bandwidth formulas from [131] it follows that spectral components aliased in the first Nyquist zone are 120 dB below the signal for the simulation parameters considered. The locally generated signal LFM up-sweep signal $x^{\text{lo}}[\kappa]$ consequently needs $K' = 72\,048\,434\text{Sa}$. The signal is represented using the complex double datatype with 128 bit/Sa. Consequently, $x^{\text{lo}}[\kappa]$ occupies 1.15 GB of memory, which implies that the RF simulation of UWB FMCW RADAR systems is computationally very expensive.

To model a single target according to (2.41) a second discrete-time LFM up-sweep signal is generated, now using a time-delay of $T_1^{\text{d}} = 100\,\text{ns}$, corresponding to a target distance of $d_1^{\text{tgt}} = 30\,\text{m}$. To represent the received signal by $x^{\text{rx}}[\kappa]$ only the real part of the time-delayed LFM waveform is used for further processing, and the waveform is weighted by $a_1^{\text{tgt}} = 1$. All other parameters correspond to the signal described above. In particular $x^{\text{rx}}[k]$ has exactly the same number of $K' = 72\,048\,434\text{Sa}$. It is represented by the real double data type and thus occupies 576.38 MB of memory.

The discrete time-representation $x^{\text{mix}}[\kappa]$ of the mixing product between locally generated and received signal from (2.26) can then be obtained by the sample-by-sample product of $x^{\text{lo}}[\kappa]$ and $x^{\text{rx}}[\kappa]$. To eliminate the component oscillating at the sum frequency from $x^{\text{mix}}[\kappa]$, a finite impulse response (FIR) equi-ripple low-pass filter with 100 taps is used. The pass-band 3 dB cutoff frequency is set to 6 GHz, which corresponds to twice the sweep start frequency f_{l}. According to section 2.1.1 thus all components oscillating at the sum frequency are attenuated by 30 dB in the low-pass filtered mixing product $x^{\text{mix,LP}}[\kappa]$. The frequency response of the filter is shown in figure 6.4. After filtering the sample rate of $x^{\text{mix,LP}}[\kappa]$ is reduced by down sampling by the factor of $M = 12000$. Simultaneously the first $\kappa = \lfloor (T_{\text{guard}} + T_1^{\text{d}})/T_{\text{s,RF}} \rfloor$ samples are truncated in the down sampling step, such that $k = 0$ corresponds to $t = T_1^{\text{d}}$. The beat signal, now indexed by k, is consequently given by $x^{\text{b}}[k] = x^{\text{mix,LP}}[kM + \lfloor (T_{\text{guard}} + T_1^{\text{d}})/T_{\text{s,RF}} \rfloor]$. The sample rate of the beat signal is given by $f_{\text{s}} = f_{\text{s,RF}}/M = 6\,\text{MHz}$.

The reference beat signal $x_{\text{ref.}}^{\text{b,QS}}[k]$ obtained from the QS model assuming

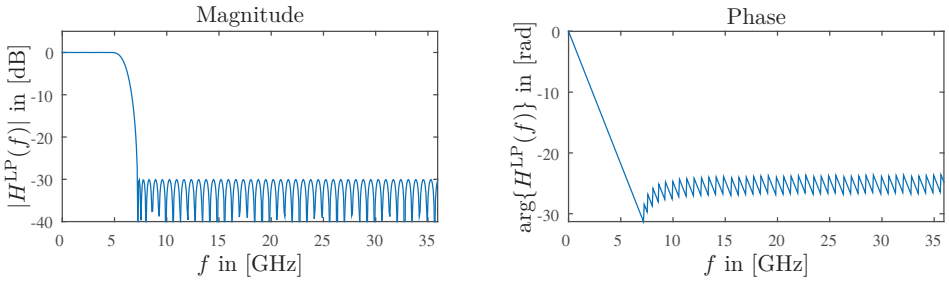

Fig. 6.4: FIR lowpass (LP) filter used for suppressing sum component in the beat signal.

ideal point sensors as antennas is directly obtained by implementing (6.12) in MATLAB®, as illustrated in figure 6.5. To model a system corresponding to the ideal RF model, i.e. without any influence of the antennas, $AM^{\mathrm{QS}} = 1\mathrm{m}$ and $PM^{\mathrm{QS}} = 0$ is used and (6.12) thus reduces to (2.42). A single target is represented by using $N = 1$, and beat frequency f^{b} and phase ϕ^{b} are computed using (2.43) and (2.44), where the beat phase is linearized according to (2.58). Again $T_1^{\mathrm{d}} = 100\,\mathrm{ns}$ is used to represent a target at $d_1^{\mathrm{tgt}} = 30\,\mathrm{m}$. As mentioned in chapter 3, the first sample $k = 0$ of $x^{\mathrm{b,QS}}[k]$ corresponds to the delay time $t = \max T_n^{\mathrm{d}}$.

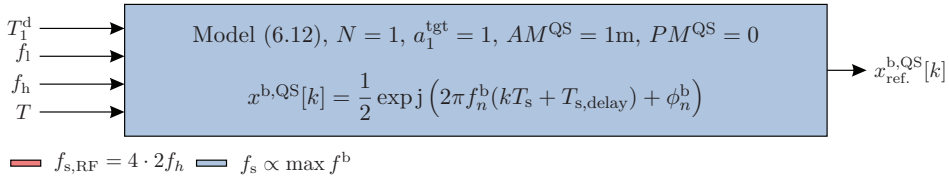

Fig. 6.5: Model for generating reference signal using QS approximation.

The beat signals resulting from both the reference simulation and the direct beat signal model are shown in figure 6.6. From figure 6.6 a) it can be seen that a beat signal with constant amplitude results. The duration of the beat signal seems to correspond to the sweep duration of $T = 1\,\mathrm{ms}$, since despite of the relatively large sweeprate used in the WBF RADAR system scenario the delay time $T_1^{\mathrm{d}} = 100\,\mathrm{ns}$ of the target still is very small compared to T. By looking at the beat signals near the start of the sweep at $t = 0$ as shown in figure 6.6 b), it can be seen that the first sample output from the direct model is at $t = T_1^{\mathrm{d}} = 100\,\mathrm{ns}$. In comparison, the reference simulation using

convolution can in principle generate values for the whole simulation time $-T_{\text{guard}} \leq t \leq T + T_{\text{guard}}$. Likewise the last sample output of the direct beat signal model corresponds to $t = T$, which can be seen by looking at the beat signals near the end of the sweep at $t = T$, as shown in figure 6.6 c). From both the zoomed plots from figure figure 6.6 b) and c) an excellent agreement between the beat signal obtained from the RF simulation as well as the direct model is obvious.

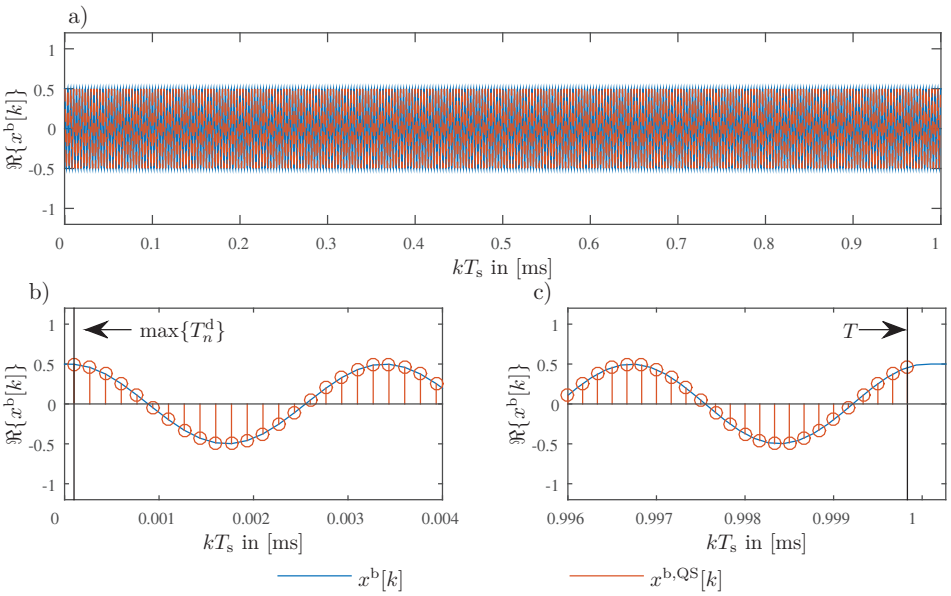

Fig. 6.6: Reference beat signal obtained from RF simulation and direct beat signal model. a) Beat signals over entire sweep range, b) beat signals at start of sweep, and c) beat signals at end of sweep. Excellent agreement between the RF simulation and the beat signal model is obvious.

6.2.2 Validation of Quasi-Stationary Approximation

In the second experiment the beat signals obtained from a RF FMCW RADAR system simulation including the antennas are compared to the direct QS approximation (6.12) for the beat signal, where the antenna effects are taken into account by an amplitude modulation AM^{QS} and phase modulation PM^{QS} of the beat signal according to (6.11). For simulating the RADAR system in the RF domain, the simulation model from figure 6.3 is extended

to take into account the characteristics of the RX antennas, as well as to model several targets. As illustrated in figure 6.7 the latter goal is achieved by a simply generating the delayed LFM signals corresponding to N targets in parallel. To take into account the RX antenna characteristics, each signal is then convolved with the co-polar component of the RX antenna impulse response evaluated at the DOA $[\theta_n, \varphi_n]$ of the target. The RX signal $x^{\mathrm{rx}}[\kappa]$ is then the sum of all target signals. The further processing then contains the multiplication of the received signal with the local oscillator (LO) signal, the low-pass filtering, and a downsampling operation to reduce the sample rate of the signal. It equals the processing steps described in more detail during discussion of figure 6.3.

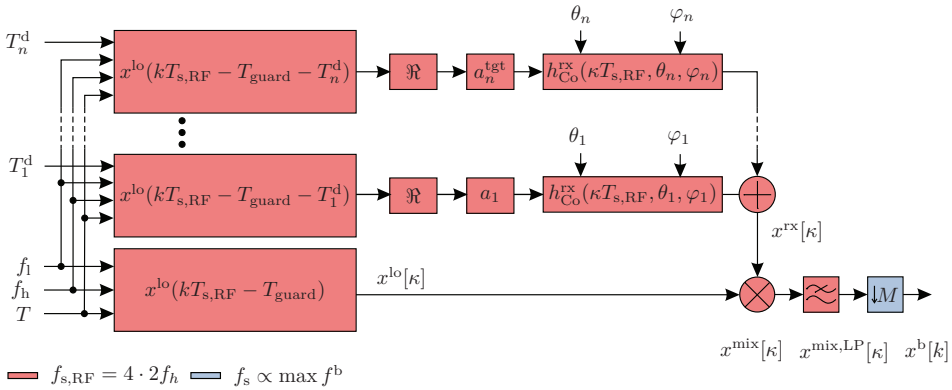

Fig. 6.7: RF simulation model including RX antennas. A local FMCW signal $x^{\mathrm{lo}}[\kappa]$ and a delayed version $x^{\mathrm{rx}}[\kappa]$ representing a single target are generated, multiplied, filtered and down sampled. DSP blocks filled with red are evaluated at the RF sample rate, blocks filled with blue at the IF sample rate.

For evaluating the convolution between delayed LFM signal and antenna impulse response, the sample rates of both signals have to coincide. However, the sample rate of the impulse response is typically determined during antenna simulation or measurement, while the sample rate of the RF simulation is adapted to the specific RADAR system scenario including f_{l}, f_{h}, and μ. To provide antenna models irrespectively of the used sample rate during measurement or simulation, the antenna impulse responses are modeled in terms of their Poles and Residues, also referred to as the singularity expansion method (SEM). The SEM was proposed by Baum in [132] for modeling the transient response of RADAR targets and applied by Licul for a unified frequency and time-domain antenna representation in [43], [47].

Consequently, $h_{\mathrm{Co}}^{\mathrm{rx}}$ is represented as a sum of P complex exponentials

$$h_{\mathrm{Co}}^{\mathrm{rx}}[\kappa] = \sum_{p=1}^{P} R_p \exp \mathrm{j}\left(s_p T_{\mathrm{s,RF}} \kappa\right), \tag{6.13}$$

where s_p are the complex poles and R_p the corresponding complex residues of the co-polar component of the antenna impulse response. For a given antenna impulse response obtained from measurements or simulations, the poles and residues are extracted using the matrix pencil method as described in [43]. The number P of Poles extracted in this work is selected by using a singular value ratio of 10^{-2} [43]. It can be seen from (6.13) that once the poles and residues of the antenna impulse response are known, the impulse response can be evaluated using an arbitrary sampling rate. Once the Poles and Residues of the antenna are known, also the antenna effective height can be computed. It is given by

$$H_{\mathrm{Co}}^{\mathrm{rx}}(\omega) = \sum_{p=1}^{P} \frac{R_p}{\mathrm{j}\omega - s_p}. \tag{6.14}$$

Note that (6.14) allows to evaluate the antenna effective height at arbitrary frequency points.

The model for generating the QS approximation of the beat signal is illustrated in 6.8. Compared to the simplified model from 6.5, now the AM and PM due to the characteristics of the antennas is taken into account and the possibility of modeling of several targets is implemented. Consequently not

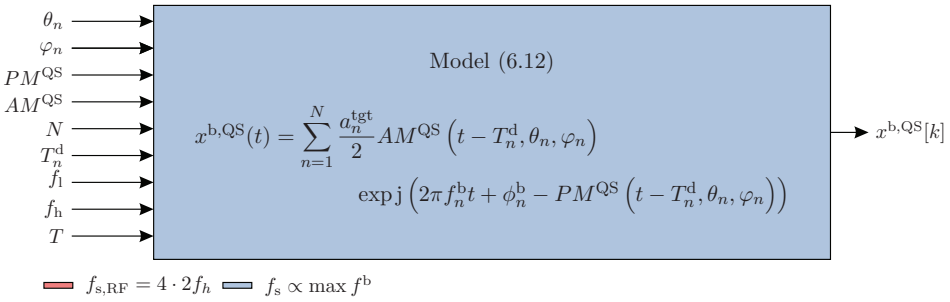

Fig. 6.8: QS simulation model including RX antennas.

only the number N of targets and the corresponding target distance in terms

of its delay-time T_n^{d}, but also the DOA $[\theta_n, \varphi_n]$ of each target must be provided. The characteristics of the antennas are provided in terms of AM^{QS} and PM^{QS}, which directly are related to the antenna normalized effective height by (6.11). The remaining parameters then are the start frequency f_{l}, the stop frequency f_{h} and the duration T of the sweep, which relate the delay time T_n^{d} to the beat frequency f_n^{b} and phase ϕ_n^{b} via (2.43) and (2.44). The QS approximation model from figure 6.8 is then implemented in MATLAB® and for given sets of parameters evaluated at $t = kT_{\mathrm{s}}$, i.e. the sampling period of the beat signal.

As an example the beat signal obtained using an isolated Dipole and an isolated Bicone antenna, respectively, is examined. The AM and PM functions AM^{QS} and PM^{QS} for the Dipole and Bicone antenna are shown in figure 6.9, where the sweep parameters of the WBF RADAR system scenario are used to evaluate (6.11). Clearly the resonant characteristics of the Dipole antenna are

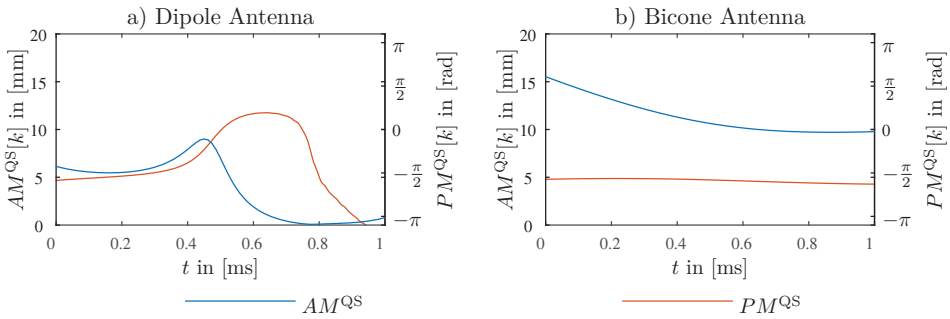

Fig. 6.9: AM and PM functions for a) Dipole and b) Bicone antenna for DOA of $\theta = 90\,^\circ$ and $\varphi = 0\,^\circ$.

obvious, since both AM^{QS} and PM^{QS} show a significant variation over the WBF sweep. In contrast the Bicone antenna shows only a smooth variation in AM^{QS}, and PM^{QS} approximately remains constant for the entire sweep.

The beat signals obtained from the RF simulation and the QS approximation model are shown in figure 6.10 for the Dipole antenna and in figure 6.11 for the Bicone antenna. As a first observation, note the excellent agreement between RF simulation and QS approximation, which in particular gets obvious looking at the zoomed plots b) and c), showing the beat signal near the start and the end of the sweep, respectively. Both the amplitude as well as the absolute phase of the signal are modeled well using the QS response approximation. From the plots a), which show the beat signal obtained for the

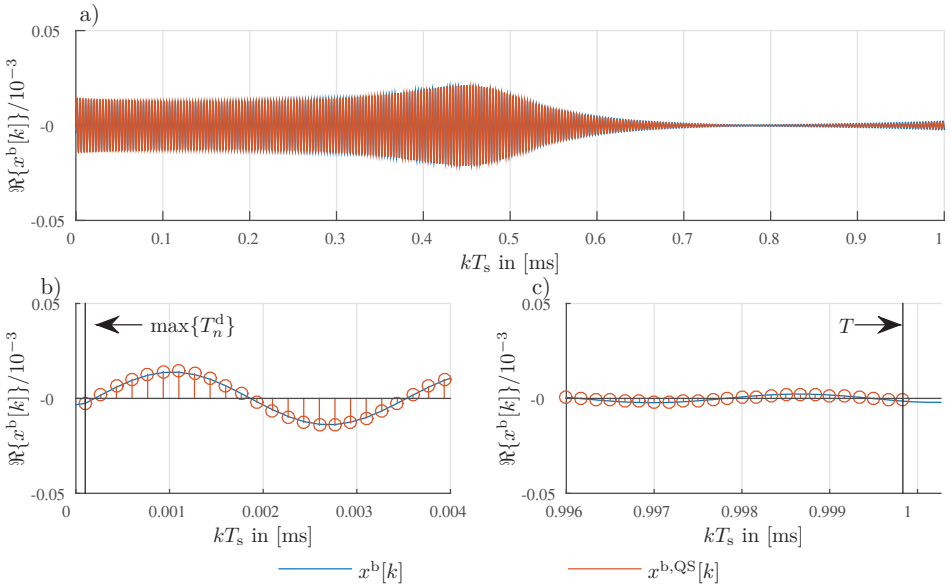

Fig. 6.10: Beat signals obtained using Dipole antenna.

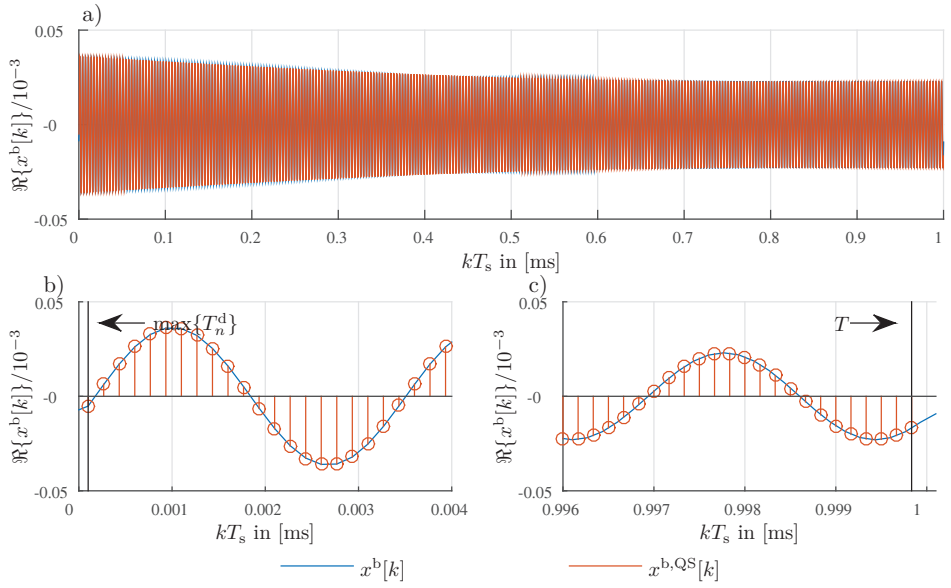

Fig. 6.11: Beat signals obtained using Bicone antenna.

complete $T = 1\,\mathrm{ms}$ sweep, especially the AM introduced by the frequency dependence of antenna normalized effective height is obvious. The beat signal obtained from the Dipole antenna thus exhibits a very strong AM, while the beat signal obtained using a Bicone antenna only exhibits a smooth decrease in amplitude with increasing sweep time, i.e. instantaneous sweep frequency.

The AM and PM present in the beat signal due to the antenna characteristics thus represent a systematic error. This systematic error will impair the FFT-based range estimation, which is based on the assumption of a linear-phase constant-amplitude beat signal. The PM in the beat signal corresponds to the effect of FMCW sweep non-linearities, which have been examined e.g. in [133]–[136]. Typically those effects are related to non-idealities of system components such as voltage-controlled oscillator (VCO), amplifiers and filters used. Indeed simple models for taking into account the characteristics of antennas have been proposed in [135], [136], but neither were the models related to the characteristics of wideband antennas, nor was the validity of the beat signal model proven. To the authors knowledge, the QS response model for the first time relates AM and PM effects present in the beat signal to state-of-the-art methods for UWB antenna and small array antenna characteristics in terms of the normalized effective antenna height.

To illustrate how both the AM and PM present in the beat signal due to the antennas influence the FFT-based range measurements, the FFT of the beat signals obtained using the Dipole antenna and the Bicone antenna are shown in figure 6.12 and figure 6.13, respectively. Clearly, the strong AM and PM present in the beat signal obtained from the Dipole antenna shown in figure 6.10 results in a distortion compared to the ideal reference beat signal. Two effects can be observed: Firstly the width of the main lobe increases and secondly the position of the FFT peak clearly deviates from its ideal position. Hence both range resolution as well as range accuracy are impaired by the Dipole antenna characteristics. In addition figure 6.10 shows both the FFTs of the beat signals obtained from the RF simulation as well as the QS approximation. The excellent agreement between QS approximation and RF simulation, which was already shown in time-domain by figure 6.10, is clearly obvious also in the frequency domain.

In contrast to the large impairments present for the Dipole antenna, the FFT of the beat signal obtained from the Bicone antenna shown in figure 6.13 hardly shows any influence of the antenna on the beat signal FFT. The FFTs

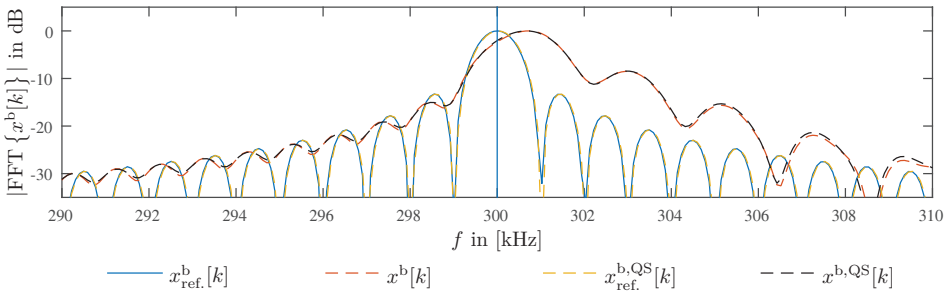

Fig. 6.12: FFT of beat signal obtained using Dipole antenna.

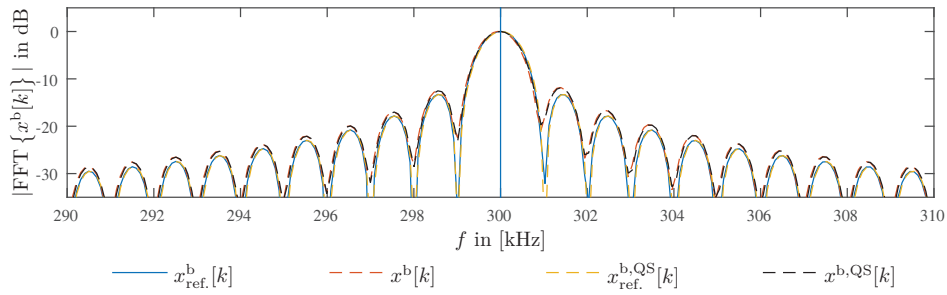

Fig. 6.13: FFT of beat signal obtained using Bicone antenna.

of the beat signals including antenna effects approximately coincide with the FFTs of the reference beat signals obtained assuming ideal sensors as antennas. No shift of the main-lobe peak is present, neither is the width of the main lobe increased. Range accuracy and range resolution are hence not influence by the Bicone antenna. Slight differences between reference signals can be seen at the FFT side lobes which due to the antenna effects increase by about 1 dB.

6.3 Application to Antenna Array Output

To apply the QS response model (6.12) to the output of a small RX antenna array, the LP model (2.59) is used as a basis. The discrete-time LP model (3.5) is extended to take into account the AM and PM introduced in the beat

signal of each RX channel by

$$\underline{\boldsymbol{x}}_{\mathrm{QS}}^{\mathrm{b,LP}}[k] = \sum_{n=1}^{N} \underset{\sim}{\boldsymbol{D}}(\theta_n, \varphi_n, k, T_{m,n}^{\mathrm{d}}) s_n[k] \underline{\boldsymbol{a}}^{\mathrm{LP}}(\theta_n, \varphi_n, kT_{\mathrm{s}} + T_{\mathrm{s,delay}}). \tag{6.15}$$

The matrix $\underset{\sim}{\boldsymbol{D}}(\theta_n, \varphi_n, k, T_{m,n}^{\mathrm{d}}) \in \mathbb{C}^{M \times M}$ is referred to as the distortion matrix. It is a diagonal matrix which can be expressed by

$$\underset{\sim}{\boldsymbol{D}} = \begin{bmatrix} D_1(\theta_n, \varphi_n, k, T_{m,n}^{\mathrm{d}}) & 0 & 0 & 0 \\ 0 & D_2(\theta_n, \varphi_n, k, T_{m,n}^{\mathrm{d}}) & 0 & \ddots \\ 0 & 0 & \ddots & 0 \\ 0 & \ddots & 0 & D_M(\theta_n, \varphi_n, k, T_{m,n}^{\mathrm{d}}) \end{bmatrix}. \tag{6.16}$$

It is the elements of $\underset{\sim}{\boldsymbol{D}}$ which contain the AM and PM introduced into the beat signal due to the active element effective height of antenna element m. The distortion matrix hence *completely* captures all effects the antenna array characteristics have on the beat frequency signals obtained in each RX channel. As shown in chapter 5 due to mutual coupling effects the active element effective height may be different for each antenna element of the array. Consequently a different AM and PM may be introduced into the beat signal of each channel m and thus the AM and PM functions are indexed with the channel number m in the following. The distortion function for each channel can then be expressed by

$$\begin{aligned} D_m(\theta_n, \varphi_n, k, T_{m,n}^{\mathrm{d}}) = {} & AM_m^{\mathrm{QS}}(kT_{\mathrm{s}} + T_{\mathrm{s,delay}} - T_{m,n}^{\mathrm{d}}, \theta_n, \varphi_n) \\ & \cdot \exp \mathrm{j} \left(-PM_m^{\mathrm{QS}}(kT_{\mathrm{s}} + T_{\mathrm{s,delay}} - T_{m,n}^{\mathrm{d}}, \theta_n, \varphi_n) \right). \end{aligned} \tag{6.17}$$

The AM and PM functions AM_m^{QS} and PM_m^{QS} for channel m are related to the active element effective height of antenna element m by

$$\begin{aligned} AM_m^{\mathrm{QS}}(t, \theta_n, \varphi_n) &= |H_{m,\mathrm{Co}}^{\mathrm{el}}(f(t), \theta_n, \varphi_n)|, \\ PM_m^{\mathrm{QS}}(t, \theta_n, \varphi_n) &= \arg\{H_{m,\mathrm{Co}}^{\mathrm{el}}(f(t), \theta_n, \varphi_n)\}. \end{aligned} \tag{6.18}$$

To illustrate the effects of the individual effective heights of the antenna elements of an array, the example shown in figure 6.14 is used. A four-element ULA of Bicone antennas with element distance $d_{\mathrm{el}} = 50\,\mathrm{mm}$ is simulated in

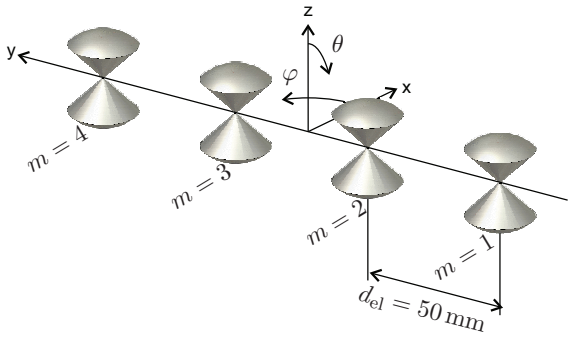

Fig. 6.14: Four-element Bicone antenna array used to illustrate the influence of the antennas on the beat signals and DSP performance.

CST MWS in the frequency range from $0 - 20\,\mathrm{GHz}$. The radiated far field of each element is recorded using $\underline{\boldsymbol{\theta}}$-polarized E-field probes which cover the entire upper hemisphere of the simulation domain, i.e. $\theta = 0\,^\circ \ldots 90\,^\circ$ and $\varphi = 0\,^\circ \ldots 360\,^\circ$. The spacing of the probes is $10\,^\circ$ in each direction. As described in chapters 4 and 5, the antenna element effective heights are obtained by post processing the simulation results in MATLAB®. The model (6.15) is then used to simulate a single target at distance $d^{\mathrm{tgt}} = 30\,\mathrm{m}$ and DOA $\theta = 90\,^\circ$, $\varphi = 60\,^\circ$ in the WBF RADAR system scenario.

The AM and PM functions AM_m^{QS} and PM_m^{QS} for each antenna element are shown in figure 6.15. It is clearly obvious that due to mutual coupling each antenna element has a different normalized effective antenna height, and hence introduces a different modulation onto the received beat signal. Com-

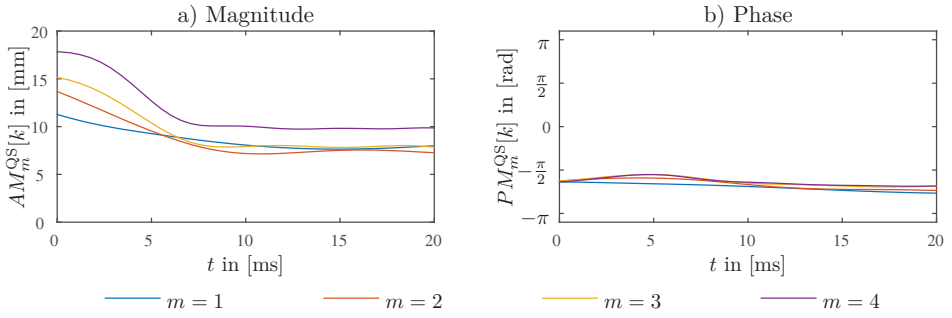

Fig. 6.15: AM and PM functions of $M = 4$ element array of Bicone antenna elements for $\theta = 0\,^\circ$, $\varphi = 60\,^\circ$.

pared to the AM and PM functions of the isolated Bicone antenna (compare figure 6.9) it can be seen that the mutual coupling effect seems to be rather small in the example. This is particularly due to the fact that the element distance of $d_{\mathrm{el}} = 50\,\mathrm{mm}$ is quite large, since it already corresponds to λ at 6 GHz.

The beat signals obtained in each RX channels are illustrated in figure 6.16. It is visible how AM_m^{QS} determines the envelope of the beat signals. Clearly, the envelope of the beat signal in each channel is different.

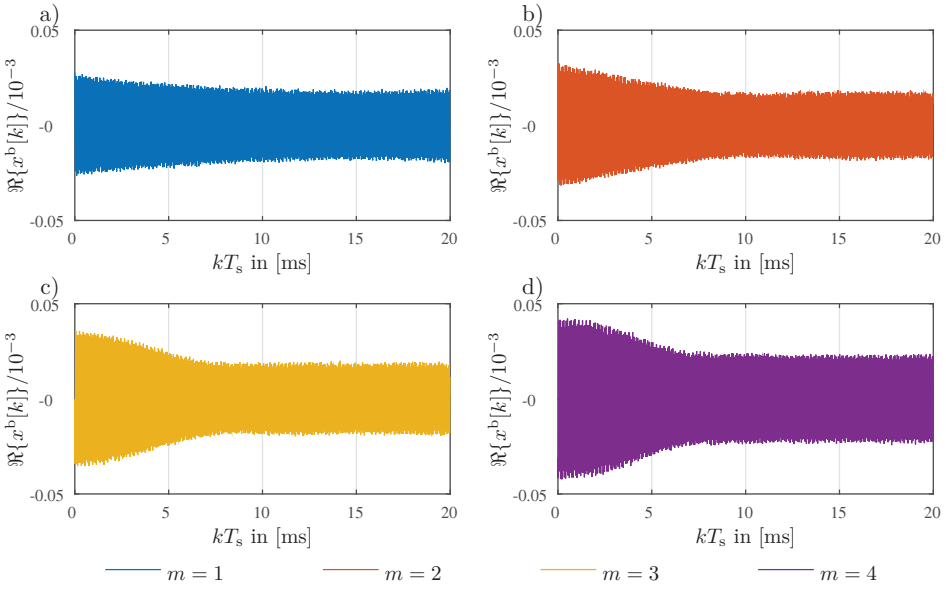

Fig. 6.16: Beat signals of $M = 4$ element array of Bicone antennas for $\theta = 0\,^\circ$, $\varphi = 60\,^\circ$.

To get an impression of the impact of both, AM_m^{QS} and PM_m^{QS}, on FFT-based range estimation, the FFTs of the beat signals is shown in figure 6.17. In addition, the reference beat signals obtained from a system simulation with ideal sensor elements, i.e. $AM_m^{\mathrm{QS}} = 1$ and $PM_m^{\mathrm{QS}} = 1$ are shown. As a first observation a good overall agreement between ideal sensor elements and the Bicone array elements is obvious. The distortion due to mutual coupling is not too large. It is obvious that depending on the element position in the array different beat frequency is observed in each RX channel. The lowest beat frequency is obtained for element $m = 4$, since it is closest to the target

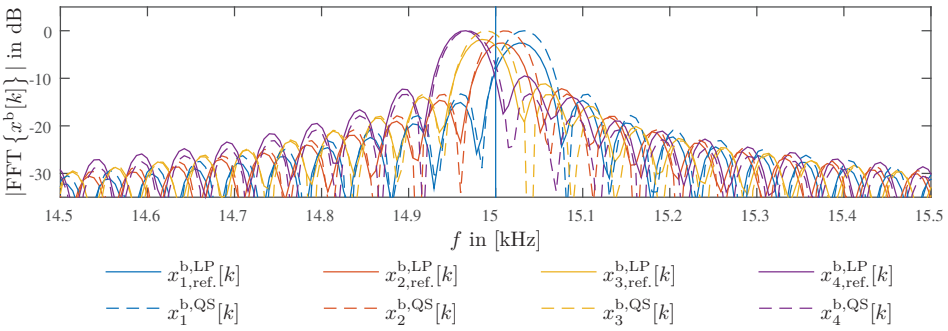

Fig. 6.17: FFT of beat signals for $M = 4$ element array of Bicone antennas for $\theta = 0\,^\circ$, $\varphi = 60\,^\circ$. The beat frequency as observed at the array center is illustrated by the blue vertical line.

for the DOA of $\theta = 90\,^\circ$, $\varphi = 60\,^\circ$. Vice versa the beat frequency obtained for element $m = 1$ is largest. Note that this phenomenon is the main difference between the beat signals observed in NB and WB FMCW RADAR systems, as also described in chapter 2. Having a closer look it can be seen that the beat signals obtained from the Bicone array antenna differ in amplitude, since the AM_m^{QS} of the elements, respectively the active element gain, differ across the antenna elements. In addition a small deviation of the main lobe peak position of elements $m = 1$ and $m = 3$ compared to the peaks obtained using ideal sensor element can be observed. For antenna elements $m = 2$,$m = 3$ and $m = 4$ also an increase of the height of the first sidelobes is present.

The performance of DOA estimation with the four-element Bicone array antenna is illustrated by the plots of the spatially filtered signals shown in figure 6.18 and the spatial spectrum shown in figure 6.19. As expected from the performance analysis of the DOA estimation algorithms of chapter 3, the WB MVDR algorithms has the best performance. Due to the large element distance of $d_{\mathrm{el}} = 50\,\mathrm{mm}$ already a grating lobe at $kT_s = 0$, corresponding to an instantaneous frequency of 6 GHz can be observed. A second grating lobe enters when the instantaneous frequency of the incident FMCW sweep approximately is 6.45 GHz. In contrast to the case of ideal sensors, two effects introduced by the use of a real antenna array can be observed: Firstly, the maximum of the main lobe of the spatially filtered signal is not a straight line at a certain α_φ, but is somehow distorted. Secondly, the magnitude itself is not constant but significantly decreases versus time. Both effects can be related to the model mismatch present in the Beamforming

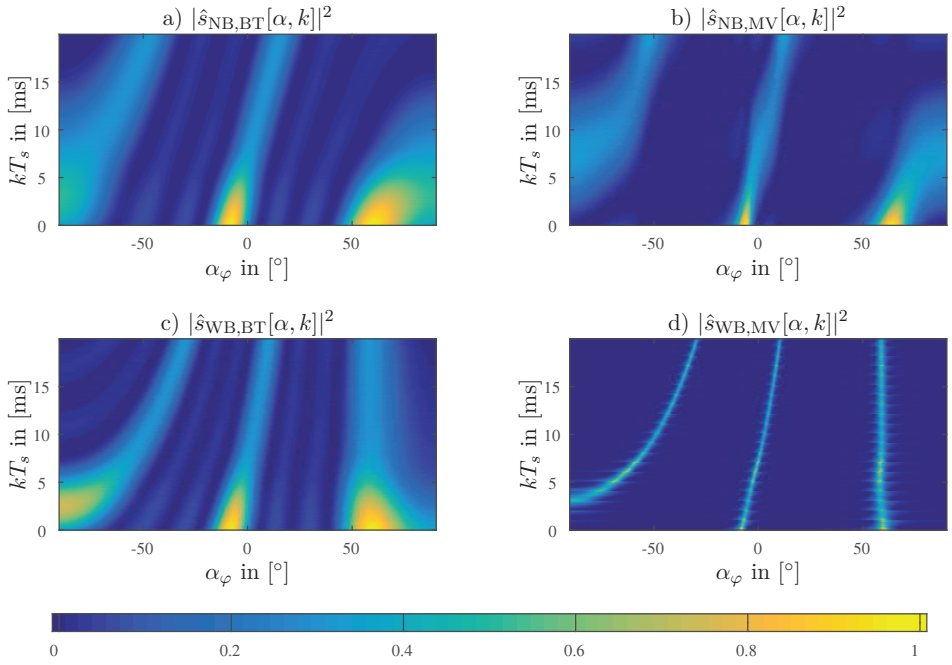

Fig. 6.18: Magnitude of spatially filtered signals obtained from NB (top) and WB (bottom) beamformers in WBF signal scenario, normalized to maximum value. The ideal LP model is used. Single signal impinging on uniform, 4-element linear Bicone antenna array from figure 6.14. Bartlett shown on the left and MVDR on the right.

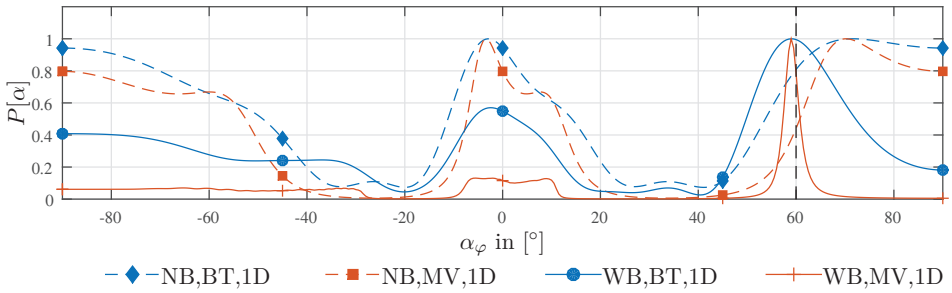

Fig. 6.19: Spatial spectra obtained from four-element Bicone antenna array from figure 6.14 in WBF RADAR signal scenario. The true DOA is indicated by a dashed line.

algorithms: While the algorithms assume a received signal according to the LP model from (2.59), the true output is influenced by the antenna elements and given by (6.15). Clearly, it is the distortion matrix $\underset{\sim}{\boldsymbol{D}}$ which captures the deviation between DOA model assumption and true output. The larger $\underset{\sim}{\boldsymbol{D}}$ deviates from an identity matrix, the larger the errors introduced in the DOA estimation will become.

The spatial spectra obtained from the spatially filtered signals are shown in figure 6.19. The true DOA of $\varphi = 60\,^\circ$ is indicated by a vertical black dashed line. Again the superior performance of the WB MVDR algorithm with its fine spatial resolution is obvious. The WB Bartlett algorithm has a comparatively larger main lobe which limited by the size of the array aperture. The main peak of both WB algorithms is at $\alpha_\varphi = 59\,^\circ$ and hence very close to the true DOA. However, due to the model mismatch an error of $1\,^\circ$ occurs. A large error can be observed for both NB algorithms. Note the attenuation of the grating lobes due to the temporal averaging, which is particularly occurs for the WB MVDR algorithm. The first grating lobe thus is reduced to an amplitude of only $1/10$ of the main peak. It is present in the spatial spectrum in the range $\alpha_\varphi = -10\,^\circ \ldots 10\,^\circ$. The second grating lobe approximately is reduced to an amplitude of only $1/20$ of the main peak. It is present in the spatial spectrum in the range $\alpha_\varphi = -90\,^\circ \ldots -30\,^\circ$.

6.4 Modified Steering Vector

From the previous discussion it is obvious that it is the mismatch between the LP model, which is the basis for the DOA estimation algorithms and the true output of the antenna array represented by (6.15). If the array was precisely characterized by simulations or measurements and the distortion matrix is known, then this knowledge can be incorporated into a modified steering vector, which takes into account the antenna element effective height. The modified steering vector, denoted by $\underline{\boldsymbol{a}}^{\mathrm{DIST}}$ since it takes into account the linear signal distortion, is then given by

$$\underline{\boldsymbol{a}}^{\mathrm{DIST}}(\theta_n, \varphi_n, k) = \underset{\sim}{\boldsymbol{D}}(\theta_n, \varphi_n, k, 0) \cdot \underline{\boldsymbol{a}}^{\mathrm{LP}}(\theta_n, \varphi_n, k). \tag{6.19}$$

Then, the LP QS beat signal output of the array can be approximated by

$$\underline{\boldsymbol{x}}_{\mathrm{QS}}^{\mathrm{b,LP}}[k] \approx \sum_{n=1}^{N} s_n[k] \underline{\boldsymbol{a}}^{\mathrm{DIST}}(\theta_n, \varphi_n, kT_\mathrm{s} + T_{\mathrm{s,delay}}). \tag{6.20}$$

Note that (6.20) is only an approximation for (6.15). Exactly speaking, each signal received from a certain target is subject to a different distortion, since depending on the distance of the target the instantaneous frequency at the RX antenna array element is different. For practically relevant sweep rates and practically relevant antenna arrays it is easy to see that the AM and PM modulating functions AM_m^{QS} and PM_m^{QS} will however be sufficiently smooth. Thus they can be assumed as identical for all target signals.

By using $\underline{\boldsymbol{a}}^{\mathrm{DIST}}$ in the signal processing algorithms proposed in chapter 3, the effects of the antenna array can be taken into account. This is generally know as *Mutual Coupling Compensation* and has been an active research area in antenna array processing over the last decades. An thorough review of decoupling methods for the mutual coupling effect in antenna arrays is provided by Hui in [137]. According to [137] taking into account the mutual coupling by (6.19) and (6.20) into the DSP algorithms thus belongs to the class of *Coupled Element Pattern Methods* and is also referred to as array calibration [138], since the exact response of the antenna array is stored in $\underset{\sim}{\boldsymbol{D}}$. Note that in the case of UWB FMCW RADAR it is however not only the mutual coupling effect which is captured by $\underset{\sim}{\boldsymbol{D}}$, but more generally also the frequency dependent effects of each antenna element, which also would be present if the antennas would be used in isolation. Although (6.19) and (6.20) provide a simple formulation, the precise characterization of an array antenna is practically challenging. Not only must $\underset{\sim}{\boldsymbol{D}}$ be measured and stored over a large set of frequencies and DOAs. In addition it has to be ensured that $\underset{\sim}{\boldsymbol{D}}$ remains valid until life cycle of the antenna array used and perturbations in $\underset{\sim}{\boldsymbol{D}}$ due to the environment surrounding the antenna array have to be taken into account. Furthermore signal processing becomes far more challenging.

Figures 6.20 and 6.21 show the effects when using (6.20) in the Bartlett and MVDR beamforming algorithms onto the beat signals obtained from the four-element Bicone array from figure 6.14. The discussion is limited to the WB algorithms since the NB algorithms clearly fail in the WB RADAR system scenario.

As a first observation compared to figure 6.18 it can be seen that the structure of the spatially filtered signals shown in figure 6.18 is significantly improved by using perfect array knowledge in the beamforming algorithms. The magnitude of the spatially filtered signals at look direction $\alpha_\varphi = 60\,^\circ$ is constant versus time. In addition the spatial distortion which was observed in figure 6.18 c) and d) is mitigated. The magnitude of the WB MVDR spatially filtered

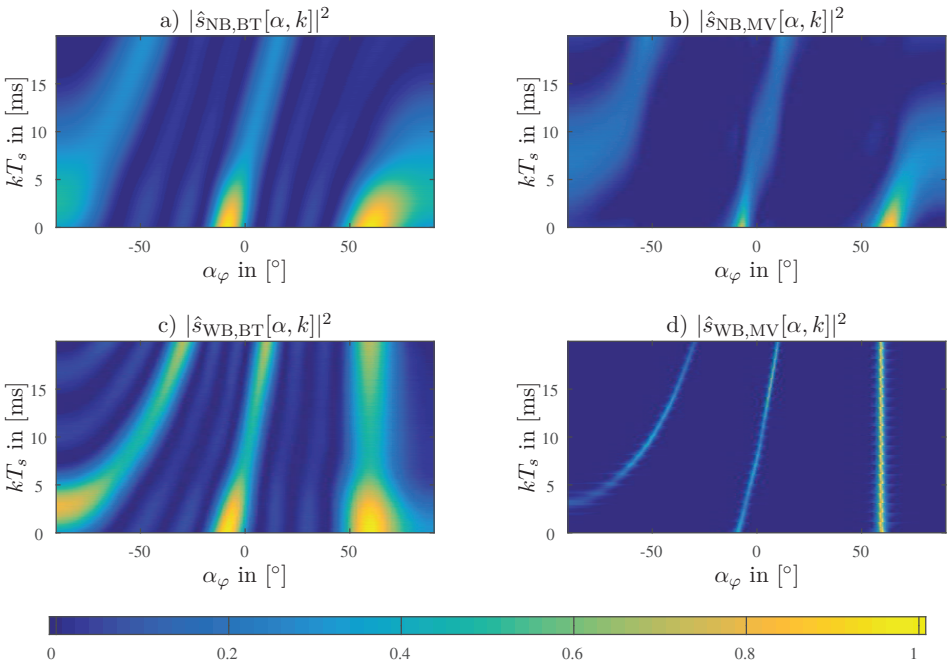

Fig. 6.20: Magnitude of spatially filtered signals obtained from NB (top) and WB (bottom) beamformers in WB signal scenario, normalized to maximum value. Perfect array knowledge by $\underline{\boldsymbol{a}}^{\mathrm{DIST}}$ is used. Single signal impinging on uniform, 4-element linear array with element spacing $\lambda_l/2$. Bartlett shown on the left and MVDR on the right.

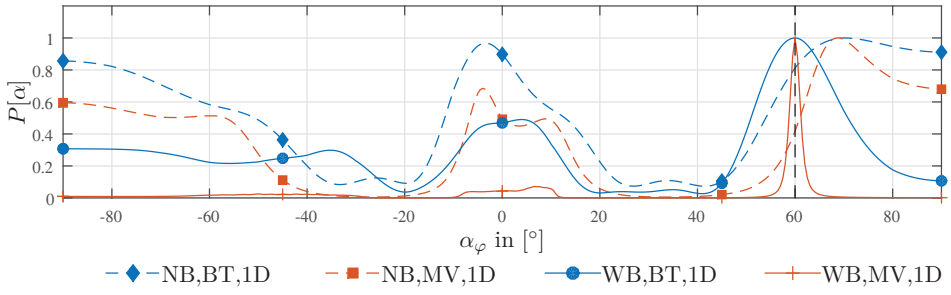

Fig. 6.21: Spatial spectra obtained from four-element Bicone antenna array from figure 6.14 in WBF RADAR signal scenario. The true DOA is indicated by a dashed line.

signal at $\alpha_\varphi = 60\,^\circ$ is significantly larger than the magnitude of the grating lobes. This is due to the fact that the ULA ambiguity present using the ideal steering vector $\underline{\boldsymbol{a}}^{\mathrm{LP}}$ is reduced by taking into account the active element effective heights in $\underline{\boldsymbol{a}}^{\mathrm{DIST}}$. The magnitude of the WB Bartlett beamformer at $\alpha_\varphi = 60\,^\circ$ interestingly shows a significant spatial distortion at low frequencies. This is due to the fact that because of the periodicity of the spatial spectrum of the ULA, the grating lobe occurring at $\alpha_\varphi = -90\,^\circ$ significantly leaks into the look direction $\alpha_\varphi = 60\,^\circ$ and thus distorts the spatially filtered signal especially at low frequencies. With increasing frequency the grating lobe moves inwards and due to the increase in array aperture also its width becomes smaller. Consequently the influence of the grating lobe onto the main lobe at $\alpha_\varphi = 60\,^\circ$ is reduced with frequency and the main lobe becomes stable around $\alpha_\varphi = 60\,^\circ$.

The spatial spectra obtained from the spatially filtered signals are shown in figure 6.21. The peak of the MVDR spectrum coincides with the DOA of $\varphi = 60\,^\circ$. The spatial distortion due to the grating lobe present in the Bartlett beamformer leads to the peak of the spatial spectrum being shifted to $\alpha_\varphi = 61\,^\circ$ and consequently introduces an DOA estimation error. The grating lobe attenuation effect of the MVDR beamformer using perfect array knowledge is further improved in comparison to figure 6.19. As mentioned above this can be reasoned on the reduction of array ambiguity. For the Bartlett beamformer only a little improvement in grating lobe attenuation is present, since the energy of both the main lobe as well as the grating lobes is improved using perfect array knowledge.

7 Design of a Small Linear Array Antenna

From the application scenario illustrated in figure 1.1 a specification for the wall-mounted array antenna ensuring desired RU operation can be derived. This specification is illustrated in 7.1. As shown in a), firstly the design of the wall-mounted array antenna is subject to mechanical design constraints. The antenna array design must be suitable to be embedded in a compact and robust unit, which can easily be deployed in various industrial environments. Naturally, the radiating part of the array antenna will be at the very

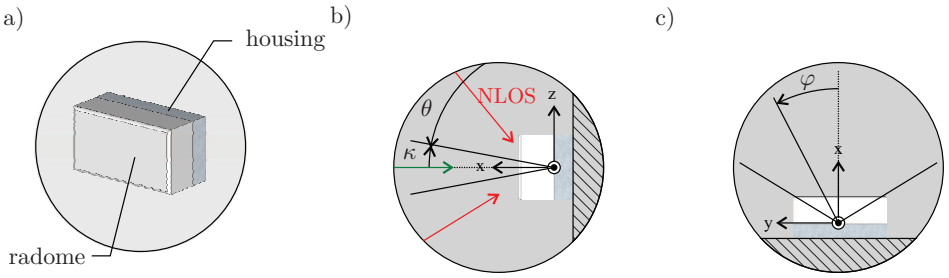

Fig. 7.1: Functional specification of ULA. The ULA must be a) embedded in a robust and compact unit suitable for deployment in industrial scenarios including a EM shielded housing for additional system components, b) should exhibit a relatively narrow elevation pattern to suppress multi-path components reflected from the ceiling and the floor and c) must have a wide field of view in the azimuth plane.

front of this unit and some kind of protective radome must be utilized to protect the antenna elements from environmental stress. Since the radome covers the radiating part of the RU, its material as well as its influence on the antennas has to be carefully selected and considered in the antenna design process. Behind this radiating part of the unit, there must be some housing for placing additional electronic circuits and components, which implement the remaining overall functionality of the RU, but do not contribute to the radiation of the antennas neither may be influenced by the radiated EM waves. Furthermore the housing is considered as the base mechanical structure which ensures overall stability of the RU as well as provides the necessary mounting options for RU deployment. Hence the housing is considered as an enclosed metallic structure. It ensures that no EM coupling

between circuits and components inside the housing with the exterior environment takes place, except through transmission lines penetrating the housing and feeding the antenna elements.

The specification regarding the radiation characteristics of the antenna is illustrated in figure 1.1 b) and c). The addressed application is a two-dimensional positioning problem, since the position of the fork-lift is fixed to movements in the xy-plane and the z-position of the fork lift will remain fixed. Consequently the radiation characteristics of the antenna array should exhibit a relatively narrow pattern in the elevation plane as shown in b). This allows to increase the gain of the antenna array towards the fork-lift and multi-path NLOS components occurring due to reflections from the ceiling or the floor of the building are attenuated. The radiation specifications for the azimuth plane are illustrated in c). A wide azimuth field of view of the antenna array is desired. Firstly the radiation pattern of each single array antenna element must be wide enough to receive a sufficient amount of energy even for large azimuth angles. Secondly the array geometry must be designed such that ambiguity free DOA estimation can be achieved in a maximally wide azimuth region. Since the exact frequency range of the UWB FMCW RADAR system was not fixed during the initial design phase, a continuous operation bandwidth from 5-9 GHz is required. This means that both, radiation pattern stability as well as a stable antenna impedance is required over the entire frequency range.

The design of a suitable small ULA based on a novel concept using column-coupled sub arrays was proposed by the author in [MG5], [MG6]. In this chapter, a review of the ULA design concept as well as an experimental characterization and qualitative DSP performance analysis is presented.

7.1 Preliminary Design Considerations

To achieve a narrow elevation pattern, each element of the ULA itself is realized as small ULA with M' antenna elements vertically stacked, i.e. placed along the z-axis. This is illustrated in figure 7.2. All the elements are fed using a fixed corporate feed network, i.e. the voltage-wave u_5^- leaving the sub-array port is the equi-phase sum of all voltage waves leaving the antenna ports

$$u_5^- = \sum_{m'=1}^{M'} u_{m'}^-. \tag{7.1}$$

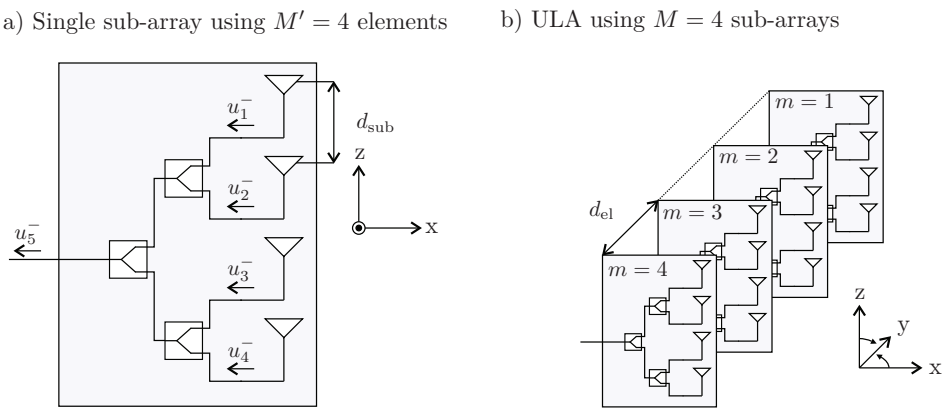

Fig. 7.2: Preliminary design considerations for the wall-mounted antenna array. To achieve a narrow elevation pattern, as illustrated in a) the use of vertical sub-arrays each consiting of M' antenna elements using a fixed corporate feed is proposed. As shown in b) $M = 4$ sub-arrays are then used to design the main ULA used for DOA estimation.

The array factor AF of the sub-array is then given by [10]

$$AF(\kappa, f) = \sum_{m'=1}^{M'} \exp(\mathrm{j}2\pi/\lambda d_{\text{sub}} \sin(\kappa)). \tag{7.2}$$

The array factor for this geometry is a function dependent on the elevation angle and the frequency and consequently, the azimuth radiation pattern remains omni-directional. The use of sub-arrays allows for a large degree of freedom for elevation pattern shaping: the more sub array elements are used, the narrower the elevation pattern can become. In addition, by introducing additional delays and amplitude weights in the feed-network, pattern synthesis methods [10] can be applied to further shape the sub-array elevation pattern, or to tilt the elevation pattern away from broadside, if required in a particular application scenario.

A sub-array consisting of $M' = 4$ elements, spaced at a distance of $d_{\text{sub}} \approx \lambda_h/2$ for $f_h = 9\,\text{GHz}$ is used. No delays and weights are applied in the feed network. The resulting array factor is shown in figure 7.3 a) for a frequency range of $f = 5-9\,\text{GHz}$. It can be seen that using the vertical linear sub-array, the array factor has its maximum at broadside $\kappa = 0\,^\circ$ and that the elevation pattern is symmetrically around $\kappa = 0\,^\circ$. Note that the radiation pattern shown in figure 7.3 a) is omni-directional in azimuth. With an increasing

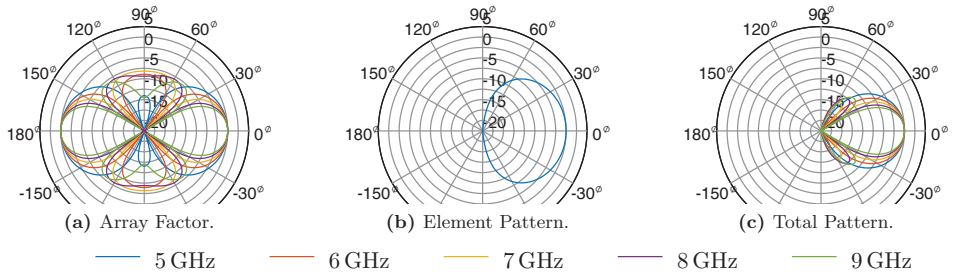

Fig. 7.3: Antenna Factor, element pattern, and total array gain.

deviation from broadside the antenna factor decreases until the first zero occurs. The decrease of the array factor with κ is faster, the higher the frequency, i.e. the larger the total array aperture size $d_{\text{sub}} \cdot (M' - 1)$ in wavelength is. Consequently, the elevation angle of the first zero is smaller, the higher the frequency is. For $f = 5\,\text{GHz}$, the first zero is approximately at $\kappa \approx 75°$ and for $f = 9\,\text{GHz}$, the first zero already occurs for $\kappa \approx 30°$. After passing the first zero, the array factor increases again, which is referred to as the first side lobe of the array. It can be seen, that the total increase of the array factor towards $\kappa = \pm 90°$ increases with frequency and significant radiation towards $\kappa = \pm 90°$ occurs for $f = 6 - 8\,\text{GHz}$. For $f = 9\,\text{GHz}$, radiation towards $\kappa = \pm 90°$ is decreased, because the second zero approaches the visible range of the sub-array but the main radiation direction of the first side lobe is already directed towards $\kappa \approx 45°$. To further shape the radiation pattern of the array, antenna elements with a uni-directional directive radiation pattern are used for sub-array design. Assuming that all antenna elements are identically oriented and exhibit the same element radiation pattern, the total pattern of the array can then be obtained by a multiplication of array factor and element pattern [10]. Assuming a radiation pattern with a $\cos^2 \kappa$ dependence as illustrated in figure 7.3 b), a total sub-array radiation pattern shown in c) results.

7.2 Single Antenna Element

The single antenna elements are based on the antipodal tapered slot antenna (ATSA). The layout and geometry definition of a single ATSA sub-array element including the definition of the simulation domain is illustrated in figure 7.4. The antenna element is fabricated utilizing both metallization

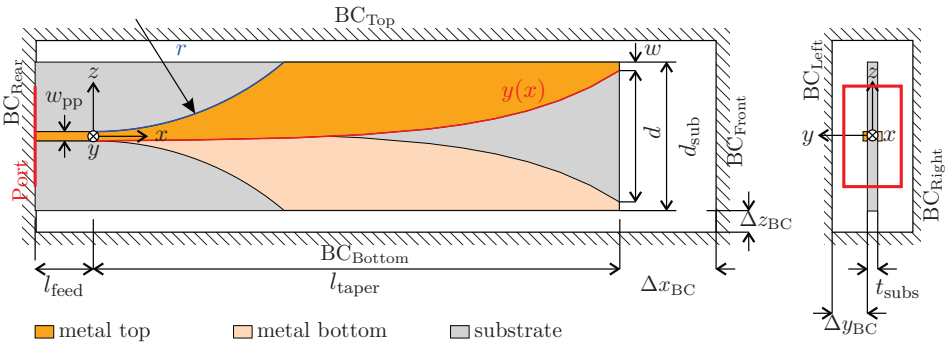

Fig. 7.4: Layout of single antipodal tapered slot antenna (ATSA) antenna element.

sides of a rectangular-shape substrate having thickness $t_{\text{subs.}}$ and permittivity $\epsilon_{r,\text{subs.}}$. The antenna element extends along the x-coordinate and is fed using a parallel-plate waveguide of w_{pp} starting at $x = -l_{\text{feed}}$ and ending at $x = 0$. Beginning at $x = 0$ the lower edge of the of the parallel-plate waveguide is tapered according to an exponential profile [82], [83] defined by

$$y(x) = c_1 \exp(Rx) + c_2, \tag{7.3}$$

$$c_1 = -c_2 - w_{\text{pp}}/2, \tag{7.4}$$

$$c_2 = d/2 + w_{\text{pp}}/2 \exp(Rl_{\text{taper}}) \left(1 - \exp(Rl_{\text{taper}})\right)^{-1}. \tag{7.5}$$

The constants c_1 and c_2 are selected such that the opening at the end of the taper profile is of size $y(l_{\text{taper}}) = d/2$. To increase the degrees of freedom in ATSA element design, a rectangular section of width w is added to the top of the tapered profile. The upper edge of the parallel-plate waveguide is tapered using a circular shape with radius r, where the center of the circle is at $x = 0$, $z = r$. The xz-extension of the substrate is then selected, such that the entire antenna metallization is supported by substrate material.

Recent approaches to UWB antenna array design show that mutual coupling can be utilized to design wideband radiating arrays from narrowband antenna elements such as small Dipoles [61], [63]. A similar design approach is followed in this thesis. To optimize the antenna element, it is simulated in an infinitely long sub-array configuration. Therefore the boundary conditions (BCs) of the simulation domain at the top boundary BC_{Top} as well as at the bottom boundary $\text{BC}_{\text{Bottom}}$ are set to periodic with zero phase-shift, and the distance Δz_{BC} between antenna structure and boundaries is set to

$\Delta z_{\mathrm{BC}} = 0$. Thus the fields and the top and bottom boundary are connected in CST MWS and the simulation domain is simulated to be periodically extended in z-direction. Since a zero-phase shift is used, the simulation corresponds to an infinitely long sub-array where all elements are fed by an equi-phase and -amplitude corporate feed network. The simulated single antenna element is then referred to as a unit cell (UC) of the infinitely long column array. The boundary condition $\mathrm{BC}_{\mathrm{Rear}}$ at the rear of the antenna element is set to perfect electric conductor (PEC) material, taking into account the metallic housing which will back the radiating part of the RU in the final application. The remaining boundary conditions are set to open, i.e. the antenna element sees free-space at its front as well as right and left sides.

To optimize the geometry of the antenna element the overall size is limited to a taper length of $l_{\mathrm{taper}} = \lambda_l$ and a height of $2w + d \approx \lambda_h/2$. The width of the parallel-plate feed is set to $w_{\mathrm{pp}} = 1.05\,\mathrm{mm}$, resulting in a $Z^{\mathrm{c}} = 50\Omega$ feed. Consequently all S-parameters are referred to an impedance of 50 Ω. For the substrate, Rogers RO4360 material with thickness $t_{\mathrm{subs.}} = 0.508\,\mathrm{mm}$ and relative permittivity $\epsilon_r = 6.15$ was selected. The choice for the relatively high-permittivity substrate was based on the feed-network implementation, where it is desired to minimize parasitic radiation and to confine the electromagnetic fields to the substrate. The thickness of the substrate is selected to obtain a necessary mechanical rigidity while keeping the effective thickness, defined as $t_{\mathrm{subs.}}(\sqrt{\epsilon_r} - 1)$ in between $0.013\lambda_0$ and $0.023\lambda_0$ [78].

A numerical optimization based on a Covariance Matrix Adaptation Evolution Strategy available in CST MWS is then conducted to optimize the return loss of the ATSA element. The simulated return loss of the optimized element is shown in figure 7.5 and the parameters of the optimized UC antenna element are given in table 7.1.

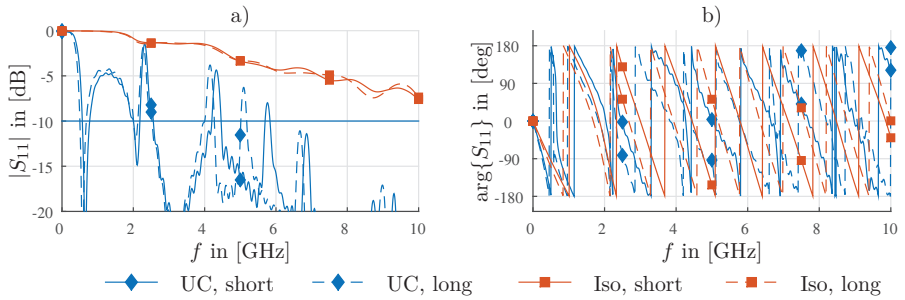

Fig. 7.5: Simulated return loss of single ATSA element.

Parameter	Dimension in [mm]	in [$\lambda_{5\mathrm{GHz}}$]	in [$\lambda_{9\mathrm{GHz}}$]
R		0.08 (dimensionless)	
l_{taper}	60	1	1.8
d	15	0.25	0.45
w	0.973	0.016	0.029
w_{pp}	1.05	0.0175	0.032
r	33.60	0.56	1.02
l_{feed}, short	2	0.03	0.06
l_{feed}, long	7.85	0.13	0.24

Tab. 7.1: Dimensions of the optimized antenna element.

The return loss of the antenna element is below –15 dB once the excitation frequency is above $f = 5\,\mathrm{GHz}$, except at some distinct frequencies where resonance effects occur. As will be seen later they are not present in the finite array and hence a further discussion is refrained from. Interestingly the good return loss properties are achieved despite the size of the ATSA element is smaller than the typical minimum dimensions required for tapered slot antennas: a lower cutoff frequency is defined for ATSA antennas operating in isolation where the maximum separation of the radiators is $d = \lambda_l/2$ [77], [78], [81]. E.g. the ATSA proposed in [82], which has a lower operation frequency of $f_l = 5\,\mathrm{GHz}$, has a corresponding height of $d = 25\,\mathrm{mm}$. In contrast, the ATSA element proposed in this thesis only needs a height of $d \approx 17\,\mathrm{mm}$. From table 7.1 it can be seen, that this maximum separation of the radiating flares of the proposed ATSA element is much smaller than half the wavelength across the entire frequency band of operation and consequently the proposed antenna element works below the cutoff frequency given in [77], [78], [81]. This phenomenon can be entirely dedicated to the beneficial effect of mutual coupling across the antenna elements in the sub-array. The return loss for the antenna element simulated in isolation, i.e. the boundary conditions $\mathrm{BC}_{\mathrm{Top}}$ and $\mathrm{BC}_{\mathrm{Bottom}}$ are set to open and a certain distance $\Delta z_{\mathrm{BC}} > 0$ is used, are also shown in figure 7.5. Since the antenna element is too small, no satisfying return loss is achieved if no mutual coupling from the other elements is present. For frequencies approaching 10 GHz the electrical dimension of the antenna element become larger and the return loss decreases. Consequently by taking into account the known element excitation across the sub-array the E-plane element spacing of $\lambda_h/2$, necessary for obtaining a grating-lobe-free elevation array factor, can be achieved.

7.3 Finite Subarray

In the next step the infinite column-array assumption is discarded and the truncation effects on the return loss of the sub-array module are examined. Therefore a four-element sub-array is designed and simulated in CST MWS, based on the optimized geometry of the single antenna element. The sub-array geometry as well as the simulation domain boundaries and dimensions are illustrated in figure 7.6 a).

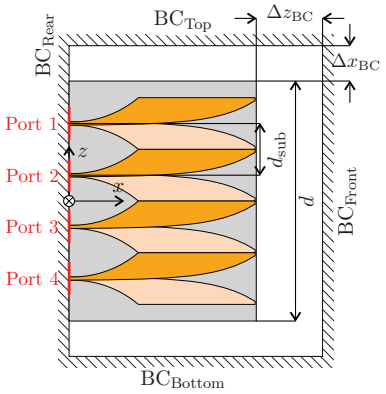

Fig. 7.6: Layout and simulation geometry of ATSA sub-array.

To provide enough spacing for mounting the sub-array modules and in anticipation of feed-network integration, the total height of the substrate is increased to d, such that the total substrate height is larger than the sum of the antenna element heights. All BCs but the c are set to open, where the $\mathrm{BC}_{\mathrm{Rear}}$ remains set to PEC simulating an infinitely large metallic reflector. To each antenna element an excitation port is assigned and four simulations are conducted. A single element is excited per simulation while the others are terminated in Z_0. Figure 7.7 shows the simulated scan reflection coefficient for each antenna element m which is obtained by implementing (5.3) in a post-processing step assuming equi-phase and -amplitude excitation. It can be seen that indeed the return loss is degraded compared to the infinite sub-array case, but still the return loss observed at each element port is below –10 dB for frequencies above 5 GHz. Since the array is symmetrical the scan reflection coefficient for both outer elements $m = \{1, 4\}$ and both inner elements $m = \{2, 3\}$ is identical. However, since the outer elements see a quite different environment than the inner elements, the scan reflection

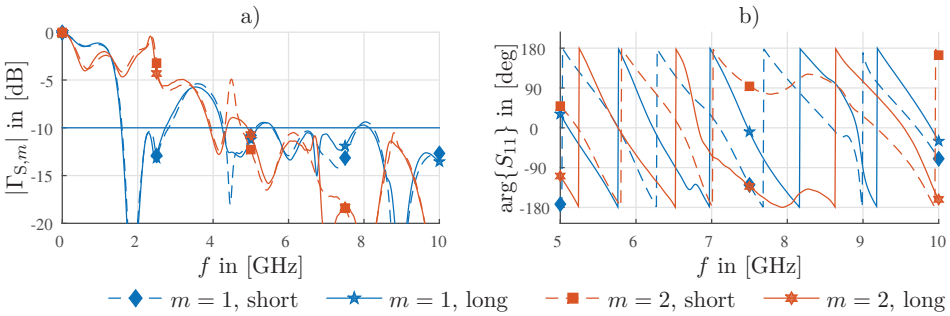

Fig. 7.7: Simulated scan reflection coefficient of ATSA array elements.

between outer and inner elements differ to a large degree in both phase and magnitude.

In the context of sub-array design, it is however not the scan reflection coefficient observed at the individual antenna elements, but the total reflection coefficient observed at the input of the corporate feed network which is of interest. Assuming an ideal corporate feed network with equi-phase and -amplitude excitation, the total reflection coefficient of the four-element sub-array $\Gamma_{\text{sub.}}$ can be expressed by [MG5]

$$\Gamma_{\text{sub.}} = \frac{1}{2}\left(\Gamma_{S,1} + \Gamma_{S,2}\right). \tag{7.6}$$

The total reflection coefficient observed at the input of an ideal corporate feed network connected to the four-element finite sub-array is illustrated in figure 7.8. Note the remarkable phenomenon, that $\Gamma_{\text{sub.}}$ is below the scan

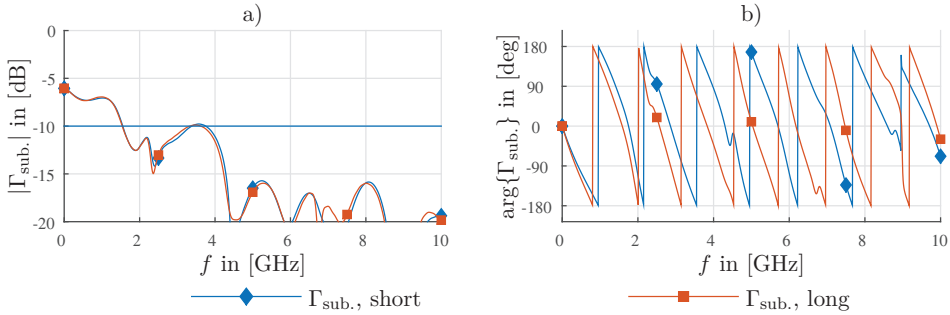

Fig. 7.8: Simulated total reflection coefficient of ATSA sub-array.

reflection coefficients observed at the individual antenna elements and that

the total reflection is below –10 dB already at 4 GHz. This can be reasoned by looking at the phases of $\Gamma_{S,m}$ shown in figure 7.7 b). The phase differences of the reflection coefficients of the outer and inner elements are such, that they interfere destructively at the input of the ideal corporate feed network and the total reflection coefficient is reduced.

The simulated realized gain of the short and long four-element sub arrays is shown in figure 7.9. In both simulations the BC_{Rear} was set to PEC, resem-

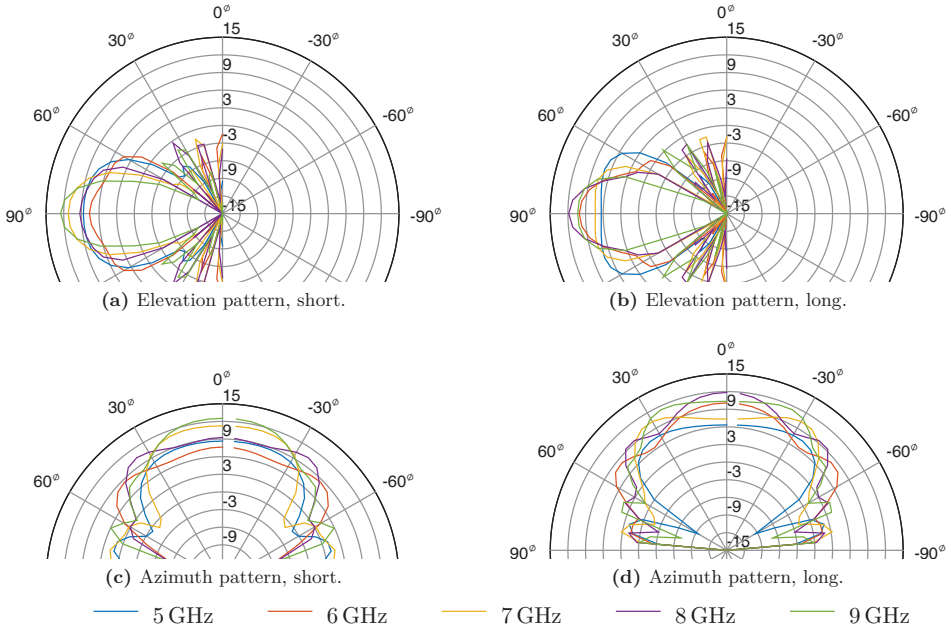

(a) Elevation pattern, short.

(b) Elevation pattern, long.

(c) Azimuth pattern, short.

(d) Azimuth pattern, long.

Fig. 7.9: Simulated realized gain of short sub-array.

bling the case of an infinitely large PEC reflector. It can be seen from both realized gain plots that the sub array exhibits the desired relatively narrow elevation pattern and wide azimuth pattern. The sub-array pattern has its maximum in broadside direction. The maximum gain across the frequency range from 5-9 GHz is between 12 dBi and 6 dBi for both the short and the long sub-array. However, whereas for the short sub array maximum gain occurs at 9 GHz and minimum gain at 6 GHz, the maximum gain for the long sub-array occurs at 8 GHz and the minimum Gain at 5 GHz. In addition, it can be seen that a breakdown in broadside gain of about 0.75 dB and a distortion of the pattern shape occurs for the long element at 5 GHz. The 3 dB elevation beamwidth is in the range of 22 ° to 58 ° for the short sub-array and

in the range of 22 ° to 68 ° for the long sub-array.

Since it is only the length of the feed which is different between the long and the short sub array designs, the differences in radiation can be accounted to the different spacing between the radiating part, the tapered section, and the PEC boundary at BC_{rear}. Although this spacing has hardly any influence on the return loss, it strongly influences radiation. The different radiation patterns of the long and short sub arrays can thus be accounted to the fields reflected from the PEC backing. Depending on the physical spacing of the radiating structure to BC_{rear} and the frequency, the fields directly radiated by the sub array elements interfere with the fields reflected at BC_{rear}. Consequently if the physical spacing is changed by a different selection of l_{feed} constructive and destructive interference of both fields occur at different frequencies, explaining the differences between the radiation patterns of the long and short sub arrays. It is thus of crucial importance to consider and control the effects of any conducting background on the radiation of the sub array elements.

7.4 Feed Network

To realize the necessary equi-phase and -amplitude UWB corporate feed network, a modified compact wideband ring coupler originally proposed in [139] is used as basic building element. Its geometry is illustrated in figure 7.10 a). The wideband ring coupler is used as power combiner by terminating the dif-

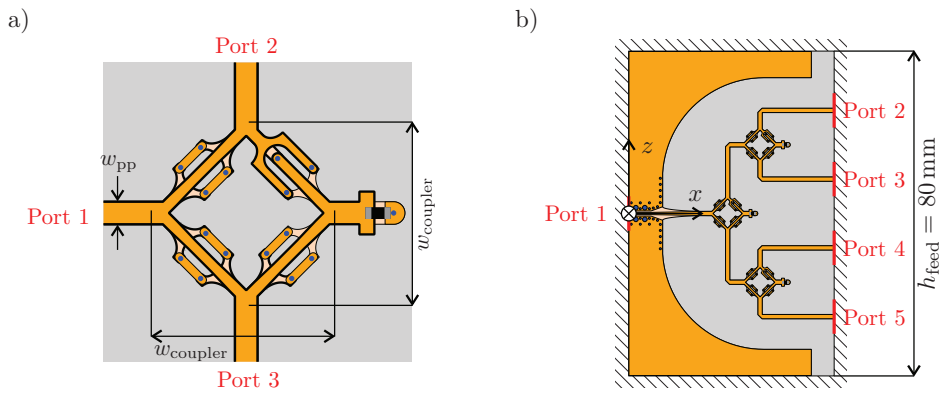

Fig. 7.10: Layout and simulation geometry of a) a single power combiner and b) the complete feed network.

ference port using a 50 Ω surface-mount device (SMD) resistor of case-size 0402. This UWB hybrid ring coupler is inherently based on parallel-plate transmission line technology and hence perfectly suited for realizing the feed network of the ATSA sub-array module, since no transition to e.g. microstrip line technology is necessary. Classical approaches of power combiners in planar transmission line technology are the T-junction and the multi-stage Wilkinson power divider. However, whereas the T-junction indeed is of small size it suffers from large return loss and only little isolation between the output ports [MG5]. The multi-stage Wilkinson power divider in contrast can be designed to have good wideband performance, but its size is too large for integration in the sub-array module with closely spaced elements. The size of the proposed power combiner is only $w_{\text{coupler}} = 8.83\,\text{mm}$, corresponding to $0.26\lambda_{9\text{Ghz}}$. Consequently, the compact feed network enables the required dense sub-array element spacing.

The simulated S-parameters of the power combiner are shown in figure 7.11. As shown in a) the transmission loss from both antenna ports $m = 2, 3$ to

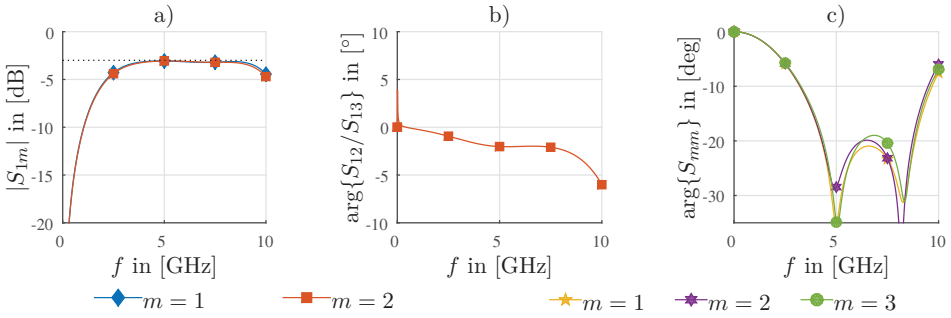

Fig. 7.11: Simulated power combiner parameters.

the sum port is less than $S_{1m} = -3.5\,\text{dB}$ in the range 3.3-9.2 GHz. The phase difference between both antenna ports is shown in b). It is less than 5 ° up to 10 GHz. The return loss on all three ports is shown in c). It is below –10 dB in the range 3.3-9.6 GHz.

Using the wideband power combiner a corporate feed network is designed. It is illustrated in figure 7.10 b). The complete feed network is designed in parallel plate transmission line technology. The transmission lines connecting the power combiners as well the feed network to the antenna ports all have a width of $w_{\text{pp}} = 1.05\,\text{mm}$ and thus have an impedance of 50 Ω. A single tapered parallel plate to microstrip transition is used to interface the

feed network to a sub-miniature-A (SMA) connector at port 1. Around port 1 a solid metallization at the top and bottom layers of the substrate is used as groundplane. The particular shape of the ground plane metallization is used to integrate each sub-array into a metallic housing. The total height of the feed network is $h_{\text{feed}} = 80\,\text{mm}$. To measure the performance of the feed network, the test circuit shown in figure 7.12 is manufactured. Here,

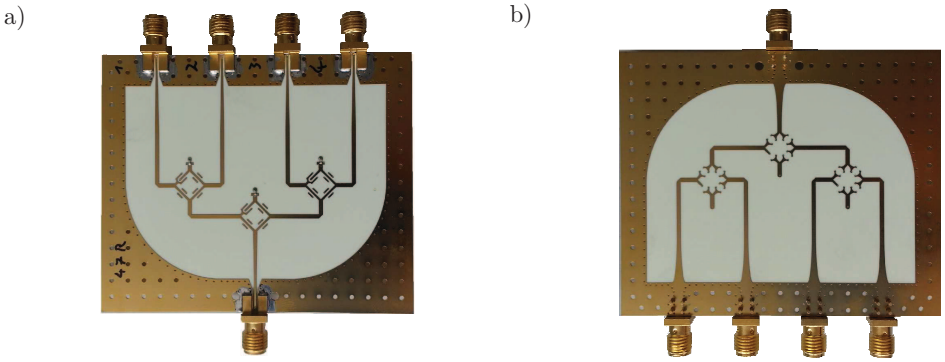

Fig. 7.12: Picture of feed network test circuit. a) view from top, b) view from bottom.

also tapered parallel plate to microstrip transitions are used to interface the antenna ports with SMA connectors. The measured transmission from port 1 to the antenna ports is shown in figure 7.13 a). The insertion loss from port 1 to each antenna port is about –8 dB and hence 2 dB below the theoretical limit of –6 dB for an ideal loss less corporate feed network. The measured phase differences between port 2 and the other antenna ports is shown in figure 7.13 b). The maximum phase error is 7.6 °.

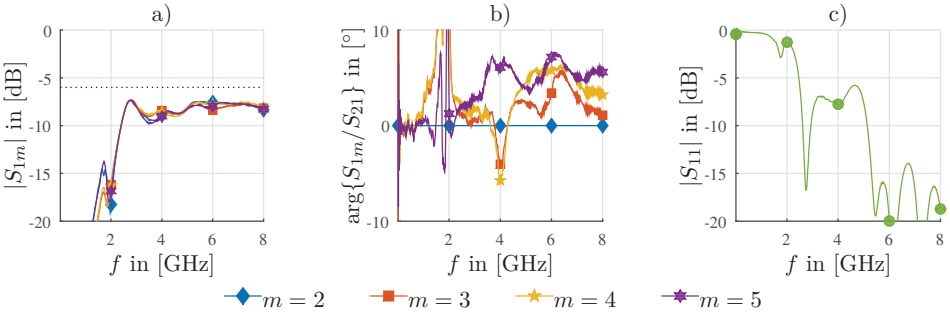

Fig. 7.13: Measured feed network parameters.

7.5 Subarray Module

The sub-array module is constructed by integrating the feed network illustrated in figure 7.10 with the sub-array antenna illustrated in figure 7.6 on a single PCB. A picture of the manufactured sub-array PCB is shown in figure 7.14. The overall height of the sub-array PCB is 80 mm, the length of the short antenna PCB is 107 mm and of the long antenna PCB 112.8 mm.

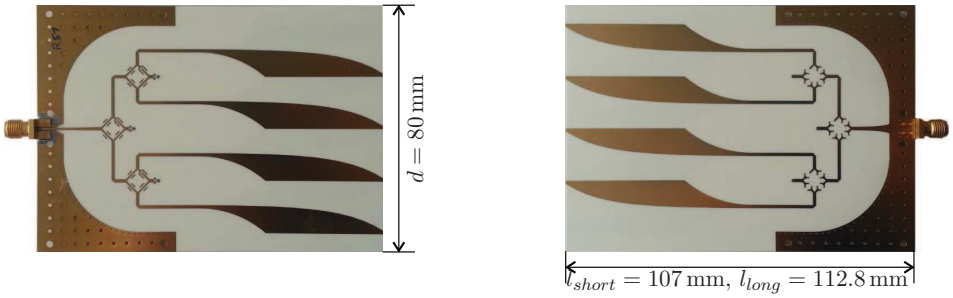

Fig. 7.14: Layout of single ATSA antenna element.

As shown in figure 7.15, the sub array module PCB is then integrated into a aluminum housing, which covers the feed network area. As illustrated in figure 7.15 a) the housing consist of two shells, one for each side of the sub array PCB. Each shell has a thickness of 10 mm and a size of $80\,\mathrm{mm} \times 45\,\mathrm{mm}$,

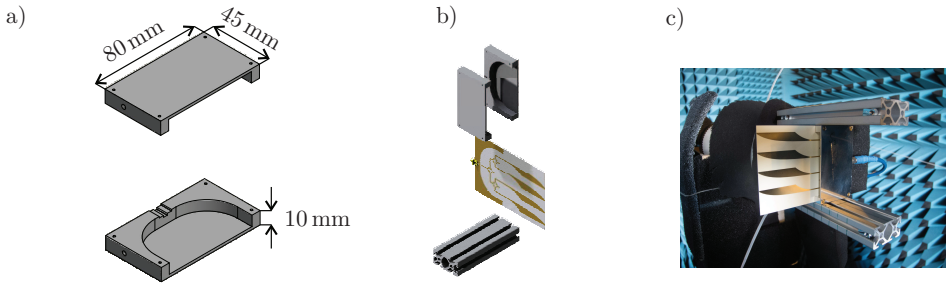

Fig. 7.15: Layout of single ATSA antenna element.

such that exactly the feed network area is covered. Above the feed network a circular-shaped cavity of thickness 8 mm is milled into the housing shells, such that the fields on the above the substrate are not disturbed. The housing is used for EM shielding of the feed network if several sub-arrays are placed next to each other as well as for providing the option to mount the

sub array module on a modular aluminum profile rail system, as illustrated in figure 7.15 b). The overall thickness of single sub array module thus corresponds to twice the housing shell thickness plus the thickness of the sub array PCB substrate. For the selected RO4360 substrate with $t_{\text{subs}} = 0.508\,\text{mm}$ the overall sub array module thickness thus is 20.508 mm. A picture of a single sub array module mounted in between two aluminum profiles is shown in figure 7.15 c).

To simulate and measure the radiation characteristics of the sub array module, the setups shown in figure 7.16 a) and b) are used. As mentioned during

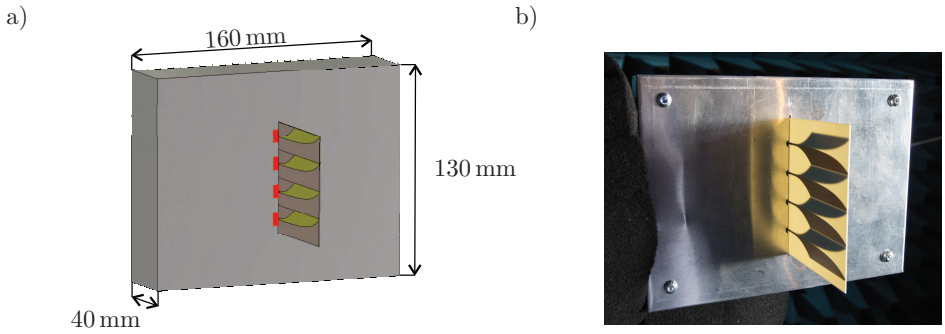

Fig. 7.16: Layout of single ATSA antenna element.

the discussion of the preliminary design considerations, a metallic shielding should be used to decouple the radiating part of the ULA from other system components behind the antenna array. Therefore a box made from aluminum sheet is used. The box has a size of $W \times H \times T = 160\,\text{mm} \times 130\,\text{mm} \times 80\,\text{mm}$. It is put over the sub array module mounted on the aluminum profile. It can be seen from figure 7.16 b) that long slit and four holes cut in the box front side allow the sub array PCB to protrude through the aluminum sheet. The holes are of diameter 5 mm and ensure that the fields propagating on the parallel-plate transmission lines between feed network and sub array are not disturbed.

The corresponding simulation model is illustrated in figure 7.16 a). It is derived from the sub array simulation model with infinite reflector illustrated in figure 7.6 by setting all boundary conditions to open and modeling the shielding box as aluminum brick. All boundaries of the simulation domain have a certain distance to the simulated geometry, such that an accurate computation of the radiated fields is ensured.

The measured as well as simulated radiation patterns of the long and short sub array module are shown in figure 7.17. Radiation measurements were conducted in an anechoic chamber of size $L \times W \times H = 6.8\,\mathrm{m} \times 4.5\,\mathrm{m} \times 6.8\,\mathrm{m}$. The substitution method with a calibrated Satimo SH2000 as reference antenna was used. It can be seen that an acceptable agreement exists between the simulated and the measured realized gain. As a source for the difference between simulation and measurement, at first the assumption of an ideal corporate feed network in the simulation can be identified. In the simulation setup shown in figure 7.16, the sub array is excited with four identical power onto each antenna element port. Power waves reflected from the antenna elements are absorbed in the reference impedance of each port. In contrast the realized feed network introduces an amplitude and phase difference onto the power wave incident on each antenna element. The realized feed network furthermore introduces an additional insertion loss of about 2-3 dB, hence the measured realized gain is generally lower than then simulated realized gain. In addition the antenna elements are not perfectly isolated, such that waves reflected at the antenna elements can couple to the other antenna elements through the feed network. Due to the large frequency range and the complicated structures, it is however not feasible to precisely include the feed network in the field simulation. As a second source of error, all parasitic effects in the measurement chamber can be mentioned. In contrast to the CST MWS simulation, where the geometry illustrated in figure 7.16 is modeled to be surrounded by free space, the measurement setup includes various fixtures, a relatively large positioner, a non-ideal quiet-zone as well as other parasitic elements.

By comparing the radiation patterns of the short and the long sub array shown in figure 7.17 it can be seen that the reflected fields also have a large influence for the case of a finite reflector. The effect is present both in the measurements and the simulations. To further stabilize the radiation pattern the option of suppressing the reflected field by covering the aluminum sheet with an absorbing material is considered. Therefore, as shown in figure 7.18, a 1 cm thick layer of ECCOSORB AN-73 is put on the aluminum sheet. The measured radiation patterns of both the short and long sub-array modules including the absorptive layer are shown in figure 7.19 and figure 7.20. It can be seen that the radiation pattern can greatly be improved by reducing the reflection of the housing.

a) - d) Long Subarray Module

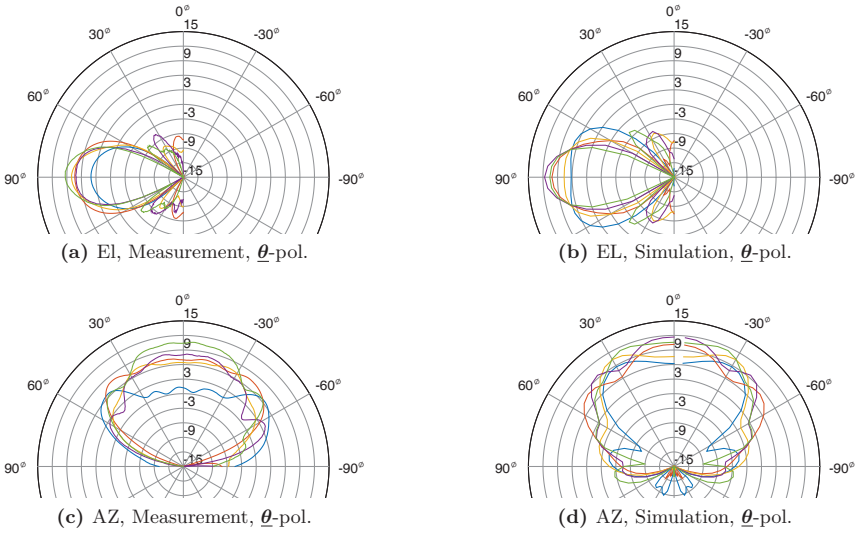

(a) El, Measurement, $\underline{\theta}$-pol. **(b)** EL, Simulation, $\underline{\theta}$-pol.

(c) AZ, Measurement, $\underline{\theta}$-pol. **(d)** AZ, Simulation, $\underline{\theta}$-pol.

e) - h) Short Subarray Module

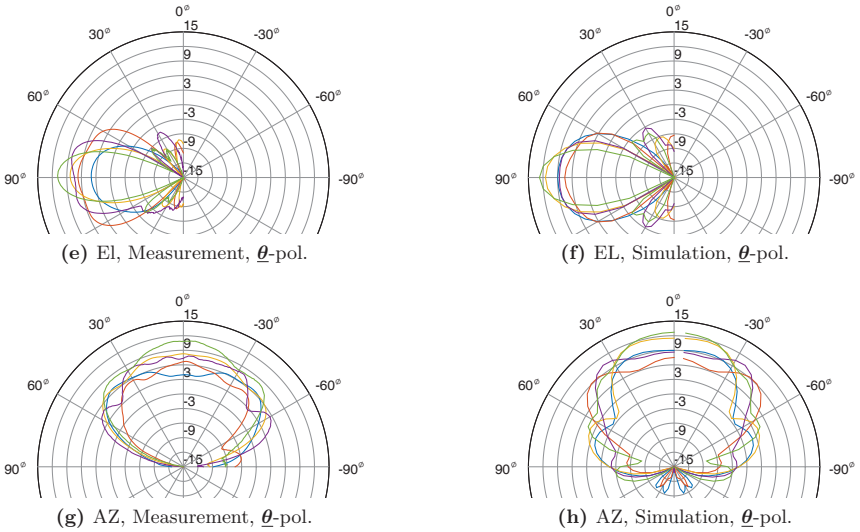

(e) El, Measurement, $\underline{\theta}$-pol. **(f)** EL, Simulation, $\underline{\theta}$-pol.

(g) AZ, Measurement, $\underline{\theta}$-pol. **(h)** AZ, Simulation, $\underline{\theta}$-pol.

5 GHz 6 GHz 7 GHz 8 GHz 9 GHz

Fig. 7.17: Measured (right) and simulated (left) realized gain of long sub array module. Elevation pattern (top) and azimuth pattern (bottom).

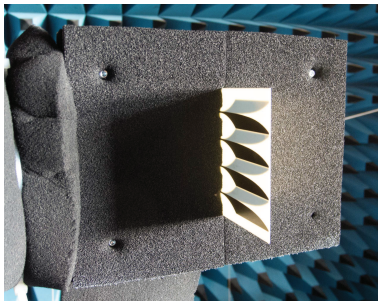

Fig. 7.18: Absorber used to stabilize radiation pattern of ATSA antenna element.

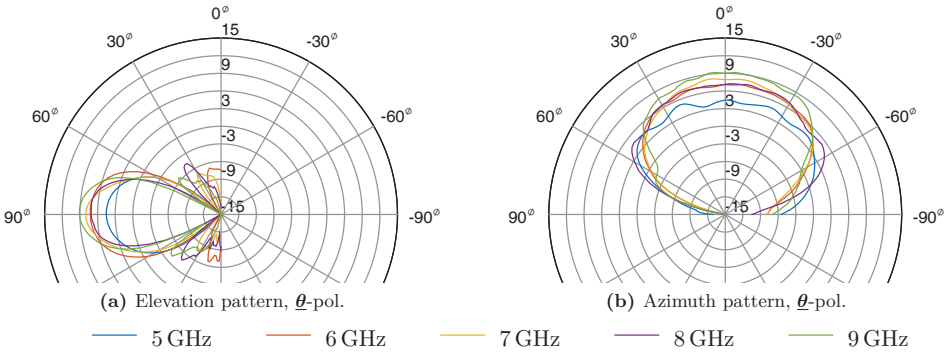

Fig. 7.19: Measured realized gain of single long L1 Element with absorber.

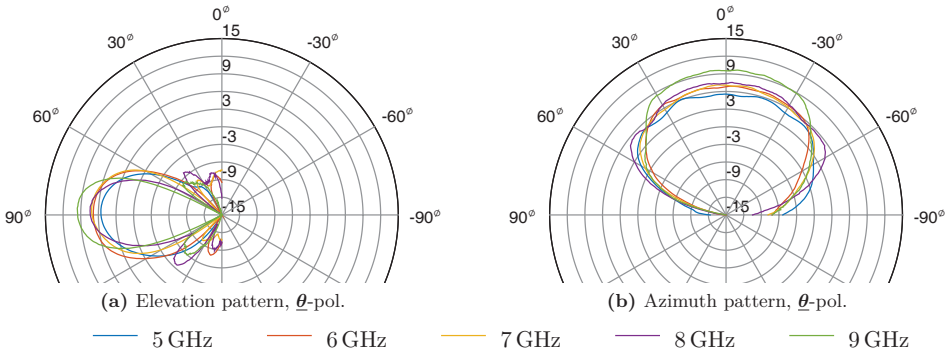

Fig. 7.20: Measured realized gain of single short S3 Element with absorber.

7.6 ATSA Array Design

From the sub array modules a ULA as illustrated in figure 7.2 is constructed by placing several modules next to each other on the aluminum profile rail. The minimum sub array spacing corresponds to the module thickness and for the particular substrate thickness and housing shell thickness a minimum spacing of $d_{\mathrm{el}} = 20.6\,\mathrm{mm}$ can be realized. Note that it is the spacing of the sub-arrays which corresponds to the element distance in the ULA and hence is referred to by d_{el}. Consequently, the minimum required element spacing of $d_{\mathrm{el}} = \lambda_l/2 = 25\,\mathrm{mm}$ for the WB radar system scenarios can be achieved. As illustrated in figure 7.21, various ULA configurations can be used.

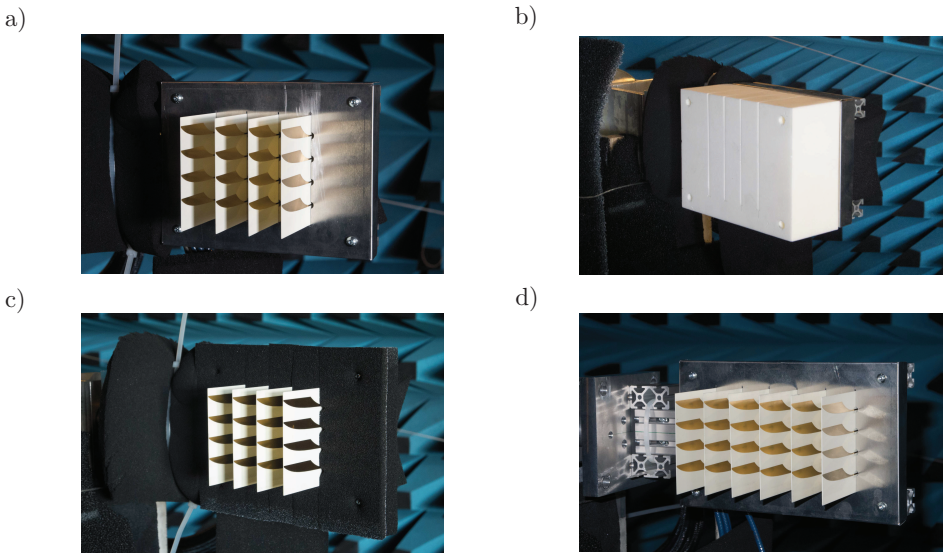

Fig. 7.21: ULA constructed from ATSA sub-array module. a) four-element ULA, b) four-element ULA using absorber, c) four-element ULA suing Rohacell radome, and d) six-element ULA.

A ULA based on four elements in front of the aluminum box is shown in figure 7.21 a). To introduce the necessary protection from mechanical stress and environmental influences, it is shown in b) how a protective radome of rigid foam material can be used. The particular radome is made from ROHACELL IG 71 HF, a material with has a relative permittivity close to one in the frequency range of interest. Recesses which exactly fit the sub array

PCBs are cut into a foam brick and the foam brick is put over the array. It is tightly connected with aluminum profile rails using Nylon screws. Such the whole antenna structure is covered with ROHACELL and the antenna PCBs are protected mechanical influence as well any bending of the relatively thin PCBs is suppressed. As shown in figure 7.21 c), also in the case of an array absorbing material can be used to stabilized the radiation pattern. Due to the modular design, the array size in terms of array elements can also be increased. Figure 7.21 d) for example shows a six-element ULA with element spacing $d_{\mathrm{el}} = 25\,\mathrm{mm}$. Although increasing the number of elements could be used to improve DOA estimation if more RX channels are available, the particular array shown in d) uses only the four inner sub arrays. The two outer sub arrays are terminated in their reference impedance. This is a traditional method known to stabilize the radiation patterns of the inner elements and to increase the DSP performance of the array [140].

The measured realized gain of the ULAs from figure 7.21 is shown in figure 7.22. The radiation patterns are shown for the desired main direction $\theta = 0\,^\circ$ of radiation and are evaluated in for $\varphi = -90{-}90\,^\circ$ and $f = 5{-}9\,\mathrm{GHz}$. Note the particular switch of the φ-axis labels with negative angles on the right, and positive angles on the left. This is used to match the plots shown with the intuitive observation one would experience residing at the array coordinate origin and looking into x-direction: a wave impinging from a DOA in the range $\varphi = 0\,^\circ \ldots 180\,^\circ$ will come from the left, and vice versa a wave with a DOA in the range $\varphi = 0\,^\circ \ldots -180\,^\circ$ will come from the right.

The radiation patterns of the four-element ULA from figure 7.21 a) are illustrated in figure 7.22 a). First of all it can be seen that the realized gain of each element has a distinct shape in the φ-frequency-plane. On the one hand side this pattern distortion can be accounted to mutual coupling between the sub arrays. It is obvious that large pattern distortion occurs at relatively low frequencies, e.g. around 5 GHz, where the electrical spacing between the sub arrays is the smallest. For example here the main beam of the leftmost element $m = 1$ is not in broadside direction, but directed towards $\varphi \approx 45\,^\circ$. With increasing frequency the electrical spacing between the sub arrays increase and consequently the pattern distortion effects due to mutual coupling are reduced. Thus the main lobe of the leftmost element moves inwards with rising frequency and for 9 GHz the main lobe direction approximately corresponds to broadside radiation. In the particular case of the ULA with finite ground plane it is however not only mutual coupling which may be responsible for the pattern distortion. In addition also the

different relative position on the ground plane may introduces pattern distortion effects. Secondly the ULA symmetry is clearly visible from the measured realized gain: while close to 5 GHz a maximum of the left element $m = 1$ occurs at $\varphi \approx 45\,^\circ$, the corresponding maximum occurs at $\varphi \approx -45\,^\circ$ for the right element $m = 4$. Similarly the shape of the radiation pattern in the range 6.5-8 GHz also remarkably reflects this array symmetry. As a third observation it can be seen from the radiation patterns of the four-element ULA that radiation is strongly frequency dependent: the gain does not only constantly increase with frequency but e.g. at 6.8 GHz as well as 8.5 GHz local minima of the gain exist.

The use of a ROHACELL radome does hardly influence the radiation pattern, as can be seen from the measurement results given in figure 7.22 b). The use of absorbing material however has a large influence on the realized gain of the active array elements: the frequency dependence of the gain is smoothed. This indicates that the reflections on the metallic box behind the ULA superimpose with the main radiation of the antenna elements. Depending on the frequency this leads to a constructive or destructive interference and the particular frequency dependence of the radiation pattern results. The use of absorber eliminates attenuates those reflections resulting in the smooth patterns shown in figure 7.22 c). Since the main part of the radiation pattern can be accounted for direct radiation of the elements, the overall gain is hardly reduced by the use of the absorbing material.

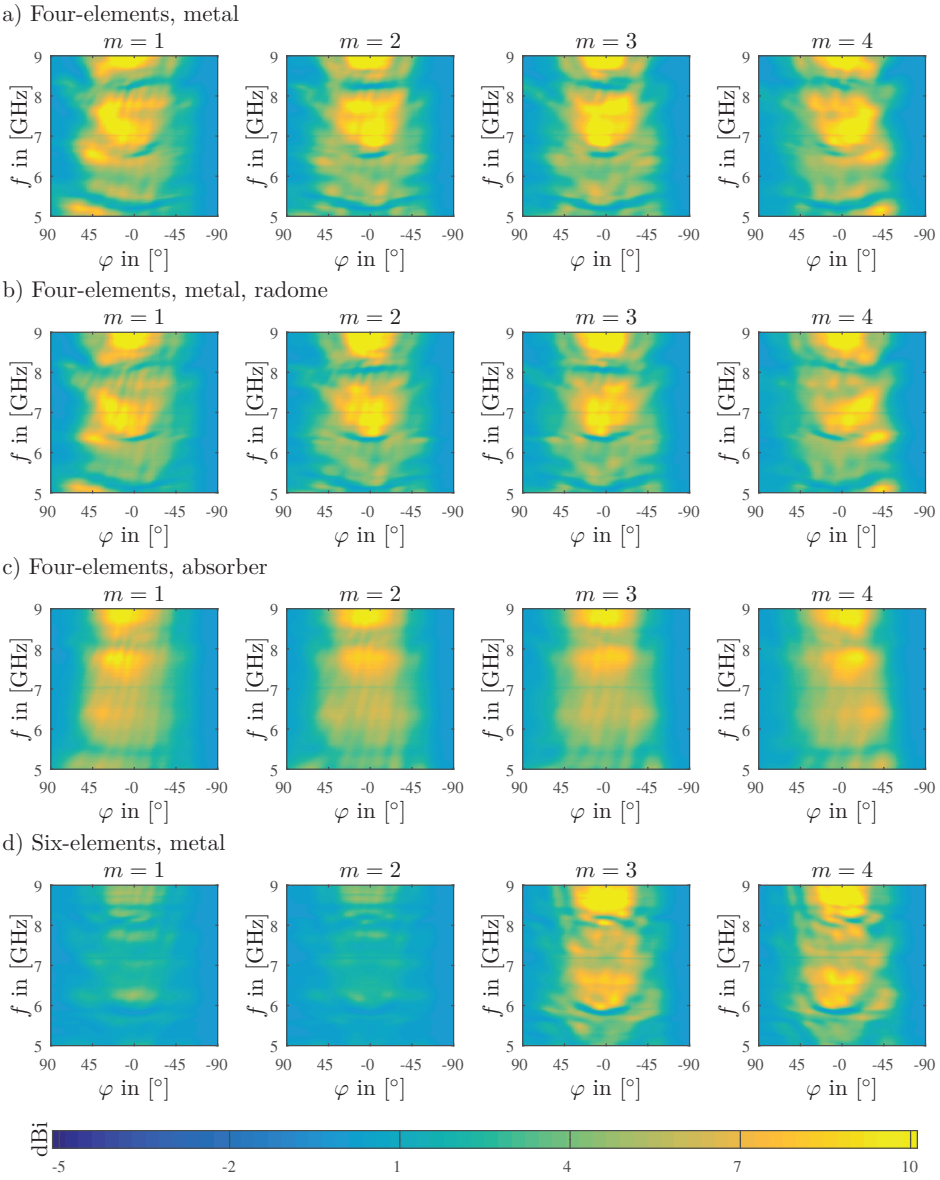

Fig. 7.22: Active element realized gain of ULAs shown in figure 7.21 a) - d).

7.7 DSP Performance

To evaluate the DSP performance of the ULA, simulation results from the simulation setup shown in figure 7.23 are used. Four the sub arrays from figure 7.6 are placed along the y-coordinate at a distance of $d_{\mathrm{el}} = 25\,\mathrm{mm}$, corresponding to an electrical separation of λ_l at the sweep start frequency of 6 GHz of the WB radar system scenarios. The four sub arrays are backed by an aluminum brick of size $W \times H \times T = 160\,\mathrm{mm} \times 130\,\mathrm{mm} \times 80\,\mathrm{mm}$. The origin of the global array coordinate system is at the center of the array.

To simulate the active element effective height of each sub array E-field probes with $\underline{\boldsymbol{\theta}}$- and $\underline{\boldsymbol{\varphi}}$-polarization are placed around the local coordinate origin (compare figure 7.6) of each sub array element. As illustrated in figure 7.23, the probes are placed on a the surface of a sphere in the range $\theta = 0 - 90\,^\circ$ and $\varphi = 0 - 360\,^\circ$. The spacing of the probes is 10 $^\circ$ in each coordinate direction. Since the array has perfect symmetry with with regard to the xy-plane it is sufficient to analyze only the upper hemispherical region.

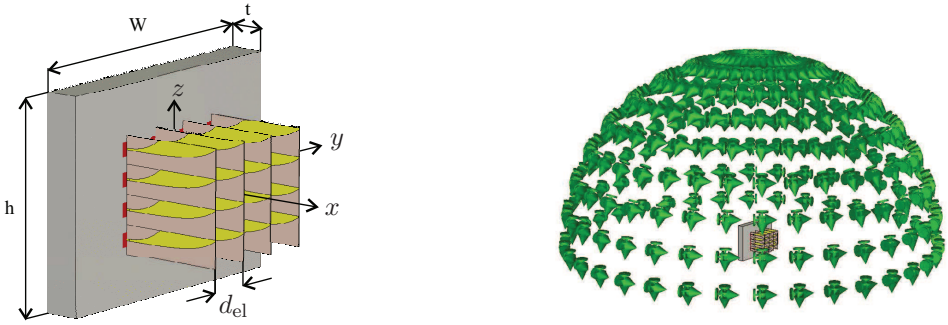

Fig. 7.23: Simulation model of the four-element ATSA antenna array with finite brick reflector. The coordinate origin is the center of antenna element $m = 1$. In total 720 Θ- and Φ-polarized E-field probes are placed at $\theta = [0°, 10°, \ldots, 90°]$ and $\varphi = [0°, 10°, \ldots, 360°]$

Generally one simulation per sub array is used to determine its active element effective height. Therefore all four elements of each sub array are simultaneously excited with an incident power wave, resembling the case of a perfect corporate feed network. To reduce simulation time, only the two sub arrays $m = 1$ and $m = 2$ are simulated. The effective height of the remaining two elements is then obtained by exploiting the ULA symmetry (5.6). For each sub array the power wave incident on and leaving all ports as well as the

E-fields recorded at the probe locations are stored. Those results are then post processed in MATLAB® as described in chapters 4 and 5, in particular to obtain the active element effective height of each sub array for each probe direction. To obtain the antenna element effective height for arbitrary angles θ, φ a linear interpolation is applied to the active element effective heights. As shown in chapter 6 the AM and PM which is introduced into the beat signal is corresponds to the co-polar component of the active element effective height. Since the sub array elements are mainly $\underline{\boldsymbol{\theta}}$-polarized only the case of $\underline{\boldsymbol{\theta}}$-polarized incident target returns is examined.

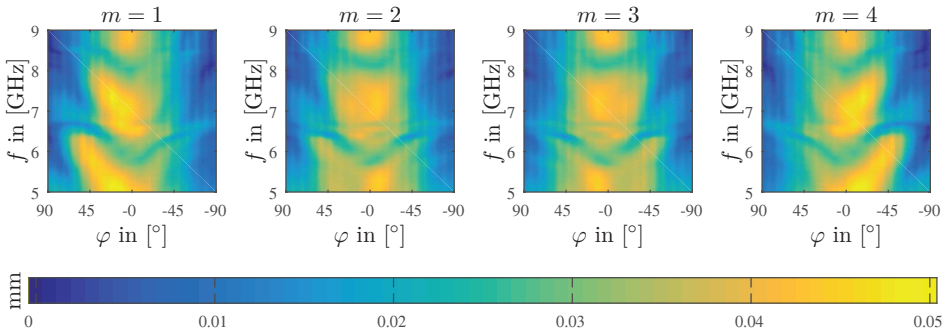

Fig. 7.24: AM^{QS} of ATSA sub-arrays in four-element ULA. $\theta = 90\,°$.

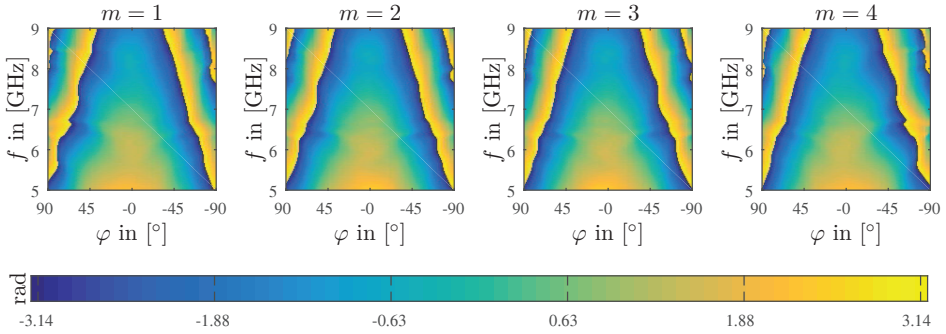

Fig. 7.25: PM^{QS} of ATSA sub-arrays in four-element ULA. $\theta = 90\,°$.

The AM^{QS} functions obtained for the four sub arrays are shown in figure 7.24. As a first observation, the good agreement to measured realized gain from figure 7.22 is obvious. With regard to the frequency dependence, it can be seen that a maximum occurs for large frequencies from 8.5-9 GHz, a minimum at about 8.25 GHz, and a next maximum between 7-8 GHz. Clearly

it is visible how due to mutual coupling the main lobe is tilted outwards from broadside direction, especially at lower frequencies. The existing difference between measured element gain and simulated AM^{QS} can mainly be accounted to non-idealities of the feed network, which are not accounted for in the simulation model. On a closer look a vertically striped pattern can be identified in the plots of figure 7.24. Since the period of this pattern is $10\,^\circ$ it can be concluded that this pattern is due to the spatial linear interpolation of the simulation results. The corresponding PM^{QS} functions are shown in figure 7.25. It can be seen that PM^{QS} is dependent on both the frequency as well as the DOA φ. The frequency dependence of PM^{QS} is rather smooth. It mainly is a function monotonically decreasing with frequency. It can be seen that a rather large variation of phase with φ is present, where the phase seems to monotonically decrease with increasing φ. The diagonal lines in the plots are phase jumps which occur when the measured phase exceeds $\pm\pi$. This effect is typically based on an offset between the antenna's phase center and the origin of the antenna element's local coordinate system origin.

For the DOA estimation experiment the look direction range is limited to $\theta = \pm 60\,^\circ$ where the array element effective height, respectively the active element realized gain, is sufficiently large. The spatially filtered signals obtained from the WB Bartlett and MVDR beamformers assuming an ideal ULA are shown in figure 7.26. A single target return impinging from four different azimuth positions $\varphi = 0\,^\circ, 25\,^\circ, 45\,^\circ, 60\,^\circ$ with a known $\theta = 90\,^\circ$ is used. The plots of the spatially filtered signal magnitudes are normalized to the magnitude of the strongest beat signal, which is given by $0.5 \max_n\{a_n^{\mathrm{tgt}}\}$, compare (6.8) and (6.9). If only a single target is present this reduces to $0.5a_1^{\mathrm{tgt}}$. The color scales of the plots are selected, such that the additional increase in amplitude by the beamforming algorithms is taken into account. As such, e.g. the MVDR beamformer normally being constrained to unity gain in the look direction will exhibit a non-unity gain if a mismatch between the underlying model and the real model exists. Since the output of the Bartlett beamformer would be weighted by the effective height of the receive elements, its spatially filtered output signal (3.33) is normalized to the effective height of an ideal isotropic antenna from (4.30).

It can be seen that due to the mismatch between the LP model and the true array characteristics two effects occur: Firstly the amplitude of the spatially filtered signal is not constant along the sweep duration. This effect is especially clear for the Bartlett beamformer, where it easily can be seen by com-

paring figure 7.24 with the results from figure 7.26 how the magnitude of the spatially filtered signal is directly influenced by AM^{QS} for the corresponding DOA φ. The AM effect is also present in the spatially filtered signal of the MVDR beamformer. However, since the weight vectors of the MVDR beamformer do not directly correspond to the complex conjugate of the steering vector a direct relation of the magnitude of the spatially filtered signal to AM^{QS} is not obvious. In addition to the AM along the sweep, it is obvious that the output of the Bartlett beamformer is also directly weighted by the element pattern. The larger the azimuth angle of the target return, the lower the gain of the ATSA antenna elements and the lower consequently the amplitude of the spatially filtered signal obtained from the Bartlett beamformer is. The MVDR beamformer automatically compensates for this loss due to the uniform-gain constraint present in the formulation of the weight vector. Secondly, it can clearly be seen that the look direction α_φ where the magnitude of the spatially filtered signal is maximum does not always correspond to the true DOA. This effect is especially eminent for the MVDR beamformer with its narrow main lobe. It can be seen how depending on the frequency the maximum of the spatially filtered signal magnitude winds around the dashed line indicating the true DOA φ. Clearly the existence of grating lobes with their particular structure for the ULA, as has been discussed in chapter 3, can be seen for $\varphi = 45\,^\circ$ and $\varphi = 60\,^\circ$. In addition the specific pattern due to the use of $P = 20$ frames for framed covariance matrix estimation is obvious.

The spatially filtered signals obtained from the WB Bartlett and MVDR beam formers now taking into account perfect array knowledge are shown in figure 7.27. As a first observation, the spatially filtered signal magnitude does not change much for the Bartlett beamformer. The AM present in the spatially filtered signal due to the varying active element realized gain still is present in the output signal. Since the weight vector of the Bartlett beamformer is normalized to unity l_2-norm (3.33), also the absolute magnitude does not change. In contrast, the use of a perfect array model in the MVDR algorithm and the unity-gain constraint lead to a spatially filtered signal with an amplitude corresponding to the expected $0.5a_1^{\mathrm{tgt}}$, note the change of the color scale for the MVDR algorithm. In addition it is eminent how the spatial distortion due to model mismatch is mitigated: The look direction with maximum signal magnitude corresponds to the true DOA. Clearly a performance loss for large DOAs is visible.

The spatial spectra obtained from the NB and WB beamformers are given

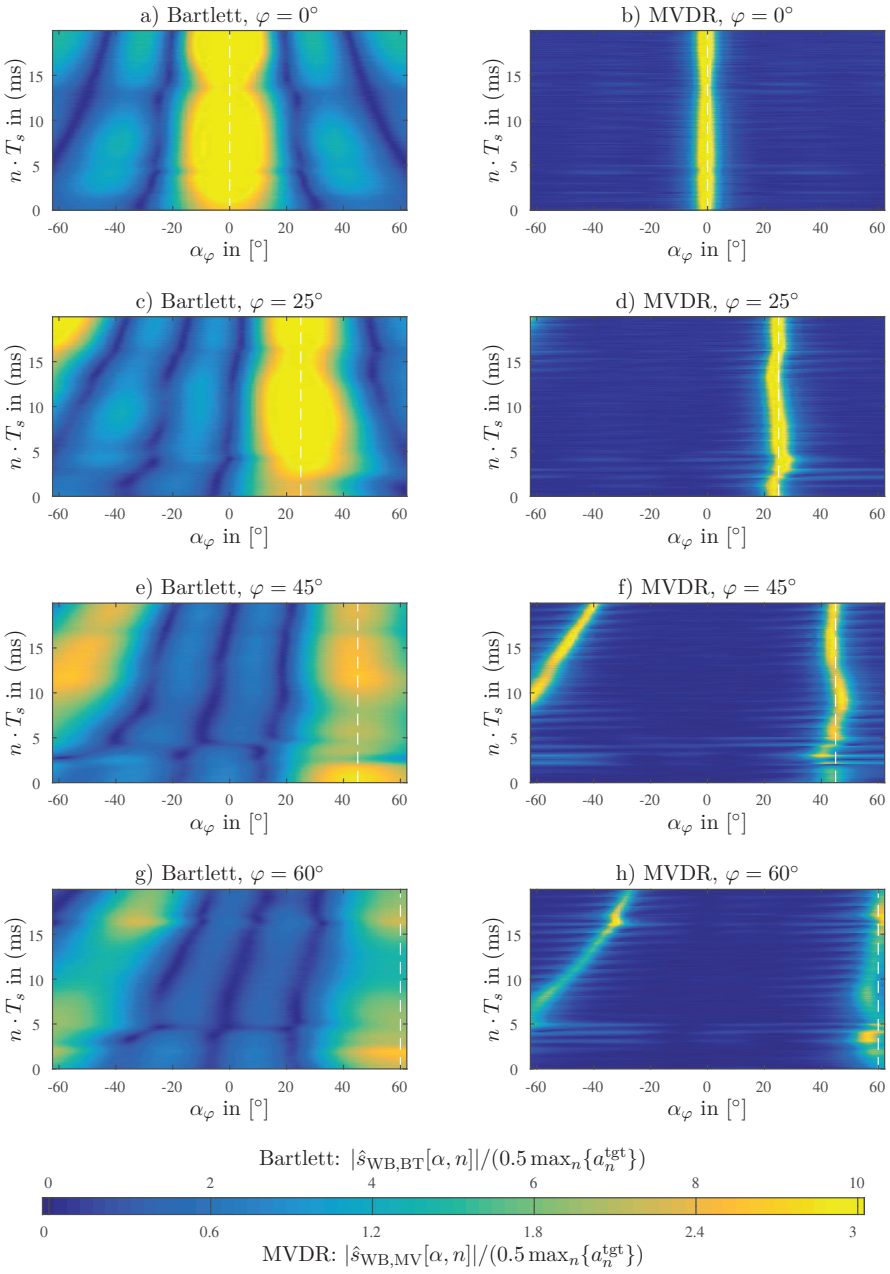

Fig. 7.26: Spatially filtered signals obtained from ULA using ideal array model. Array based on short ATSA antenna elements and metallic reflector. Single target at DOA $\varphi = 0\,°, 25\,°, 45\,°, 60\,°$ and $\theta = 90\,°$, distance $d^{\mathrm{tgt}} = 50\,\mathrm{m}$.

in figure 7.26 and figure 7.27. The superior performance of the WB beamformers over their NB counterparts is striking. Interestingly, although the spatially filtered signals without perfect array knowledge clearly showed a spatial distortion, hardly any difference between the spatial spectra with and without array knowledge is present. In both cases the peak position coincides with the true DOA. This can be reasoned on the averaging process which is used to compute the spatial spectra. Since without array knowledge the maximum magnitude of the spatially filtered signal winds around the look direction corresponding to the true DOA, sometimes having a positive and sometimes a negative deviation, the total error is averaged out when computing the spatial spectrum. When closely looking at the spatial spectrum for e.g. $\varphi = 45\,^\circ$ shown in figure 7.26 c) and figure 7.27 c), it can be seen that instead of a mismatch in peak position the model error thus only results in a slight increase of main lobe width.

The normalized FFTs taken from the spatially filtered signals along the look direction α_φ corresponding to the true DOA φ are shown in figure 7.30. For a large SNR of 30 dB, they illustrate the effect of array knowledge onto target distance estimation. When assuming an ideal array in the combined range and DOA estimation, the AM and PM introduced by the active element effective is also present in the spatially filtered beat signal. As a consequence, the position of the FFT maximum does not coincide with the true distance d^{tgt} of the target. For the particular example, the offset in peak position corresponds to a distance error of about 4 cm. In addition it can be seen that the sidelobe structure is distorted. Clearly the sidelobe distortion is more pronounced for the MVDR algorithm, where it was already seen from figure 7.26 and figure 7.27 that the model mismatch has a more significant influence. By using perfect array knowledge, both the range error as well as the distortion of the sidelobe structure is mitigated. This is due to the fact that by incorporation of perfect array knowledge, the PM can be eliminated from the beat signal. From the FFTs obtained at a small SNR of –20 dB, it can be seen that the processing gain of the FFT is not influenced by a model mismatch in the ULA case.

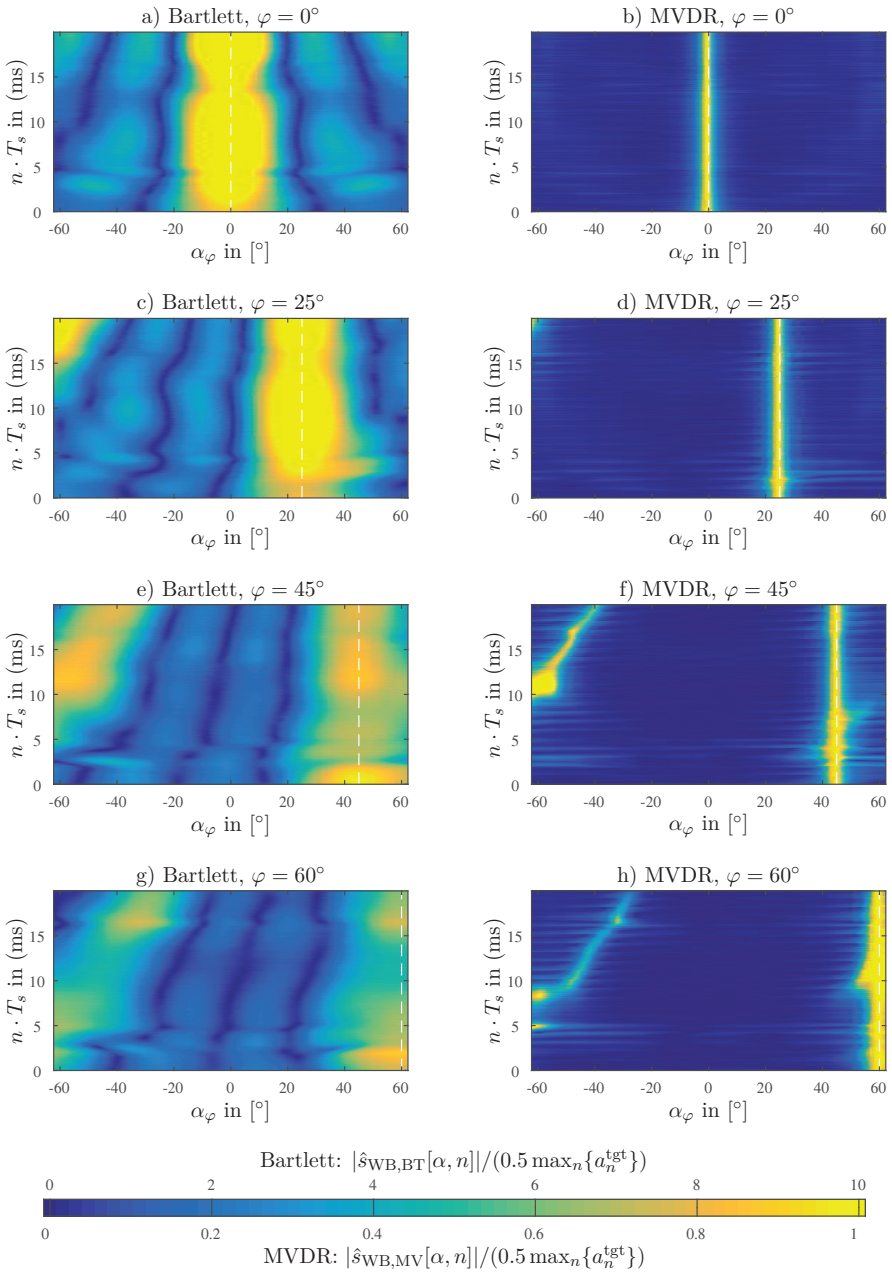

Fig. 7.27: Spatially filtered signals obtained from ULA using perfect array knowledge. Array based on short ATSA antenna elements and metallic reflector. Single target at DOA $\varphi = 0\,°, 25\,°, 45\,°, 60\,°$ and $\theta = 90\,°$, distance $d^{\mathrm{tgt}} = 50\,\mathrm{m}$.

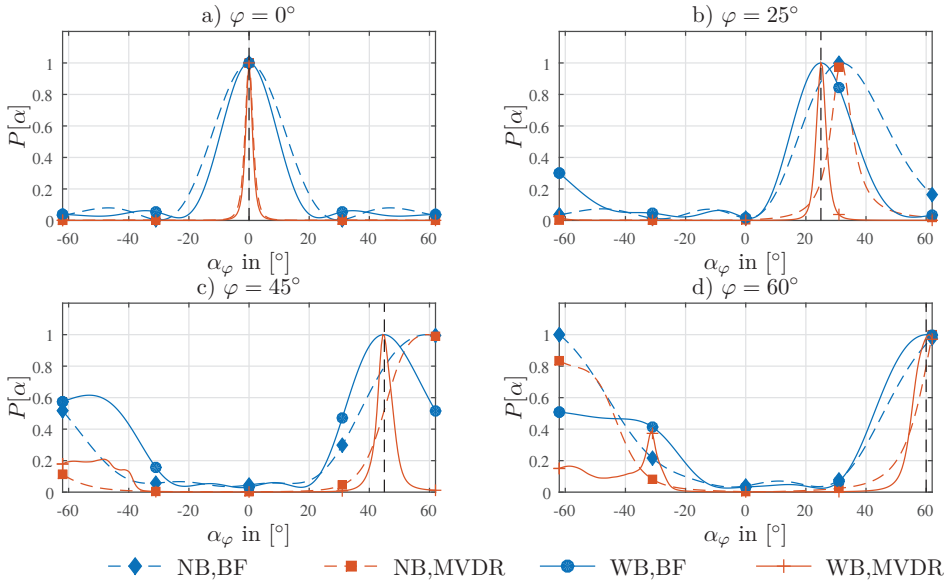

Fig. 7.28: Spatial spectra obtained from ULA using ideal array model.

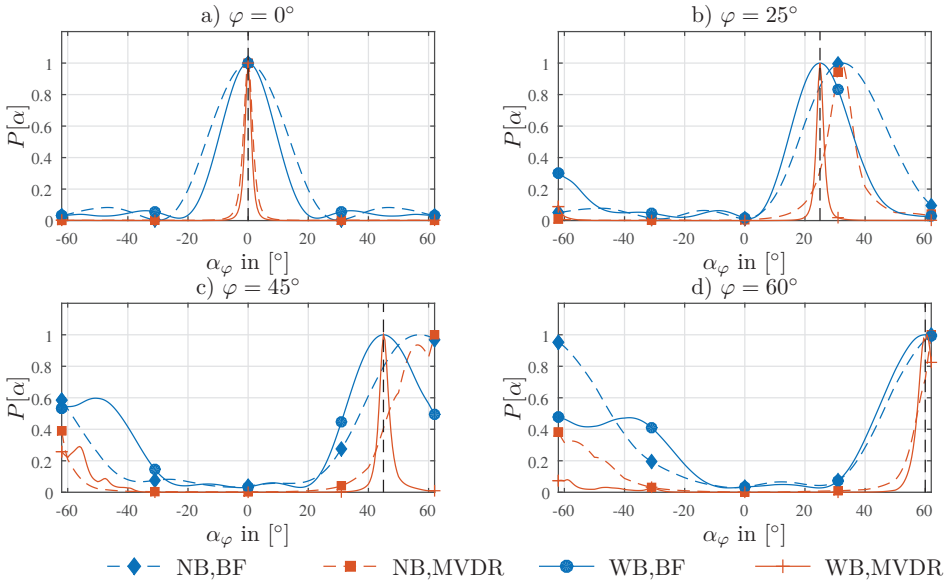

Fig. 7.29: Spatial spectra obtained from ULA using perfect array knowledge.

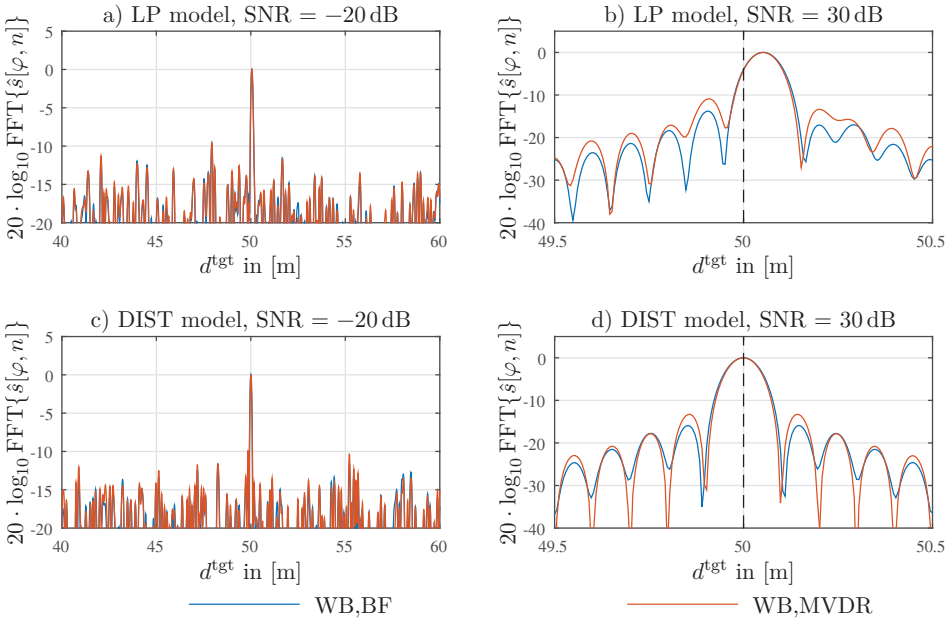

Fig. 7.30: Normalized range FFTs obtained from ULA. Single target at DOA $\varphi = 25\,^\circ$ and $\theta = 90\,^\circ$ and $\theta = 60\,^\circ$, distance $d^{\text{tgt}} = 50\,\text{m}$.

8 Design of a Small Circular Array Antenna

Similar to the ULA design it is the application scenario from figure 1.1 from which a design specification for the ULA is derived. First of all, the ULA should be mounted on the rooftop of an industrial vehicle - in the particular scenario a fork lift as illustrated in figure 8.1 a). Consequently the array will have to operate over a rather large conductive plane, which directly must be taken into account in array design. In contrast to the ULA, which remains at a fixed location once it is deployed, the ULA is deployed on a moving platform. The typical operation of a fork lift includes rapid movements, transitions between indoor and outdoor operation in all-weather conditions. The UCA thus must be robust towards acceleration and vibration and tolerant towards dust, rain, snow, condensation and defrost water. Furthermore it must be of compact size since typically structures protruding from the forklift are not acceptable from both an operational as well as a occupational safety perspective.

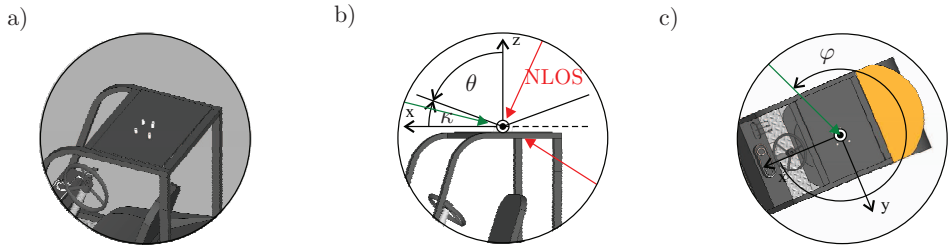

Fig. 8.1: Functional specification of UCA.

The specifications regarding the radiation characteristics of the UCA are illustrated in figure 8.1 b) and c). The elevation pattern should be relatively narrow with a maximum towards $\varphi = 90\,^\circ$ to increase the gain towards the RU along the LOS path. The antenna elements should be vertically polarized to be polarization-matched with the ULA at the RU. Parasitic reflections from the floor and the ceiling should be attenuated. The radiation characteristics and the DOA estimation performance of the array should be omni-directional in azimuth. Although it has been shown that a circular array geometry is favorable from for applications where uniform performance

at all azimuths is a necessity, the design of the array geometry as well as the array elements should include the possibility to examine different non-uniform and non-circular geometries.

The design of a small UCA based on a robust and size-reduced Monocone antenna element was proposed by the author in [MG1], [MG2], [MG8], [MG9]. In this chapter, a review of the UCA design concept as well as an experimental characterization and qualitative DSP performance analysis is presented.

8.1 Preliminary Design Considerations

Taking into account the conducive nature of the vehicle rooftop and the fact that the antenna should be directly mounted on the rooftop leads to the approach of considering the antenna as monopole. The impedance and radiation characteristics of a monopole which is mounted on an ideally infinite ground plane can be deduced from that of a Dipole of twice its length in free space [141]. This pattern can be derived analytically and is plotted in figure 8.2 for a Monopole of length $\lambda/4$ at 5 GHz, in the frequency range 5-9 GHz. It can be seen that in theory the monopole antenna on on infinite

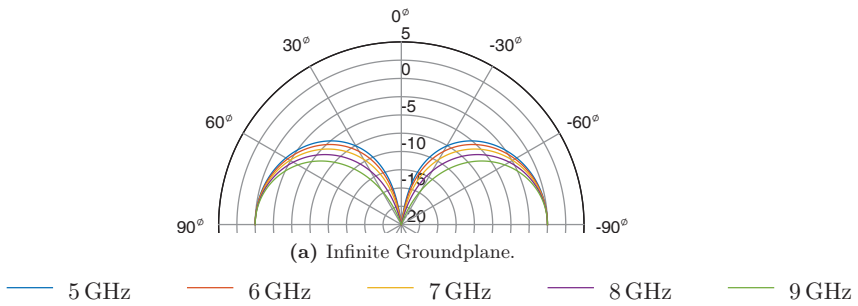

Fig. 8.2: Radiation pattern of monopole over infinite ground plane.

ground plane provides the desired radiation pattern: The maximum gain is in the horizontal plane and rapidly decreases for larger elevation angles. The practical implementation of the monopole antenna however will use a finite ground plane. While the exact size of the ground plane does have a minor influence on the monopole impedance if the size is at least 10 λ [141], it is a well-known fact that the radiation pattern is strongly influenced by the size and shape of the ground plane [141], [142]. In particular the radiation maximum will no longer be in the horizontal plane but occur for smaller θ.

8.2 Single Antenna Element

To realize a UWB monopole antenna, the Monocone antenna geometry is a prominent candidate. It has almost been used over one century, but the actual trend towards UWB systems has renewed research interest in Monocone antenna elements [143]–[145]. In this thesis, based on the author's work in [MG8], a robust implementation of the Monocone antenna is used as a element for designing a UCA. The geometry of the Monocone antenna elements is illustrated in figure 8.3. Two versions of the antenna element are

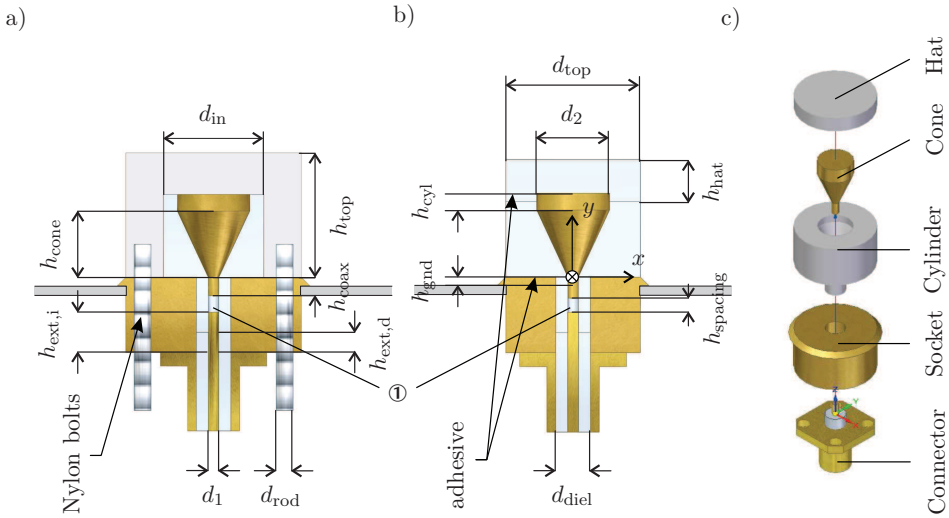

Fig. 8.3: Monocone antenna elements used for UCA. In a) a cut throught the MCB antenna is shown, in b) a cut through the MCA antenna. In c) an explosion view of the MCA element is shown. The shape of both antenna elements is identical and for improving clarity the dimensioning shown is distributed over a) and b). The local reference coordinate system of the antenna is at the cone apex.

used: the Monocone antenna using bolts (MCB) shown in figure 8.3 a) and the Monocone antenna using adhesive (MCA) shown in b). The shape of both antenna versions is identical, it is merely the parameter values which differ. As will be explained later this is due to a manufacturing point of view. To improve the clarity of the illustration, the dimensioning of the antenna geometry is thus distributed over a) and b).

The main radiating part of the antenna element is a cone of height h_{cone}, circular base of diameter d_2 and a flattened apex of diameter d_1. The base of the

cone is further extended by a cylindrical section of height h_{cylinder} and the apex by a cylindrical section of h_{coax}. The cone is mounted above a socket such that the flat apex of the cone is exactly aligned with the top surface of the socket. The socket provides the feeding of the antenna element and a mechanical structure such that the antenna can be inserted into a larger ground plane, e.g. the roof top of a vehicle. The antenna element is fed using a vertical coaxial transmission line with dielectric diameter d_{diel} and inner conductor diameter d_1. Therefore a hole of diameter d_{diel} is drilled into the center of the socket. To tightly fix the cone above the center of the socket and to provide the dielectric of the coaxial feed line, a two-section stepped cylinder made from polytetrafluoroethylene (PTFE) is used. The upper section is of diameter d_{top} and the lower section of diameter d_{diel}, such that the lower section can be firmly pressed into the feed line bore. Into the stepped cylinder, an imprint of the cone is milled such that the cone vice versa can be pressed into it. The PTFE cylinder not only serves as a robust fixture for the cone. The relative permittivity of $\epsilon_{\text{r}} \approx 2.1$ of PTFE simultaneously allows to reduce the size of the antenna element while maintaining its electrical properties. In addition, due to the excellent non-stick properties of PTFE, its robustness towards moisture and various chemicals, and its mechanical stability, it is serves as a protecting radome for the antenna. It can be seen that after mating cone, cylinder, and socket the cylindrical extension of the cone apex together with the PTFE dielectric provide a short coaxial transmission line, penetrating into the socket from the top. To provide a connection with standard measurement cables, a coaxial connector is mounted at the bottom of the socket. The connector is a flange-mount SMA connector from Emerson, which has an dielectric extending by $h_{\text{ext,d}}$ as well as an inner conductor extending by $h_{\text{ext,i}}$ from the connector flange plane. Similar to the stepped PTFE cylinder, the extended dielectric of the SMA connector is tightly pressed into the socket bore and the connector is fixed with screws to the socket. Socket height and height of the small section of the PTFE cylinder are selected such, that the dielectrics of the SMA connector and the stepped cylinder meet in the socket bore. It can be seen from figure 8.3 that thus a continuous coaxial feed results, except the discontinuation of the inner conductor at the position indicated by ①.

As illustrated in figure 8.3, a particular challenge is the connection between the inner conductor of the coaxial feed line, respectively the SMA connector, and the feed point at the cone apex. Typically, in experimental designs of Monocone antennas the cone apex is soldered to the inner conductor of the

coaxial feed line [143]–[145]. However, having in mind the specified tolerance of the antennas towards vibrations and repeated mechanical stress, it is easy to follow that a soldered joint between cone apex and feed line would be exposed to the threat of braking. Even more importantly is the fact that the connection point between the extended cone apex and the feed line inner conductor is completely embedded in the Teflon cylinder and not accessible from outside. Once feed line and cone mate there is no more access from outside and soldering is impossible.

To tackle those challenges, a solder less connection based on flexible contact pins is used. Those contact pins are commercially available under the trademark FuzzButton®. A picture is shown in figure 8.4. A FuzzButton® is

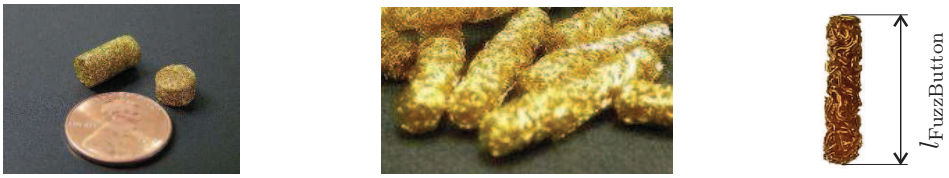

Fig. 8.4: FuzzButtons® from CustomInterconnects used for a solderless impedance-controlled connection between feed line and Monocone antenna.

a cylindrical spring like structure made from Gold-plated Beryllium Copper. A FuzzButton® of length $l_{\text{FuzzButton}} \approx 2h_{\text{spacing}}$ is inserted between extended cone apex and feed line inner conductor (① in figure 8.3). When mating all parts of the antenna element, the FuzzButton® is condensed, firmly pressed against extended cone apex and feed line inner conductor and thus provides a reliable and mechanically robust connection. Furthermore the compression in length yields an expansion in diameter, such that the FuzzButton® completely fills out the remaining space and no impedance discontinuity between feed line and extended cone apex occurs.

After pressing SMA connector, FuzzButton®, socket, stepped PTFE cylinder and cone together, as shown in figure 8.3 c) the final step is to completely embed the cone into PTFE by applying another PTFE cylinder, referred to as the hat, to the antenna structure and to tightly fix all parts together. It is the particular shape of the hat which is the main difference between the MCB and the MCA antenna element design, shown in figure 8.3 a) and b), respectively. The size of the hat is selected such that an overall outer height of h_{top} and an diameter of d_{top} results for the antenna element. In the MCB antenna design, the diameter d_{top} of the hat is significantly larger than d_{in}.

Then the hat geometry is a cylinder of height $h_{\text{hat}} = h_{\text{top}}$ with an inner bore of diameter d_{in} an depth $h_{\text{cone}} + h_{\text{cylinder}}$. Thus the hat can be pressed over the remaining antenna structure like a capsule. To tightly fix all antenna parts together, four threaded Nylon bolts are screwed into female threads located at the marginal area of the hat. The nylon bolts are then pushed through corresponding bores in the socket. The whole antenna structure can then be tightened securely by using Nylon nuts which are screwed on the Nylon bolts protruding the socket at the bottom. Clearly, it can be seen that the space required for providing the female threads in the hat increases the overall diameter of the antenna.

Since the diameter if the singe antenna element is the crucial parameter defining element distance in the array, it is desired to reduce the antenna diameter as far as possible. Therefore the Nylon bolts fixing the antenna structure can be replaced by adhesive connections leading to the geometry of the MCA antenna from figure 8.3 b). Note however that due to the non-stick properties of PTFE, which make it a preferred radome material, adhesive connections between PTFE are not easy to realize. It was found out by empirical production studies conducted in the scope of this thesis that two methods for preliminary treatment of PTFE are suitable to nevertheless realize reliable adhesive PTFE connections: The first methods uses a pretreatment of the adhesive surfaces with a plasma. Thus the surface energies of PTFE are increased providing enough energy to bond with adhesives. The second method uses a chemical pretreatment of the adhesive surfaces with an N-Heptane-based primer. Once the surfaces have been pretreated they can be bonded with Cyanoacrylate or a two-component epoxy resin glue. As can be seen from figure 8.3 b) in the MCA antenna design the diameter d_{top} of the hat exactly corresponds to d_{in}. The height h_{hat} of the hat thus only covers the part not already covered by the stepped PTFE cylinder. To reduce the shear force on the adhesive connection between hat and stepped cylinder, the geometry is selected such that a part of the cone penetrates the hat. To tightly fix all antenna elements together, the hat is glued onto the stepped cylinder and the stepped cylinder is glued onto the socket. Both adhesive connections also serves as a seal between all parts of the antenna providing the specified environmental robustness.

The geometry of both antenna elements has been optimized in CST MWS based on initial parameters [MG8], [141] to obtain a good match to the 50 Ω reference impedance across the whole frequency band from 5-9 GHz. Since the variation of the antenna's resistance and reactance is less than 1 Ω if the

diameter of the ground plane is larger than 10 wavelengths [141] the optimization has been performed assuming in infinitely large ground plane, as illustrated in figure 8.5 a). The optimized parameter values are given in ta-

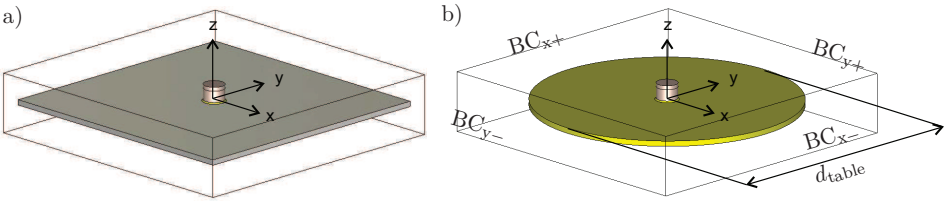

Fig. 8.5: Simulation models for Monocone antenna element. In a) the quadratic-shaped table touches the BC$_x$ and BC$_y$ boundary conditions, thus that the simulation corresponds to an infinitely large groundplane. In b) the Monocone element is simulated on a finite circular disc of diameter d_{table}.

ble 8.1. It can be seen that the overall diameter of the MCB antenna element with $d_{\text{top}} = 21\,\text{mm}$ is significantly larger than the overall diameter of the MCA antenna element with $d_{\text{top}} = 16\,\text{mm}$. Clearly an element distance of $d_{\text{el}} = \lambda_l/2$ would lead to only very little separation of the MCB antenna elements and consequently it can be expected that the mutual coupling effects would be stronger. The MCA antenna element in consequence is preferred for the array application.

Pictures of the individual parts of the Monocone antenna element, of the MCB and MCA Monocone elements as well as of the measurement setup for antenna element radiation measurements are shown in figure 8.6. The

Fig. 8.6: a) Individual parts, b) manufactured prototypes and c) measurement setup of Monocone antenna. Note the size difference between the MCB element shown on the left side of b) and the MCA element on the right.

difference in size between MCB and MCA elements is clearly visible in b). To measure the radiation characteristics of the antenna element, as illustrated in c) a circular disc made from brass, of diameter $d_{\text{table}} = 200\,\text{mm}$, is used.

Parameter	MCB			MCA		
	mm	λ_l	λ_h	mm	λ_l	λ_h
d_{top}	21 mm	0.42	0.63	16 mm	0.32	0.48
d_{diel}	4.1 mm	0.082	0.124	4.1 mm	0.082	0.123
d_{rod}	2 mm	0.04	0.06	n.a.	n.a	n.a
h_{top}	15 mm	0.3	0.45	11.5 mm	0.23	0.345
h_{gnd}	1 mm	0.02	0.03	1 mm	0.02	0.03
h_{cone}	8 mm	0.16	0.24	8 mm	0.16	0.24
h_{cyl}	2 mm	0.04	0.06	3 mm	0.06	0.09
h_{coax}	2.5 mm	0.05	0.075	2.5 mm	0.05	0.075
h_{spacing}	2 mm	0.04	0.06	3 mm	0.06	0.09
h_{hat}	15 mm	0.3	0.45	3 mm	0.06	0.09
d_1	1.25 mm	0.025	0.0375	1.25 mm	0.025	0.0375
d_2	8.67 mm	0.173	0.2601	7 mm	0.14	0.21
d_{in}	12 mm	0.24	0.36	16 mm	0.32	0.48
$h_{\text{ext,d}}$	2.4 mm	0.048	0.072	2.4 mm	0.048	0.072
$h_{\text{ext,i}}$	4.8 mm	0.096	0.144	4.8 mm	0.096	0.144

Tab. 8.1: Values of geometry parameters for MCB and MCA Monocone antenna elements.

To compare the measurements with simulations, as illustrated in figure 8.5 a corresponding simulation model with finite-size circular disc ground plane serves as basis. In contrast to the infinite ground plane simulation model, no BCs touch the circular disc.

The simulated and measured return loss of both the MCB as well as MCA Monocone antenna elements are given in figure 8.7. It can be seen that both antennas exhibit the desired impedance bandwidth and a good agreement between simulation and measurement results is obvious. In addition the simulation results show that the antenna impedance is only influenced to a minor degree by introducing a finite-size ground plane. It is remarkable that an outstanding impedance match across a frequency range from 5-17 GHz is provided by the MCA antenna element. In contrast the impedance match of the MCA antenna element is limited to about 5-10 GHz. The limitation of the MCB element's impedance match to frequencies below 10 GHz can be attributed to the four Nylon bolts which are located close to the cone. Nylon has a relative permittivity of $\epsilon_{\text{r}} \approx 4 \ldots 5$, i.e. twice as large as the relative permittivity of PTFE. Hence, in contrast to the MCA antenna element

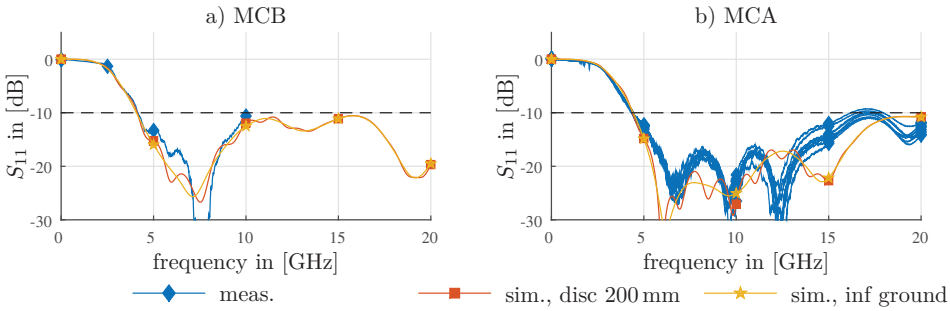

Fig. 8.7: Simulated and measured Return Loss of a) MCB and b) MCA antenna elements. From the MCA antenna the measurement results of eight prototypes is shown, four using a cyanoacrylate adhesive and four using a two-component epoxy resin adhesive.

where the EM waves propagating away from the cone apex see a homogeneous PTFE medium and thus can propagate away freely, the waves in the MCB antenna encounter the discontinuities of the Nylon bolts where they are reflected. As further shown in figure 8.7 b), eight prototypes of the MCA Monocone antenna element have been manufactured and measured. In four of the antenna elements a Cyanoacrylate-based adhesive was used and in the remaining four antenna element a two-component Epoxy resin adhesive was used. The good agreement between the measurements show that both manufacturing tolerances as well as the specific type of adhesive do influence the return loss only to a negligible extent.

The measured and simulated realized gain of both the MCA and the MCB antenna elements are shown in figure 8.8 and figure 8.9, respectively. Due to the perfect rotational symmetry of the antenna element only elevation-plane measurements are shown. The antenna element has an excellent $\underline{\boldsymbol{\theta}}$-polarization purity, the maximum cross-polarization realized gain of –20 dBi occurs in the range $\theta = 30 - 120\,^\circ$. Consequently only the $\underline{\boldsymbol{\theta}}$-polarization realized gain is shown.

A good agreement between simulation and measurements is obvious. In addition it can be seen that the realized gain of MCB and MCA antenna elements is quite similar. For both antenna elements, the main beam in the frequency range from 5-9 GHz is in the range $\theta = 57 - 67\,^\circ$, with a maximum realized gain in the range 3-6 dB. The 3 dB beam width varies in between 30-37 $^\circ$, and the realized gain at $\theta = 90\,^\circ$ is typically 4-5 dB below its maximum.

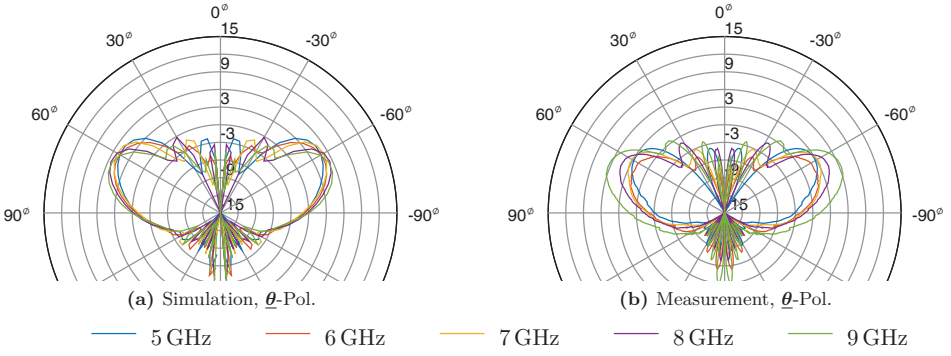

Fig. 8.8: Simulated and measured realized gain of single MCA antenna element. The radiation pattern has been measured in the range $\theta = [0° \ldots 180°]$. For better illustration, the measured pattern has been extended to $\theta = [180° \ldots 360°]$ by mirroring the measured pattern.

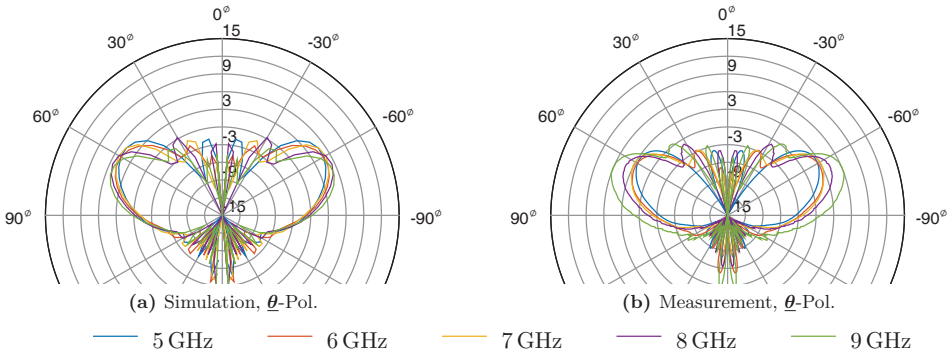

Fig. 8.9: Simulated and measured realized gain of single MCB antenna element. The radiation pattern has been measured in the range $\theta = [0° \ldots 180°]$. For better illustration, the measured pattern has been extended to $\theta = [180° \ldots 360°]$ by mirroring the measured pattern.

8.3 Monocone Array Design

The small size of the MCA elements generally allows for the design of arbitrary array geometries based on a $d_{\text{grid}} = \lambda_l/2 = 25\,\text{mm}$ grid spacing. In the scope of this thesis is the design and characterization of a four-element ULA with an element spacing $d_{\text{el}} = \lambda_l/2 = 25\,\text{mm}$ corresponding to an radius of $R_{\text{UCA}} = d_{\text{grid}}/\sqrt{2} = 17.67\,\text{mm}$, as illustrated in figure 8.10 a). The

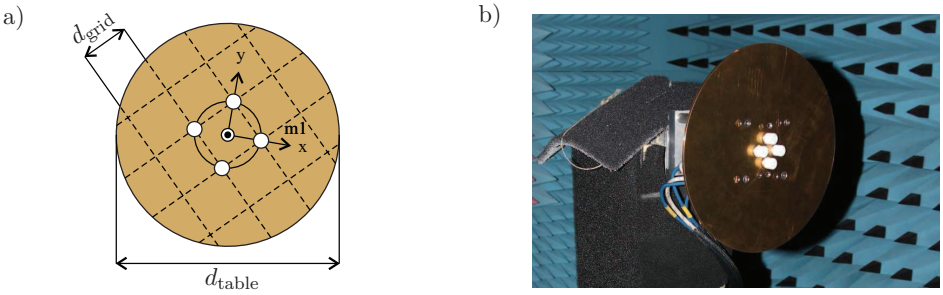

Fig. 8.10: Four-element UCA using MCA antenna elements. a) Illustration and b) picture of measurement setup.

UCA is located around the center of a circular disc table made from 4 mm thick brass with a table diameter of $d_{\text{table}} = 400\,\text{mm}$, which acts as a ground plane for the MCA antenna elements. Figure 8.10 b) shows the manufactured prototype UCA mounted on the positioner of the anechoic chamber. Due to the specific setup of the positioner with a side-mounting for the AUT, the UCA is mounted such that the positioner elevation axis corresponds to θ and the positioner azimuth axis corresponds to φ. Thus it is assured that the complete mounting structure is below the UCA for $\varphi = 0\,^\circ \ldots 360\,^\circ$ and the influence of the mounting structure on the measurements are reduced.

The measured active element realized gain is shown in figure 8.11. The absolute method with a distance of $d = 3.75\,\text{m}$ between EXA reference plane and UCA array center was used. Since the VNA used for antenna measurements had four ports, and one port was used for EXA excitation, only three ports for connecting the antenna elements remained. Therefore, the remaining element was terminated in the reference impedance of $Z^{\text{c}} = 50\,$. As already indicated by the measured active element realized gain from figure 8.11, the UCA and the used measurement setup exhibits excellent symmetry properties. Consequently it was desisted from explicitly measuring the terminated element, since its active element realized gain is expected to correspond to

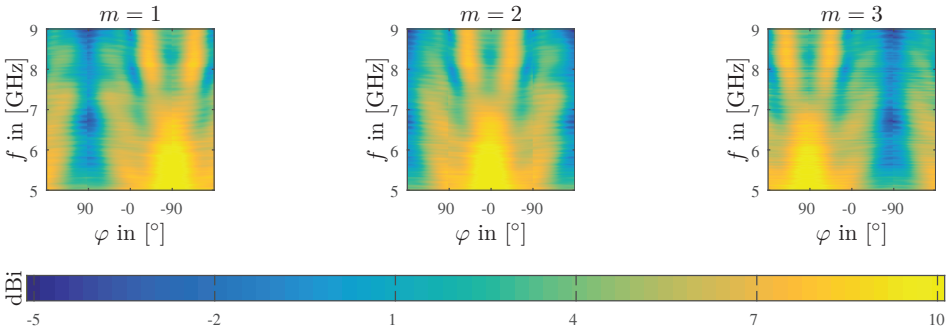

Fig. 8.11: Measured active element realized gain of 4-element UCA using MCA antenna elements. $\theta = 60\,°$.

the gain of the remaining elements.

It can be seen from figure 8.11 that the active element realized gain is not omni-directional in azimuth but gets distorted. Especially at 5 GHz, where the electrical distance between the array elements is smallest, a significant radiation main lobe pointing outward from the array center forms. With increasing frequency the main lobe splits into four lobes, whose magnitude reduces with frequency yielding a smaller amplitude ripple along φ.

8.4 DSP Performance

To evaluate the DSP performance of the UCA, simulation results from the simulation setup shown in figure 8.12 are used. The simulation model precisely corresponds to the measurement setup, including the circular disc ground plane of 400 mm diameter. To simulate the antenna effective height of each antenna element, $\underline{\theta}$- and $\underline{\varphi}$-polarized probes are hemispherically placed around the element's local reference coordinate system which is at the cone apex (compare figure 8.3). As a result of precisely modeling the measurement setup including the circular disc ground plane, the simulation domain becomes rather large. In addition due to the comparatively small structures present in the MCA antenna elements and an upper simulation frequency limit of 20 GHz, more than 14 million mesh cells result. The simulation time for a single element excitation is about 24 h on a GPU-accelerated dedicated simulation server. Consequently, it is obvious that reducing simulation time is of great interest in analyzing the antenna array.

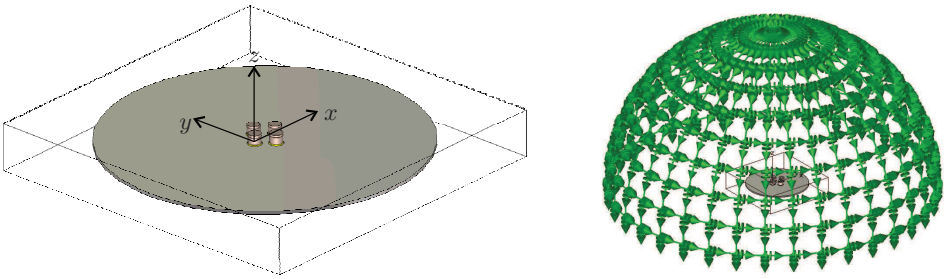

Fig. 8.12: Simulation model of the four-element Monocone antenna array with finite ground plane. The coordinate origin is the center of antenna element $m = 1$. In total 720 Θ- and Φ-polarized E-field probes are placed at $\theta = [0°, 10°, \ldots, 90°]$ and $\varphi = [0°, 10°, \ldots, 360°]$

Although the active element effective height of each MCA element is necessary for evaluating its DSP performance, the perfect symmetry of the UCA can be exploited and only one simulation is necessary. Therefore, once a single array element has been simulated, (5.7) can be used to derive the active element effective height of all other array elements. The AM^{QS} functions obtained for each MCA antenna element are shown in figure 8.13. The good agreement between the simulation results and the measurement of the active element realized gain from figure 8.11 is obvious. It is obvious that depending on the DOA a AM will be introduced to the beat signal. Depending on the DOA the beat signal's amplitude on an individual element may vary by a factor of approximately 4 corresponding to the 12 dB of active element realized gain variation.

The PM^{QS} functions obtained for each element are shown in figure 8.14. It can be seen that only a minor variation of phase with φ is present, especially at low frequencies. This indicates that a relatively frequency stable phase-center exists, and that the origin of the coordinate system local to the antenna elements coincides with the phase center quite well. Especially for frequencies larger than 6.5 GHz a phase-ripple with φ can be observed.

The spatially filtered signals obtained from the WB Bartlett and MVDR algorithms using the four-element UCA are illustrated in figure 8.15. A single target return impinging from a knwon elevation $\theta = 60\,°$ is assumed. Four different azimuth positions $\varphi = 0\,°, 25\,°, 45\,°, 60\,°$ are examined. The distance of the target is $d^{\mathrm{tgt}} = 50\,\mathrm{m}$. Again, results obtained from ideal array knowledge are compared to taking into account perfect array knowledge.

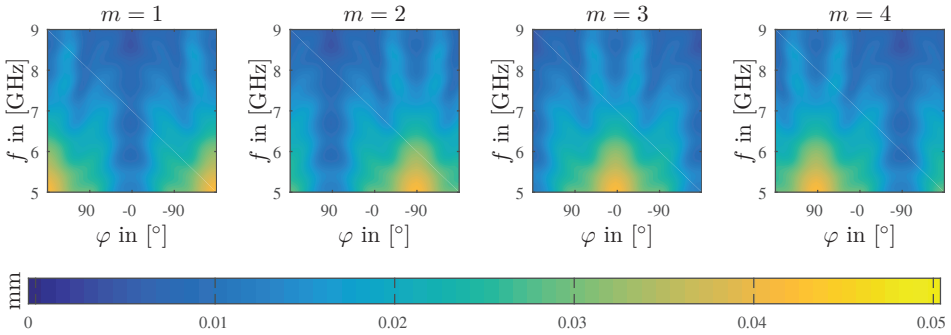

Fig. 8.13: AM^{QS} of MCA antenna elements in four-element UCA. $\theta = 60\,°$

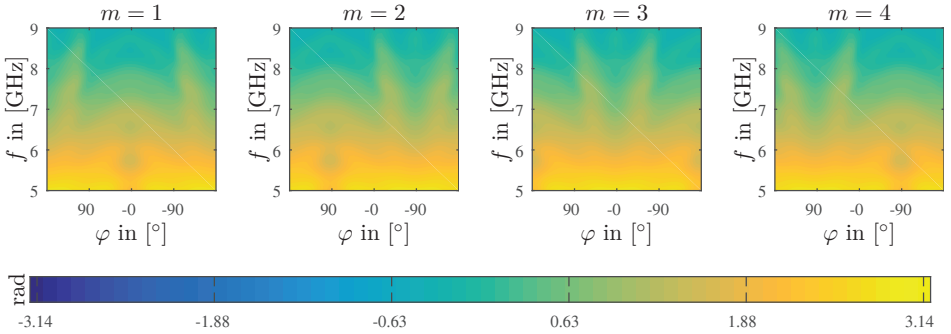

Fig. 8.14: PM^{QS} of MCA antenna elements in four-element UCA. $\theta = 60\,°$

Similar to the effects observed for the ULA, it can be seen that the deviation of the LP model from the true array manifold leads to a distortion of the spatially filtered signals. Neither is the maximum amplitude of the spatially filtered signals fixed at the look direction α_φ corresponding to the true DOA, nor is the amplitude of the spatially filtered signals constant along the sweep duration. Compared to the ULA the grating lobe properties of the UCA are eminent. There is not a single grating lobe which occurs at a certain frequency and then continuously approaches the main lobe. Instead, depending on the instantaneous frequency of the impinging signal as well as its DOA ambiguities occur at various positions in the spatially filtered signal. Compared to the ULA, where the maximum of the spatially filtered signal's magnitude was winding around the true DOA with approximately equal positive and negative deviations, it can be seen from the MVDR spatially filtered signals for e.g $\varphi = 45\,°$ (figure 8.15 c)), that the predominant deviation is towards a smaller look direction.

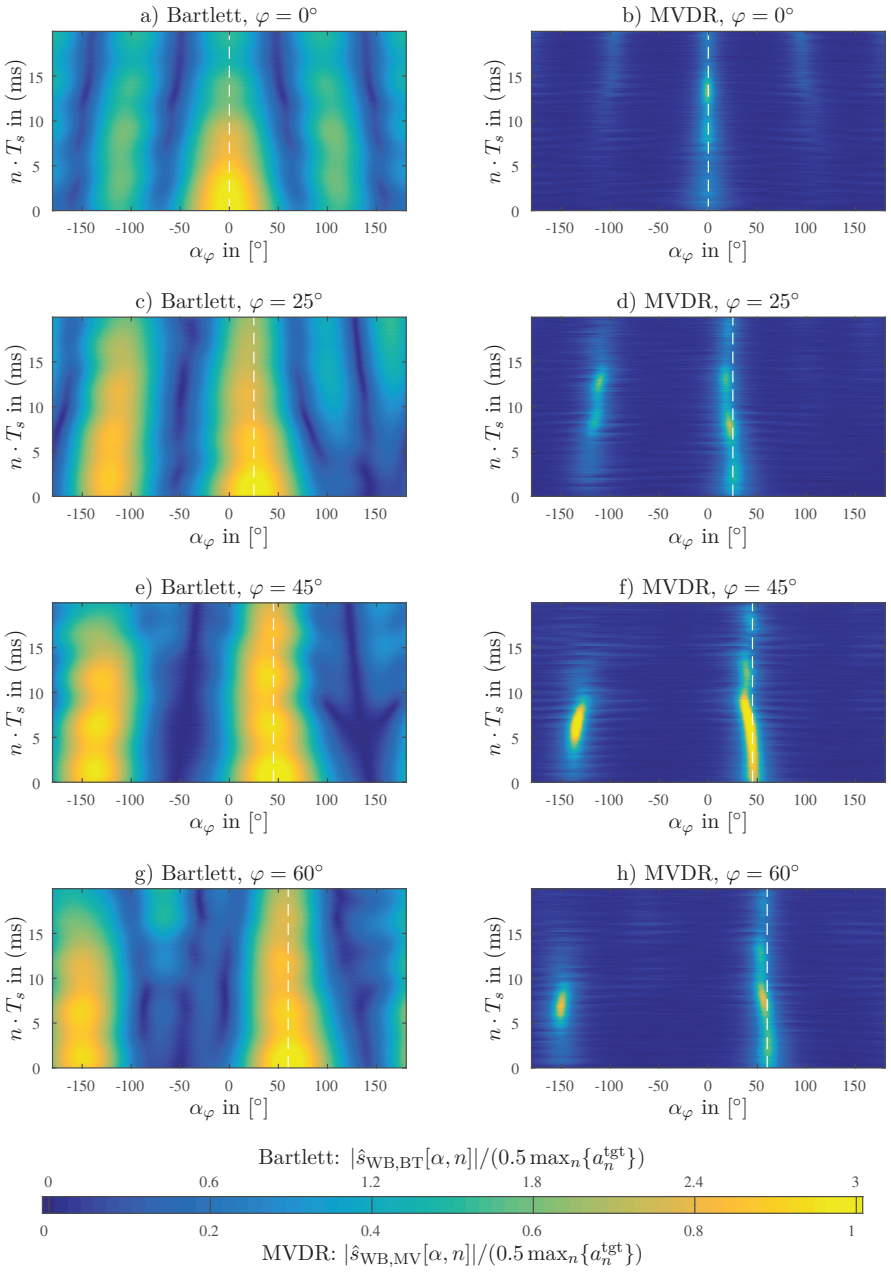

Fig. 8.15: Spatially filtered signals obtained from UCA using ideal array model. Array based on MCA antenna elements. Single target at DOA $\varphi = 0\,°, 25\,°, 45\,°, 60\,°$ and $\theta = 60\,°$, distance $d^{\mathrm{tgt}} = 50\,\mathrm{m}$.

The spatially filtered signals obtained by incorporating full array knowledge are shown in figure 8.16. As expected the position of the main lobe for the MVDR beamformer now remains at the look direction corresponding to the true DOA and the magnitude becomes constant along the sweep. Hardly any influence on the spatially filtered signal obtained can be observed.

The spatial spectra obtained from both beamformers are shown in figure 8.17 and figure 8.18. It can be seen that assuming an ideal array manifold, the spatial spectra peak position deviates from the true DOA. In particular the error is in between 2-3 $^\circ$ for the WB Bartlett and MVDR algorithms. Interestingly in most of the cases the NB algorithms show a lower error, which is in between 0-3 $^\circ$. However, the sidelobes of the NB algorithms are larger than the sidelobes of the WB estimator. For $\varphi = 45^\circ$, the sidelobe peak of the NB Bartlett beamformer at –135 $^\circ$ is even larger than the mainlobe peak and a large DOA estimation error would result. For $\varphi = 0^\circ$ no error is present in the spatial spectra of all algorithms. By using perfect array knowledge as shown in figure 8.18, the DOA estimation errors are mitigated. The peaks of the spatial spectra of all WB algorithms now correspond to the true DOAs and the grating lobe suppression of the WB algorithms is improved.

The range FFTs obtained are shown in figure 8.19. Again a SNR of –20 dB is used to illustrate the FFT processing gain and aSNR of 30 dB is used for illustrating the effects onto the FFT peak position and shape. While the former is used to illustrate the effects of model mismatch onto the FFT processing gain, the latter is used to illustrate systematic errors introduced into the FFT-based range estimation. Effects similar to the ULA scenario can be observed. Without array knowledge, the FFT peak exhibits a shift towards a larger distance. This is due to the fact that the delay from the antenna element to the calibration plane at the connector is not taken into account. Since the active element antenna height however takes into account this delay, the peak position offset is mitigated when incorporating perfect array knowledge in the beamforming algorithms. Again, the sidelobe structure is strongly influence due to the AM present in the MVDR output signal assuming an ideal array and restored using perfect array knowledge.

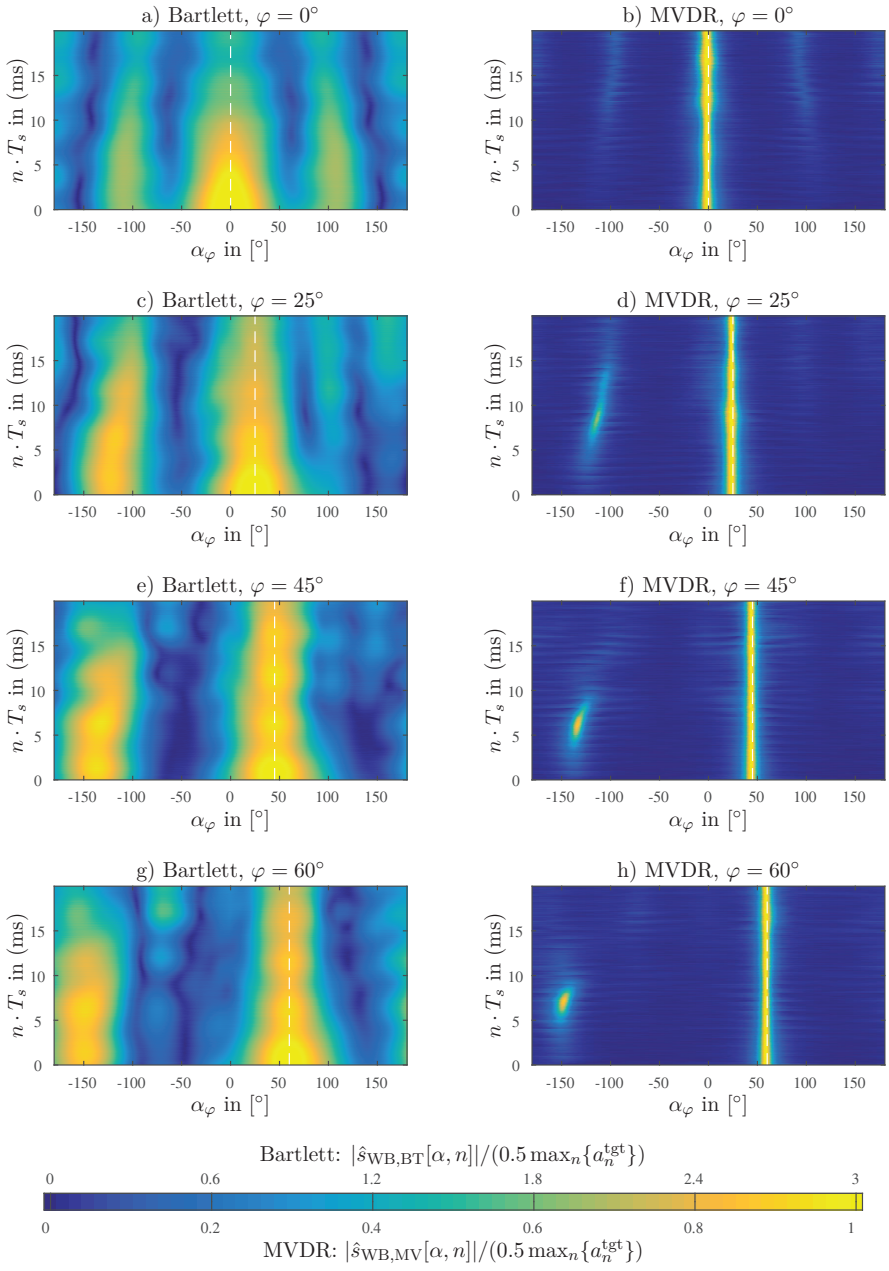

Fig. 8.16: Spatially filtered signals obtained from UCA using perfect array knowledge. Array based on MCA antenna elements. Single target at DOA $\varphi = 0\,°, 25\,°, 45\,°, 60\,°$ and $\theta = 60\,°$, distance $d^{\mathrm{tgt}} = 50\,\mathrm{m}$.

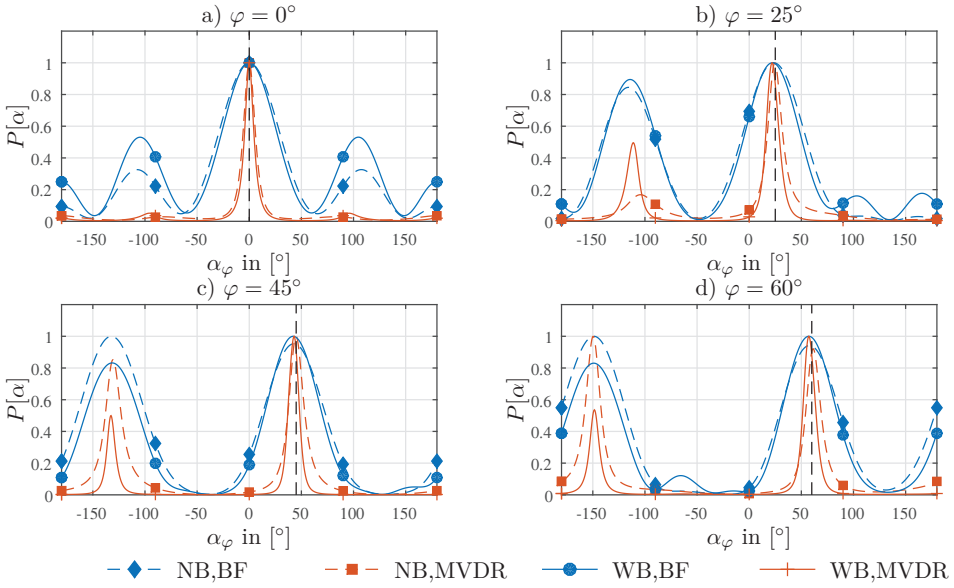

Fig. 8.17: Spatial spectra obtained from UCA using ideal array model.

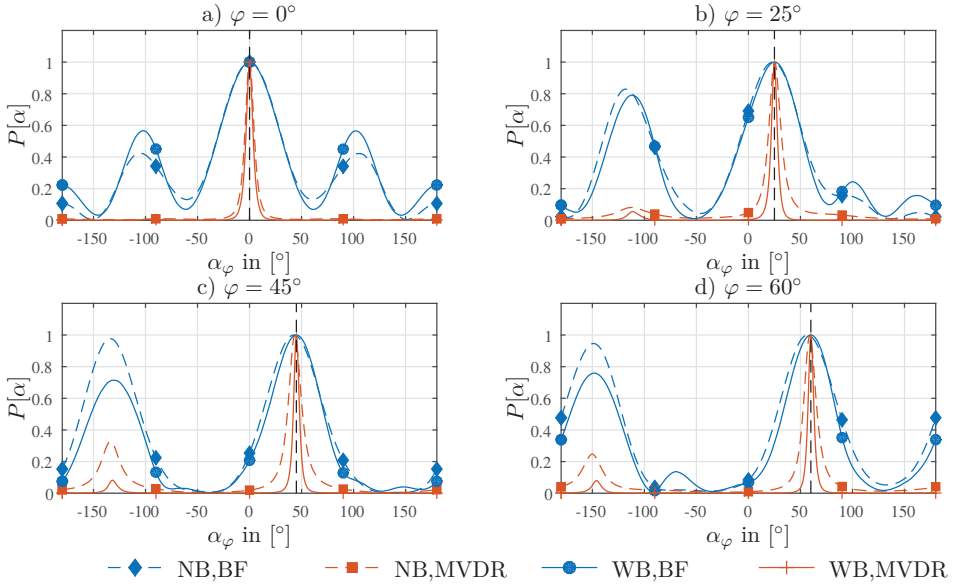

Fig. 8.18: Spatial spectra obtained from UCA using perfect array knowledge.

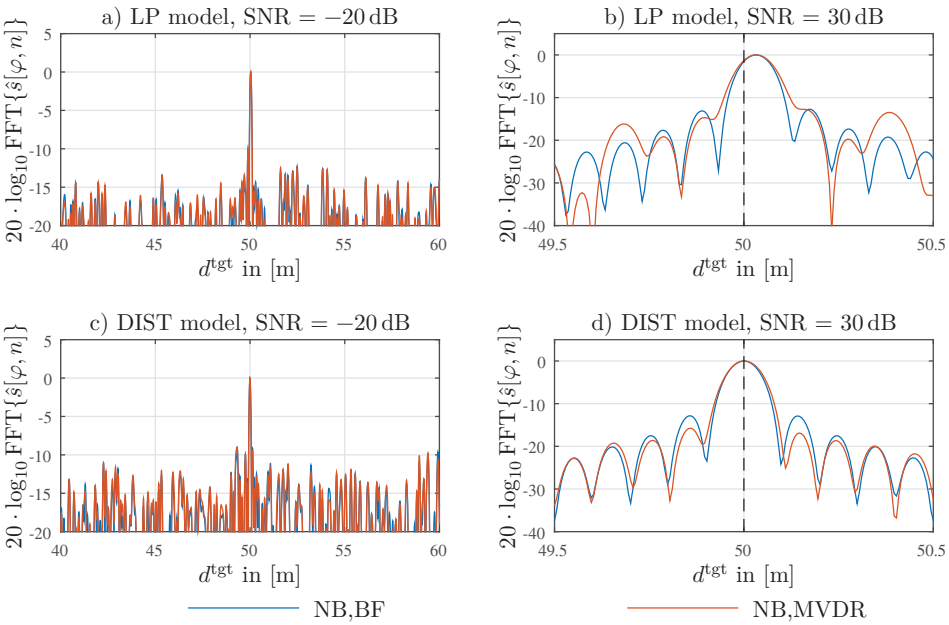

Fig. 8.19: Normalized range FFTs obtained from UCA. Array based on MCA antenna elements. Single target at DOA $\varphi = 25\,^\circ$ and $\theta = 60\,^\circ$, distance $d^{\mathrm{tgt}} = 50\,\mathrm{m}$.

9 Conclusions and Outlook

A holistic approach for the characterization and design of small array antennas, referred to as antenna in the loop development cycle, for DOA estimation in UWB industrial FMCW RADAR systems was proposed in this thesis. The state of the art in UWB antenna characterization has been reviewed and extended to model the individual elements of a small RX antenna array in terms of the active element effective height. A comprehensive model which allows to directly compute the beat signals observed at the output of an RX antenna array taking into account the simulated or measured active element height was derived. The proposed beat signal model has been validated against RF system simulations.

Two small array antennas, a ULA and a UCA, for DOA estimation in an UWB secondary RADAR system for industrial positing applications have been designed and experimentally characterized. The ULA is based on a novel design approach, taking into account the mutual coupling across the columns of a vertical sub array for improving the sub array bandwidth and radiation performance. The UCA is based on small Monocone antenna elements which are embedded in a PTFE radome allowing for size reduction as well as mechanical protection of the array elements. It uses a solder less feed connection for to simplify the manufacturing process as well as to increase robustness towards vibration and mechanical stress.

In addition improved WB beamforming algorithms based on the Bartlett and MVDR beamformer have been proposed and extended to combined range and angle estimation. The concept of fragmented covariance matrix estimation, relating the beamforming algorithms to the class of non-coherent DOA estimation algorithms has been introduced and its performance gain in WB RADAR systems has been shown. It has been shown how the knowledge from the comprehensive model for the beat signal can be used to take into account the characteristics of array antennas in the DOA estimation algorithms.

Using the proposed characterization approach, the influence of the designed array antennas onto the combined range and angle estimation algorithms has directly been evaluated. It further has been shown how taking into

account precise array knowledge can improve the performance of the combined range and angle estimation algorithms

In the scope of this thesis, the two extrema of using an ideal array model and perfect array knowledge have been compared. For practical applications perfect array knowledge typically cannot be assumed. Robust calibration of array antennas and the compensation of the antenna element characteristics in array signal processing is however still an active field of research, even in the case of NB systems. For WB systems it is even a more sophisticated challenge since both spatial as well as temporal and frequency dependencies have to be taken into account. Future work can thus be dedicated to deriving robust and adaptive models for the active element effective height of antenna elements embedded in an array environment

Using the proposed antenna in the loop development cycle and the mathematical framework proposed in this thesis the performance of more sophisticated range and angle estimation algorithms or the use of improved array antennas can directly be studied. Both research disciplines offer a lot of room for further improvements. It is however obvious that signal processing and antenna design should not be considered as separate research disciplines. Instead they always should be considered hand in hand for improving the performance of the RADAR systems of the future.

A Derivation of Beat Signals

The product $x^{\text{mix}}(t)$ of a complex phase-modulated exponential function with a phase modulated cosine function, where cosine phase is a time-delayed version of the phase of the exponential function is expressed by

$$x^{\text{mix}}(t) = e^{\text{j}\phi(t)} \cdot \cos\left(\phi(t - T_d)\right), \tag{A.1}$$

where T_d refers to the time-delay between both phases. The cosine function can be expanded using Euler's formula

$$x^{\text{mix}}(t) = \frac{1}{2} e^{\text{j}\phi(t)} \left(e^{\text{j}\phi(t-T_d)} + e^{-\text{j}\phi(t-T_d)} \right), \tag{A.2}$$

and consequently $x^{\text{mix}}(t)$ can be rewritten by

$$x^{\text{mix}}(t) = \frac{1}{2} \left(e^{\text{j}\phi^{\text{mix,sum}}(t)} + e^{\text{j}\phi^{\text{mix,diff}}(t)} \right), \tag{A.3}$$

where

$$\phi^{\text{mix,diff}}(t) = \phi(t) - \phi(t - T_d), \tag{A.4}$$

$$\phi^{\text{mix,sum}}(t) = \phi(t) + \phi(t - T_d). \tag{A.5}$$

For the particular case of an LFM waveform of rising frequency (upsweep) with sweep duration T the instantaneos phase $\phi(t)$ is expressed by

$$\phi(t) = \begin{cases} 2\pi f_l t + \phi_0 & -\infty \leq t < 0 \\ 2\pi f_l t + \pi\mu t^2 + \phi_0 & 0 \leq t < T \\ 2\pi f_h (t - T) + 2\pi f_l T + \pi\mu T^2 + \phi_0 & T \leq t < \infty \end{cases}, \tag{A.6}$$

and the delayed version $\phi(t - T_d)$ can be expressed by

$$\phi(t - T_d) = \begin{cases} 2\pi f_l (t - T_d) + \phi_0 & -\infty \leq t < T_d \\ 2\pi f_l (t - T_d) + \pi\mu (t - T_d)^2 + \phi_0 & T_d \leq t < T + T_d \\ 2\pi f_h ((t - T_d) - T) + 2\pi f_l T + \pi\mu T^2 + \phi_0 & T + T_d \leq t < \infty \end{cases} \tag{A.7}$$

If the time delay T_d is nonnegative and $T_d < T$, it gets obvious that the resulting phases of the mixing products are functions piecewise defined over five intervals

$$\phi^{\text{mix,diff}}(t) = \begin{cases} {}^1\phi^{\text{mix,diff}}(t) & t \leq 0 \\ {}^2\phi^{\text{mix,diff}}(t) & 0 \leq t \leq T_d \\ {}^3\phi^{\text{mix,diff}}(t) & T_d \leq t \leq T \\ {}^4\phi^{\text{mix,diff}}(t) & T \leq t \leq T + T_d \\ {}^5\phi^{\text{mix,diff}}(t) & T + T_d \leq t \end{cases}, \tag{A.8}$$

$$\phi^{\text{mix,sum}}(t) = \begin{cases} {}^1\phi^{\text{mix,sum}}(t) & t \leq 0 \\ {}^2\phi^{\text{mix,sum}}(t) & 0 \leq t \leq T_d \\ {}^3\phi^{\text{mix,sum}}(t) & T_d \leq t \leq T \\ {}^4\phi^{\text{mix,sum}}(t) & T \leq t \leq T + T_d \\ {}^5\phi^{\text{mix,sum}}(t) & T + T_d \leq t \end{cases}. \tag{A.9}$$

The single phase functions of the difference component are given by

$${}^1\phi^{\text{mix,diff}}(t) = 2\pi f_l T_d, \tag{A.10}$$

$${}^2\phi^{\text{mix,diff}}(t) = 2\pi f_l T_d + \pi\mu t^2, \tag{A.11}$$

$${}^3\phi^{\text{mix,diff}}(t) = 2\pi f_l T_d + 2\pi\mu t T_d - \pi\mu T_d^2, \tag{A.12}$$

$${}^4\phi^{\text{mix,diff}}(t) = 2\pi f_l T_d + 2\pi\mu t T_d + 2\pi\mu t T - \pi\mu T^2 - \pi\mu t^2 - \pi\mu T_d^2, \tag{A.13}$$

$${}^5\phi^{\text{mix,diff}}(t) = 2\pi f_l T_d + 2\pi\mu T T_d, \tag{A.14}$$

and for the sum component by

$${}^1\phi^{\text{mix,sum}}(t) = 4\pi f_l t - 2\pi f_l T_d + 2\phi_0, \tag{A.15}$$

$${}^2\phi^{\text{mix,sum}}(t) = 4\pi f_l t - 2\pi f_l T_d + \pi\mu t^2 + 2\phi_0, \tag{A.16}$$

$${}^3\phi^{\text{mix,sum}}(t) = 4\pi f_l t - 2\pi f_l T_d + 2\pi\mu t^2 - 2\pi\mu t T_d + \pi\mu T_d^2 + 2\phi_0, \tag{A.17}$$

$${}^4\phi^{\text{mix,sum}}(t) = 4\pi f_l t - 2\pi f_l T_d + \pi\mu t^2 + 2\pi\mu t T - 2\pi\mu t T_d - \pi\mu T^2 + \pi\mu T_d^2 + 2\phi_0, \tag{A.18}$$

$${}^5\phi^{\text{mix,sum}}(t) = 4\pi f_l t - 2\pi f_l T_d + 4\pi\mu t T - 2\pi\mu T^2 - 2\pi\mu T T_d + 2\phi_0. \tag{A.19}$$

The instantaneous frequency is the time derivative of the instantaneous phase function

$$f(t) = \frac{1}{2\pi}\frac{\partial}{\partial t}\phi(t) \tag{A.20}$$

and thus the instantaneous frequencies of the difference component for the corresponding five time intervals are

$$
\begin{aligned}
{}^{1}f^{\text{mix,diff}}(t) &= 0, && \text{(A.21)}\\
{}^{2}f^{\text{mix,diff}}(t) &= \mu t, && \text{(A.22)}\\
{}^{3}f^{\text{mix,diff}}(t) &= \mu T_d, && \text{(A.23)}\\
{}^{4}f^{\text{mix,diff}}(t) &= \mu T_d + \mu T - \mu t && \text{(A.24)}\\
{}^{5}f^{\text{mix,diff}}(t) &= 0, && \text{(A.25)}
\end{aligned}
$$

and for the sum component

$$
\begin{aligned}
{}^{1}f^{\text{mix,sum}}(t) &= 2f_l, && \text{(A.26)}\\
{}^{2}f^{\text{mix,sum}}(t) &= 2f_l + \mu t, && \text{(A.27)}\\
{}^{3}f^{\text{mix,sum}}(t) &= 2f_l + 2\mu t - \mu T_d, && \text{(A.28)}\\
{}^{4}f^{\text{mix,sum}}(t) &= 2f_l + \mu t + \mu T - \mu T_d, && \text{(A.29)}\\
{}^{5}f^{\text{mix,sum}}(t) &= 2f_l + 2\mu T = 2f_h. && \text{(A.30)}
\end{aligned}
$$

Next consider the case where the cosine function is weighted by a amplitude function $AM(t)$ and modulated by an additional phase function $PM(t)$

$$
x^{\text{mix}}(t) = e^{\text{j}\phi(t)} AM(t - T_d) \cos\left(\phi(t - T_d) + PM(t - T_d)\right). \qquad \text{(A.31)}
$$

Then the expansion using Euler's formula yields

$$
\begin{aligned}
x^{\text{mix}}(t) = \frac{1}{2} e^{\text{j}\phi(t)} AM(t - T_d) \Big(& e^{\text{j}(\phi(t-T_d)+PM(t-T_d))} \\
& + e^{-\text{j}(\phi(t-T_d)+PM(t-T_d))} \Big), \qquad \text{(A.32)}
\end{aligned}
$$

which consequently can be simplified to

$$
\begin{aligned}
x^{\text{mix}}(t) = \frac{1}{2} AM(t - T_d) \Big(& e^{\text{j}\left(\phi^{\text{mix,sum}}(t)+PM(t-T_d)\right)} \\
& + e^{\text{j}\left(\phi^{\text{mix,diff}}(t)-PM(t-T_d)\right)} \Big). \qquad \text{(A.33)}
\end{aligned}
$$

Acronyms

AM	amplitude modulation
API	application programming interface
ATSA	antipodal tapered slot antenna
AUT	antenna/antenna array under test
AUTO	automotive
AWGN	additive white Gaussian noise
BC	boundary condition
CEM	computational electro-magnetics
cisoid	complex sinusoid
COTS	commercial off-the-shelf
CPS	cyber physical systems
CRLB	Cramer-Rao lower bound
CST	computer simulation technology
CW	continuous wave
DFT	discrete Fourier transform
DOA	direction of arrival
DSP	digital signal processing
DTFT	discrete-time Fourier transform
EIRP	equivalent isotropically-radiated power
EM	electro-magnetic
EXA	excitation antenna
FF	far-field
FFT	fast Fourier transform
FIR	finite impulse response
FIT	finite integration technique
FMCW	frequency-modulated continuous-wave
FO	front-end-only
IF	intermediate frequency
ISM	industrial, scientific, and medical
LADAR	laser detection and ranging
LFM	linear frequency modulation
LFMCW	linear frequency-modulated continuous-wave
LIDAR	light detection and ranging

LO	local oscillator
LOS	line-of-sight
LP	lowpass
LTI	linear time invariant
MATLAB®	matrix laboratory software package
MCA	Monocone antenna using adhesive
MCB	Monocone antenna using bolts
ML	maximum likelihood
MSE	mean square error
MU	measurement unit
MUSIC	multiple signal classification
MVDR	minimum variance distortionless response
MWS	microwave studio
NB	narrowband
NF	near-field
NLOS	non-line-of-sight
PA	power amplifier
PCB	printed circuit board
PEC	perfect electric conductor
PM	phase modulation
PTFE	polytetrafluoroethylene
QS	quasi-stationary
RADAR	radio detection and ranging
RCS	radar cross section
REF	reference antenna
RF	radio frequency
RMSE	root mean square error
RU	reference unit
RX	receive
SAR	synthetic aperture radar
SEM	singularity expansion method
SMA	sub-miniature-A
SMD	surface-mount device
SMI	sample matrix inversion
SNR	signal-to-noise ratio
SoA	state-of-the-art
TDOA	time difference of arrival
TEM	transversal electro-magnetic

TOA	time of arrival
TOF	time of flight
TX	transmit
UC	unit cell
UCA	uniform circular array
ULA	uniform linear array
UWB	ultra-wideband
VCO	voltage-controlled oscillator
VNA	vector network analyzer
WB	wideband
WBF	wideband fast-sweep
WBS	wideband slow-sweep

List of Symbols

AM^{QS}	amplitude-modulating signal
AM_m^{QS}	amplitude-modulating signal for antenna m
α	look direction index
α_φ	look direction
a^{tx}	power wave incident on TX antenna
$a_{m,n}^{\text{tgt}}$	amplitude coefficient of target n at antenna m
a_n^{tgt}	amplitude coefficient of target n
BW	absolute sweep bandwidth
$\text{BW}^{\text{rel.}}$	relative sweep bandwidth
b_m	power wave leaving port m
b^{tx}	power wave leaving TX antenna
c_0	vacuum velocity of light
d_{el}	array element distance
d_{sub}	sub-array element distance
Δ_{DL}	diagonal loading power factor
δ	Dirac function
$d_{0,n}^{\text{tgt,rx}}$	distance between coordinate system origin and target n
$d^{\text{tx,r}}$	distance between coordinate r and TX antenna
$d^{\text{ru,mu}}$	distance between RU and MU
$d_n^{\text{tgt,rx}}$	distance between target n and RX antenna
$d_{m,n}^{\text{tgt,rx}}$	distance between target n and RX antenna m
$d^{\text{tx,rx}}$	distance between TX antenna and RX antenna
d^{tgt}	distance of target
d_n^{tgt}	distance of target n
$d_n^{\text{tgt,r}}$	distance between coordinate r and target n
$d_n^{\text{tx,tgt}}$	distance between TX antenna and target n
$\underline{\boldsymbol{d}}_m^{\text{tx,el}}$	antenna TX distortion factor of antenna element m
$E_{\text{Co}}^{\text{tx}}$	transmitted E-field co-pol., frequency domain
$\underline{\boldsymbol{E}}^{\text{rx}}$	E-field vector at RX, frequency domain
$\underline{\boldsymbol{E}}^{\text{tx}}$	transmitted E-field vector, frequency domain
$e_{\text{Co}}^{\text{tx}}$	transmitted E-field, co-pol., time domain
ϵ_{DL}	diagonal loading value

ϵ_r	relative electric permittivity
$e_{\underline{\varphi}}^{\mathrm{tx}}$	transmitted E-field, $\underline{\varphi}$-component, time domain
$e_{\underline{\theta}}^{\mathrm{tx}}$	transmitted E-field, $\underline{\theta}$-component, time domain
$E_{\underline{\varphi}}^{\mathrm{rx}}$	received E-field vector, $\underline{\varphi}$-component, frequency domain
$E_{\underline{\theta}}^{\mathrm{rx}}$	received E-field vector, $\underline{\theta}$-component, frequency domain
$e_{\underline{\varphi}}^{\mathrm{rx}}$	received E-field vector, $\underline{\varphi}$-component, time domain
$e_{\underline{\theta}}^{\mathrm{rx}}$	received E-field vector, $\underline{\theta}$-component, time domain
$\underline{\boldsymbol{e}}^{\mathrm{rx}}$	E-field vector at RX, time domain
$\underline{\boldsymbol{e}}^{\mathrm{tgt}}$	target E-field vector, time domain
$\underline{\boldsymbol{e}}_n^{\mathrm{tgt}}$	target n E-field vector, time domain
$\underline{\boldsymbol{e}}^{\mathrm{tot}}$	total E-field vector, time domain
$\underline{\boldsymbol{e}}^{\mathrm{tx}}$	transmitted E-field vector, time domain
f	instantaneous frequency
f_n^{b}	beat frequency of target n
f^{b}	beat frequency
$f_{m,n}^{\mathrm{b}}$	beat frequency at antenna m of target n
f_c	carrier frequency
f_h	highest instantaneous frequency of sweep
f_l	lowest instantaneous frequency of sweep
${}^1f^{\mathrm{mix,diff}}$	inst. frequency of diff. component in interval 1
${}^2f^{\mathrm{mix,diff}}$	inst. frequency of diff. component in interval 2
${}^3f^{\mathrm{mix,diff}}$	inst. frequency of diff. component in interval 3
${}^4f^{\mathrm{mix,diff}}$	inst. frequency of diff. component in interval 4
${}^5f^{\mathrm{mix,diff}}$	inst. frequency of diff. component in interval 5
$f_n^{\mathrm{mix,diff}}$	inst. frequency of diff. component target n
${}^1f^{\mathrm{mix,sum}}$	inst. frequency of sum component in interval 1
${}^2f^{\mathrm{mix,sum}}$	inst. frequency of sum component in interval 2
${}^3f^{\mathrm{mix,sum}}$	inst. frequency of sum component in interval 3
${}^4f^{\mathrm{mix,sum}}$	inst. frequency of sum component in interval 4
${}^5f^{\mathrm{mix,sum}}$	inst. frequency of sum component in interval 5
$f_n^{\mathrm{mix,sum}}$	inst. frequency of sum component target n
f_s	sampling frequency for IF signals
$f_{\mathrm{s,RF}}$	sampling frequency for RF signals
G_{IEEE}	IEEE antenna gain
G	realized antenna gain
$\underline{\boldsymbol{H}}^{\mathrm{ant}}$	antenna normalized effective height
$\underline{\boldsymbol{H}}_m^{\mathrm{el}}$	antenna element m normalized effective height
$H_{\mathrm{Co}}^{\mathrm{AUT}}$	AUT normalized effective height, co-pol.

$H_{m,\mathrm{Co}}^{\mathrm{el,AUT}}$	AUT element m normalized effective height, co-pol.
H_{Co}	antenna normalized effective height, co-pol.
$H_{m,\mathrm{Co}}^{\mathrm{el}}$	element m effective height, co-pol.
$H_{\varphi}^{\mathrm{rx}}$	RX antenna normalized effective height, $\underline{\varphi}$ component
$H_{\varphi}^{\mathrm{tx}}$	TX antenna normalized effective height, $\underline{\varphi}$ component
$H_{\mathrm{Co}}^{\mathrm{REF}}$	REF antenna normalized effective height, co-pol.
$H_{\mathrm{Co}}^{\mathrm{rx}}$	RX antenna normalized effective height, co-pol.
H_{θ}^{rx}	RX antenna normalized effective height, $\underline{\boldsymbol{\theta}}$ component
H_{θ}^{tx}	TX antenna normalized effective height, $\underline{\boldsymbol{\theta}}$ component
$\underline{\boldsymbol{H}}^{\mathrm{rx}}$	RX antenna normalized effective height
$\underline{\boldsymbol{H}}^{\mathrm{tx}}$	TX antenna normalized effective height
$\underline{\boldsymbol{h}}^{\mathrm{ant,rx}}$	antenna receive impulse response
$\underline{\boldsymbol{h}}^{\mathrm{ant,tx}}$	antenna transmit impulse response
$\underline{\boldsymbol{h}}_{m}^{\mathrm{el}}$	antenna element m impulse response
$h_{\phi}^{\mathrm{ant,rx}}$	$\underline{\varphi}$-component of RX antenna impulse response
$h_{\phi}^{\mathrm{ant,tx}}$	$\underline{\varphi}$-component of TX antenna impulse response
$h_{\theta}^{\mathrm{ant,rx}}$	$\underline{\boldsymbol{\theta}}$-component of RX antenna impulse response
$h_{\theta}^{\mathrm{ant,tx}}$	$\underline{\boldsymbol{\theta}}$-component of TX antenna impulse response
h_{Co}	antenna impulse response, co-pol.
$h_{m,\mathrm{Co}}^{\mathrm{el}}$	element m impulse response, co-pol.
$h_{\varphi}^{\mathrm{rx}}$	RX antenna impulse response, $\underline{\varphi}$ component
$h_{\varphi}^{\mathrm{tx}}$	TX antenna impulse response, $\underline{\varphi}$ component
$h_{\mathrm{Co}}^{\mathrm{rx}}$	RX antenna impulse response, co-pol.
$h_{n,\varphi}^{\mathrm{tgt}}$	$\underline{\varphi}$-component of abstract target n rad. field
$h_{n,\theta}^{\mathrm{tgt}}$	$\underline{\boldsymbol{\theta}}$-component of abstract target n rad. field
h_{θ}^{rx}	RX antenna impulse response, $\underline{\boldsymbol{\theta}}$ component
h_{θ}^{tx}	TX antenna impulse response, $\underline{\boldsymbol{\theta}}$ component
$\underline{\boldsymbol{h}}^{\mathrm{rx}}$	RX antenna impulse response
$\underline{\boldsymbol{h}}_{n}^{\mathrm{tgt}}$	time-domain radar cross section of target n
$\underline{\boldsymbol{h}}^{\mathrm{tx}}$	TX antenna impulse response
κ	elevation angle
λ	wavelength
λ_{h}	wavelength at highest frequency of operation
λ_{l}	wavelength at lowest frequency of operation
μ	sweep rate
N	number of targets
$\underline{\boldsymbol{O}}^{\mathrm{tx}}$	antenna transmit transmit factor

$\underline{\boldsymbol{O}}_m^{\text{el}}$	antenna transmit factor of antenna element m
$O_{\text{Co}}^{\text{tx}}$	antenna transmit factor, co-pol.
$\underline{\boldsymbol{o}}^{\text{tx}}$	antenna transmit factor
$\underline{\boldsymbol{o}}_m^{\text{el}}$	transmit factor of antenna element m
o_{φ}^{tx}	antenna transmit factor, $\underline{\boldsymbol{\varphi}}$ component
o_{θ}^{tx}	antenna transmit factor, $\underline{\boldsymbol{\theta}}$ component
PM^{QS}	phase-modulating signal
PM_m^{QS}	phase-modulating signal for antenna m
φ	φ coordinate of spherical coordinate system
φ^{aut}	φ coordinate in AUT antenna coordinate system
ϕ^{b}	beat phase
$\underline{\boldsymbol{\varphi}}$	basis vector in φ direction
$\underline{\boldsymbol{\varphi}}^{\text{rx}}$	basis vector in φ direction, RX ant. coordinate system
$\underline{\boldsymbol{\varphi}}_m^{\text{tgt}}$	basis vector in φ direction, TGT n coordinate system
$\underline{\boldsymbol{\varphi}}^{\text{tx}}$	basis vector in φ direction, TX ant. coordinate system
ϕ_n^{b}	beat phase of target n
$\phi_{m,n}^{\text{b}}$	beat phase at antenna m of target n
ϕ	instantaneous phase
$\phi^{\text{mix,diff}}$	instantaneous phase of difference component
${}^1\phi^{\text{mix,diff}}$	inst. phase of diff. component in interval 1
${}^2\phi^{\text{mix,diff}}$	inst. phase of diff. component in interval 2
${}^3\phi^{\text{mix,diff}}$	inst. phase of diff. component in interval 3
${}^4\phi^{\text{mix,diff}}$	inst. phase of diff. component in interval 4
${}^5\phi^{\text{mix,diff}}$	inst. phase of diff. component in interval 5
$\phi_n^{\text{mix,diff}}$	inst. phase of diff. component target n antenna m
$\phi^{\text{mix,sum}}$	instantaneous phase of sum component
${}^1\phi^{\text{mix,sum}}$	inst. phase of sum component in interval 1
${}^2\phi^{\text{mix,sum}}$	inst. phase of sum component in interval 2
${}^3\phi^{\text{mix,sum}}$	inst. phase of sum component in interval 3
${}^4\phi^{\text{mix,sum}}$	inst. phase of sum component in interval 4
${}^5\phi^{\text{mix,sum}}$	inst. phase of sum component in interval 5
$\phi_n^{\text{mix,sum}}$	inst. phase of sum component target n antenna m
φ^{ref}	φ coordinate in REF antenna coordinate system
φ^{rx}	φ coordinate in RX antenna coordinate system
φ_m^{rx}	φ coordinate in RX antenna m coordinate system
φ^{tx}	φ coordinate in TX antenna coordinate system
φ	direction of arrival
φ_n	direction of arrival of target n

φ_{start}	φ start angle used in DOA estimation
φ_{step}	φ stepsize used in DOA estimation
$\underline{\boldsymbol{p}}^{\text{mu}}$	position of MU
$\underline{\boldsymbol{p}}^{\text{ru}}$	position of RU
$\underline{\boldsymbol{p}}^{\text{rx}}$	position of receiver/RX antenna
$\underline{\boldsymbol{p}}^{\text{rx}}_m$	position of receiver/RX antenna m
$\underline{\boldsymbol{p}}^{\text{tgt}}_n$	position of target/reflector n
$\underline{\boldsymbol{p}}^{\text{tx}}$	position of TX antenna
$\underline{\boldsymbol{r}}$	arbitrary point in space
r_n	range of target n
r	range
$\hat{r}$	estimated range
$\underline{\boldsymbol{\rho}}^{\text{tx}}$	basis vector in ρ direction, TX ant. coordinate system
ρ^{tx}	ρ coordinate in TX antenna coordinate system
$\underline{\boldsymbol{r}}^{\text{tx}}$	position vector in TX antenna coordinate system
R_{UCA}	UCA radius
T^{d}_n	propagation delay between target n and RX antenna
$T^{\text{d}}_{m,n}$	propagation delay between target n and RX antenna m
T_{guard}	guard interval
$T^{\text{rt}}_{m,n}$	round-trip time of target n and RX antenna m
T^{rt}_n	round-trip time between TX, target n and RX
T_{s}	sampling period for IF signals
$T_{\text{s,delay}}$	time delay before starting sampling
$T_{\text{s,RF}}$	sampling period for RF signals
$T^{\text{tgt,r}}_n$	propagation delay between target n and position $\underline{\boldsymbol{r}}$
$T^{\text{tgt,rx}}_n$	propagation delay between target n and RX
$T^{\text{tx,r}}$	propagation delay between TX and coordinate r
$T^{\text{tx,rx}}$	propagation delay between TX and RX
$T^{\text{tx,tgt}}_n$	propagation delay between target n and TX
θ	direction of arrival
θ	θ coordinate of spherical coordinate system
θ^{aut}	θ coordinate in AUT antenna coordinate system
$\underline{\boldsymbol{\theta}}$	basis vector in θ direction
$\underline{\boldsymbol{\theta}}^{\text{rx}}$	basis vector in θ direction, RX ant. coordinate system
$\underline{\boldsymbol{\theta}}^{\text{tgt}}_m$	basis vector in θ direction, TGT n coordinate system
$\underline{\boldsymbol{\theta}}^{\text{tx}}$	basis vector in θ direction, TX ant. coordinate system
θ_{const}	θ angle used for DOA estimation
θ_n	direction of arrival of target n

θ^{ref}	θ coordinate in REF antenna coordinate system
θ^{rx}	θ coordinate in RX antenna coordinate system
θ_m^{rx}	θ coordinate in RX antenna m coordinate system
θ^{tx}	θ coordinate in TX antenna coordinate system
U^{G}	generator voltage, frequency domain
$U_{\text{norm}}^{\text{rx}}$	normalization voltage receiver
$U_{\text{norm}}^{\text{tx}}$	normalization voltage transmitter
U^{rx}	total received voltage, frequency domain
U^{+}	voltage wave incident on port, frequency domain
$U^{\text{tx+}}$	voltage wave incident on TX side port, frequency domain
U^{-}	voltage wave leaving port, frequency domain
$U^{\text{rx-}}$	voltage wave leaving RX side port, frequency domain
$U^{\text{tx-}}$	voltage wave leaving TX side port, frequency domain
u^{G}	generator voltage, time domain
u^{rx}	total received voltage, time domain
u^{+}	voltage wave incident on port, time domain
$u^{\text{tx+}}$	voltage wave incident on TX side port, time domain
u^{-}	voltage wave leaving port, time domain
$u^{\text{rx-}}$	voltage wave leaving RX side port, time domain
$u_m^{\text{tx+}}$	voltage wave incident on TX side port m, time domain
$\hat{\varphi}$	estimated direction of arrival
ω	angular frequency
X^{rx}	received signal
X^{tx}	transmitted signal
x^{b}	beat signal
$\underline{\boldsymbol{x}}^{\text{b}}$	beat signal vector
$\underline{\boldsymbol{x}}^{\text{b,FF}}$	beat signal vector, far field approximation
$\underline{\boldsymbol{x}}^{\text{b,LP}}$	beat signal vector, linear-phase approximation
$\underline{\boldsymbol{x}}_{\text{QS}}^{\text{b,LP}}$	beat signal, linear-phase and quasi-stationary approximation
x_m^{b}	beat signal at RX antenna m
$x^{\text{b,QS}}$	QS approximation of beat signal
x^{lo}	local oscillator signal
$x^{\text{lo,mu}}$	local oscillator signal in MU
$x^{\text{lo,ru}}$	local oscillator signal in RU
x^{mix}	mixed signal
$x^{\text{mix,LP}}$	low-pass filtered mixed signal
$x_m^{\text{mix,LP}}$	low-pass filtered mixed signal at RX antenna m
x_m^{mix}	mixed signal at RX antenna m

$x^{\mathrm{rx,QS}}$	QS approximation of RX signal
x^{rx}	received signal
x_m^{rx}	received signal at RX antenna m
x^{tx}	transmitted signal
Z^{c}	characteristic impedance
$Z_{\mathrm{c}}^{\mathrm{rx}}$	characteristic impedance on RX side
$Z_{\mathrm{c}}^{\mathrm{tx}}$	characteristic impedance on TX side
Z_{F0}	free space wave impedance, for vacuum $Z_{\mathrm{F0}} \approx 377$

List of Figures

Bibliography

[1] Z. Sahinoglu, S. Gezici, and I. Guvenc, *Ultra-wideband Positioning Systems*. Cambridge, UK: Cambridge University Press, 2008.

[2] J. Chung, M. Donahoe, C. Schmandt, I.-J. Kim, P. Razavai, and M. Wiseman, "Indoor location sensing using geo-magnetism", in *Proceedings of the 9th International Conference on Mobile Systems, Applications, and Services*, Washington, DC, Jun. 2011, pp. 141–154.

[3] M. I. Skolnik, *Introduction to Radar Systems*, 3rd ed. New York, NY: Mc Graw Hill International Editions, 2001.

[4] M. Skolnik, *Radar Handbook*, 3rd ed. New York, NY: McGraw-Hill Professional, 2008.

[5] A. Stove, "Linear FMCW radar techniques", *IEE Proceedings of Radar and Signal Processing*, vol. 139, no. 5, pp. 343–350, 1992.

[6] B. A. Atayants, V. M. Davydochkin, V. V. Ezerskiy, V. S. Parshin, and S. M. Smolskiy, *Precision FMCW Short-Range Radar for Industrial Applications*. Boston, MA: Artech House, 2014.

[7] I. V. Komarov and S. M. Smolskiy, *Fundamentals of Short-Range FM Radar*. Boston, MA: Artech House, 2003.

[8] E. Lee, "Cyber physical systems: design challenges", in *11th IEEE International Symposium on Object Oriented Real-Time Distributed Computing (ISORC)*, Orlando, FL, May 2008, pp. 363–369.

[9] Federal Ministry of Education and Research. (Apr. 2015). Industrie 4.0: Innovationen für die Produktion von morgen. In German, [Online]. Available: http://www.bmbf.de/publikationen.

[10] C. A. Balanis, *Antenna Theory: Analysis and Design*, 2nd ed. Hoboken, NJ: John Wiley & Sons, 2005.

[11] S. Roehr, P. Gulden, and M. Vossiek, "Precise distance and velocity measurement for real time locating in multipath environments using a frequency-modulated continuous-wave secondary radar approach", *IEEE Transactions on Microwave Theory and Techniques*, vol. 56, no. 10, pp. 2329–2339, 2008.

[12] S. Röhr, *System-Theoretic Analysis and Optimization of a Novel Secondary Radar Concept for Precise Distance and Velocity Measurement*, in German. Berlin, Germany: Logos-Verlag, 2010.

[13] R. Gierlich, *A Reconfigurable MIMO System For High-Precision FM-CW Radiolocation*, in German. Munich, Germany: Dr. Hut, Mar. 2010.

[14] C. Zhang, M. Kuhn, B. Merkl, A. Fathy, and M. Mahfouz, "Real-time noncoherent UWB positioning radar with millimeter range accuracy: theory and experiment", *IEEE Transactions on Microwave Theory and Techniques*, vol. 58, no. 1, pp. 9–20, Jan. 2010.

[15] Symeo GmbH. (Apr. 2015). LPR-2D, [Online]. Available: http://www.symeo.com.

[16] M. Maser, G. Fischer, R. Weigel, and T. Ussmueller, "An integrated SiGe bipolar VCO with linearized tuning behavior and ultra-wide tuning range for UWB FMCW local positioning systems", in *International Semiconductor Conference Dresden - Grenoble (ISCDG)*, Sep. 2012, pp. 25–28.

[17] B. Waldmann, R. Weigel, and P. Gulden, "Method for high precision local positioning radar using an ultra wideband technique", in *IEEE MTT-S International Microwave Symposium Dig.*, Atlanta, GA, 2008, pp. 117–120.

[18] C. Meier, A. Terzis, and S. Lindenmeier, "A robust 3D high precision radio location system", in *IEEE MTT-S International Microwave Symposium Dig.*, Honolulu, HI, Jun. 2007, pp. 397–400.

[19] ——, "Investigation and suppression of multipath influence on indoor radio location in the millimeter wave range", in *Wave Propagation in Telecommunications, Microwave Remote Sensing, Navigation, and High-Speed Digital Data Transmission (WFMN)*, Chemnitz, Germany, Jul. 2007, pp. 21 –24.

[20] T. McEwan, "Radiolocation system having writing pen application", pat. US6747599 B2, Jun. 2004.

[21] G. Ossberger, T. Buchegger, E. Schimback, A. Stelzer, and R. Weigel, "Non-invasive respiratory movement detection and monitoring of hidden humans using ultra wideband pulse radar", in *International Workshop on Ultra Wideband Systems. Joint with*

Conference on Ultrawideband Systems and Technologies (UWBST IWUWBS), Kyoto, Japan, May 2004, pp. 395–399.

[22] A. Fujii, H. Sekiguchi, M. Asai, S. Kurashima, H Ochiai, and R. Kohno, "Impulse radio UWB positioning system", in *IEEE Radio and Wireless Symposium*, Long Beach, CA, Jan. 2007, pp. 55–58.

[23] Z. Low, J. Cheong, C. Law, W. Ng, and Y. Lee, "Pulse detection algorithm for line-of-sight (LOS) UWB ranging applications", *IEEE Antennas and Wireless Propagation Letters*, vol. 4, pp. 63–67, 2005.

[24] R. Zetik, J. Sachs, and R. Thoma, "UWB localization - active and passive approach [ultra wideband radar]", in *21st IEEE Instrumentation and Measurement Technology Conference (IMTC)*, vol. 2, Como, Italy, May 2004, pp. 1005–1009.

[25] A. Stelzer, C. Diskus, K. Lubke, and H. Thim, "A microwave position sensor with submillimeter accuracy", *IEEE Transactions on Microwave Theory and Techniques*, vol. 47, no. 12, pp. 2621–2624, Dec. 1999.

[26] A. Stelzer, K. Pourvoyeur, and A. Fischer, "Concept and application of LPM - a novel 3-D local position measurement system", *IEEE Transactions on Microwave Theory and Techniques*, vol. 52, no. 12, pp. 2664–2669, Dec. 2004.

[27] F. Ellinger, R. Eickhoff, R. Gierlich, J. Huttner, A. Ziroff, S. Wehrli, T. Ussmuller, J. Carls, V. Subramanian, M. Krcmar, R. Mosshammer, S. Spiegel, D. Doumenis, A. Kounoudes, K. Kurek, Y. Yashchyshyn, C. Papadias, P. Tragas, A. Kalis, and E. Avatagelou, "Local positioning for wireless sensor networks", in *IEEE Globecom Workshops*, Washington, DC, Jan. 2007, pp. 1–6.

[28] R. Mosshammer, M. Huemer, R. Szumny, K. Kurek, J. Huttner, and R. Gierlich, "A 5.8 GHz local positioning and communication system", in *IEEE MTT-S International Microwave Symposium Dig.*, Honolulu, HI, Jun. 2007, pp. 1237–1240.

[29] P. Tragas, A. Kalis, C. Papadias, F. Ellinger, R. Eickhoff, T. Ussmuller, R. Mosshammer, M. Huemer, A. Dabek, D. Doumenis, and A. Kounoudes, "RESOLUTION: reconfigurable systems for mobile local communication and positioning", in *Mobile and Wireless Communications Summit*, Budapest, Hungary, Jul. 2007, pp. 1–5.

[30] R. Feger, C. Wagner, S. Schuster, S. Scheiblhofer, H. Jager, and A. Stelzer, "A 77-GHz FMCW MIMO radar based on an SiGe single-chip transceiver", *IEEE Transactions on Microwave Theory and Techniques*, vol. 57, no. 5, pp. 1020–1035, May 2009.

[31] D. Shmakov, R. Ebelt, and M. Vossiek, "Wireless sensor network with 24 GHz local positioning transceiver", in *IEEE MTT-S International Microwave Symposium Dig.*, Montreal, QC, Canada, Jun. 2012, pp. 1–3.

[32] C. Meier, A. Terzis, and S. Lindenmeier, "Accurate distance measurement with a wideband high resolution pseudo noise coded radar", in *European Radar Conference (EuRAD)*, Munich, Germany, Oct. 2007, pp. 460–463.

[33] B. Waldmann, *Design of a Pulsed Frequency Modulated Ultra-Wideband System for High Precision Local Positioning*, in German. Berlin, Germany: Logos Verlag, 2011.

[34] P. Scherz, A. Haderer, R. Feger, G. Stelzhammer, and A. Stelzer, "Array processing system for the local position measurement system LPM", in *Proc. International Conference on Applied Electromagnetics and Communications (ICECom)*, Dubrovnik, Croatia, Sep. 2010, pp. 1–4.

[35] R. Feger, C. Pfeffer, W. Scheiblhofer, C. Schmid, M. Lang, and A. Stelzer, "A 77-GHz cooperative radar system based on multi-channel FMCW stations for local positioning applications", *IEEE Transactions on Microwave Theory and Techniques*, vol. 61, no. 1, pp. 676–684, Jan. 2013.

[36] R. Ebelt, A. Hamidian, D. Shmakov, T. Zhang, V. Subramanian, G. Boeck, and M. Vossiek, "Cooperative indoor localization using 24-GHz CMOS radar transceivers", *IEEE Transactions on Microwave Theory and Techniques*, vol. 62, no. 9, pp. 2193–2203, Sep. 2014.

[37] R. Gierlich, J. Huttner, A. Ziroff, R. Weigel, and M. Huemer, "A reconfigurable MIMO system for high-precision FMCW local positioning", *IEEE Transactions on Microwave Theory and Techniques*, vol. 59, no. 12, pp. 3228–3238, 2011.

[38] R. Feger, A Haderer, S. Schuster, S. Scheiblhofer, and A Stelzer, "A four channel 24-GHz FMCW radar sensor with two-dimensional target localization capabilities", in *IEEE MTT-S International Microwave Symposium Dig.*, Atlanta, GA, Jun. 2008, pp. 125–128.

[39] R. Feger, S. Schuster, S. Scheiblhofer, and A Stelzer, "Sparse antenna array design and combined range and angle estimation for FMCW radar sensors", in *IEEE Radar Conference*, Rome, Italy, May 2008, pp. 1–6.

[40] M.-S. Lee, "Signal modeling and analysis of a planar phased-array FMCW radar with antenna switching", *IEEE Antennas and Wireless Propagation Letters*, vol. 10, pp. 179–182, 2011.

[41] T. Jaeschke, C. Bredendiek, and N. Pohl, "A 240 GHz ultra-wideband FMCW radar system with on-chip antennas for high resolution radar imaging", in *IEEE MTT-S International Microwave Symposium Dig.*, Seattle, WA, Jun. 2013, pp. 1–4.

[42] A. Anghel, G. Vasile, R. Cacoveanu, C. Ioana, and S. Ciochina, "Short-range wideband FMCW radar for millimetric displacement measurements", *IEEE Transactions on Geoscience and Remote Sensing*, vol. 52, no. 9, pp. 5633–5642, Sep. 2014.

[43] S. Licul, "Ultra-wideband antenna characterization and measurements", PhD thesis, Virginia Polytechnic Institute & State University, Blacksburg, VA, Sep. 2004.

[44] W. Sörgel, *Charakterisierung von Antennen für die Ultra-Wideband-Technik*. Karlsruhe, Germany: KIT Scientific Publishing, May 2007.

[45] W. Sörgel and W. Wiesbeck, "Influence of the antennas on the ultra-wideband transmission", *EURASIP Journal on Advances in Signal Processing*, vol. 2005, pp. 296–305, Jan. 2005.

[46] W. Wiesbeck, G. Adamiuk, and C. Sturm, "Basic properties and design principles of UWB antennas", *Proceedings of the IEEE*, vol. 97, no. 2, pp. 372–385, 2009.

[47] S. Licul and W. A. Davis, "Unified frequency and time-domain antenna modeling and characterization", *IEEE Transactions on Antennas and Propagation*, vol. 53, no. 9, pp. 2882–2888, 2005.

[48] O. Allen, D. Hill, and A. Ondrejka, "Time-domain antenna characterizations", *IEEE Transactions on Electromagnetic Compatibility*, vol. 35, no. 3, pp. 339–346, Aug. 1993.

[49] A. Shlivinski, E. Heyman, and R. Kastner, "Antenna characterization in the time domain", *IEEE Transactions on Antennas and Propagation*, vol. 45, no. 7, pp. 1140–1149, 1997.

[50] E. G. Farr and C. E. Baum, "Extending the definitions of antenna gain and radiation pattern into the time domain", *Sensor and Simulation Notes*, 1992.

[51] C. Baum, "General properties of antennas", *IEEE Transactions on Electromagnetic Compatibility*, vol. 44, no. 1, pp. 18–24, 2002.

[52] M. Neinhus, S. Held, and K. Solbach, "FIR-filter based equalization of ultra wideband mutual coupling on linear antenna arrays", in *2nd International ITG Conference on Antennas (INICA)*, Munich, Germany, Mar. 2007, pp. 115–119.

[53] Y. Duroc, A. Najam, and S. Tedjini, "System modeling of the mutual coupling of multiple uwb antennas", in *IEEE Antennas and Propagation Society International Symposium (APSURSI)*, Toronto, Ontario, Canada, Jul. 2010, pp. 1–4.

[54] M. Ciattaglia and G. Marrocco, "Investigation on antenna coupling in pulsed arrays", *IEEE Transactions on Antennas and Propagation*, vol. 54, no. 3, pp. 835–843, Mar. 2006.

[55] D. Pozar, "The active element pattern", *IEEE Transactions on Antennas and Propagation*, vol. 42, no. 8, pp. 1176–1178, 1994.

[56] D. M. Pozar, "A relation between the active input impedance and the active element pattern of a phased array", *IEEE Transactions on Antennas and Propagation*, vol. 51, no. 9, pp. 2486–2489, 2003.

[57] S. Foo and S. Kashyap, "Time-domain array factor for UWB antenna array", *Electronics Letters*, vol. 39, no. 18, pp. 1304–1305, Sep. 2003.

[58] G. Kotyrba and H. Chaloupka, "On signal distortion in compact UWB arrays due to element interaction", in *IEEE Antennas and Propagation Society International Symposium (APSURSI)*, vol. 1A, Washington, DC, Jul. 2005, pp. 614–617.

[59] A.-C. Tan, M.-W. Chia, and K. Rambabu, "Time domain characterization of circularly polarized ultrawideband array", *IEEE Transactions on Antennas and Propagation*, vol. 58, no. 11, pp. 3524–3531, Jan. 2010.

[60] R. D'Errico and A. Sibille, "Single and multiple scattering in UWB bicone arrays", *International Journal of Antennas and Propagation*, vol. 2008, p. 12, 2008.

[61] S. Livingston and J. Lee, "Evolution of wide band array designs", in *IEEE Antennas and Propagation Society International Symposium (APSURSI)*, Pokane, WA, Jul. 2011, pp. 1957–1960.

[62] W. F. Croswell, T. Durham, M. Jones, D. Schaubert, P. Friederich, and J. G. Maloney, "Modern antenna handbook", in, C. A. Balanis, Ed. Hoboken, NJ: John Wiley & Sons, 2008, ch. Wideband Arrays, pp. 581 –599.

[63] B. Munk, *Finite Antenna Arrays and FSS*. Hoboken, NJ: John Wiley & Sons, 2003.

[64] Y. Ito, M. Ameya, M. Yamamoto, and T. Nojima, "Unidirectional UWB array antenna using leaf-shaped bowtie elements and flat reflector", *Electronics Letters*, vol. 44, no. 1, pp. 9–11, 2008.

[65] M. Chen and J. Wang, "Planar UWB antenna array with CPW feeding network", in *Asia-Pacific Microwave Conference (APMC)*, Hong Kong, Dec. 2008, pp. 1–4.

[66] B. Huang, Y. Yao, and Z. Feng, "Planar UWB antenna array for multifunctional wireless communication system", in *IEEE Antennas and Propagation Society International Symposium (APSURSI)*, San Diego, CA, Jul. 2008, pp. 1–4.

[67] A. Hees and J. Detlefsen, "Ultra broadband dual polarized dipole array with metallic reflector", in *IEEE International Conference on Ultra-Wideband (ICUWB)*, Vancouver, Canada, Sep. 2009, pp. 744–747.

[68] G. Adamiuk, M. Janson, W. Wiesbeck, and T. Zwick, "Dual-polarized UWB antenna array", in *IEEE International Conference on Ultra-Wideband (ICUWB)*, Vancouver, Canada, Sep. 2009, pp. 164–169.

[69] M. Chen and J. Wang, "Planar UWB antenna array with microstrip feeding network", in *IEEE International Conference on Ultra-Wideband (ICUWB)*, vol. 1, Nanjing, China, Sep. 2010, pp. 1–3.

[70] D. Sipal, A. Basu, M. Abegaonkar, and S. Koul, "Planar pattern reconfigurable uwb antenna array for scanning in personal area network application", in *International Symposium on Antennas and Propagation (ISAP)*, Kaohsiung, Taiwan, Dec. 2014, pp. 91–92.

[71] S. A. Schelkunoff, *Electromagnetic waves*. Toronto, Canada: D.Van Nostrand Company, 1951.

[72] H. Schantz, *The Art and Science of Ultra-Wideband Antennas*. Norwood, MA: Artech House, 2005.

[73] D. M. Grimes, "Biconical receiving antenna", *Journal of Mathematical Physics*, vol. 23, no. 5, pp. 897–914, 1982.

[74] B. Stockbroeckx and A. Vander Vorst, "Electromagnetic modes in conical transmission lines with application to the linearly tapered slot antenna", *IEEE Transactions on Antennas and Propagation*, vol. 48, no. 3, pp. 447–455, 2000.

[75] R. Gunnarsson, T. Martin, and A. Ouacha, "Wide-band circular antenna arrays consisting of bicone, semi bicone or bowtie elements", in *Asia-Pacific Microwave Conference (APMC)*, Yokohama, Japan, Dec. 2006, pp. 2074–2077.

[76] V. Kononov and C. Balanis, "Bow-tie and bicone array designs for broad band performance specifications", in *IEEE Antennas and Propagation Society International Symposium (APSURSI)*, Charleston, SC, Jun. 2009, pp. 1–4.

[77] P. J. Gibson, "The Vivaldi aerial", in *European Microwave Conference*, Brighton, England, Sep. 1979, pp. 101–105.

[78] D. Schaubert, E. Kollberg, T. Korzeniowski, T. Thungren, J. Johansson, and K. Yngvesson, "Endfire tapered slot antennas on dielectric substrates", *IEEE Transactions on Antennas and Propagation*, vol. 33, no. 12, pp. 1392–1400, Dec. 1985.

[79] K. Ebnabbasi, D. Busuioc, R. Birken, and M. Wang, "Taper design of Vivaldi and co-planar tapered slot antenna (tsa) by Chebyshev transformer", *IEEE Transactions on Antennas and Propagation*, vol. 60, no. 5, pp. 2252–2259, May 2012.

[80] D.-C. Chang, C.-H. Liao, and P. Hsu, "UWB antenna array", in *International Workshop on Antenna Technology (iWAT)*, Hong Kong, Mar. 2011, pp. 164–167.

[81] J. D. S. Langley, P. S. Hall, and P. Newham, "Balanced antipodal Vivaldi antenna for wide bandwidth phased arrays", *IEE Proceedings Microwaves, Antennas and Propagation*, vol. 143, no. 2, pp. 97–102, 1996.

[82] H. Xu, G. Zhao, Z. Zhang, H. Sun, and X. Lv, "Antipodal Vivaldi antenna for phased array antenna applications", in *5th Global Symposium on Millimeter Waves (GSMM)*, Harbin, Heilongjiang, China, May 2012, pp. 200 –203.

[83] Y. Yang, C. Zhang, S. Lin, and A. Fathy, "Development of an ultra wideband Vivaldi antenna array", in *IEEE Antennas and Propagation Society International Symposium (APSURSI)*, vol. 1A, Washington, DC, Jul. 2005, pp. 606 –609.

[84] A. Elboushi, D. Joanes, M. Derbas, S. Khaled, A. Zafar, S. Attabibi, and A. Sebak, "Design of UWB antenna array for through-wall detection system", in *IEEE Symposium on Wireless Technology and Applications (ISWTA)*, Kuching, Malaysia, Sep. 2013, pp. 349–354.

[85] C. Rodenbeck, S.-G. Kim, W.-H. Tu, M. Coutant, S. Hong, M. Li, and K. Chang, "Ultra-wideband low-cost phased-array radars", *IEEE Transactions on Microwave Theory and Techniques*, vol. 53, no. 12, pp. 3697–3703, Dec. 2005.

[86] C. Zhang, M. Kuhn, M. Mahfouz, and A. E. Fathy, "Planar antipodal Vivaldi antenna array configuration for low cross-polarization and reduced mutual coupling performance", in *Proc. IEEE Antennas and Propagation Society Int. Symp.*, Honolulu, HI, Jun. 2007, pp. 725–728.

[87] G. Vinci and R. Weigel, "Multiband planar Vivaldi antenna for mobile communication and industrial applications", in *International Conference on Electromagnetics in Advanced Applications (ICEAA)*, Sydney, NSW, Sep. 2010, pp. 93–96.

[88] *Quantities and Units - Part 2: Mathematical signs and symbols to be used in the natural science and technology*, ISO 8000-2. International Organization for Standardization (ISO).

[89] Z. Chen, G. K. Gokeda, and Y. Yu, *Introduction to Direction-of-Arrival Estimation*. Boston, MA: Artech House, 2010.

[90] H. F. Mathis, "A short proof that an isotropic antenna is impossible", *Proceedings of the IRE*, vol. 39, no. 8, p. 970, 1951.

[91] ——, "On isotropic antennas", *Proceedings of the IRE*, vol. 42, no. 12, p. 1810, 1954.

[92] W. Van Cappellen, R. V. De Jongh, and L. Ligthart, "Potentials of ultra-short-pulse time-domain scattering measurements", *IEEE Antennas and Propagation Magazine*, vol. 42, no. 4, pp. 35–45, Aug. 2000.

[93] S. Ayhan, P. Pahl, T. Kayser, M. Pauli, and T. Zwick, "Frequency estimation algorithm for an extended FMCW radar system with additional phase evaluation", in *German Microwave Conference (GeMIC)*, Darmstadt, Germany, Mar. 2011, pp. 1–4.

[94] S. Ayhan, M. Pauli, T. Kayser, S. Scherr, and T. Zwick, "FMCW radar system with additional phase evaluation for high accuracy range detection", in *European Radar Conference (EuRAD)*, Manchester, United Kingdom, Oct. 2011, pp. 117–120.

[95] R. Feger, C. Wagner, S. Schuster, S. Scheiblhofer, and A Stelzer, "Accuracy improvement for direction of arrival estimation by the use of a mirror element", *IEEE Transactions on Microwave Theory and Techniques*, vol. 59, no. 4, pp. 1016–1024, Apr. 2011.

[96] C. Pfeffer, R. Feger, C. Wagner, and A Stelzer, "FMCW MIMO radar system for frequency-division multiple TX-beamforming", *IEEE Transactions on Microwave Theory and Techniques*, vol. 61, no. 12, pp. 4262–4274, Dec. 2013.

[97] M. Eric, A Zejak, and M. Obradovic, "Ambiguity characterization of arbitrary antenna array: type I ambiguity", in *Proccedings of the IEEE 5th International Symposium on Spread Spectrum Techniques and Applications*, vol. 2, Sep. 1998, 399–403 vol.2.

[98] C. P. Mathews and M. Zoltowski, "Eigenstructure techniques for 2-D angle estimation with uniform circular arrays", *IEEE Transactions on Signal Processing*, vol. 42, no. 9, pp. 2395–2407, Sep. 1994.

[99] W. Xiao, X.-C. Xiao, and H.-M. Tai, "Rank-1 ambiguity DOA estimation of circular array with fewer sensors", in *The 45th Midwest Symposium on Circuits and Systems (MWSCAS)*, vol. 3, Tulsa, OK, Aug. 2002, pp. III–29–III–32.

[100] S. Chan and C. Pun, "On the design of digital broadband beamformer for uniform circular array with frequency invariant characteristics", in *IEEE International Symposium on Circuits and Systems (ISCAS)*, vol. 1, Phoenix-Scottsdale, AZ, May 2002, I–693–I–696 vol.1.

[101] H. Steyskal, "Circular array with frequency-invariant pattern", in *Antennas and Propagation Society International Symposium (APS)*, vol. 3, San Jose, CA, Jun. 1989, pp. 1477–1480.

[102] H. Chen, S. Chan, and K. Ho, "Adaptive beamforming using frequency invariant uniform concentric circular arrays", *IEEE Transactions on Circuits and Systems I: Regular Papers*, vol. 54, no. 9, pp. 1938–1949, Sep. 2007.

[103] S. Chandran, Ed., *Advances in Direction-of-Arrival Estimation*. Boston, MA: Artech House, Dec. 2005.

[104] H. L. Van Trees, *Optimum array processing*, ser. Detection, estimation, and modulation theory. New York: Wiley, 2002, vol. 4, XXIV, 1443 S. : graph. Darst.

[105] B. Carlson, "Covariance matrix estimation errors and diagonal loading in adaptive arrays", *IEEE Transactions on Aerospace and Electronic Systems*, vol. 24, no. 4, pp. 397–401, Jul. 1988.

[106] Y. L. Chen and J.-H. Lee, "Finite data performance analysis of MVDR antenna array beamformers with diagonal loading", *Progress In Electromagnetics Research*, vol. 134, pp. 475–507, 2013.

[107] J.-F. Synnevag, A. Austeng, and S. Holm, "Adaptive beamforming applied to medical ultrasound imaging", *IEEE Transactions on Ultrasonics, Ferroelectrics, and Frequency Control*, vol. 54, no. 8, pp. 1606–1613, Aug. 2007.

[108] A. Stelzer, M. Pichler, and S. Schuster, "Frequency estimation in linear frequency modulated radar systems", *Frequenz*, vol. 60, no. 1-2, pp. 31–36, 2006.

[109] A. Stelzer and M. Pichler, "Resolution enhancement with model-based frequency estimation algorithms in radar signal processing", *Subsurface Sensing Technologies and Applications*, vol. 4, no. 3, pp. 241–261, 2003.

[110] P. Gulden, M. Vossiek, E. Storck, and P. Heide, "Application of state space frequency estimation techniques to radar systems", in *IEEE International Conference on Acoustics, Speech, and Signal Processing (ICASSP)*, vol. 5, Salt Lake City, UT, May 2001, pp. 2877–2880.

[111] M. Abou-Khousa, D. Simms, S. Kharkovsky, and R. Zoughi, "High-resolution short-range wideband FMCW radar measurements based on MUSIC algorithm", in *IEEE Instrumentation and Measurement Technology Conference (I2MTC)*, Singapore, May 2009, pp. 498–501.

[112] F. Harris, "On the use of windows for harmonic analysis with the discrete fourier transform", *Proceedings of the IEEE*, vol. 66, no. 1, pp. 51–83, Jan. 1978.

[113] E. Jacobsen and P. Kootsookos, "Fast, accurate frequency estimators [DSP tips tricks]", *IEEE Signal Processing Magazine*, vol. 24, no. 3, pp. 123–125, May 2007.

[114] H. Krim and M. Viberg, "Two decades of array signal processing research: the parametric approach", *IEEE Signal Processing Magazine*, vol. 13, no. 4, pp. 67–94, 1996.

[115] F. Belfiori, W. van Rossum, and P. Hoogeboom, "2D-MUSIC technique applied to a coherent FMCW MIMO radar", in *IET International Conference on Radar Systems (Radar 2012)*, Glasgow, United Kingdom, Oct. 2012, pp. 1–6.

[116] Y. Bucris, I Cohen, and M. Doron, "Bayesian focusing for coherent wideband beamforming", *IEEE Transactions on Audio, Speech, and Language Processing*, vol. 20, no. 4, pp. 1282–1296, May 2012.

[117] T. E. Tuncer and B. Friedlander, *Classical and Modern Direction-of-Arrival Estimation*. Burlington, MA: Academic Press, 2009.

[118] D. Rife and R. Boorstyn, "Single tone parameter estimation from discrete-time observations", *IEEE Transactions on Information Theory*, vol. 20, no. 5, pp. 591–598, Sep. 1974.

[119] S. Kay, *Fundamentals of Statistical Signal Processing*. Upper Saddle River, NJ: Prentice Hall, 1993, vol. 1.

[120] D. M. Pozar, *Microwave Engineering*, 4th ed. Hoboken, NJ: John Wiley & Sons, 2011.

[121] D. B. Davidson, *Computational Electromagnetics for RF and Microwave Engineering*. Cambridge, UK: Cambridge University Press, 2010.

[122] T. Weiland, M. Timm, and I. Munteanu, "A practical guide to3-D simulation", *IEEE Microwave Magazine*, vol. 9, no. 6, pp. 62–75, Dec. 2008.

[123] I. Munteanu, M. Timm, and T. Weiland, "It's about time", *IEEE Microwave Magazine*, vol. 11, no. 2, pp. 60–69, Apr. 2010.

[124] *IEEE Standard Test Procedures for Antennas*, ANSI/149-1979. IEEE, Dec. 1979.

[125] M. Hiebel, *Fundamentals of Vector Network Analysis*. Munich, Germany: Rohde & Schwarz GmbH & Co. KG, 2011.

[126] J. L. Allen and B. L. Diamond, "Mutual coupling in array antennas", Massachusetts Institute of Technology Lincoln Laboratory, Tech. Rep., 1966.

[127] R. C. Hansen, *Phased Array Antennas*. Hoboken, New Jersey: John Wiley & Sons, 2009.

[128] H. Steyskal and J. Herd, "Mutual coupling compensation in small array antennas", *IEEE Transactions on Antennas and Propagation*, vol. 38, no. 12, pp. 1971–1975, 1990.

[129] R. Hansen, "Relationships between antennas as scatterers and as radiators", *Proceedings of the IEEE*, vol. 77, no. 5, pp. 659–662, May 1989.

[130] M. Demirkan and R. R. Spencer, "UWB antenna characterization for circuit design", in *IEEE International Conference on Ultra-Wideband (ICU)*, Zurich, Switzerland, Sep. 2005.

[131] M. Turley, "Bandwidth formula for linear FMCW radar waveforms", in *International Radar Conference (RADAR)*, Bordeaux, France, Oct. 2009, pp. 1–6.

[132] C. Baum, E. Rothwell, Y. Chen, and D. Nyquist, "The singularity expansion method and its application to target identification", *Proceedings of the IEEE*, vol. 79, no. 10, pp. 1481–1492, 1991.

[133] J. Scheer, "Coherent radar system performance estimation", in *Record of the IEEE International Radar Conference*, Arlington, VA, May 1990, pp. 125–128.

[134] M. Pichler, A. Stelzer, P. Gulden, and M. Vossiek, "Influence of systematic frequency-sweep non-linearity on object distance estimation in FMCW/FSCW radar systems", in *33rd European Microwave Conference*, Munich, Germany, Oct. 2003, pp. 1203–1206.

[135] F. Perez-Martinez, M. Burgos-Garcia, and A. Asensio-Lopez, "Group delay effects on the performance of wideband cw-lfm radars", *IEE Proceedings Radar, Sonar and Navigation*, vol. 148, no. 2, pp. 95–100, 2001.

[136] P. Bezousek, M. Hajek, and M. Pola, "Effects of signal distortion in a FMCW radar on range resolution", in *Proc. of the 15th International Microwave Techniques Conference (COMITE)*, Brno, Czech Republic, Apr. 2010, pp. 113–116.

[137] H. T. Hui, "Decoupling methods for the mutual coupling effect in antenna arrays: a review", *Recent Patents on Engineering*, vol. 1, pp. 187 –193, 2007.

[138] S. Henault and Y. Antar, "Comparison of various mutual coupling compensation methods in receiving antenna arrays", in *IEEE Antennas and Propagation Society International Symposium (APSURSI)*, Charleston, SC, Jun. 2009, pp. 1–4.

[139] Y.-G. Kim, S.-Y. Song, and K. W. Kim, "A compact wideband ring coupler utilizing a pair of transitions for phase inversion", *IEEE Microwave and Wireless Components Letters*, vol. 21, no. 1, pp. 25–27, 2011.

[140] B. Lindmark, "Comparison of mutual coupling compensation to dummy columns in adaptive antenna systems", *IEEE Transactions on Antennas and Propagation*, vol. 53, no. 4, pp. 1332–1336, 2005.

[141] J. L. Volakis, Ed., *Antenna Engineering Handbook*, 4th ed. New York, NY: McGraw-Hill Professional, 2007.

[142] M. M. Weiner, *Monopole Antennas*. New York, NY: Marcel Dekker Inc., 2003.

[143] T. Taniguchi and T. Kobayashi, "An omnidirectional and low-VSWR antenna for the FCC-approved UWB frequency band", in *IEEE Antennas and Propagation Society International Symposium (APSURSI)*, vol. 3, Columbus, OH, Jun. 2003, pp. 460–463.

[144] D. W. Aten and R. L. Haupt, "Genetically optimized, low profile, wideband, shorted monocone antenna", in *IEEE Antennas and Propagation Society International Symposium (APSURSI)*, Charleston, SC, Jun. 2009, pp. 1–4.

[145] M. Armanious and J. S. Tyo, "UWB self-compensating antennas: numerical demonstration of the electromagnetic working principle", *IEEE Transactions on Antennas and Propagation*, vol. 57, no. 12, pp. 3736–3745, 2009.

Author's Publications

[MG1] M. Gardill, G. Fischer, R. Weigel, and A. Koelpin, "Single-element based ultra-wideband antenna array concepts for wireless high-precision 2D local positioning", in *U.R.S.I. Kleinheubacher Tagung*, Miltenberg, Germany, Sep. 2012.

[MG2] ——, "Single-element based ultra-wideband antenna array concepts for wireless high-precision 2D local positioning", *Advances in Radio Science*, vol. 11, pp. 297–305, 2013.

[MG3] ——, "Receiving mode simulations for ultra-wideband characterization of small antenna arrays and a novel look on mutual coupling", in *29th International Review of Progress in Applied Computational Electromagnetics*, Monterey, CA, Mar. 2013.

[MG4] M. Gardill, D. Kay, R. Weigel, and A. Koelpin, "Numerical investigations on the quasi-stationary response of antennas to wideband LFMCW excitation", in *European Signal Processing Conference (EUSIPCO)*, Lisbon, Portugal, Sep. 2014, pp. 969 –973.

[MG5] M. Gardill, J. Schneider, F. Oesterle, G. Fischer, R. Weigel, and A. Koelpin, "Ultra-wideband small antenna subarray module with narrow elevation pattern", in *IEEE-APS Topical Conference on Antennas and Propagation in Wireless Communications*, Torino, Italy, Oct. 2013, pp. 1261 –1264.

[MG6] M. Gardill, R. Weigel, and A. Koelpin, "Ultra-wideband small modular array antenna based on column-coupled vivaldi subarrays", in *European Conference on Antennas and Propagation (EuCAP)*, The Hague, Netherlands, Apr. 2014, pp. 3629 –3633.

[MG7] ——, "A wideband unidirectional antenna array element with stable radiation pattern", in *Proc. IEEE-APS Topical Conf. Antennas and Propagation in Wireless Communications (APWC)*, Cape Town, South Africa, Sep. 2012, pp. 554–557.

[MG8] M. Gardill, G. Fischer, R. Weigel, and A. Koelpin, "Design of a robust and low-cost monocone antenna element for use in vehicle

roof-mounted antenna arrays", in *IEEE Radio and Wireless Symposium*, Austin, TX, Jan. 2013, pp. 112 –114.

[MG9] ——, "Design of an ultra-wideband monocone circular antenna array for vehicle-integrated industrial local positioning applications", in *Proceedings of the Seventh European Conference on Antennas and Propagation (EuCAP)*, Gothenburg, Sweden, Apr. 2013, pp. 2211 –2215.

[MG10] M. Gardill, K. Finkenzeller, W. Hinz, G. Fischer, R. Weigel, and A. Koelpin, "A review and comparative study of on- and off-body performance of platform-tolerant UHF RFID tag antennas", in *8th International Conference on Body Area Networks*, Boston, MA, Oct. 2013, pp. 256–262.

[MG11] S. Zorn, M. Gardill, R. Rose, A. Goetz, R. Weigel, and A. Koelpin, "A smart jamming system for UMTS/WCDMA cellular phone networks for search and rescue applications", in *Proc. IEEE MTT-S Int. Microwave Symp. Digest (MTT)*, Montreal, QC, Canada, Jun. 2012, pp. 1–3.

[MG12] A. Sehr, M. Gardill, and W. Kellermann, "Adapting HMMs of distant-talking ASR systems using feature-domain reverberation models", in *17th European Signal Processing Conference*, Glasgow, Scotland, UK, Aug. 2009, pp. 540 –543.

[MG13] F. Oesterle, M. Gardill, R. Weigel, and A. Koelpin, "Evaluation of a microwave based contact-free testing method for mechanical sensitivity analysis of MEMS for inline integration of on-wafer measurements", in *IEEE European Microwave Week (EuMW)*, Nuremberg, Germany, Oct. 2013, pp. 72 –75.

[MG14] M. Gardill, S. Zorn, R. Weigel, and A. Koelpin, "Influencing cell reselection of UMTS user equipment using interference injection", in *Radar, Communication and Measurement Workshop*, Hamburg, Germany, Apr. 2011.

[MG15] M. Maser, M. Gardill, P. Gulden, G. Fischer, R. Weigel, and T. Ussmueller, "Local Positioning mit einem integrierten Breitband-FMCW System", in *Electrical and Electronic Engineering for Communication (EEEfCOM)*, Ulm, Germany, May 2012.

[MG16] M. Gardill, S. Zorn, R. Weigel, and A. Koelpin, "Triggering UMTS user equipment inter-RAT cell reselection using noise jammers", in *Proc. German Microwave Conf. (GeMIC)*, Darmstadt, Germany, Mar. 2011, pp. 1–4.

[MG17] M. Gardill, G. Fischer, R. Weigel, and A. Koelpin, "Receiving mode CST MWS-Matlab Co-simulations for time and frequency domain UWB small antenna array characterization", in *CST European User Conference*, Stuttgart, Germany, Apr. 2013.

[MG18] M. Hamouda, G. Guarin, M. Gardill, B. Laemmle, R. Weigel, D. Kissinger, and T. Ussmueller, "A clock synchronization for M-sequence-based ultra-wideband systems", *IEEE Transactions on Microwave Theory and Techniques*, vol. 62, no. 12, pp. 3549–3561, Dec. 2014.

[MG19] G. Guarin, M. Gardill, G. Fischer, and R. Weigel, "Ultra-wideband compressed sensing radar based on pseudo random binary sequences", in *Proc. German Microwave Conf. (GeMIC)*, Nuremberg, Germany, Mar. 2015.

This book covers the characterization and design of small array antennas for ultra-wideband (UWB) industrial linear frequency-modulated continuous-wave (FMCW) RADAR systems. Although the techniques developed in this work are not limited to a certain application scenario, in particular the design of a four-element uniform linear and four-element uniform circular array antenna is considered.

The antenna arrays are used for implementing direction-of-arrival (DOA) estimation in a novel UWB secondary RADAR system for industrial local positioning applications. The system‘s frequency range is from 6 GHz to 9 GHz and hence possesses a relative bandwidth of 40 %.

State of the art industrial FMCW RADAR systems in contrast traditionally operate in the narrowband regime with relative bandwidths much smaller than 10 %. In consequence methods traditionally used for characterizing the antennas, for modeling the influence of the antennas on the RADAR system performance, for implementing direction-of-arrival estimation in FMCW RADAR systems, and for designing antenna arrays are not sufficient.

Their application to UWB FMCW RADAR systems is carefully reviewed, and where necessary extended to take into account effects emerging due to the large relative bandwidth.

ISBN 978-3-944057-35-4

9 783944 057354

FAU UNIVERSITY PRESS 2015